Dottorato di Ricerca in Ingegneria delle Strutture

PhD School in Structural Engineering

Dipartimento di Ingegneria Civile, Ambientale, Aerospaziale, dei Materiali
Università degli Studi di Palermo
Viale delle Scienze, 90128 Palermo (Italy)

Coordinatore: **Prof. Ing. Giuseppe Giambanco**

Experimental analysis, numerical and analytical modeling of shear strength mechanisms in Hybrid Steel Trussed Concrete Beams

Tesi di Dottorato di

Ing. Alessia Monaco

Relatore: ***Prof. Ing. Lidia La Mendola***

Settore Scientifico Disciplinare ICAR 09

Dottorato di Ricerca in Ingegneria delle Strutture - XXIV Ciclo
Palermo, 15 Gennaio 2014

Ai miei amati genitori

RINGRAZIAMENTI

Questa tesi rappresenta la conclusione di un percorso tanto desiderato quanto complesso, talvolta arduo ma sempre entusiasmante, che mi ha arricchito professionalmente e fatto crescere come persona.

Il primo ringraziamento, particolarmente sentito, va al mio relatore, Prof. Lidia La Mendola, per aver sin da subito creduto in me, dandomi fiducia e fornendomi l'impeccabile guida e i preziosi insegnamenti che hanno accompagnato con costanza lo sviluppo di questa ricerca, arricchendone i contenuti e rendendone possibile il compimento.

Doveroso è anche il ringraziamento per il Prof. Piero Colajanni che ha collaborato con attivo e sincero interesse allo sviluppo di questo lavoro, contribuendo significativamente a districarne i passaggi più difficili.

È ancora al mio relatore che va, inoltre, il sincero apprezzamento per avermi offerto la possibilità, durante questo triennio, di maturare la mia esperienza di studio collaborando con gruppi di ricerca di università italiane e straniere. Ricorderò sempre, infatti, con grande piacere i mesi trascorsi presso l'Università di Salerno, dove ho lavorato sotto l'ineccepibile guida del Prof. Gianvittorio Rizzano. E, al contempo, non posso trascurare di far menzione dell'intensa e vivace collaborazione con l'Ing. Massimo Latour, prezioso compagno dell'elaborazione di complessi modelli, dal quale ho molto imparato e a cui riservo la mia più sincera e affettuosa stima.

Più recente è il ricordo del periodo trascorso negli Stati Uniti con la guida speciale dei Professori Roberto Ballarini e Jaliang Le che mi hanno accolto presso il *Department of Civil Engineering, University of Minnesota*. I loro magistrali insegnamenti e l'attività di ricerca condotta hanno fornito un

prezioso valore aggiunto a questo lavoro. È doveroso ringraziare, altresì, il *Minnesota Supercomputing Institute* per il supporto computazionale ad alcune delle più onerose simulazioni numeriche facenti parte della tesi.

Desidero esprimere, inoltre, un sentito ringraziamento al Prof. Giuseppe Campione per gli originali spunti di riflessione forniti in numerose occasioni.

Per la riuscita delle prove sperimentali presso il Laboratorio del DICAM, esprimo un particolare ringraziamento al Prof. Salvatore Benfratello per l'attività di coordinamento svolta, ad Erasmo Cataldo per l'importante contributo tecnico, nonché all'Ing. Salvo Priolo per i suoi preziosi consigli.

Ringrazio, altresì, il Sig. Ruggero Garaffa che, in numerose occasioni, mi ha fornito i riferimenti bibliografici anche più rari di cui gli facevo richiesta.

Un ricordo affettuoso ai colleghi della stanza dottorandi, Nino, Giovanni, Giuseppe, Fabio e Marcello, con i quali ho condiviso molte ore di lavoro.

Infine, il più importante e sentito ringraziamento, che, per quanto altisonante, sarà sempre inadeguato ad esprimere ciò che veramente sento: alla mia famiglia, mio padre, mia madre e mia sorella Flavia, punto di riferimento di tutta la mia vita, che non hanno mai trascurato di incoraggiarmi e sostenermi, condividendo con me ogni più piccolo particolare del mio vissuto. A loro va il mio più grande "grazie" per l'immenso amore che mi riservano e che mai abbastanza riuscirò a ricambiare. È a loro che dedico ogni singola pagina di questa tesi.

ACKNOWLEDGEMENTS

This thesis represents the conclusion of a really desired, as well as complex, road which has been arduous, sometimes, but always exiting and which enriched me professionally and made me grow as a person.

The first particularly felt acknowledgement has to be addressed to my advisor, Prof. Lidia La Mendola, for believing in me since the beginning, trusting me and providing her excellent guide and precious teachings which accompanied constantly the development of this research, enriching its contents and making it possible to be accomplished.

It is also due to thank Prof. Piero Colajanni who collaborated to the development of this work with sincere and active interest, significantly contributing in the solution of some of the most difficult issues.

Moreover, it is still to my advisor that my most sincere appreciation is devoted for giving me the opportunity, during this period, to improve my study experience collaborating with other research groups of both Italian and foreign universities. I will always remember, in fact, with great pleasure the months spent at the University of Salerno, where I worked under the exceptional guidance of Prof. Gianvittorio Rizzano. And, in the meantime, I cannot neglect to mention the intense and challenging collaboration with Eng. Massimo Latour, precious companion in the development of complex models, from whom I learned a lot and to whom I reserve my most sincere and affectionate esteem.

More recent is the memory of the time spent in the United States with the special guidance of Professors Roberto Ballarini and Jaliang Le who welcomed me at the Department of Civil Engineering, University of Minnesota. Their excellent teachings and the research carried out constituted

a precious added value to the enhancement of this work. A dutiful thanks must also be addressed to the Minnesota Supercomputing Institute for the computational support in performing some of the more costly numerical simulations part of this thesis.

Moreover, I would like to express my sincere gratitude to Prof. Giuseppe Campione for his really original insights provided in numerous occasions.

For the performance of the experimental tests at the Laboratory of Structures of DICAM, I would like to express a special acknowledgement to Prof. Salvatore Benfratello for the coordination activities, to Mr. Erasmo Cataldo for the important technical contribution and also to Eng. Salvo Priolo for his valuable practical advice.

I want also to thank Mr. Ruggero Garaffa for providing me even the rarer references in the literature which I did request.

Furthermore, an affectionate memory for my colleagues, Nino, Giovanni, Giuseppe, Fabio and Marcello, with whom I shared several hours of work.

Finally, the most important and sincere thanks, that, even if majestic, will always be inadequate to express what I really feel: to my family, my father, my mother and my sister Flavia, the reference point of all my life, who never neglected to encourage me and support me, sharing with me every little detail of my own experience. To them my biggest "thank you" for their incommensurable love I will never be able enough to reciprocate. It is to them that I dedicate every single page of this thesis.

SOMMARIO

Oggetto della presente ricerca è lo studio del comportamento a taglio di travi prefabbricate reticolari miste, denominate nella recente letteratura scientifica internazionale *Hybrid Steel Trussed Concrete Beams (HSTCBs)*. Si tratta di una tipologia strutturale costituita da un travatura reticolare metallica completata da un getto di calcestruzzo in modo che, a maturazione avvenuta, si realizza la solidarietà dei due materiali e il traliccio metallico viene a costituire l'armatura della trave stessa.

A partire dagli anni Settanta, le travi reticolari miste hanno trovato largo impiego nelle costruzioni civili in quanto consentono di industrializzare, seppure in parte, il processo edilizio, evitando di modificare sostanzialmente i processi costruttivi e i protocolli organizzativi delle imprese esecutrici.

Con riferimento all'introduzione di tale tipologia strutturale nei telai sismoresistenti, risulta necessario adottare criteri di progetto basati sulla gerarchia delle resistenze, garantendo sia una soglia di taglio resistente adeguata a scongiurare rotture fragili, che un comportamento ciclico dei nodi trave-colonna adeguatamente dissipativo. Mentre il problema flessionale, con particolare riferimento alla deformabilità e alla resistenza della connessione, è stato ampiamente studiato in letteratura, le problematiche relative al taglio sono rimaste ancora aperte. In questo ambito si colloca la presente ricerca che si pone l'obiettivo di indagare il comportamento a taglio di tali travi interpretandone i *meccanismi resistenti* e le *modalità di trasmissione degli sforzi* fra traliccio metallico e matrice di calcestruzzo.

Nell'ambito dello studio del trasferimento degli sforzi sono state sviluppate analisi teoriche che si pongono l'obiettivo di interpretare prove sperimentali di push-out (ovvero di puro scorrimento) effettuate su spezzoni

di travi reticolari miste. Tali modelli di previsione della massima forza di scorrimento fanno riferimento sia ai classici modelli a traliccio con inclinazione variabile della biella di calcestruzzo compressa, tipicamente adottati per le strutture classiche in c.a., sia ai modelli con meccanismo di rottura governato dall'effetto spinotto, generalmente impiegati per le strutture composte. L'applicazione di tali modelli, secondo la loro formulazione originale, conduce generalmente ad una sottostima del carico massimo sperimentalmente ottenuto dai vari autori dalle prove di push-out. Per tale ragione si è proceduto alla formulazione di ulteriori modelli di tipo tirante-puntone, da un lato, e governati da dowel-mechanism, dall'altro, in cui sono state introdotte opportune modifiche atte a tener conto delle peculiarità geometriche e meccaniche della trave oggetto di studio.

Accanto all'interpretazione analitica del carico massimo ottenuto nelle prove di push-out, è stato anche elaborato un modello bidimensionale non lineare ad elementi finiti con la finalità di cogliere, sotto determinate ipotesi semplificative, la risposta meccanica della trave individuando i meccanismi di trasferimento degli sforzi. Il risultato della modellazione 2D mette in evidenza la difficoltà di cogliere con un modello estremamente semplificato la grande varietà dei parametri da cui dipendono i meccanismi di trasmissione degli sforzi e le modalità di rottura. Tra questi parametri, quelli che giocano un ruolo preminente sono la tridimensionalità della geometria e l'effettivo legame di aderenza tra le superfici delle barre d'acciaio (liscio o nervato) e del calcestruzzo all'interno del quale esse sono inglobate.

Alla fase della modellazione semplificata segue, pertanto, quella di una modellazione dettagliata tridimensionale con elementi "solid" realizzata attraverso il software Abaqus 6.10 che è stata sviluppata in collaborazione con il gruppo di ricerca del Prof. Gianvittorio Rizzano del *Dipartimento di Ingegneria Civile dell'Università di Salerno*. In particolare, sono stati sviluppati modelli rappresentativi, da un lato, del caso in cui le barre del traliccio metallico sono nervate, dall'altro, del caso in cui tali barre sono lisce, a partire da simulazioni sotto l'ipotesi di perfetta aderenza acciaio-calcestruzzo o di scorrimento tra le superfici, fino a modelli in cui si è implementato un legame *tensione d'aderenza-scorrimento* specifico per

barre lisce e nervate. Successivamente alla modellazione delle prove sperimentali è stata anche effettuata un'analisi parametrica per valutare l'influenza delle caratteristiche geometriche e meccaniche dei vari componenti delle travi tralicciate miste, quali per esempio la deformabilità del fondello, il tipo di acciaio liscio o nervato, oltre che le caratteristiche meccaniche dei materiali impiegati.

Successivamente allo studio del problema locale della trasmissione degli sforzi, sono stati condotti studi teorico-sperimentali atti ad investigare il comportamento globale a taglio degli elementi strutturali. In particolare si è condotta una sperimentazione su travi prefabbricate reticolari miste in semplice appoggio caricate con una forza concentrata agente in mezzeria e progettate per esibire una modalità di rottura a taglio. Per l'esecuzione delle prove è stata adottata una particolare tipologia di traliccio prodotto dalla ditta *Sicilferro Torrenovese* di Torrenova (ME) e impiegato nelle cosiddette travi SER. I campioni realizzati sono sei e sono stati classificati in due serie, "A" e "B". In particolare, i campioni della serie "A" sono stati testati a momento positivo, ovvero applicando il carico in modo che il fondello in acciaio della trave risultasse in trazione; viceversa i campioni della serie "B" sono stati testati a momento negativo, ovvero con fondello inferiore compresso. Prima dell'esecuzione del getto di calcestruzzo, i campioni sono stati strumentati mediante estensimetri elettrici a resistenza collocati in corrispondenza delle barre diagonali tese e compresse (nella sezione in prossimità dell'attacco al fondello inferiore) e nella barra del corrente superiore in corrispondenza della maglia centrale rispetto alla luce di taglio. Dopo il getto di calcestruzzo, a maturazione avvenuta, anche sul fondello inferiore sono stati collocati degli estensimetri. Il risultato sperimentale ottenuto è stato confrontato con il modello numerico dettagliato ad elementi finiti rappresentativo delle suddette prove, evidenziando un buon accordo in termini di curva carico-spostamento nonché di quadro fessurativo.

All'analisi numerica fa seguito un'interpretazione analitica per la stima della resistenza a taglio delle travi. In prima battuta sono stati applicati i modelli di previsione esistenti in letteratura tipicamente impiegati per le classiche strutture in c.a. che possono essere classificati prevalentemente in

"modelli additivi" e "modelli tirante-puntone". Nei modelli additivi il valore di resistenza a taglio è calcolato come somma del contributo dovuto al calcestruzzo e del contributo aggiuntivo fornito dalle armature trasversali. I modelli tirante-puntone invece sono prevalentemente modelli a traliccio in cui si adotta l'ipotesi dell'inclinazione variabile o a 45° della biella di calcestruzzo compressa. Accanto a queste classiche formulazioni, vengono anche presi in considerazione modelli di calcolo recentemente elaborati da alcuni autori per le travi prefabbricate reticolari miste. Successivamente, viene proposto uno specifico modello che interpreti il meccanismo di resistenza a taglio della tipologia di trave sottoposta a sperimentazione.

Prendendo in considerazione le prove di flessione su tre punti eseguite, un ulteriore modello tridimensionale, realizzato con il software Abaqus 6.11, è stato sviluppato, in via semplificata, con l'obiettivo di gestire un modello sufficientemente accurato nella stima del carico massimo che consentisse tempi di elaborazione e di calcolo idonei alla generazione di diversi casi per lo studio dell'effetto scala su travi di geometria simile. Il modello è stato elaborato con la guida dei Professori Roberto Ballarini e Jialiang Le del *Department of Civil Engineering, University of Minnesota*. A partire da specifici criteri di scaling, sono state considerate tre diverse dimensioni per le travi oggetto di studio e si è valutata numericamente la curva carico-spostamento interpretando i meccanismi di rottura e l'evoluzione del quadro fessurativo. Le analisi numeriche sono state elaborate con l'ausilio dei calcolatori e dei software del *Minnesota Supercomputing Institute*.

Parallelamente alle suddette indagini, sono stati condotti ulteriori studi con un diverso grado di approfondimento riguardanti i problemi della trave nella fase precedente il getto di calcestruzzo e il comportamento della struttura composta nella zona del pannello di nodo. Relativamente al primo ambito, è stato condotto uno studio analitico finalizzato all'interpretazione del comportamento del traliccio nudo sottoposto a prova di push-out con lo scopo di investigare il fenomeno dell'instabilità delle barre compresse. Riguardo al pannello di nodo, è stato indagato il comportamento ciclico di nodi trave-colonna appartenenti a strutture intelaiate sismoresistenti a cui afferiscono travi reticolari miste e pilastri in c.a. gettati in opera.

SUMMARY

The purpose of the present dissertation is the study of the shear behavior of the so-called, in the recent scientific literature, *Hybrid Steel Trussed Concrete Beams (HSTCBs)*. Such beams represent a structural typology which usually consists of a steel truss embedded into a concrete core so that, after curing and maturation, the two materials behave as a unique structural system, the steel members working as the reinforcement of the beam itself.

Since the Seventies, the HSTCBs are widely employed in civil constructions because they allow to industrialize the building process, avoiding substantial alterations in the construction processes and organizational protocols of the industries.

With regard to the introduction of this beam typology within seismic framed structures, it is necessary to develop specific design criteria based on the capacity design approach, ensuring both an adequate shear resistance in order to prevent brittle failure modes and a cyclic dissipative behavior of beam-to-column joints.

While the issues concerning the flexural behavior has been widely investigated in the literature, particularly focusing on the connection deformability and strength, the problems related to the shear behavior still represent an open issue. Within this framework, the present thesis aims at investigating the shear response of HSTCBs and the stress transfer mechanism between the steel members and the surrounding concrete.

With reference to the stress transfer mechanisms, theoretical analyses with the aim of interpreting the experimental results of push-out tests on pieces of HSTCBs are developed. Such models for the prediction of the maximum slip force refer both to the classical truss models with variable

inclination of the compressed concrete strut, typically adopted for the classical Reinforced Concrete (R.C.) structures, and models with a failure mechanism governed by the dowel effect, generally used for composite structures. The application of these models, according to their original formulation, generally leads to an underestimation of the maximum load experimentally obtained by various authors from the push-out tests. For this reason, the formulation of further strut and tie models, on one hand, and dowel-mechanism models, on the other hand, has been developed. In those models proper changes have been introduced in order to take into account the geometrical and mechanical characteristics of the beam object of study.

Besides the analytical interpretation of the maximum load obtained in the push-out tests, a two-dimensional (2D) non-linear finite element (FE) model is also developed with the aim to simulate, under few simplified hypotheses, the mechanical response of the beam identifying the stresses transfer mechanisms. The result of the 2D modeling highlights the difficulty of grasping, with an extremely simplified model, the large variety of parameters on which the transferring of the stresses and the failure modes depend. Among these parameters, the ones playing a preeminent role are the three-dimensional (3D) geometry and the actual bond between the surfaces of the steel bars (smooth or ribbed) and the concrete in which they are embedded.

Therefore, after the developing of the simplified modeling, a detailed 3D FE model containing solid elements is realized by means of the software Abaqus 6.10. The model was developed in collaboration with the research group of Prof. Gianvittorio Rizzano of the Department of Civil Engineering, University of Salerno. Particularly, the developed models are representative, on one hand, of cases in which the diagonals of the steel truss are ribbed and, on the other hand, cases in which they are made up of smooth steel. The simulation concern cases in which the hypothesis of perfect bond between the surfaces is assumed or, similarly, cases in which there is no bond between the steel and the concrete as well as the more realistic case in which a specific bond stress-slip relationship at the interface is introduced. Besides the modeling of the experimental tests, also a parametric numerical analysis

is provided with the aim of evaluating the influence of the geometrical and mechanical features of the various components of the HSTCB, such as the deformability of the bottom steel plate, the type of steel constituting the diagonal web bars (smooth or ribbed) as well as the mechanical characteristics of the materials.

In addition to the study of the local problems of stresses transfer, some theoretical and experimental studies are carried out in order to investigate the global behavior of the structural elements. In particular, an experimental campaign is performed on simply supported HSTCB specimens loaded with a concentrated force in the midspan and designed to exhibit a shear failure. For the execution of the tests, a particular type of steel truss produced by the industry *Sicilferro Torrenovese* Torrenova (ME) is employed. Six specimens have been manufactured and classified into two series, "A" and "B". Particularly, the specimens of series "A" have been tested inducing a positive bending moment; on the contrary, the specimens of series "B" have been tested so that a negative bending moment arises. Before the concrete casting, electric strain gauges have been placed on the specimens in correspondence of the tensile and compressed diagonal bars (in the section near the welding to the inferior plate) and in the bar of the upper chord in correspondence with the central mesh of the truss in the shear span. After casting and curing of the concrete, strain gauges were placed even on the bottom steel plate. The obtained experimental results are compared with the detailed numerical FE model representative of the abovementioned tests, showing a good agreement in terms of load-displacement curve as well as crack pattern evolution.

The numerical analysis is followed by the analytical interpretation for the assessment of the shear strength of the beams. In the first instance, the prediction models existing in the literature and typically employed for the classic R.C. structures have been applied. They can be mainly classified into "additive models" and "strut and tie models". In the additive models the value of shear strength is calculated as the sum of the contribution due to the concrete and the additional contribution provided by the shear reinforcement. The strut and tie models, instead, are primarily truss models

in which the hypothesis of the variable inclination or 45° inclination of the compressed concrete strut is assumed. In addition to these classical formulations, also other computational models recently developed by some authors for the HSTCBs are taken into account. Successively, also a specific model able to interpret the shear strength mechanism in the tested beam typology is proposed.

Considering the three-point bending tests performed on the HSTCBs, a further 3D model, realized with the software Abaqus 6.11, is developed in a simplified way, with the aim of managing a model sufficiently accurate in the estimation of the maximum load that, in the same time, would allow computational efforts appropriate for the generation of a certain number of different cases for the study of the size effect on beams with similar geometry. The model has been developed under the guide of Professors Roberto Ballarini and Jialiang Le of the *Department of Civil Engineering, University of Minnesota*. Starting from specific scaling criteria, three different sizes of beams are considered and the numerical load-displacement curve is obtained also interpreting the failure mechanisms and the evolution of the cracks. The numerical analyses have been developed with the aid of computers and software provided by the *Minnesota Supercomputing Institute*.

In addition to the aforesaid investigations, further studies have been conducted with a different degree of detail, dealing with the problems of the beam in the phase preceding the concrete casting, on one side, and the behavior of the composite structure corresponding to the panel zone, on the other side. Particularly, concerning the first issue, an analytical study aimed at interpreting the behavior of the bare steel truss under push-out test is carried out with the purpose of investigating the buckling phenomenon arising in the compressed bars.

Concerning the panel zone, instead, the cyclic behavior of beam-to-column joints in framed seismic structures, where HSTCBs are joined to R.C. columns cast in situ, is investigated through the execution of an experimental campaign.

«O Muse, o alto ingegno, or m'aiutate,
o mente che scrivesti ciò ch'io vidi,
qui si parrà la tua nobilitate»

(Dante Alighieri, Divina Commedia, Inferno, canto II, 7-9)

CONTENTS

RINGRAZIAMENTI ..... **I**

ACKNOWLEDGEMENTS ..... **III**

SOMMARIO ..... **V**

SUMMARY ..... **IX**

CONTENTS ..... **XV**

CHAPTER 1 INTRODUCTION **1**

1.1 Structural typology *1*

1.2 Main issues concerning the HSTCBs *4*

1.3 Regulatory guidance *6*

1.4 Scope and objective of the work *8*

1.5 Thesis organization *10*

CHAPTER 2 STATE OF THE ART ON THE SHEAR BEHAVIOR OF HSTCBs **13**

2.1 Push-out tests in phase II *13*

2.2 Bending tests with shear failure *23*

2.3 Expressions of the shear strength *28*

CHAPTER 3 ASSESSMENT OF PUSH-OUT TESTS RESPONSE IN PHASE II: ANALYTICAL CALCULATIONS AND SIMPLIFIED NUMERICAL MODELS 35

3.1 Analytical interpretation of the maximum load 35
3.1.1 Strut and tie models 36
3.1.2 Dowel mechanism models 40
3.1.3 Modified dowel mechanism model 45

3.2 2D simplified finite element models 51

CHAPTER 4 STRESS TRANSFER MECHANISMS INVESTIGATION: 3D FINITE ELEMENT MODELS OF PUSH-OUT TESTS ..59

4.1 General features 60

4.2 Constitutive model of steel 63

4.3 Constitutive model of concrete 65
4.3.1 Main theories for concrete cracking mechanics 66
4.3.2 Concrete Damaged Plasticity model 74

4.4 Modeling of the steel - concrete interface 80

4.5 Check of the proposed approach 83

4.6 Numerical vs. experimental results 87

4.7 Parametric simulations of push-out tests 90
4.7.1 Influence of the investigated parameters 91
4.7.2 Interpretation of the numerical results 96

CHAPTER 5 SHEAR BEHAVIOR OF HSTCBs: THREE POINT BENDING TESTS 101

5.1 Experimental program 101
5.1.1 Description of the specimens 102
5.1.2 Mechanical characterization of materials 107
5.1.3 Testing machine and measurement technology 114
5.1.4 Test setup and data acquisition 121

5.2 Experimental results 126
5.2.1 Load-displacement curves 126
5.2.2 Strain gauges measurements 136
5.2.3 Some remarks on the experimental data 142

5.3 Interpretation of the experimental results 145
5.3.1 Numerical finite element model 146

5.3.2 Analytical expressions for the shear resistance 158

5.4 Proposed analytical model *159*

CHAPTER 6 SHEAR BEHAVIOR AND SIZE EFFECT INVESTIGATION OF HSTCBs BY NUMERICAL MODELING 171

6.1 Finite element simulation *172*
6.1.1 Description of the finite element models 173
6.1.2 Scaling criteria 175

6.2 Numerical results *177*
6.2.1 Model Size 1 177
6.2.2 Model Size 2 200
6.2.3 Model Size 3 218

6.3 Observations *234*

CHAPTER 7 COMPLEMENTARY INVESTIGATIONS ON THE STRUCTURAL TYPOLOGY 237

7.1 Behavior of the bare steel truss subjected to push-out test *237*
7.1.1 Experimental results available in the literature 240
7.1.2 Analytical interpretation of the experimental results 243

7.2 Shear behavior of beam-to-column joints under cyclic loading *249*
7.2.1 Experimental program and description of the specimens 250
7.2.2 Test set-up and measurement technology 255
7.2.3 Experimental results 257
7.2.4 Numerical models 270
7.2.5 Observations 273

CONCLUSIONS 275

REFERENCES 281

CHAPTER 1

INTRODUCTION

In this introductory Chapter the main features concerning the structural typology subject of the present thesis are provided together with some issues of paramount importance dealing with the understanding of the mechanical behavior carried out by few authors and published in the recent scientific literature. Within this framework the scope and the objective of the work is then described and the thesis organization is presented with the aim of providing the reader a guide towards the covered topics all focused on the investigation of the shear strength mechanisms occurring in the Hybrid Steel Trussed Concrete Beams.

1.1 Structural typology

A Hybrid Steel Trussed Concrete Beam (HSTCB) is a typical Italian structural typology constituted by a steel truss embedded in a concrete core. The truss is usually made up of a steel plate or a precast concrete slab, which represents the bottom chord, a system of ribbed or smooth steel bars welded in order to form the diagonals of the truss and some single or coupled rebars constituting the upper chord. Figure 1.1a-d shows the details of few examples of cross-section which can be a single or multi-planar as well as a space cross-section. The web bars working as strut and tie can be

both inclined or, according to different geometries, they can be manufactured with vertical compressed bars and inclined tensile bars (see Figure 1.2). Sometimes the chords of the truss can also be realized by means of steel angles as shown in Figure 1.1d. Moreover, in order to realize the connection within the beam-to-column joint, the steel truss can also be manufactured introducing a certain offset with respect to the axis of the bottom steel plate (see Figure 1.3a) so that the truss itself represents the reinforcement within the joint. However, according to other technical solutions, the beam-to-column connection can be realized by means of specific devices at supports (Figure 1.3b), or introducing upper and inferior added rebars as typically done in classical R.C. structures (Figure 1.3c) or, finally, placing the end of the steel truss on the column (Figure 1.3d).

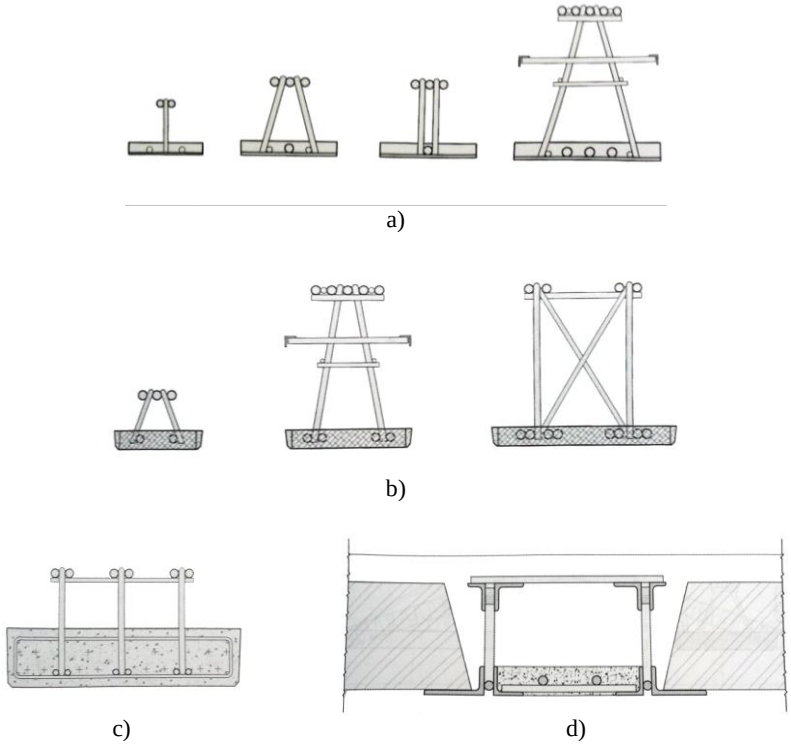

Figure 1.1. Typical cross-sections of HSTCBs: a) with bottom steel plate; b) with bottom concrete slab; c) with prestressed concrete plank; d) with steel angles (VV. AA. 2011).

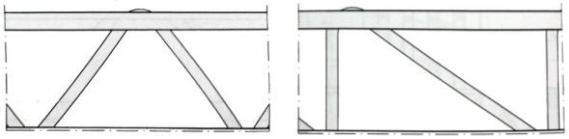

a) b)

Figure 1.2. Lateral view: a) inclined web bars ; b) vertical strut and inclined tie (VV. AA. 2011).

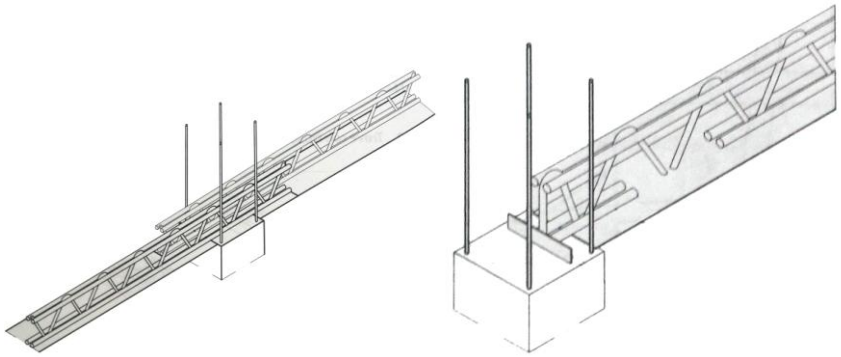

a) b)

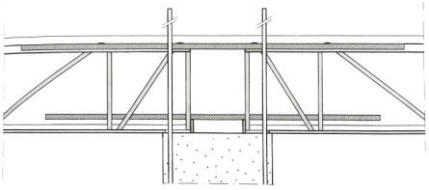

c)

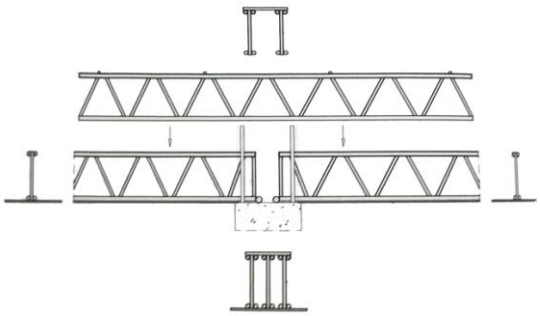

d)

Figure 1.3. Beam-to-column connection: a) offset of the steel truss ; b) specific devices at supports; c) added rebars; d) steel truss across the column (VV. AA. 2011).

The HSTCBs represent a structural solution for light industrialization in use in the Italian construction industry since fifty years and they are also frequently introduced within seismic framed structures. The main advantages in their use are the higher construction speed with the minimum site labour, the possibility of covering wide spans with low depths and a final economical convenience.

HSTCBs are typically subjected to three different operative phases herein briefly described. In the preliminary phase, called *phase zero*, the beam is manufactured in the industry, moved and put in place. Then in the following *phase I* the beam, already placed in situ, is subjected to a load condition mainly due to its own weight and the weight of the wet concrete. Finally, the last phase, called *phase II*, is ruled by the mechanical response of the composite beam made up of the steel truss embedded within the hardened concrete: the two materials work together as a unique system.

In the present thesis, the attention is particularly focused on HSTCBs characterized by a space truss welded to a bottom steel plate, with single or coupled bars as upper chord, encased within a block of concrete and behaving in *phase II* (Figure 1.4).

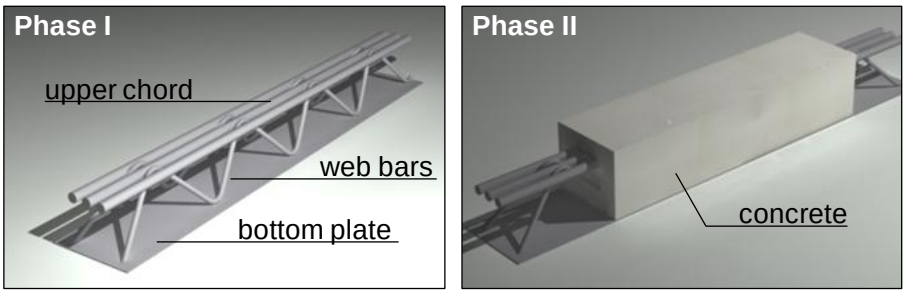

Figure 1.4. Main features of the HSTCB typology studied in the thesis.

1.2 Main issues concerning the HSTCBs

After a long period in which HSTCBs have been applied in practice basing only on the existing guidance for Reinforced Concrete (R.C.) or for composite steel-concrete beams, recently a significant research activity has taken action, aiming at developing specific guidelines. For the beam in the

first phase, the main research topics have regarded the study of the buckling of steel trusses before the concrete cast (Vincenzi and Savoia 2010) as well as the prediction of the strength value in welded joints (Colajanni et al. 2013a). Similarly, the topics of main interest concerning such beam typology in *phase II* are the flexural and shear strength of the beam (Tesser and Scotta 2013), the behavior of beam-to-column joints (Sanpaoles et al. 1987; Mele et al. 1993; Mele and Sassone 2002; Ju et al. 2007; Amadio et al. 2008; Amadio et al. 2011), the seismic behavior of the beams (Hsu et al. 2004; Badalamenti et al. 2010), the issues related to the creep (Sassone and Chiorino 2005; Sassone and Casalegno 2011) and the problem of stress transferring from the bottom chord of the truss to the concrete core (Puhali and Smotlack 1980; Tullini 2006; Badalamenti et al. 2008a; Badalamenti 2010; Aiello 2008; Colajanni et al. 2011; Desiderio et al. 2011; Colajanni et al. 2013b; Colajanni et al. 2014).

With reference to the last issue, in fact, after the concrete casting, the beam can be viewed as a steel–concrete hybrid beam with deformable shear connection represented by the web members of the steel truss welded to the steel plate at the bottom (Tullini and Minghini 2013). This is the reason why, in most of the problems related to the behavior in *phase II*, a preeminent role is played by the transfer mechanism of the stresses from the steel truss to the concrete core. As a consequence, recently, various experimental tests carried out by some authors have been devoted to investigate the load transfer mechanism between the steel truss and the concrete. As far as there is not a standardized experimental procedure to evaluate the resistance and the stiffness of the steel-concrete shear connection, usually the slip-load curve is characterized by means of push-out tests inspired to the classical tests developed for steel-concrete composite beams according to Eurocode 4 (2005). In particular, in the work carried out by Aiello (2008) and Badalamenti (2010) the experimental analysis aimed to investigate the main geometrical and mechanical parameters affecting the steel-concrete shear transfer mechanism. Tests were performed by varying the following parameters: the type of rebars used to form the truss (smooth or ribbed), the

concrete and steel quality, the diameter and the slope of the truss diagonal and the depth of the beam.

From the modeling standpoint, recently some attempts to provide simplified analytical formulation able to predict the load carrying capacity of the shear connection between the steel plate and the concrete were made (Amadio et al. 2010; Colajanni et al. 2011; Desiderio et al. 2011). Nevertheless, despite the significant work made by the scientific community in last few years, the limited number of available experimental tests requires new efforts in order to fill the knowledge gap surrounding the stress transfer mechanism from the steel truss to the concrete of HSTCBs.

With the introduction of the HSTCBs within seismic framed structures it is necessary to formulate some design criteria concerning the *capacity design* general approach mainly based on shear overstrength as well as the energy dissipation at joints. As a consequence, aiming at understanding the mechanical behavior of such beams, the flexural response has been deeply investigated focusing on the evaluation of the rotational capacity and ductility of the end sections of the beams in which the plastic hinges are usually placed; the evaluation of the yielding and ultimate moment of the section and the stress transfer mechanism corresponding to the beam-to-column joint. On the contrary, from the shear behavior standpoint, some preliminary experimental tests have been carried out by few authors (Izzo et al. 2006 and more recently Amadio et al. 2012) but the understanding of the shear response is still an interesting open topic subject of the current research on the HSTCBs. Studies mainly aim at investigating the shear strength mechanisms and the stress transfer modes by means of numerical models and analytical calculations trying to interpreter the available experimental data.

1.3 Regulatory guidance

Despite the widespread use of the HSTCBs in various fields of the civil engineering, nowadays there are no specific rules provided by the national building code for their structural design.

Before the publication of the new Italian technical standard codes on constructions, the behavior of the HSTCBs under load was usually interpreted making use of the existing models for the design of R.C. beams or classical steel-concrete composite beams. Conversely, the current codes make a clear reference to this kind of beams which are considered as structures made up of non-traditional materials or whose design techniques are not explicitly covered in the current rules. In order to employ such a kind of beam within a civil structure, the approval of the Italian standard commission for constructions, C.S.LL.PP. is required.

As a consequence, in order to regulate the design procedure for the HSTCBs, the C.S.LL.PP. recently published some guidelines (C.S.LL.PP. 2011) classifying the beam typologies in three different categories: a) steel-concrete composite structures; b) R.C. structures; c) different structures which require the formulation of specific models. Particularly, for the third typology, a key point for the design is a detailed knowledge of the mechanical behavior of the beam under various load conditions and, as a consequence, the calculation models typically have to be derived by means of design-by-testing procedures.

The beams may be classified within the category a) when the resisting system can be assimilated to the one constituted by a steel beam cooperating with a concrete slab. According to this structural hypothesis, only the mechanical contribution of all steel members can be considered (plates, profiles, rebars, etc...) and the transferring of all solicitations across the beam-to-column joints has to be ensured only by the elements of the steel truss. Alternatively, the beam may be classified in the category b) if the load-bearing capacity in *phase II* is due only by the contribution of the concrete and the reinforcing steel and if the tensile bars of the steel truss are properly distributed through the cross-section width. Finally, if the structural typology of steel-concrete trussed beam cannot be classified within the two previous categories a) and b), then it has to be considered as an hybrid system for which the current Italian and European codes have not yet provided specific design rules. Generally, the HSTCBs belong to this latter category c) if they are constituted by a bottom steel plate and present an additional

reinforcement typical of R.C. structures. Similarly, they are considered hybrid structures also if they are made up with smooth steel, typical of bare steel structures, which then, in *phase II*, is considered working as R.C. reinforcement, aiding the block of concrete in the mechanical response as well as in the stress transfer mechanism.

1.4 Scope and objective of the work

Within this framework, the scope of the present thesis is to investigate the shear behavior of HSTCBs interpreting the resisting mechanisms and the transfer of stresses between the steel truss and the surrounding concrete.

In order to achieve the goal, two main fields are investigated: on one hand, the study of local problems of stresses transfer from the steel members to the concrete matrix using the experimental results of push-out tests in *phase II* available in the literature; on the other hand, the analysis of the global shear behavior of the beam subjected to three-point bending tests designed in order to exhibit a shear failure.

As regards the study of the local problems concerning the shear connection, the results of some push-out tests available in the literature are considered. The first attempt is to introduce simplified analytical models developed for the assessment of the maximum load; then also two dimensional (2D) non-linear Finite Element (FE) models are employed to simulate in a simplified way the behavior of the tested beams. Nevertheless, the complexity of the mechanical response leads to the necessity of a detailed numerical formulation in which the three-dimensional (3D) geometry as well as the material non-linearities (strain-softening damage of the concrete, plasticity of the steel and constitutive behavior at the steel-concrete interface) are taken into account allowing a detailed investigation of the stress transfer mechanism during a push-out test to be performed. The proposed model is calibrated on some of the existing experimental push-out tests carried out by Aiello (2008). Afterwards, it is used to simulate the slip-load curve of a number of push-out tests in order to individuate the main geometrical and mechanical parameters influencing the maximum load that can be transferred from the steel plate to the concrete core. The results of

such a parametric simulation could be finally used to support the calibration of analytical models for the prediction of the ultimate shear load of the steel-concrete connection of HSTCBs.

From the global shear behavior standpoint, an experimental campaign of three-point bending tests is performed on specimens of HSTCB and the obtained results are then analyzed by means of both analytical and numerical models characterized by different degrees of detail. Particularly, the analytical interpretation of the mechanical behavior is based on the sum of the two classical shear mechanisms occurring in the R.C. structures: the "beam effect" and the "arch effect" mechanism. Two other contributions have to be considered in the model because of the peculiarities of the structural typology: the contribution of the diagonal web bars and the bottom steel plate. On the other hand, the numerical model is developed with a high degree of detail both in the definition of the 3D geometry and in the implementation of the steel-concrete interface characterized by a specific bond stress-slip relationship. Furthermore, also a simplified model of HSTCB under the load condition of the three-point bending test is elaborated for three different geometric sizes of beam established according to some specific scaling criteria and devoted to investigate the size effect in this particular typology of steel-concrete beam. The results of the numerical simulations concerning the size effect have been deeply analyzed and interpreted, remarking the different aspects in the mechanical response of the beams especially in terms of globally brittle or ductile behavior and different crack pattern evolution.

In addition to the investigations which represent the main subject of the present thesis, some other studies have been developed as complementary researches dealing with the behavior of the bare steel truss under push-out test in *phase I* and, on the other hand, the experimental response to cyclic loading of beam-to-column joints belonging to seismic framed structures in which HSTCBs are connected to R.C. columns cast in situ.

1.5 Thesis organization

In order to provide a guide through the reading of the present dissertation, in this section a scheme of the thesis organization is presented and the corresponding synoptic frame is shown in Table 1.1.

The first two introductory Chapters aim at providing some preliminary notions about the peculiarities of the structural typology (Chapter 1) and the main experimental and theoretical studies available in the recent literature on the topic (Chapter 2). It is worth to note that the presentation of the state of the art is specifically focused on the shear behavior of the HSTCBs, reporting experimental data and analytical formula that will be employed in the following Chapters for the check and calibration of the developed analytical and numerical models.

The local problems of the stress transfer mechanism from the steel members to the concrete core are investigated in Chapter 3 and Chapter 4. Particularly, Chapter 3 deals with the attempt of providing an analytical interpretation of the maximum load achieved during a push-out test in *phase II* on HSTCBs by means of simple *strut-and-tie models* as well as *dowel-mechanism models*. Furthermore, in the same Chapter, the effort of developing a simplified 2D simulation of the mechanical response to the push-out test by means of a non-linear FE code is presented. On the other hand, Chapter 4 is rather focused on the accurate 3D FE model which simulates such beams under push-out test, giving also the details of the implementation of the constitutive behavior of the materials as well as the steel-concrete interface. A parametric simulation of push-out tests with the interpretation of the obtained numerical results is presented.

The global shear behavior of the HSTCBs is, thus, the subject of the following Chapter 5 and Chapter 6. In Chapter 5 the experimental campaign of three-point bending tests is described and the obtained results are interpreted by means of detailed FE models, previously employed for the calibration of the test set-up. The experimental data are also utilized to investigate the ability of analytical formula for the prediction of the shear resistance available in the literature and, then, to check the proposed analytical approach for the assessment of the shear strength value. Chapter 6

is rather focused on the evaluation of the size effect in the same HSTCB typology described in the previous Chapter. The study is carried out by means of numerical simulations of three-point bending tests, adopting specific scaling criteria. The numerical results are deeply discussed and some remarks on the specific typology are deducted.

Finally, Chapter 7 collects the results of further researches on two problems of paramount importance dealing with the behavior of the beam in *phase I* and *phase II*, respectively. In fact, the interpretation of the results of push-out test in *phase I* on specimens of bare steel trusses before the concrete casting, on one side, and the cyclic response of HSTCB-to-column joints after the concrete curing, on the other side, are briefly presented. Such issues are treated with a different degree of detail and, as a consequence, they can be viewed as suggestions for further insights on the topic.

Table 1.1. Synoptic frame of the thesis organization.

Fields of study	**Tests of reference**	**FE modeling**	**Analytical modeling**
Local slip problems	**Push-out tests** *(available in the literature)*	Simplified 2D models (Drain 2D-X) Detailed 3D models (ABAQUS 6.10)	▪ Strut and tie ▪ Dowel mechanism
Global shear behavior	**Three-point bending tests**	Detailed 3D models (ABAQUS 6.10) Simplified 3D models for the size effect simulations (ABAQUS 6.11)	▪ Assessment of P_{max} (without specific size effect contribution)

CHAPTER 2

STATE OF THE ART ON THE SHEAR BEHAVIOR OF HSTCBs

Although the HSTCBs are produced by the Italian industry since almost fifty years and they are commonly employed in the civil constructions, only few studies on this structural typology have been carried out and the scientific literature on the topic is mostly recent.

In this Chapter some experimental investigations on the shear behavior of HSTCBs are presented. Particularly, dealing with the local slip problems involving the mechanism of the transfer of the stresses, the results of push-out tests in *phase II* performed by various Italian authors are presented. Furthermore, experimental analyses focused on the global shear behavior of such beams are briefly described. Finally, in the last part of the Chapter, the expressions for the prediction of the shear resistance provided in the main national and international codes for classical R.C. beams are reported as well as some formula derived from analytical models specifically developed for the HSTCBs available in the literature.

2.1 Push-out tests in phase II

In spite of the large variety of HSTCB typologies commonly in use, only few authors have presented experimental results addressed to study the stress

transfer mechanism between steel and concrete. In the available literature such a problem is usually investigated by means of experimental push-out tests that are inspired to the test procedures specified in Eurocode 4 (2005) for classical composite beams. Commonly, the tested specimens are made up of a steel plate working as the bottom chord of the truss, one or more longitudinal steel bars constituting the upper chord, steel bars welded to the chords working as diagonals of the truss and a concrete core. As for classical push-out tests, two equal trusses are joined by means of a steel plate welded perpendicularly to the truss bottom chords and properly strengthened at the end where the load is applied. The employed bars can be either ribbed bars or smooth steel bars. Figure 2.1 shows the layout of the push-out tests on HSTCBs available in the technical literature. All results are used in the following Chapters in terms of maximum load in order to check the ability of some analytical approaches for the assessment of the push-out test response. Furthermore, the experimental tests by Badalamenti (2010) and Aiello (2008) are also employed for the calibration of both simplified and detailed numerical FE models.

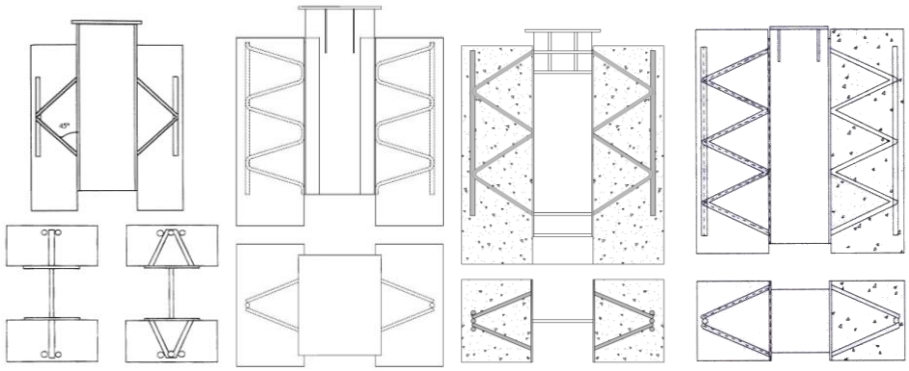

a) b) c) d)

Figure 2.1. Geometry of specimens: a) Puhali and Smotlack (1980); b) Tullini et al. (2006); c) Badalamenti (2010); d) Aiello (2008).

First push-out tests on HSTCBs were carried out by Puhali and Smotlack (1980). They considered planar and space trusses. For each typology, three specimens were tested, all of them having steel plate 6 mm thick, web bars and upper chord with the same diameter, which varied in a range from 14 to 32 mm. The bars and the plate were both realized with smooth steel having nominal yielding strength of 355 N/mm^2 (S355), while the concrete had a cubic compressive resistance varying in the range 26-30 N/mm^2. All specimens with space truss (B-P4, B-P5 and B-P6) exhibited both higher stiffness and strength with respect to the single planar truss counterpart (specimens A-P1, A-P2 and A-P3). Table 2.1 shows the features of the specimens and the experimental results.

The more recent experimental investigation carried out by Tullini et al. (2006) concerned three identical specimens whose truss was realized with a S355 4 mm thick steel plate, web bars of 12 mm diameter and upper chord with diameter 18 mm; the bars were made up of steel with nominal yielding stress 440 N/mm^2 and the concrete had mean cubic compressive strength equal to 42.24 N/mm^2. In all tests the ultimate load was achieved prematurely due to the welding failure.

Table 2.1. Specimen features and experimental results by Puhali and Smotlack 1980.

ID	web bars	upper chord	ultimate load [kN]	failure
A-P1	no.1 bar (d_w=14 mm)	no.2 bars (d_{up}=14 mm)	463.0	steel
A-P2	no.1bar (d_w=24 mm)	no.2 bars (d_{up}=24 mm)	647.5	concrete
A-P3	no.1 bar (d_w=32 mm)	no.2 bars (d_{up}=32 mm)	843.5	concrete
B-P4	no.2 bars (d_w=14 mm)	no.3 bars (d_{up}=14 mm)	735.5	steel
B-P5	no.2 bars (d_w=24 mm)	no.3 bars (d_{up}=24 mm)	1177.5	concrete
B-P6	no.2 bars (d_w=32 mm)	no.3 bars (d_{up}=32 mm)	1324.5	steel plate buckling

Badalamenti (2010) also realized three identical specimens, P1, P2 and P3 (see Figure 2.2a-b), where the diagonals of the truss were made up of ribbed bars of 12 mm diameter, the upper chord was made by three bars of 16 mm diameter and the bottom plate was constituted by a plate of 5 mm. The bars were realized with steel having nominal yielding strength equal to 450 N/mm^2 (B450C) while the base plate was made of S355 steel class. The concrete had a cylindrical resistance equal to 27.77 N/mm^2. In order to evaluate the stress in the web bars, electric strain gauges were placed before the concrete casting as shown in Figure 2.2b-c-d. After cure and maturation, in all specimens two other strain gauges were also placed on the steel plate on two sides of the truss bottom joint, in order to evaluate the stress transfer in the truss joint.

In all tests the obtained ultimate loads were very similar, with a mean value of 1104.7 kN, and the specimen collapse was due to the concrete failure. Particularly, the maximum load values recorded for specimens P1 and P2 are equal to 1051.6 kN and 1004.9 kN respectively while for specimen P3 a higher value was achieved, equal to 1257.5 kN. Figure 2.3 shows the load-displacement curves for the three tests considering the displacement values recorded by the testing machine.

During the load history, appreciable cracks began to appear at a load value of 1000 kN; they propagated until the maximum load, corresponding to the maximum concrete tensile strength, was achieved. In the descending branches the curves show the progressive strength reduction that during the test was associated with a typical noise of breaking of metallic parts; it can be observed that the specimens exhibited a somewhat ductile branch to which a rapid increase in vertical cracking of the concrete corresponds; the configuration of specimen P1 at the end of the test can be observed in the pictures reported in Figure 2.4. Particularly in Figure 2.4a side views of the specimen are shown, while in Figure 2.4b a view of the top face of the specimen is represented (a similar failure type was observed for the other two specimens).

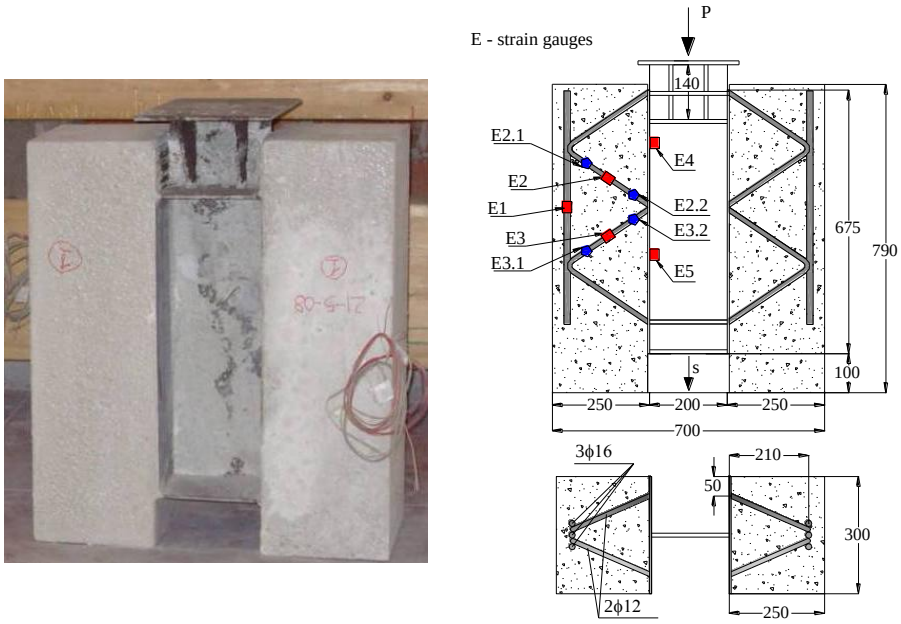

a) b)

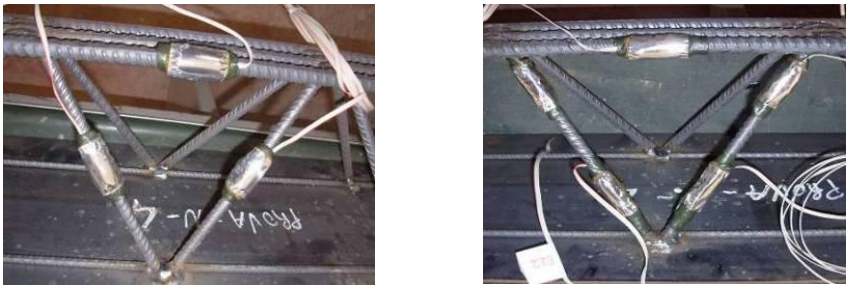

c) d)

Figure 2.2. Specimen for push-out test in phase II: a) picture of a specimen; b) geometry and instrumentation (dimensions in millimeters); c) stain gauges in specimens P1 and P2; d) strain gauges in specimen P3 (Badalamenti 2010).

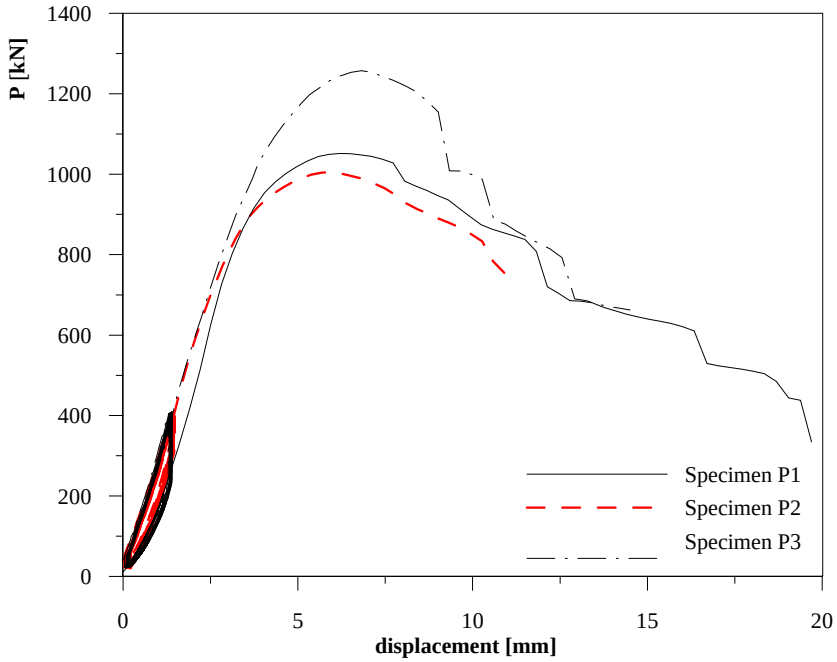

Figure 2.3. Load-displacement curves for push-out test in phase II (Badalamenti 2010).

a) b)

Figure 2.4. Specimen P1 at failure: a) lateral views; b) top view (Badalamenti 2010).

For all specimens, the failure was due to the achievement of the tensile strength in the concrete with formation of large amplitude cracks in the longitudinal direction of the specimen. The cracking caused a progressive transfer of tensile stresses from the concrete to the tensile web bars of steel trusses. The latter underwent large plastic strains near the connection to the plate, as it had been seen after removing the concrete from the specimen. In particular, by analysing the pictures in Figure 2.5 which refer to specimen P1, it emerges that the compressed bars exhibited large deformations at a distance of about 50 mm from the plate, presumably corresponding to the longitudinal crack. A progressive reduction in the strength of the specimen was revealed, corresponding to the progressive rupture of the tensile web bars next to the plate. In all three tests the welding remained undamaged.

a) b)

Figure 2.5. Deformed steel truss of specimen P1 at the end of the test: a) global view; b) zoom of deformed bars (Badalamenti 2010).

Finally, the main characteristics of push-out tests carried out by Aiello (2008) are presented. The experimental analysis concerns eight tests on specimens of four typologies. Their characteristics are described in Table 2.2 where ϕ_w and ϕ_{uc} indicate the diameter of the diagonal bars and the upper chord; P_u is the maximum load achieved in each test. The geometry of the specimens includes three meshes with space truss. The details of the

geometry are represented in Figure 2.6, while Figure 2.7a-b shows the steel truss before casting and the complete specimen placed into the compression testing machine. In all specimens, the bars constituting the upper chords are made up of B450C steel. The diagonals of the truss are made up of B450C steel in case of specimens B12 and B14, and S355 steel in specimens S12 and S14. The bottom chord is constituted by a steel plate of 6 mm made up of S355 steel. The concrete has an average cubic compressive strength of 42.6 N/mm^2. In specimens with identity tag S14 the welding between the initial and end diagonals and the base plate are removed. In almost all cases the collapse of the specimens is due to the failure of the concrete but, sometimes, the failure of the welding also occurred. Figure 2.8 shows the load-displacement curves obtained from the LVDTs measurements for each test representative of the specimens having all weldings. The LVDTs are collocated on the upper front side of the specimen (LVDT As and Ad) and next to one welding (LVDT Ps). In Figure 2.9 the deformed shape of the steel truss at the end of the test for specimen B12_2 is reported.

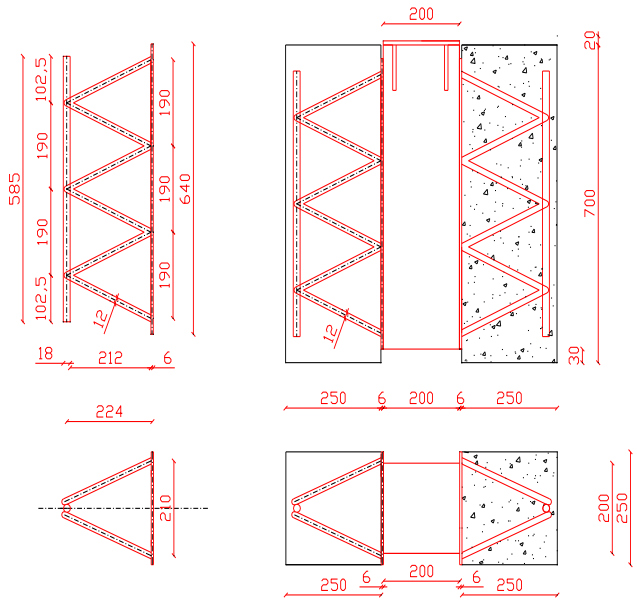

Figure 2.6. Geometry of specimens tested by Aiello (2008).

a) b)

Figure 2.7. Specimen tested by Aiello (2008): a) steel truss before casting; b) specimen into the testing machine.

Table 2.2. Features of specimens tested by Aiello (2008).

ID	ϕ_w	ϕ_{uc}	P_u [kN]	Failure
S12_1	S355 2ϕ12	B450C 1ϕ18	817.1	concrete
S12_2			842.1	
S14_2	S355 2ϕ14	B450C 1ϕ18	787.1	concrete
S14_3			808.1	concrete
S14_4			861.1	welding
B12_1	B450C 2ϕ12	B450C 1ϕ18	996.1	concrete
B12_2			1007.5	welding
B14_1	B450C 2ϕ14	B450C 1ϕ18	1139.0	steel

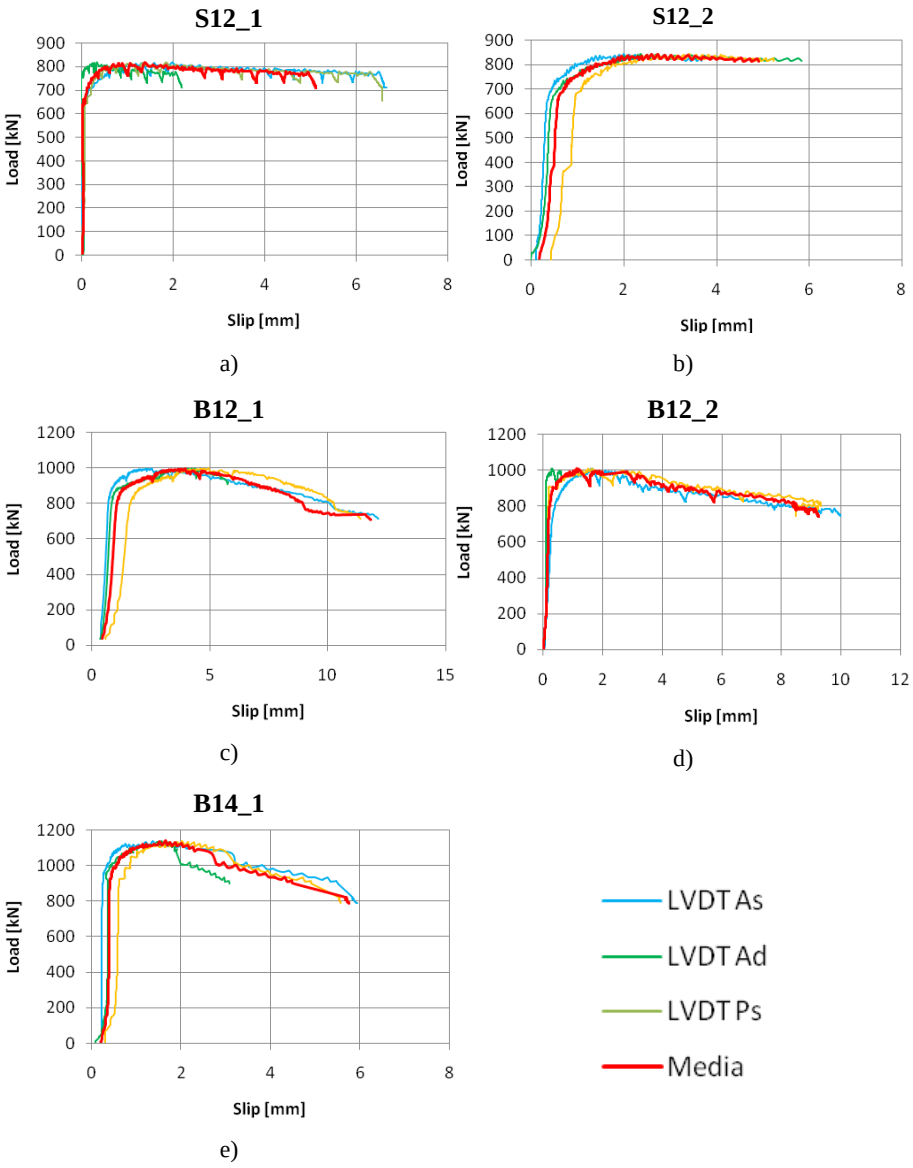

Figure 2.8. Load-displacement curves by Aiello (2008): a) specimen S12_1; b) specimen S12_2; c) specimen B12_1; d) specimen B12_2; e) specimen B14_1. (Aiello, 2008).

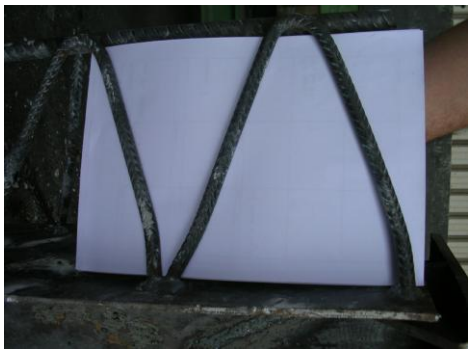

Figure 2.9. Deformed shape of the steel truss at the end of the test B12_2 (Aiello, 2008).

2.2 Bending tests with shear failure

The first shear tests on HSTCBs have been executed between 1987 and 1990 by the Italian industry CSP on specimens whose geometry is represented in Figure 2.10 (VV. AA. 1987, 1990). The simply supported beam is subjected to a concentrated load applied in the midspan.

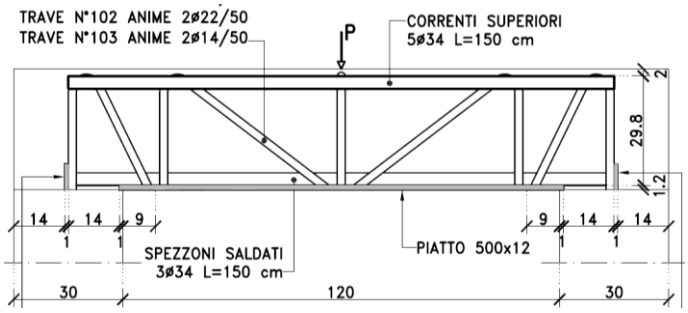

Figure 2.10. Specimen for shear test (conceded by CSP industry).

The results pointed out that the shear resistance mechanisms are different than the ones observed in similar R.C. beams and the maximum load achieved is higher in most cases. However, it is worth to note that the behavior of each beam is highly depending on the geometric typology of the truss which can be constituted by inclined or vertical compressed web bars. Figure 2.11 shows a typical shear failure occurred in the tested beams and in

the following Figure 2.12 the detail of the crack pattern is represented. Certainly, the steel truss and the bottom plate give a significant contribution to the shear overstrength of the system and this concept has to be taken into account in the analytical modeling of the shear mechanism with respect to the classical models for R.C. structures mainly based on the perfect bond between the steel reinforcement and the concrete matrix. As stressed in Izzo et al. 2006, such hypothesis, in fact, is not always realistic because sometimes the truss of the beam is realized with smooth steel instead of ribbed steel. For this reason, the understanding of the stress transfer mechanisms between the steel members and the concrete proves to be an aspect of paramount importance since it has to be granted almost only by the steel truss. Within this framework, considering the role of the bond stress, the arch effect occurring in the shear mechanism of the HSTCBs is a preeminent effect which leads to the increased risk of failure due to the crushing of the compressed concrete strut.

Figure 2.13 shows the specimen at the end of the test focusing on the collocation of the failed concrete strut with respect to the web steel bars. It can also be observed that the spalling of the concrete corresponding to the inferior face of the beam is prevented by the presence of the bottom steel plate. Finally, in Figure 2.14 the deformed shape of the bare truss at the end of the three-point bending test is showed.

More recently, another experimental campaign of bending tests with shear failure on HSTCBs has been carried out by Amadio et al. 2012. The tests have been carried out on three types of specimens all characterized by the presence of the bottom steel plate. The cross-section of the specimens are reported in Figure 2.15: they differ for the number of inferior added rebars welded to the steel plate, zero (Acc0), three (Acc3) or five rebars (Acc5) respectively. The added rebars have the aim of increasing the bond between the bottom steel plate and the concrete. Furthermore, it is worth to note that, for each cross-section, three different specimen have been manufactured realizing cases in which the upper chord and the diagonal bars are both ribbed (cn-an), the upper chord is ribbed while the web bars are smooth (cn-al), the upper chord is smooth and the diagonals are ribbed (cl-an).

Figure 2.11. Shear failure of HSTCB.

Figure 2.12. Crack pattern of HSTCB with separation of the inferior steel plate.

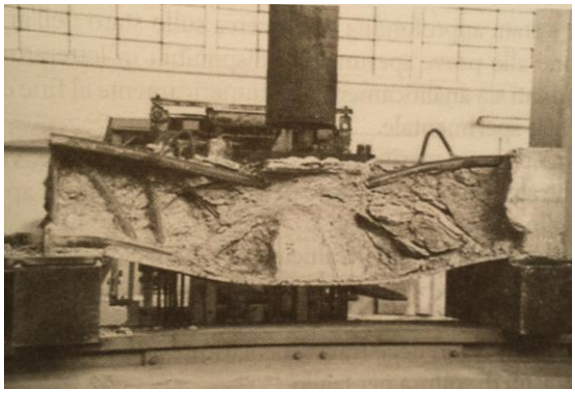

Figure 2.13. Specimen at the end of the test with no spalling of the concrete thanks to the presence of the inferior steel plate.

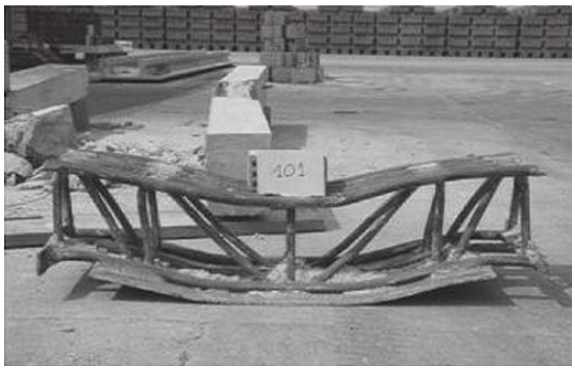

Figure 2.14. Deformed shape of the steel truss at the end of the test.

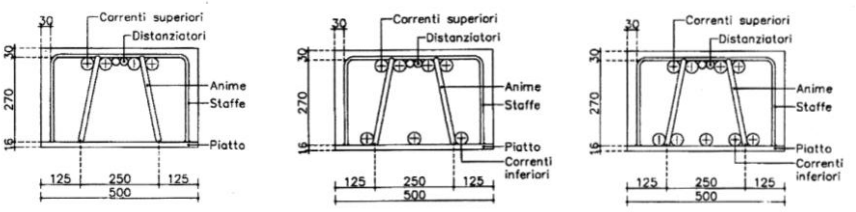

Figure 2.15. Cross-sections of the three typologies of tested beams (Amadio et al. 2012).

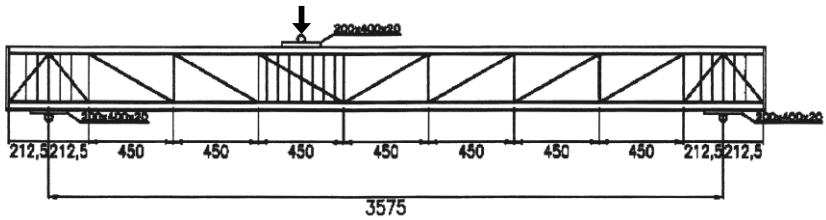

Figure 2.16. Geometry of the beam and load condition (Amadio et al. 2012).

The beams are simply supported at the ends and loaded with a concentrated force asymmetrically applied with respect to the midspan of the beam. The tests have been performed in displacement control. The scheme of the geometry and the load condition is represented in Figure 2.16.

The load-displacement curves showed that the three specimens without inferior added rebars exhibited almost the same behavior with a maximum load of about 860 kN (see Figure 2.17a). As regards the specimens with three added rebars, the beam constituted by both ribbed upper chord and diagonal bars exhibited an higher peak load equal to 1080 kN, while the

other two specimens achieved a maximum load of about 930 kN (see Figure 2.17b). Finally, with reference to the third series of specimens realized with five added inferior rebars, the beams exhibited almost the same behavior achieving a peak load whose value is in the range between 975 and 1050 kN (see Figure 2.17c).

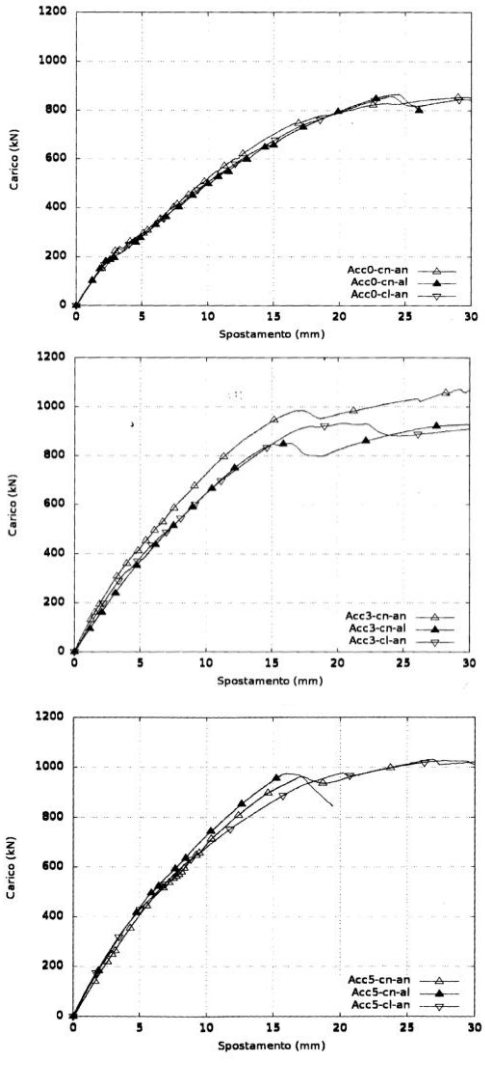

Figure 2.17. Load-displacement curves: a) beams without inferior rebars; b) beams with three added inferior rebars; c) beams with five inferior added rebars (Amadio et al. 2012).

2.3 Expressions of the shear strength

For the prediction of the shear strength several expressions are available in the literature and most of them are also given in national and international codes. Particularly, the expressions in the codes herein considered are those provided by the European codes UNI EN 1992-1-1:1992 and UNI EN 1992-1-1:2005 (herein briefly denoted as EC2-92 and EC2-05 respectively), the American code ACI 318-08, the Canadian code CAN-CSA 2004 as well as the new and the previous Italian building code, D.M. 09-01-1996 and D.M. 14-01-2008, herein shortly indicated as DM-96 and DM-08 respectively. These models are conceived for classical R.C. elements. On the other hand, other authors have also proposed some models for the evaluation of the shear strength in HSTCBs (Amadio et al. 2010; Amadio et al. 2012).

In the follow, the expressions proposed by the aforementioned codes and scientific papers are presented by means of a classification in two categories: additive model, on one side, and truss models, on the other side.

Additive models. EC2-92, DM 1996, ACI 318-08, CAN-CSA 2004 models, as well as the model proposed by Amadio et al. 2010 and 2012, are based on the evaluation of the shear strength, V_R, as sum of the contribution due to concrete, V_c, and the contribution due to stirrups, V_{sw}:

$$V_R = V_c + V_{sw} \tag{2.1}$$

As a consequence, they differ each other for the way these two contributions are taken into account.

In EC2-92 the contribution of the concrete is calculated as:

$$V_c = [\tau_{Rd} k(1.2 + 40\rho_l) + 0.15\sigma_{cp}]b_w d \tag{2.2a}$$

with $\tau_{Rd} = \dfrac{0.25 f_{ctk0.05}}{\gamma_c}$ the concrete resistance, k=1.6-d a size effect coefficient, ρ_l the longitudinal reinforcement geometric ratio and σ_{cp} a term taking into account an eventual compressive force, b_w the width of the beam and d the effective depth.

On the other hand, the contribution due to the stirrups is evaluated as:

$$V_{sw} = 0.9d \frac{A_{sw}}{s} f_{yw}(1+\cot\alpha)\sin\alpha \tag{2.2b}$$

where A_{sw} is the area of the transverse shear reinforcement, f_{yw} is the yielding stress of the steel, α is the inclination of the stirrups and s the spacing.

In the Italian building code of 1996, DM-96, a similar additive model is considered, where the resistance contribution of the concrete has the following form:

$$V_c = 0.6 f_{ctd} b_w d \delta \tag{2.3}$$

being f_{ctd} the tensile strength of concrete and δ a coefficient equal to 1 in case that there is no compression force acting along the beam axis.

The contribution of the stirrups can be assumed equal to the one expressed in Eq. 2.2b.

Also in the American building code the shear strength of a R.C. beam is calculated in an additive way. Particularly the expressions of V_c and V_{sw} are respectively:

$$V_c = \frac{1}{7}\left(\sqrt{f_c^{'}} + 120\frac{A_s}{b_w d}\frac{Vd}{M}\right) b_w d\,, \qquad f_c^{'} \text{ in MPa} \tag{2.4a}$$

and

$$V_{sw} = \frac{A_{sw}}{s} f_{yw} d\left(\sin\alpha + \cos\alpha\right) \tag{2.4b}$$

Finally, the Canadian Standard Code provides the following expressions to calculate the shear strength of the concrete and the contribution of the transverse reinforcement respectively:

$$V_c = \phi_c \lambda \beta \sqrt{f_c^{'}} b_w d\,, \qquad f_c^{'} \text{ in MPa} \tag{2.5a}$$

$$V_{sw} = \phi_s \frac{A_{sw}}{s} f_{yw} d \cot\vartheta \tag{2.5b}$$

where ϕ_c and ϕ_s are the coefficients for concrete and steel, λ is a coefficient equal to 1 in the case of normal weight concrete and ϑ and β can be derived according to Bentz and Collins (2006) as follows:

$$\beta = \frac{0.40}{1+1500\frac{f_y}{2E_s}} \tag{2.6}$$

$$\vartheta = 29° + 7000\frac{f_y}{2E_s} \tag{2.7}$$

The model proposed by Amadio et al. 2010 is specifically developed for the structural typology of an HSTCB in whose geometry also some steel angles are introduced. As a consequence, the expression of the shear strength takes into account three contributions instead of two and can be formulated as follows:

$$V_R = V_c + V_{sw} + V_{ang} \tag{2.8}$$

being V_{ang} the shear resistance due to the steel angles.
Figure 2.18 shows the schematization of the three contributions.

In order to apply such a model to the experimental results showed in the previous sections, this latter contribution will be neglected because there are no steel angles in the tested specimens.

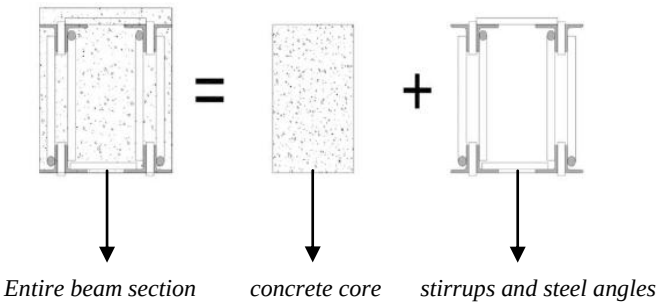

Figure 2.18. Scheme of the contributions to the shear strength in the model by Amadio et al. (2010).

The expression used for calculating V_c is the one provided in the current Italian building code for the shear resistance of members not requiring design shear reinforcement, whose form is similar to Eq. 2.2a:

$$V_c = [\frac{0.18}{\gamma_c} k(100\rho_l f_c^{'})^{1/3} + 0.15\sigma_{cp}]b_w d \quad (2.9a)$$

with $k = 1 + \sqrt{\frac{200}{d}} \leq 2$ (d in mm) a size effect coefficient, ρ_l the reinforcement geometric ratio and σ_{cp} an eventual compressive stress.

On the other hand, the contribution V_{sw} is evaluated considering the scheme of a simple truss with a compressive upper chord made up of concrete and an inferior tensile steel bar linked by means of tensile and compressive diagonal bars (Figure 2.19).

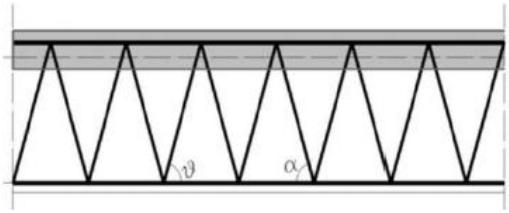

Figure 2.19. Scheme of the truss system according to Amadio et al. (2010).

As a consequence, the shear contribution of the diagonal bars is simply evaluated as:

$$V_{sw} = A_{sw} f_{yw} \sin\alpha \quad (2.9b)$$

The last additive model herein considered is the one proposed by Amadio et al. (2012). The model is calibrated on the basis of the FE simulations of experimental tests both carried out by the author and presented in the previous section. In the analytical model, the shear mechanism is assumed to be similar to the one occurring in a concrete panel reinforced by means of a steel tie that, in the case of the HSTCB is represented by the diagonal web bar. The panel is subjected to diagonal compression along the unloaded diagonal direction. By the resolution of this hyperstatic structure, which

requires the assumption of some parameters from the FE results, the shear resistance of the beam can be evaluated as the sum of the contribution due to the concrete and the contribution due to the steel reinforcement as:

$$V_c = \frac{f_c^{'} f_{ct}}{0.66 f_c^{'} + 1.99 f_{ct}} bh \tag{2.10a}$$

$$V_{sw} = \left(A_{sw} f_{yw} - \frac{V_c}{\sin\alpha} \frac{1}{k_2 \left(\frac{1}{k_1} + \frac{a}{E A_{sw} \cos\alpha} \right)} \right) \sin\alpha \tag{2.10b}$$

with

$$k_1 = 0.963 G b \sin\alpha \text{ and } k_2 = k_1 \left(\frac{1}{\left(\frac{s}{h} - 0.628 \right)^2} + 1 \right)$$

being G the shear modulus of the concrete and h the depth of the panel.

Truss models. Beyond the additive models, in this section also the strut and tie models provided by the current European and Italian codes are considered. The truss model for the shear reinforced members can be represented through the scheme in Figure 2.20 where the following legend is adopted:

A: compression chord;

B: struts;

C: tensile chord;

D: shear reinforcement;

α: angle between shear reinforcement and the main tension chord;

θ : angle between concrete compression strut and the main tension chord;

F_{td}: tensile force in the longitudinal reinforcement;

F_{cd}: concrete compression force in the longitudinal direction;

b_w: web width;

z: inner lever arm whose approximate value is *0.9d*.

Such a design method is known as the *variable strut inclination method* and the shear resistance provided by the concrete, V_{Rc}, and by the steel reinforcement, V_{Rs}, can be expressed respectively as:

$$V_{Rc} = \nu \alpha_c 0.9 d f_c^{'} b_w \frac{\cot\theta + \cot\alpha}{1 + \cot^2\theta}; \tag{2.11a}$$

$$V_{Rs} = 0.9d \frac{A_{sw}}{s} f_{yw} \left(\cot\theta + \cot\alpha\right) \sin\alpha; \tag{2.11b}$$

$$\text{where } 1 \le \cot\theta = \sqrt{\nu \frac{s b_w f_c^{'}}{A_{sw} f_{yw} \sin\alpha} - 1} \le 2.5 \tag{2.12}$$

In Eq. 2.11a the term ν represents the softening coefficient, equal to 0.5 according to DM-08 and equal to $0.6\left(1 - f_c^{'}/250\right)$ according to EC2-05 while the term α_c is equal to 1 for non-prestressed structures.

If the value of $\cot\theta$, calculated as in Eq. 2.12, proves to be in the range between 1 and 2.5, then Eq. 2.11a or, alternatively, Eq. 2.11b, allows to determine the shear strength of the beam due to the simultaneous failure of concrete and steel. Otherwise, if the value of $\cot\theta$ exceeds 2.5, then the failure must be attributed to the steel reinforcement and the shear resistance calculated by means of Eq. 2.11b assuming the value 2.5 for $\cot\theta$. In a similar way, if the value of $\cot\theta$ is below 1, then the failure must be attributed to the concrete strut and the shear strength evaluated according to Eq. 2.11a assuming $\cot\theta$ equal to 1.

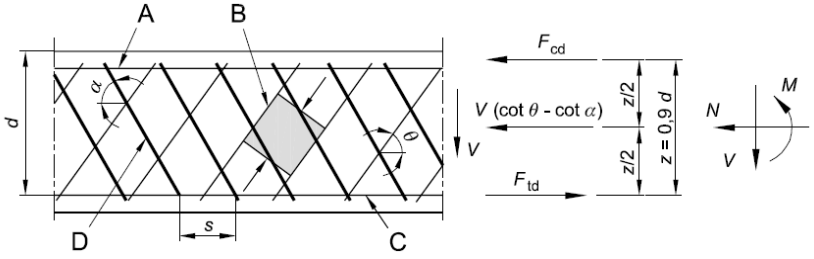

Figure 2.20. Scheme of the truss model (from UNI EN 1992-1-1:2005).

CHAPTER 3

ASSESSMENT OF PUSH-OUT TESTS RESPONSE IN PHASE II: ANALYTICAL CALCULATIONS AND SIMPLIFIED NUMERICAL MODELS

On the basis of the experimental results reported in the previous Chapter, both analytical and numerical simplified interpretations of the maximum load achieved in the push-out tests in *phase II* are herein presented and discussed. The analytical models are mainly based on strut and tie formulations, on one hand, and dowel-effect mechanism, on the other hand. Conversely, the numerical FE models are representative of a single mesh of the truss of the beam considered only in the 2D plane containing the diagonal web bars.

3.1 Analytical interpretation of the maximum load

As aforesaid in the previous sections, push-out tests on specimens representing HSTCBs in *phase II* were developed by few authors in order to investigate the stress transfer mechanisms between the steel elements constituting the truss of the beam and the surrounding hardened concrete.

Herein the attempt of a simplified analytical interpretation of such results is proposed. According to the current guidelines provided by CC.SS.LL.PP. (2011), already described in Chapter 1, the considered analytical models for the assessment of the push-out tests response are elaborated on the basis of the classification of the beams in R.C. beams (category b) and classical composite beams (category a). Thus, strut-and-tie models and dowel-mechanism models are proposed and the theoretical results are compared with the available experimental data reported in Chapter 2.

3.1.1 Strut and tie models

The first attempt of interpreting the experimental data is made up by means of a typical truss model (see Colajanni et al. 2014) according to the indications provided in the current Italian building code (D.M.LL.PP. 14 Jan 2008) as well as in Eurocode 2 (2005) for R.C. beams. To this aim the HSTCBs are considered belonging to the R.C. structures typology. Thus, an equivalent planar truss model (see Figure 3.1) is defined, consisting of a compressed concrete top chord, a tensile bottom steel plate, web ties made up of diagonal steel bars and, finally, steel and concrete struts inclined at an angle α and ϑ respectively. It has to be mentioned that the angle ϑ is chosen so that it can make maximum the strength of the system, fulfilling the condition that $1 \leq \text{ctg}\vartheta \leq 2.5$. It should be noted that, approximately, it is possible to refer to the statically determinate truss system obtained neglecting the contribution of the compressed web steel bars and, using the expressions present in the Italian code and in Eurocode 2 properly adapted to the current problem (see Figure 3.2), thus, it is possible to calculate the failure load as the minimum value corresponding to the collapse of the compressed concrete or the tensile steel.

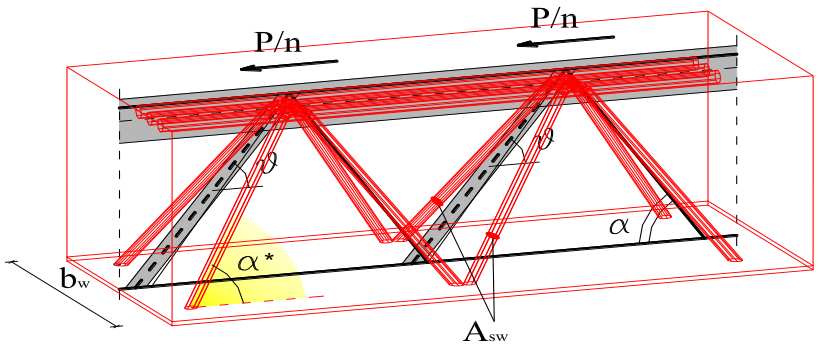

a)

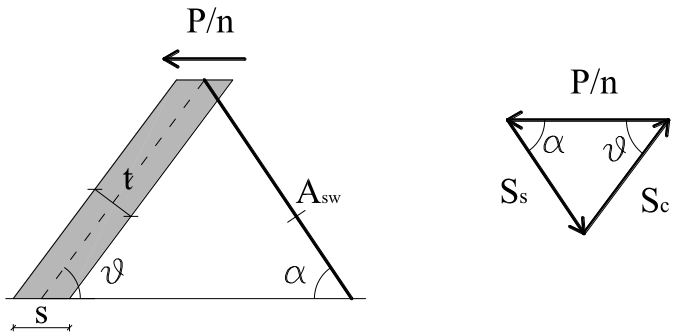

b)

Figure 3.1. Truss planar model for push-out specimen: a) axonometric scheme; b) planar single mesh.

With reference to the symbols in the single mesh of Figure 3.1b, the slippage force is P/n, n being the number of meshes which can form in relation to the choice of the angle ϑ and to the geometry of the specimen. Considering the ultimate strength in the compressed concrete strut (whose cross-section area is equal to $b_w\ t$ with $t = s\ \sin\vartheta$), $S_{c,u}=b_w\ t\ f'_{cu}$, or the ultimate strength in the tensile web bars, $S_{s,u}= A_{sw}\ f_{su}$, the following expressions can be obtained:

$$P_{Rc,u} = n b_w\, s\, f_{cu}^{'} (ctg\alpha + ctg\vartheta) / (1 + ctg^2\vartheta) \qquad (3.1a)$$

$$P_{Rs,u} = n A_{sw} f_{su} (ctg\alpha + ctg\vartheta) \sin\alpha \tag{3.1b}$$

In these expressions s is the distance between two successive web bars, b_w is the width of the cross-section, A_{sw} is the area of the web steel reinforcement, f_{su} and f'_{cu} are, respectively, the values of the ultimate strength in the steel and the reduced strength in the concrete ($f'_{cu}=0.5\ f_{cu}$). It can be observed that the presence of steel compressed web bars inclined of α makes possible the existence of meshes in the steel truss inclined at an angle ϑ so that $\text{ctg}\alpha \leq \text{ctg}\vartheta$. Therefore, when $\text{ctg}\alpha = \text{ctg}\vartheta$ is assumed, Eq. 3.1b gives the resistance of the bare steel truss, being the instability of the compressed bar prevented.

In this section the described model will be indicated as Model 1. As already mentioned, such model, shown in Figure 3.2a, is based on the application of Eqs. 3.1 as usually done for R.C. structures. The angle ϑ is chosen in order to make the value of the steel strength equal to the concrete resistance, and then, modifying the lower limit of $ctg\vartheta$, the following assumption is adopted:

$$ctg\alpha \leq ctg\vartheta = \sqrt{\frac{s b_w f'_{cu}}{A_{sw} f_{su} \sin\alpha} - 1} \leq 2.5 \tag{3.2}$$

Because of the geometric dimensions of the real specimens tested in the literature, in some cases this model cannot be applied since the condition in Eq. 3.2 proves to be not compatible with the geometry of the specimen whose dimensions do not allow the formation of the equivalent truss mesh. As a consequence, two other models are considered with different inclinations of the concrete strut, called Model 2 and Model 3 (Figure 3.2b-c). Particularly, Model 2 is obtained by choosing the angle $\vartheta = \vartheta*$ in order to allow the largest number of strengthening meshes of the steel-concrete truss to form also taking advantage of the presence of the diagonal compressed steel bar according to the lower limit for ϑ as in Eq. 3.2. Such hypotheses lead to the structural scheme represented in Figure 3.2b. A further increase of the strength predicted by the model can be obtained by means of Model 3,

allowing each mesh to have a different inclination of the concrete strut as indicated in Figure 3.2c, compatibly with the limitation in Eq. 3.2 and those imposed by the specimen geometry.

Table 3.1 shows the comparison between theoretical and experimental results in terms of ratio between the peak load values. Model 1 is applicable only in few cases. Model 2 shows a quite good agreement with the experimental data (the average value, r_m, of the ratio $P_{u,\,theo}/P_{u,\,exp}$ is equal to 0.891) but with a relatively high coefficient of variation, C_{vr}, equal to 0.446 denoting a certain scatter between the analytical results. On the other hand, Model 3 provide an almost 12% overestimation of the experimental maximum load but presents a lower value of C_{vr} equal to 0.238.

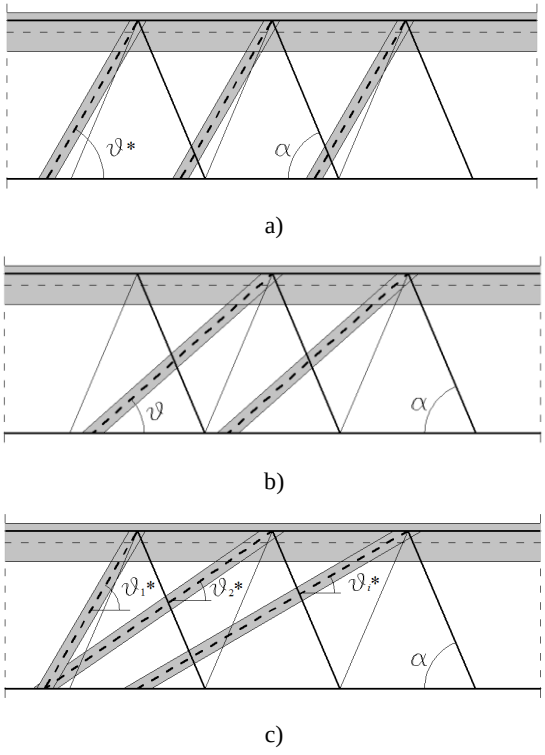

Figure 3.2. Truss model: a) Eurocode 2 (2005) (Model 1); b) maximum number of web struts (Model 2); c) concrete struts with different slope (Model 3).

3.1.2 Dowel mechanism models

For the evaluation of the resistance against the maximum slip force of HSTCBs which can be considered as classical steel-concrete composite structures (Johnson 1994) classified within category a), in the case of ductile connection, it is possible to refer to the dowel-concrete interaction model originally proposed by Gelfi and Giuriani (1987). The model was developed for the evaluation of the resistance of the connection between the steel beam and the concrete slab schematically shown in Figure 3.3a. The model (Figure 3.3b-d), indicated as Model 4, is based on some experimental observations which showed that the failure occurs for both local crushing of the concrete, subjected to the strong pressure due to the dowel, and for the formation of one or two plastic hinges in the shank of the latter. The failure mechanism depends on the length of the dowel with respect to the mechanical characteristics of steel and concrete. Three different failure mechanisms, in fact, can be individuated: a short, medium and long dowel mechanism. The different behavior is identified on the basis of the following simplified assumptions:

- uniform distribution of the pressure of the dowel against the concrete, in the radial direction as well as along the axis of the dowel;
- the ultimate stress in the concrete, σ_{cu}, which develops within the plastic process zone, is approximately four times the cubic strength of the concrete;
- the formation of the plastic hinge at the base of the dowel is placed at a distance equal to a certain aliquot, a, of the diameter of the dowel, ϕ.

The short dowels are subject to a uniform stress state (Figure 3.3b) and the failure occurs by crushing of the concrete; the long-dowel failure mechanism is characterized by two plastic hinges (Figure 3.3d), one at the base of the dowel, corresponding to section A, and the other one in section B, placed at a distance from section A so that the actions transmitted by the concrete allow the achievement of the ultimate moment (cross-section with zero shear force). This section identifies the *effective length* within which the action between steel and concrete must be assessed, while the remaining part of the dowel is subjected to actions that have zero resultant. The prediction of the ultimate load, P_u, is given by the following expression:

$$P_u = \sigma_{cu}\,\phi\,L_{eff} \tag{3.3}$$

with L_{eff} the effective length of the dowel that varies depending on the failure mechanism.

Denoting by f_y the yield stress of the steel, then the *limit lengths* of the short dowel, L_1^*, and the medium dowel, L_2^*, can be evaluated by imposing, in the first case, the condition that makes possible the formation of the plastic hinge at the base of the dowel (see Figure 3.3b), in the second case, the formation of both the plastic hinges (see Figures 3.3c and 3.3d).

Thus, the two *limit lengths* are respectively:

$$L_1^* = a + \phi\sqrt{\frac{1}{3}\frac{f_y}{\sigma_{cu}}}\ ;\ L_2^* = a + 2\phi\sqrt{\frac{2}{3}\frac{f_y}{\sigma_{cu}}} \tag{3.4}$$

If the dowel is short, its effective length, $L_{eff}^{(S)}$, is equal to the total length L, while, for the medium dowel, the effective length, $L_{eff}^{(M)}$, is equal to:

$$L_{eff}^{(M)} = a(L-a)\left[-1+\sqrt{2+\frac{2}{3}\frac{f_y}{\sigma_{cu}}\left(\frac{\phi}{L-a}\right)^2}\right] \tag{3.5}$$

Finally, when $L \geq L_2^*$, the dowel is defined as long dowel and its effective length, $L_{eff}^{(L)}$, is equal to:

$$L_{eff}^{(L)} = a + \phi\sqrt{\frac{2}{3}\frac{f_y}{\sigma_{cu}}} \tag{3.6}$$

If we assume the length of the plastic hinge $a=\phi/2$ (a value more conservative than $a=1.5\phi$ proposed by Gelfi and Giuriani 1987), and the ratio $f_y/\sigma_{cu}\cong 3.5$, the trend of L_{eff}/ϕ with respect to L/ϕ, in the range of the long dowels, corresponds to the one obtained by means of the expressions proposed in Eurocode 4 (2005). These latter provide the shear strength P_{Rd} of studs with the diameter ϕ in the range between 16 and 25 mm. With reference to the symbols in Figure 3.3, the resistance of the shear connection is provided by the smallest of the two following values:

$$P_{Rd1} = \frac{1}{\gamma_v}\frac{0.8\, f_u \pi \phi^2}{4}; \tag{3.7a}$$

$$P_{Rd2} = \frac{0.29\,\alpha\,\phi^2\sqrt{f_{ck}\,E_{cm}}}{\gamma_v} \tag{3.7b}$$

where

$\alpha = 0.2\left(\frac{L}{\phi}+1\right)$ for $3 \le \frac{L}{\phi} < 4$

$\alpha = 1$ for $\frac{L}{\phi} \ge 4$

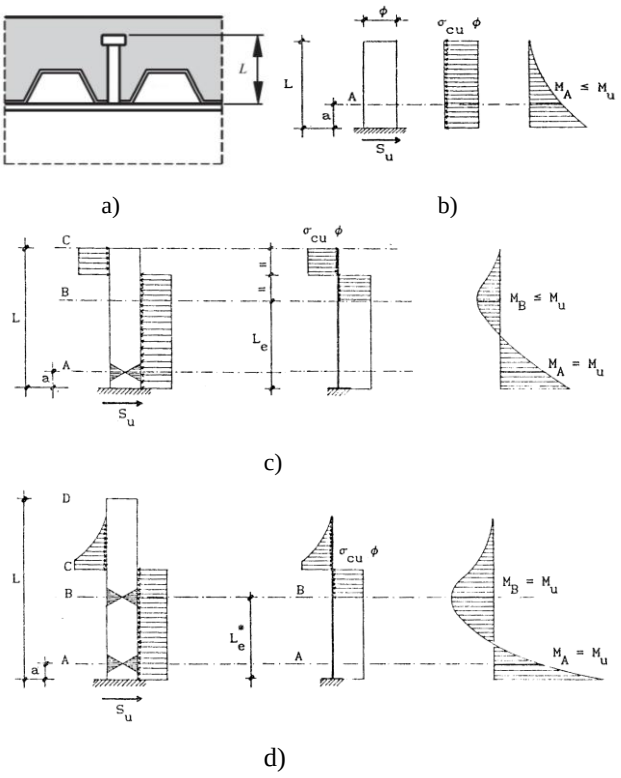

Figure 3.3. Dowel-mechanism model (Model 4): a) connection between the steel beam and the concrete slab through the connector; b) short dowel; c) medium dowel; d) long dowel (Gelfi e Giuriani, 1987).

In Eqs. 3.7a and 3.7b, f_u is the ultimate strength of the material constituting the dowel (not exceeding 500 N/mm^2); f_{ck} is the cylindrical concrete compressive strength, of density not less than 1750 kg/m^3; the coefficient γ_v is assumed equal to 1.

The results provided by this model assuming ductile connection, i.e. by multiplying the resistance of the single dowel for the number of diagonal bars of the truss welded to the plate, are given in Table 3.1. The average value, r_m, of the ratio between the analytical results and the experimental values is equal to 0.956 and the coefficient of variation is CVr=0.382. From the same table it can be observed, in fact, that the data for the specimens tested by Puhali and Smotlack (1980), which are characterized by a single mesh and the smallest diameter of the web bar (14 and 24 mm), the model underestimates the peak load, proving that the resistance mechanism in the HSTCB should be modified with respect to the one of the classical steel-concrete composite beam. On the other hand, values greater than one found for all the specimens tested by Aiello (2008), show that in the presence of meshes with elements close together, the hypothesis of ductile connection is not always reasonable and the resistance of the connection cannot be calculated as a simple sum of the resistance of the individual dowels. Such remarks are supported by the load-slip diagrams for these specimens represented by the author (Aiello 2008), showing in many cases displacements at failure less than 6 mm which are required, instead, by both national and international codes to classify a connection as ductile.

As a consequence, the model proposed by Gelfi and Giuriani (1987) is revised in order to take into account the actual geometry of the connection system in the HSTCBs. Particularly, the inclination angle α^* of the diagonal web bars is now considered (Figure 3.1a).

Maintaining the schematization of the concrete in layers modeled as slabs loaded along the plane containing the axis of the specimen, it results that the bar is subject to both axial force and bending moment rather than simple bending. It is also worth to note that in the presence of bars made up of ribbed steel, the friction that develops between the two materials significantly changes the stress state. On the basis of those observations, the

resistance of the bar (similar to a dowel welded to the steel plate) must be assessed taking into account the interaction domain at the ultimate limit state between the normal force, N_u, and the bending moment, M_u, expressed by following relationship (Campione et al. 2012):

$$N_u = \frac{1}{4} f_y \phi^2 \left\{ \pi - 2\arcsin\left[\frac{1}{\phi} \sqrt[3]{\frac{6M_u}{f_y}} \right] + \sin\left[2\arcsin\left(\frac{1}{\phi} \sqrt[3]{\frac{6M_u}{f_y}} \right) \right] \right\} \quad (3.8)$$

The model in which such a modification is introduced is herein called Model 5. Figure 3.4 shows the trend of the ultimate load estimated using the simple dowel mechanism model with respect to the variation of the ratio L/ϕ for the diagonal web bars belonging to the specimens tested by Badalamenti (2010). The comparison between the two curves, neglecting the bond between steel and concrete, allows to appreciate the reduction in resistance due to the interaction between the normal force N_u and the moment M_u. The first linear branch of the curve represents the range of the short dowels; the second non-linear branch represents the range of the medium dowels and, finally, the third constant branch represents the range of the long dowels. It can be observed how the interaction N_u - M_u produces a reduction in strength up to 21% compared to the case of simply bended dowel.

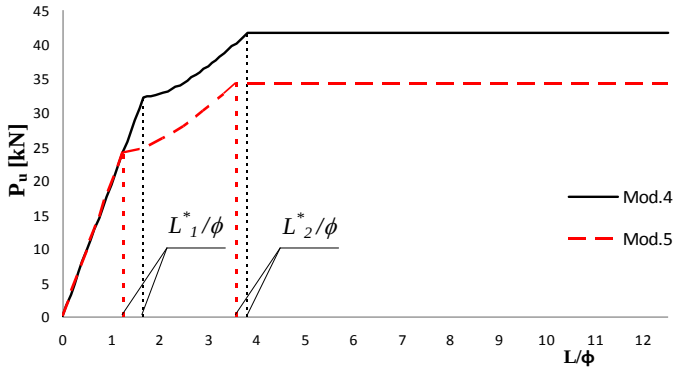

Figure 3.4. Effects of the interaction N_u-M_u on the resistance of the dowel: comparison between Model 4 and Model 5.

Table 3.1. $P_{u,theo}$ /$P_{u,exp}$ ratios.

ID	Model 1	Model 2	Model 3	Model 4
A-P1	-	0.593	0.593	0.397
A-P2	-	1.247	1.247	0.834
A-P3	-	1.702	1.702	1.138
B-P4	-	0.747	0.747	0.500
B-P5	-	1.371	1.371	0.917
PB	0.594	0.662	0.746	0.604
S12	-	0.643	1.182	1.251
S14	-	0.591	0.843	1.438
B12	-	0.675	1.241	1.131
B14	0.674	0.673	1.441	1.352
***Average* (r_m)**	0.634	0.891	1.117	0.956
CV*r*	0.089	0.446	0.238	0.382

As a consequence, the results reported in Table 3.1 provided by the simple dowel mechanism model, that is Model 4, which already strongly underestimates the resistance experimentally observed in the presence of a single mesh of the truss (specimens tested by Puhali and Smotlack 1980), should be, actually, further reduced to take into account the interaction domain N_u-M_u.

3.1.3 Modified dowel mechanism model

On the basis of such observations and with the aim of better understanding the evolution of the stress state in the steel members and in the concrete, a simple non-linear FE model is developed assuming the same main hypotheses which are on the basis of the analytical Model 4 (case of smooth steel bars, mechanical response of the concrete in the direction of the applied load). The details concerning the formulation of the simplified FE model will be presented in the following paragraph.

The diagram of the numerical results reported in Figure 3.5 refers to the analysis carried out on the single mesh of the truss, according to the scheme represented in Figure 3.6 where the geometry, the load condition and the

constraints of the problem are showed. As already said, the modeling of the steel-concrete interaction is developed according to the same simplified approach which represents the basis for the derivation of the model proposed by Gelfi and Giuriani (1987) (Model 4), that is considering the concrete located between two diagonal bars of the truss as a two-dimensional slab. Conversely, the resistance of the web bar of the truss is modeled taking into account the effects of interaction between axial force and bending moment. The simplified model has allowed to highlight that, in the absence of bond between the concrete and both the diagonal bars and the upper chord, both ends of the diagonal bar are involved in the transfer of the stresses from concrete to steel, as shown in Figure 3.5 where the evolution of stresses in the concrete at the ultimate state is represented. Being the instability of the bar prevented by the presence of the compressed concrete, the system is emisymmetric. Furthermore it has to be noted that, in relation to the different level of axial force in the sections of the bar, the upper effective length, where the normal stress is smaller, is greater than the lower one. However the model neglects the stiffening action of the concrete in the direction orthogonal to applied load, action that, if taken into account, considerably reduces the magnitude of the actions transmitted from the diagonal bar to the concrete near the upper chord.

Thus, on the basis of the numerical outcome, a simplified analytical model, very similar to the one by Gelfi and Giuriani (1987), is formulated taking into account the involvement of both ends of the bar in the stress transfer from concrete to steel. Furthermore, the upper and lower limit lengths, that identify the conditions for transition between long-dowel and medium-dowel truss, are evaluated. The model thus obtained is identified as Model 6. The analysis is carried out exploiting the condition of emisimmetrical loading, represented in Figure 3.6, where a structural diagram corresponding to the presence of four medium dowels can be recognized (see Figure 3.3c). The diagram refers once again to a planar truss that, in this case, is contained in the inclined plane of the spatial mesh (the yellow plane in Figure 3.1a) rather than the vertical projection of the same. This means that the length of the diagonals of the truss in Model 6 is the

actual length of the bars of the beam and their angle of inclination is the angle α^* rather than its projection α (Figure 3.1).

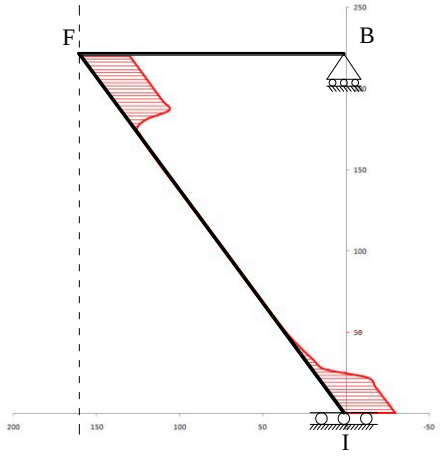

Figure 3.5. Finite Element Analysis: reactions corresponding to the upper and lower ends of the dowel.

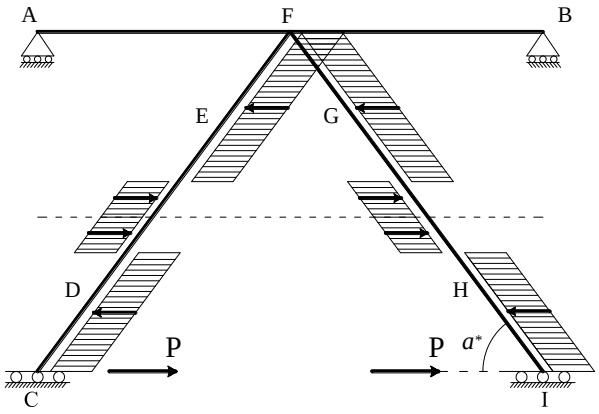

Figure 3.6. Modified dowel mechanism model (Model 6): geometry of the truss, load condition and constraints.

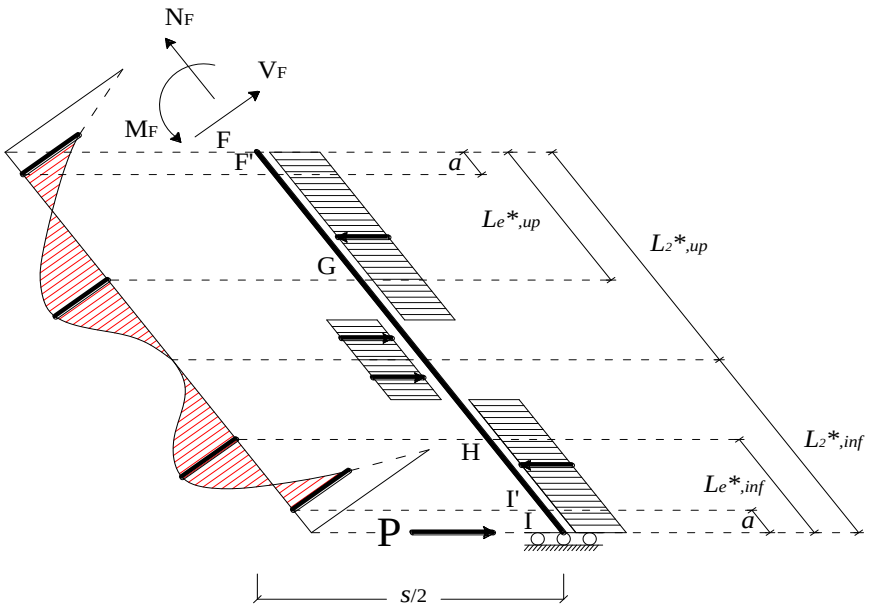

a)

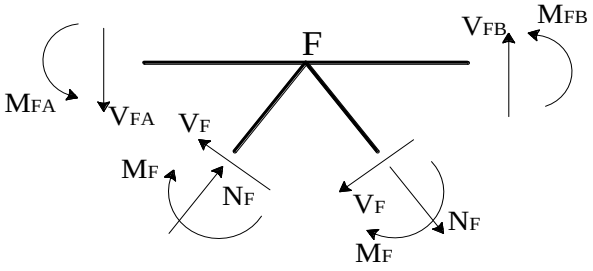

b)

Figure 3.7. Model 6: a) bending moment diagram on the diagonal bar; b) equilibrium at the node F.

Figure 3.7a represents, for one of the two bars, the structural scheme analyzed with the indication of the effective upper and lower lengths, $L^*_{e,up}$ and $L^*_{e,inf}$, and the corresponding limit lengths, $L^*_{2,up}$ and $L^*_{2,inf}$, the load scheme and the corresponding moment diagram. In Figure 3.7b the equilibrium at node F of the mesh of the truss is represented, showing that the development of such a mechanism requires that the sum of the resisting moments at the upper chord is not less than the sum of the moments of the diagonal bars. Once again, for semplicity, the bond between steel and concrete is neglected. The lenght $L^*_{e,up}$ can be obtained by imposing that in sections F' e G, in which the plastic hinges are formed, the couples $N_{F'}$-$M_{F'}$ end N_G-M_G satisfy Eq. 3.8. Then, considering that in the absence of bond action on the upper chord, the horizontal component of the actions on the "dowel" at node F is zero, by exploiting the following equilibrium relationships:

$$V_{F'} = \sigma_{cu}\phi(L^*_{e,\mathrm{up}} - a)\sin\alpha^* \tag{3.9a}$$

$$N_{F'} = \frac{V_{F'}\sin\alpha^* + \sigma_{cu}\phi\, a}{\cos\alpha^*} \tag{3.9b}$$

$$M_G = -\frac{1}{2}\sigma_{cu}\phi(L^*_{e,\mathrm{up}} - a)^2\sin\alpha^* - M_{F'} + V_{F'}(L^*_{e,\mathrm{up}} - a) \tag{3.10a}$$

$$N_G = \sigma_{cu}\phi(L^*_{e,\mathrm{up}} - a)\cos\alpha^* + N_{F'} \tag{3.10b}$$

it is possible to derive the upper effective length $L^*_{e,up}$, and then, by means of simple equilibrium conditions, the upper limit length, $L^*_{2,up}$, as:

$$L^*_{2,\mathrm{up}} = L^*_{e,\mathrm{up}} + \sqrt{4M_G/(\phi\sigma_{cu})} \tag{3.11}$$

Taking into account that the actions of the concrete between point G and H represent two couples of equal intensity and opposite direction, then the solicitations in the two points will be the same (N_H=N_G, M_H=M_G); therefore, the inferior effective length $L^*_{e,inf}$ is calculated imposing that at the end I',

where the plastic hinge is formed, also the couple $N_{I'}$-$M_{I'}$ satisfy Eq. 3.8. These forces are expressed by the following relationships:

$$M_{I'} = -M_H + \frac{1}{2}\sigma_{cu}\phi(L^*_{e,\inf} - a)^2 \sin\alpha^* \tag{3.12a}$$

$$N_{I'} = N_H + \sigma_{cu}\phi(L^*_{e,\inf} - a)\cos\alpha^* \tag{3.12b}$$

$$V_{I'} = \sigma_{cu}\phi(L^*_{e,\inf} - a)\sin\alpha^* \tag{3.12c}$$

and the inferior limit length $L^*_{2,inf}$ is:

$$L^*_{2,\inf} = L^*_{e,\inf} + \sqrt{4M_H/(\phi\sigma_{cu})} \tag{3.13}$$

In the presence of ductile elements, the total load, $P_{u,theo}$, is obtained as the sum of the resistance provide by each dowel:

$$P_{u,theo} = \sigma_{cu}\phi(L^*_{e,\mathrm{up}} + L^*_{e,\inf})n \tag{3.14}$$

where *n* indicates the number of diagonal web bars, that is the number of dowels.

Finally, in order to take into account the simultaneous presence of the shear stresses due to the shear action, *V*, the yield stress should be reduced as follows:

$$f_y^{red} = \left[1 - \left(8V/0.8\, f_y \pi \phi^2 - 1\right)^2\right] f_y \quad \text{for } V \geq \left(0.8\, f_y\, \pi\, \phi^2 / 4\right)/2 \tag{3.15}$$

The results obtained using Model 6 for the interpretation of the cases described in the previous Chapter are reported in Table 3.2; even in this case the results by Tullini et al. (2006) and the results by Puhali and Smotlack (1980) relative to the specimen B-P6 are excluded. Furthermore, the ultimate loads used in the calculation for the specimens tested by Aiello (2008) and Badalamenti (2010) are the mean values of the tests carried out on each

specimen typology. Thus, in the same table, the tag attributed to the tests carried out by Badalamenti (2010) is PB, while the tags which identify the specimens tested by Aiello (2008) are S12, S14, B12 and B14. It is worth to note that, although the model is designed to obtain an upper bound of the load, in three cases for smooth bars, and in two cases for ribbed bars, the assessment of the resistance is still conservative. The results concerning the only specimens with smooth steel provide an average value of r_m = 1.168, while for the entire database of Table 3.2 the resistance value is close to the experimental one, being r_m = 1.094 with a coefficient of variation $CVr_{Mod.6}$=0.338.

Table 3.2. Model 6 results.

ID	$P_{u,theo}/P_{u,exp}$	$L_2^*{}_{,up}$ (mm)	$L_e^*{}_{,up}$ (mm)	$L_2^*{}_{,inf}$ (mm)	$L_e^*{}_{,inf}$ (mm)
A-P1	0.656	43.46	28.75	34.41	19.70
A-P2	1.380	74.51	49.28	58.99	33.77
A-P3	1.883	99.34	65.71	78.66	45.03
B-P4	0.782	40.93	26.92	32.90	18.89
B-P5	1.434	70.18	46.15	56.41	32.38
PB	0.910	32.23	21.07	26.48	15.33
S12	0.950	11.09	10.37	6.83	6.12
S14	1.092	12.94	12.10	7.97	7.14
B12	0.842	12.79	10.93	8.55	6.69
B14	1.008	14.93	12.76	9.98	7.81
Average* (r_m)**= 1.094 **CV*r= 0.338					

3.2 2D simplified finite element models

Behind the development of the analytical expressions discussed in the previous section, a first attempt of a simplified numerical modeling of the HSTCB is considered and herein presented. The geometry of the beam and the mechanical characteristics of materials are those of the experimental campaign of push-out tests performed in 2008 at the University of Palermo Badalamenti (2010) and already described in Chapter 2.

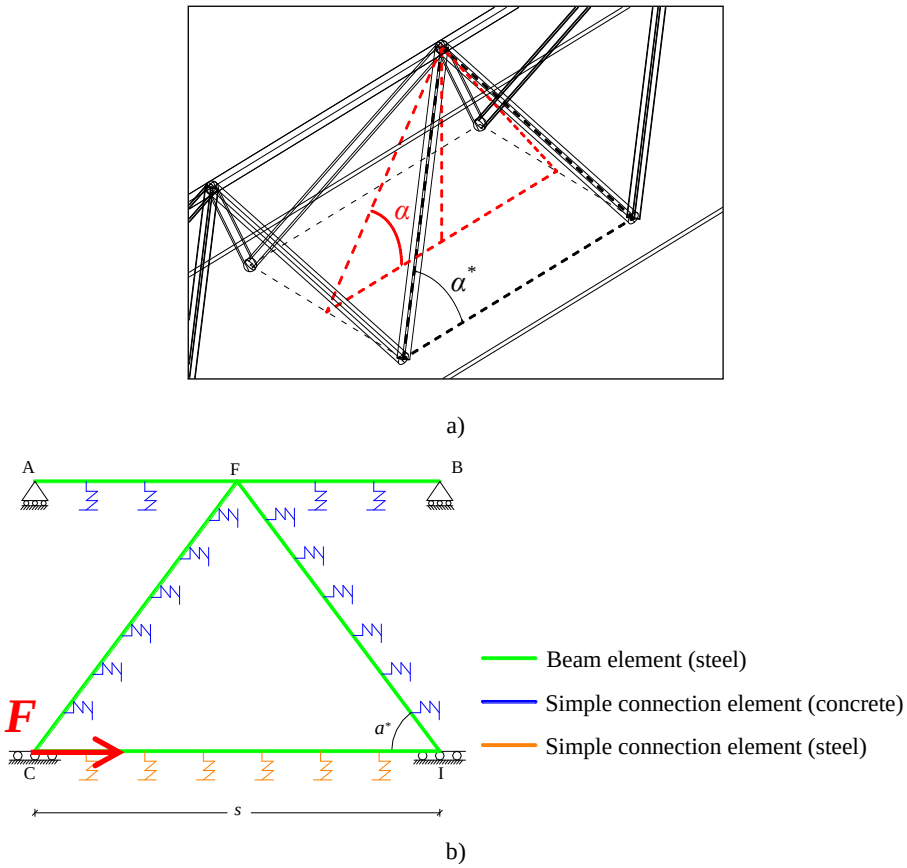

Figure 3.8. Scheme of the planar single mesh of the truss: a) axonometric view of the geometry; b) scheme of the FE model.

The main features of such models are the following: the 2D schematization of one single mesh of the steel truss constituting the real beam (Figure 3.8a) and the use of only two-node "beam elements" and "connectors" in whole the model. Particularly, the "beam elements" are employed to model the diagonal web bars of the truss, while the "connectors" are supposed to represent the concrete response while some other connectors are introduced in order to model the stiffness of the bottom steel plate (Figure 3.8b). This kind of model is conceived deliberately in a very simple way in order to figure out if such a complex mechanism of

transmission of stresses and the resulting failure mode can be immediately represented through an extremely simplified scheme or if it is absolutely necessary to develop a detailed numerical simulation. The proposed 2D simplified modeling is generated by means of the software DRAIN 2D-X. Few consecutive steps are developed in order to improve the onset of some issues related to the simplified method. In the first step only simple beam elements are used to model the two diagonal steel bars (see Figure 3.8a) and, therefore, a problem arises dealing with the maximum axial force carried by the bar during the analysis, due to the formulation of the element itself. As shown in Figure 3.9, the axial force in the bar resulting from the analysis exceeds the maximum value allowed according to the interaction domain M-N expressed by Eq. 3.8.

In order to solve this inconvenience, a simple device is introduced in the model, that is a "truss element" whit a very small length placed next to the section of the diagonal bar welded to the bottom steel plate and which aims at controlling the maximum value of the axial force (Figure 3.10a). So doing, the maximum value of *N* achieved in the sections of the diagonal bar not far from the truss is quite contained (Figure 3.10b).

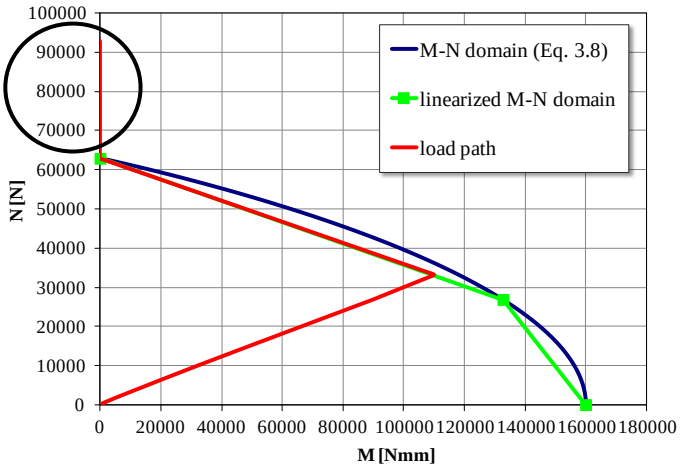

Figure 3.9. Load path within the M-N domain of a 12 mm diameter steel bar.

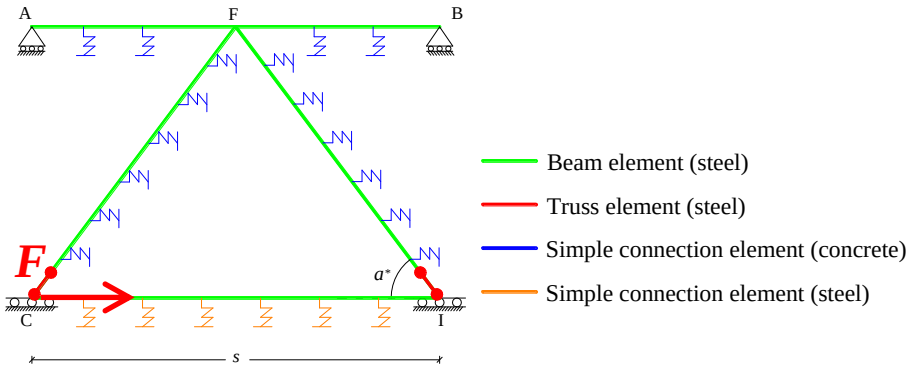

a)

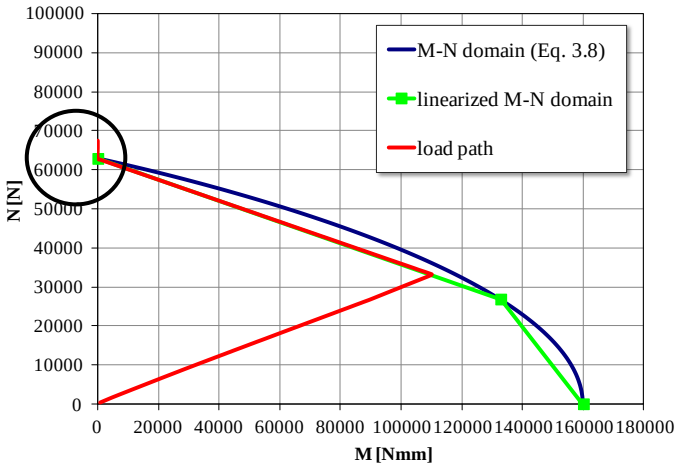

b)

Figure 3.10. Introduction of the truss element: a) scheme of the model; b) M-N domain in the section of the bar next to the truss.

Figure 3.11 shows then the comparison between the numerical and the experimental results in terms of load-displacement curves. Particularly the experimental values are those measured by the LVDTs during the tests on specimens P1, P2 and P3. The numerical load is evaluated multiplying the value of the force obtained from the FE model for the total number of meshes constituting the real specimen. The maximum numerical load is,

thus, equal to 1074.19 kN. The initial stiffness of the numerical curve fits quite well the one of the experimental results.

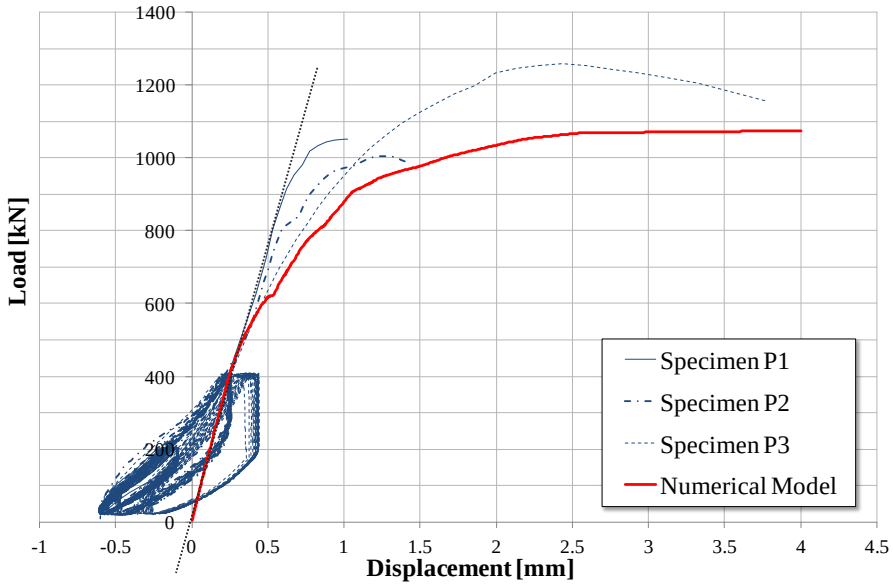

Figure 3.11. Numerical vs. Experimental load-displacement curves.

As it can be observed, such a model neglects the bond between steel and concrete. The numerical simulation showed that in this case the stress transfer mechanism is also involving the upper extreme of the diagonal steel bar as already represented in Figure 3.5.

With the aim of taking into account the bond between steel and concrete, some further connectors, whose constitutive law is based on the classical τ-s relationship proposed by Eligehausen et al. (1983) for ribbed bars (see Figure 3.12), are introduced in the model. Thus now the scheme of the FE model is the one showed in Figure 3.13. The finite elements used for the diagonal steel bars are, in this case, "fiber beam elements", discretized into five further segments, which are able to take into account the M-N interaction effects. The load path of the control section of the fiber beam element within the M-N domain, has been checked and it is shown in Figure 3.14.

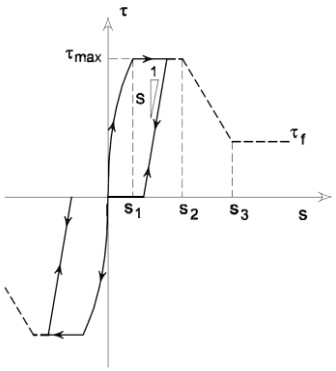

Figure 3.12. Scheme of the bond-slip relationship by Eligehausen et al. (1983).

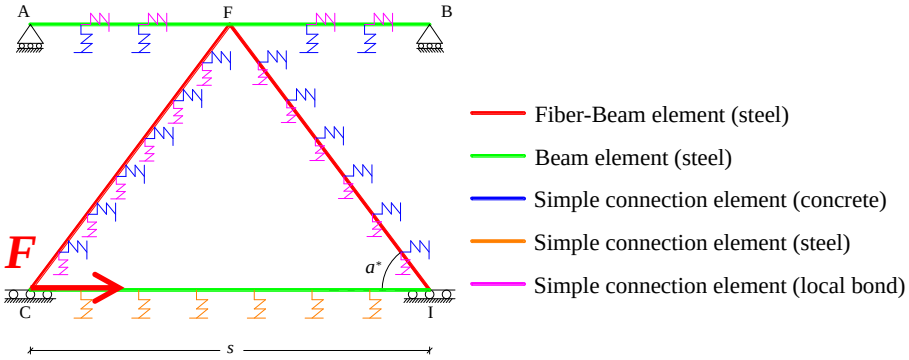

Figure 3.13. FE model for ribbed bars.

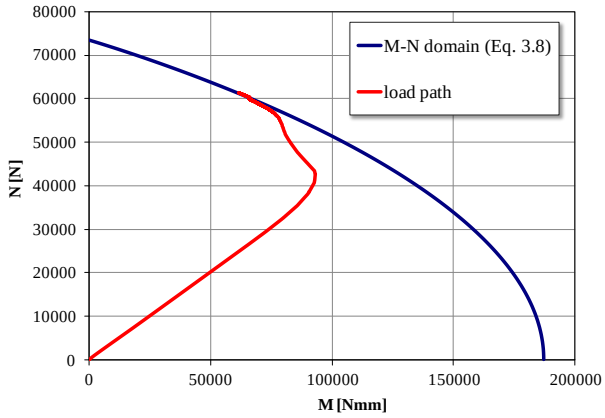

Figure 3.14. Load path of the control section of the fiber beam element.

As regards the stress transfer, in this case the numerical analysis shows that the bottom extreme of the diagonal bar is the only one involved in the mechanism. In terms of maximum numerical load, in this case, the model underestimates the experimental results of about 30%, being the numerical resistance equal to 771.70 kN. Therefore, the numerical load-displacement curve is not reported.

As a consequence, on the basis of the results presented in this section, it arises the necessity to develop a more accurate FE model aimed at taking into account the 3D geometry of the beam, the extreme variety of all parameters on which the stress transfer mechanisms depend and the consequent failure modes, all issues that can be difficulty grasped from a simplified representation of this structural typology.

Thus, in the following Chapter, the development of a detailed FE model of push-out tests on HSTCBs is presented and discussed.

CHAPTER 4

STRESS TRANSFER MECHANISMS INVESTIGATION: 3D FINITE ELEMENT MODELS OF PUSH-OUT TESTS

In this Chapter some accurate non-linear FE models with different degree of detail are presented and discussed (see Colajanni et al. 2013b). Such models are developed with the aim of investigating the complex stress transfer mechanism between the steel members and the surrounding concrete occurring in a HSTCB subjected to the stress state due to a push-out test. With the aim of accurately grasping the complicate dowel and bond phenomena arising at the steel-concrete interface, the 3D solid model is realized to account for the actual contact surfaces between the truss and the concrete. HSTCB constituted by either deformed or smooth steel diagonal bars is considered, and four models for steel-concrete interface are proposed: two models refer to ribbed steel truss (Ribbed Steel Bar Models, RSBM-1 and RSBM-2) and two other models to smooth steel truss (Smooth Steel Bar Models, SSBM-1 and SSBM-2), representing the various cases of perfect bond or no-bond between surfaces and the cases of a specific τ-s law at the interface of both ribbed and smooth truss.

The models have been developed in collaboration with the research group of Prof. Gianvittorio Rizzano, Department of Civil Engineering, University of Salerno, by means of the software ABAQUS 6.10. They are calibrated on

the basis of the experimental tests carried out at the University of Salento by Aiello (2008) in order to verify their accuracy. Then, the developed model is used to provide a parametric analysis aimed at individuating the main geometrical and mechanical parameters influencing the load carried by the truss-concrete system in push-out tests.

4.1 General features

The FE analysis aims at simulating experimental push-out tests in order to investigate in detail the interaction mechanism arising between the steel web bars of the truss and the concrete. In order to reach this goal, the FE model has necessarily to account for the specimen actual geometry, the material geometrical nonlinearity and the interaction stresses between bars and surrounding concrete. The accuracy of the FE model has been evaluated with reference to the aforementioned experimental tests carried out at the University of Salento (Aiello 2008) and already described in Chapter 2.

The first step is the characterization of the beam geometry taking into account the actual contact surfaces between the truss and the concrete. The steel truss and the bottom plate have been generated as a unique element by means of sweep and extrusion commands. Also the bar constituting the upper chord has been realized as an extrusion solid and the concrete core has been obtained by subtracting to a solid parallelepiped the geometry of the truss defining in this way the empty volume.

Concerning the meshing of the beam, the truss has been discretized by means of brick elements adopting a structured meshing technique. In order to favorite convergence and reduce the computational times, the simplest and lighter element type has been chosen, the C3D8R, that is a 8-node linear brick with reduced integration and hourglass control. Conversely, the concrete block has been discretized by using a free meshing technique that is more effective in cases of complicate geometries. As far as it is not possible to use prismatic bricks in case of free meshing, the element type chosen for the concrete is the C3D4, that is a 4-node linear tetrahedron.

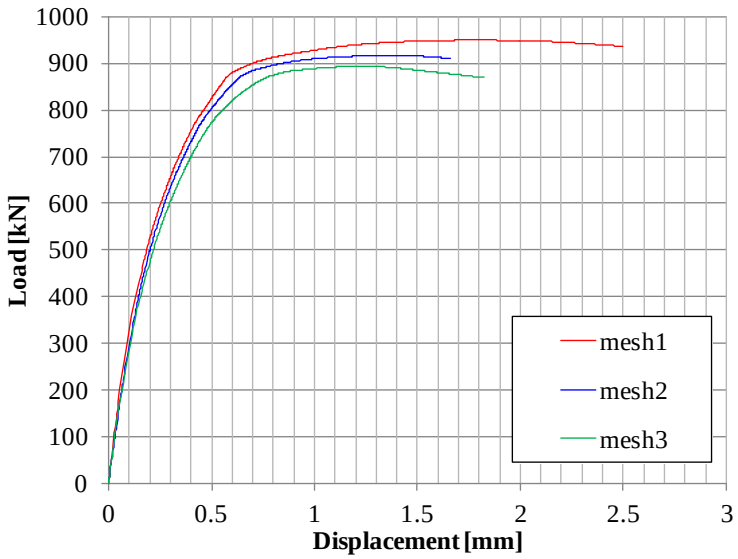

Figure 4.1. Mesh sensitivity analysis.

In order to evaluate the mesh sensitivity of the FE model and verify that it converges for few different mesh sizes, some preliminary analyses have been carried out and the results are presented in Figure 4.1.

From the computational effort standpoint, such analyses have allowed to determine the most effective size of the mesh. Table 4.1 shows the execution time referred to the three different combinations of mesh size adopted for the concrete and the diagonal web bars. As can be seen, passing from one case to the other one, the time requested for the analysis almost doubles. Concerning the value of the maximum load, once passing from the analysis carried out with the first mesh size combination to the second one and, then, from the second one to the last one, it decreases of 3.50% and 2.47% respectively. Thus, the mesh size finally adopted within the model corresponds to Mesh 1 in Table 4.1. Particularly, the concrete has been seeded with a maximum element size of 50 mm and with a deviation factor around the holes of 0.05 while the steel plate and the bars have been meshed by using a maximum element size of 30 mm and a curvature control

parameter equal to 0.1. The mesh of the elements is represented in Figure 4.2.

The FE model has been defined by exploiting the symmetry condition and, therefore, only one half specimen has been considered by introducing a symmetry constraint. The concrete support has been modeled by means of a hinge and the displacement history has been applied on the loading plate (Figure 4.3). Afterwards, the displacement, s, in the direction of the applied load, P, has been evaluated.

Table 4.1. Computational effort for the mesh sensitivity analysis.

	Concrete mesh size [mm]	Web bars mesh size [mm]	Execution Time [sec]
Mesh 1	50	30	17364 (4.8h)
Mesh 2	30	30	26381 (7.33h)
Mesh 3	25	25	51495 (14.3h)

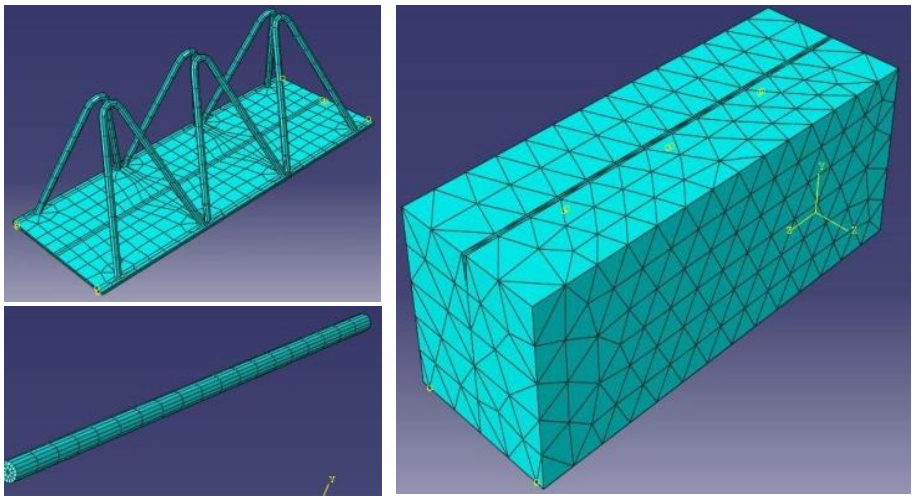

Figure 4.2. Mesh of the elements.

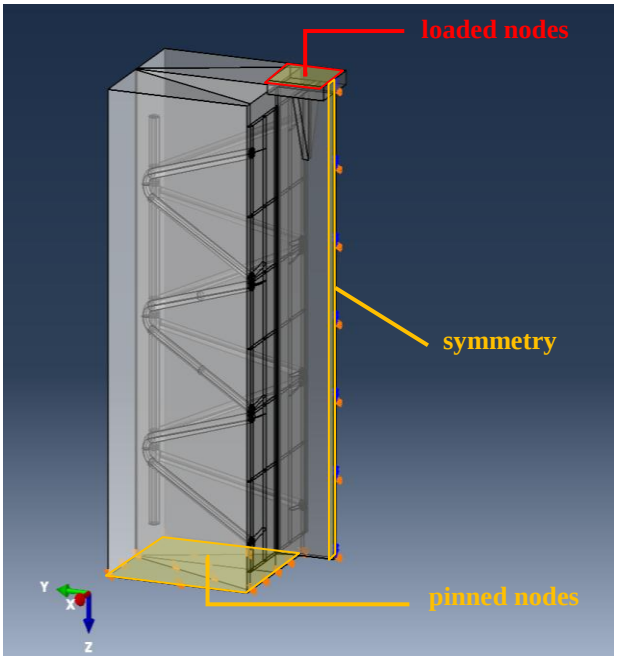

Figure 4.3. Load and boundary conditions.

4.2 Constitutive model of steel

In order to model the mechanical behavior of the steel composing the plates and the bars, the constitutive law has been obtained starting from the experimental coupon tensile tests by means of a quadri-linear approximation as shown in Figure 4.4 (Faella et al. 2000). Such elasto-plastic behavior with hardening is modeled using a classical plasticity model available in Abaqus. Most of the plasticity models in the software are derived from "incremental" theories in which the mechanical strain rate is decomposed into an elastic part and a plastic (inelastic) part. Such incremental plasticity models are usually formulated in terms of a *yield surface*, which generalizes the concept of "yield load"; a *flow rule*, which defines the inelastic deformation that occurs if the material is no longer responding purely elastically and, finally, evolution laws that define the *hardening*, that is the way in which the yield and/or flow definitions change as the inelastic deformation occurs.

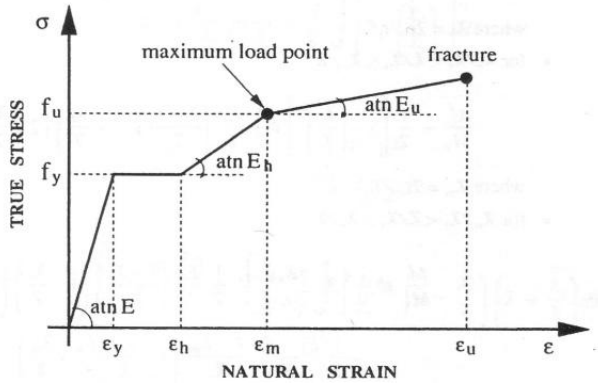

Figure 4.4. Constitutive law of steel (Faella et al. 2000).

Particularly, for the definition of the elastic branch, "Linear elasticity" represents the simplest form of elasticity available in Abaqus Material Library. The linear elastic model can define isotropic, orthotropic, or anisotropic material behavior and is valid for small elastic strains. In this simple model the total stress is classically defined from the total elastic strain as:

$$\sigma = D^{el}\varepsilon^{el} \tag{4.1}$$

where σ is the total stress that is the "true" or Cauchy stress, D^{el} is the elasticity matrix and ε^{el} is the total logarithmic elastic strain.

The simplest form of linear elasticity is the isotropic case which leads to the following well known stress-strain relationship:

$$\begin{Bmatrix} \varepsilon_{11} \\ \varepsilon_{22} \\ \varepsilon_{33} \\ \gamma_{12} \\ \gamma_{13} \\ \gamma_{23} \end{Bmatrix} = \begin{bmatrix} 1/E & -\nu/E & -\nu/E & 0 & 0 & 0 \\ -\nu/E & 1/E & -\nu/E & 0 & 0 & 0 \\ -\nu/E & -\nu/E & 1/E & 0 & 0 & 0 \\ 0 & 0 & 0 & 1/G & 0 & 0 \\ 0 & 0 & 0 & 0 & 1/G & 0 \\ 0 & 0 & 0 & 0 & 0 & 1/G \end{bmatrix} \begin{Bmatrix} \sigma_{11} \\ \sigma_{22} \\ \sigma_{33} \\ \sigma_{12} \\ \sigma_{13} \\ \sigma_{23} \end{Bmatrix} \tag{4.2}$$

The elastic properties are completely defined by giving the Young's modulus, E, and the Poisson's ratio, ν. The shear modulus, G, can be expressed in terms of E and ν as $G = 0.5E/(1+\nu)$.

On the other hand, for the definition of the inelastic behavior, the yield and inelastic flow of a metal at relatively low temperatures, where loading is relatively monotonic and creep effects are not important, can typically be described with the "Classical metal plasticity" model. First of all it is necessary to specify that, if the experimental available data consist in nominal stress-strain values $(\sigma_{nom}, \varepsilon_{nom})$ derived from a uniaxial test and the material is isotropic, then both stress and strain components have to be transformed in terms of true stresses and logarithmic strains $(\sigma_{true}, \varepsilon_{\ln}^{pl})$ according to the following expressions:

$$\sigma_{true} = \sigma_{nom}(1+\varepsilon_{nom}); \tag{4.3}$$

$$\varepsilon_{\ln}^{pl} = \ln(1+\varepsilon_{nom}) - \frac{\sigma_{true}}{E} \tag{4.4}$$

where E is the Young's modulus.

The "Classical metal plasticity" model can make use of the standard Mises or Hill yield surfaces with associated plastic flow and allows the definition of both perfect plasticity and isotropic hardening. Particularly the Mises yield surface is used to define isotropic yielding while the Hill yield surface allows anisotropic yielding to be modeled. Our case deals with the isotropic hardening, that means that the yield surface changes size uniformly in all directions such that the yield stress increases in all stress directions as plastic straining occurs.

4.3 Constitutive model of concrete

As regards concrete, in this section the implementation of its mechanical non-linear behavior is presented, also focusing on the fundamental theories that form the basis for the constitutive material models mainly implemented within FE codes. In the FE modeling described in the present Chapter, the

mechanical behavior of concrete has been defined by means of the Concrete Damaged Plasticity (CDP) model which is generally suitable for modeling concrete as well as other quasi-brittle materials.

4.3.1 Main theories for concrete cracking mechanics

The non-linear behavior of concrete and the numerical implementation of proper mechanical models involving its cracking, is the subject of a really substantial part of the international scientific literature. Some examples can be found in Chen (1982), Chen and Han (1995), Elfgren (1989), Weihe et al. (1998), Bangash (2001), De Borst (2002), Jirásek and Bažant (2002), Rots (2002), Mang et al. (2003), Karihaloo (2003), Malm (2009).

There are three main theories by which the continuum mechanics of concrete cracking can be described: *Non-linear fracture mechanics (NLFM)*, *Plasticity theory* and *Damage theory*. Usually combinations of these theories are implemented in the FE codes.

It is well known that the behavior at failure of concrete highly depends on the pressure regime acting: at low pressures, the failure is typically brittle, while for higher values, it might become more ductile that means that the material can deform plastically on its failure surface before the failure strains are achieved (Chen 1982). For this reason, the *Plasticity theory*, that is generally a tool for describing ductile material behavior, is also used to represent quasi-brittle behavior.

According to Lubliner et al. (1989), problems in which tension and the attendant crack development play a significant role - such as shear failure in reinforced concrete structures - the usual procedure is to apply the plasticity theory in the compression zone and the fracture mechanics in the zones in which at least one of the principal stresses is a tensile stress.

As a consequence, in the follow a brief description of each one of these theories is provided, particularly focusing on the *plasticity theory with damage* which is on the basis of the CDP model.

NLFM and NLFM based on crack bands. The first non-linear theory of fracture mechanics was proposed by Hillerborg et al. (1976) who introduced the fracture process zone by means of a fictitious crack in front of a pre-existing traction-free crack of length a_0 (Figure 4.5). Within the process zone there is a distribution of residual stresses, $\sigma(w)$, with a tension softening law which provides that the stress increases from zero at the tip of the pre-existing macro-crack to the full strength of the material, f_t. This model is known as *Fictitious Crack Model.* Once implemented in FE codes, when the crack extends through a certain node, the node is supposed to be split into two further nodes and that is why the method is also known with the alternative name of *discrete crack model* (Karihaloo 2003).

The parameters shown in Figure 4.5 are the length of the fracture process zone, l_p, the inelastic crack opening displacement, w, and the crack opening displacement when the crack can be considered as traction-free, w_c.

In the discrete crack model there are two main parameters apt to describe the material behavior: the stress-displacement relation $\sigma(w)$ in the softening zone and the fracture energy, G_f , which is defined as the area under the tension softening curve (Karihaloo 2003). Particularly the fracture energy represents the amount of energy necessary to open a unit area of a crack obtaining a traction-free crack. It can be determined according to different methods such as RILEM 50-FMC (1985); however the typical value of G_f for ordinary concrete is normally in the range between 50 and 200 N/m depending on the compressive strength of concrete.

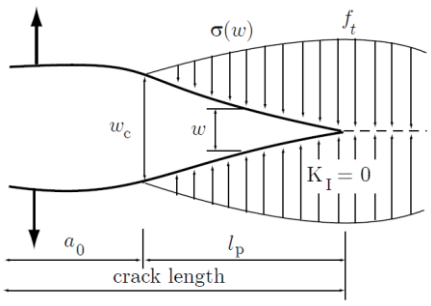

Figure 4.5. Traction-free crack of length a_0 terminating in a fictitious crack with residual stress transfer capacity $\sigma(w)$ (Hillerborg et al. 1976; Karihaloo 2003).

On the other hand, concerning the stress-displacement relation $\sigma(w)$, it is usually defined by means of linear, bilinear or exponential softening functions. The linear softening law can in most cases provide an accurate results, even though the material response tends to be slightly too stiff. The bilinear description was derived by Hillerborg (1985) and have been shown for several cases to be sufficiently accurate. Finally, the exponential function was experimentally derived by Cornelissen et al. (1986) and is considered to be the best and most accurate description, according to Karihaloo (2003).

However it has to be noted that the micro-cracking in the fracture process zone is not continuous and it does not necessary develop in a discrete region strictly in line with the traction-free crack. Consequently, further studies showed that the tension softening relation $\sigma(w)$ can be well approximated by a strain softening relation $\sigma(\varepsilon)$ in which stress decreases with increasing values of inelastic strain. Such inelastic strains are related to the inelastic crack opening displacement and the fracture energy, meaning that the strain is now defined by a fracture criterion, better known as *smeared crack approach*, which was introduced the first time by Bažant (1979) and was further developed by Bažant and Oh (1983). In order to relate the inelastic strain, ε, to the crack opening displacement, w, and the fracture energy, G_f, it has to be assumed that the micro-cracks in the fracture process zone are distributed over a band of width h, so that $\varepsilon = w/h$. Starting from this assumption, the method is also known as *crack band model*. Finally, as the micro-cracks are assumed to be smeared over an element, the whole element fails as the tensile strength is reached (Karihaloo 2003).

Plasticity theory. The main components of a plasticity theory-based model are the *yield function*, the *flow rule* and the *hardening law*, described in the follow.

Concerning the yield function, a coordinated effort between experimental and analytical research is required in order to investigate the evolution of the concrete multidimensional yield surface from the initial inelastic response through the complete loss of strength. Carrying out biaxial tests on concrete, it can be observed how the material volume exhibits significant changes

when subjected to severe inelastic states. Figure 4.6a shows how the increase in volume can be more than twice for the hydrostatic compressive stress state (see $\sigma_1 / \sigma_2 = -1/-1$ in Figure 4.6a) with respect to the uniaxial compression (see $\sigma_1 / \sigma_2 = -1/0$ in Figure 4.6a). Furthermore, in the same figure, some points are marked on the stress-volumetric strain curves, indicating some limit states. The critical surfaces corresponding to these material states are illustrated in Figure 4.6b showing how, in biaxial stress state, the various critical surfaces in the stress space are similar (Kupfer and Gerstle 1969). The surfaces give an indication of the expansion of the failure surface, starting from the moment in which the elastic limit is reached until the material completely undergoes to failure (Karihaloo 2003).

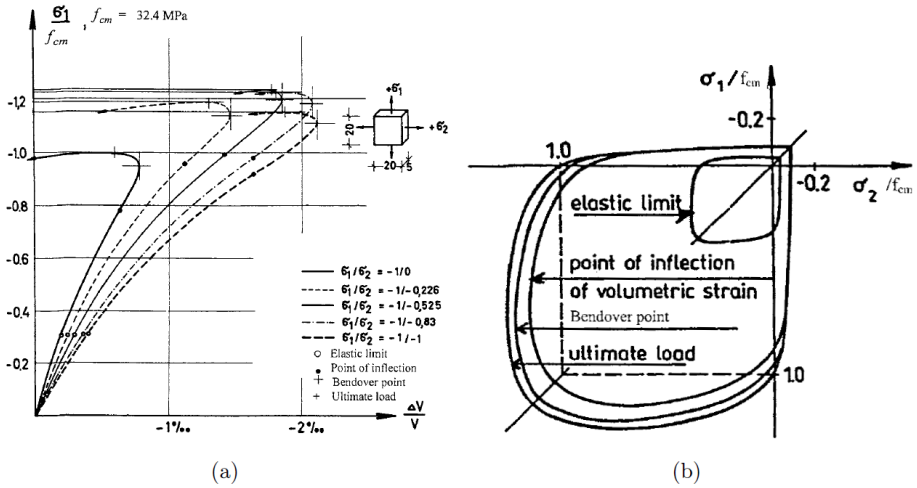

Figure 4.6. Biaxial tests on concrete: a) volumetric strain in biaxial compression; b) typical critical surfaces under biaxial stresses (Karihaloo 2003).

The same result is not found in triaxial compression tests, at least not for sufficiently high hydrostatic pressures, in the meaning that, while the yield surface is a closed surface, the failure surface is open in the direction of hydrostatic pressure (Lubliner et al. 1989).

Since the critical surfaces are similar in the biaxial behavior of concrete, a *yield function* is used in the plasticity based models. This yield function is

initially defined in such a way to correspond to the elastic limit starting from which the surface expands during subsequent loading up to failure.

In the case of concrete loaded in multi-dimensions, according to Lubliner et al. (1989), the limit of the elastic domain can be appropriately defined on the basis of the uniaxial stress-strain response. It is known that several different yield criteria have been developed for this material. In Figure 4.7 some common failure surfaces are presented together with experimental data from Kupfer and Gerstle (1969). Generally, anyway, the von Mises failure criterion (Figure 4.7a) is used for ductile materials while the Drucker-Prager and Mohr-Coulomb criteria (Figure 4.7b and 4.7c respectively) are the ones usually employed for concrete. Particularly, in accordance with the Drucker-Prager criterion, failure is determined by non-dilatational strain energy and the boundary surface in the stress space assumes the shape of a cone, as shown in Figure 4.8.

The main advantage in the use of this yield criterion is the surface smoothness which is able to avoid difficulties in numerical applications. Nevertheless, as remarked by Lubliner et al. (1989), these criteria do not represent experimental results for concrete very well and they need to by properly modified, as will be discussed in the following sections (Lubliner et al. 1989; Lee and Fenves 1998).

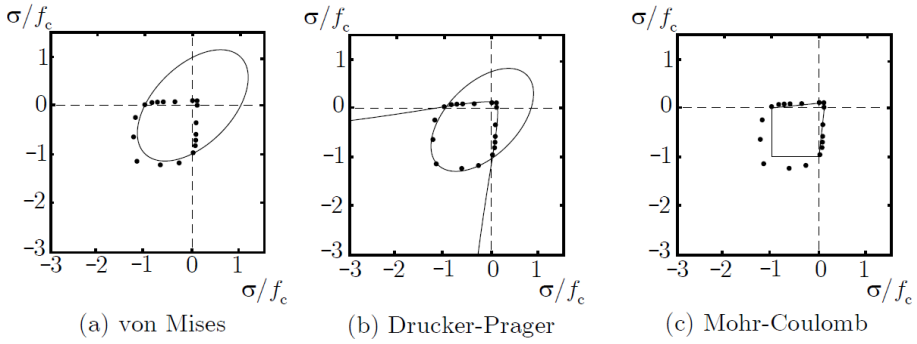

Figure 4.7. Failure criteria for biaxial stress state (Jirásek and Bažant 2002).

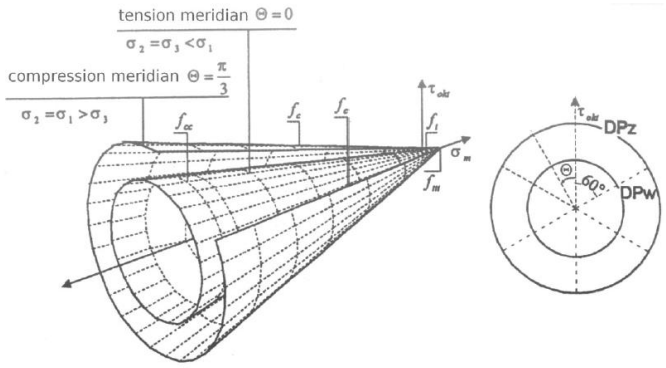

Figure 4.8. Drucker-Prager limit surface: a) view; b) deviatoric cross-section.

The motion of the subsequent yield surfaces during the plastic loading is defined by means of a scalar hardening variable, *k*. The evolution of this internal variable is usually expressed by means of a rate equation which is function of the plastic strain rate:

$$\dot{k} = f\left(\dot{\varepsilon}^{p}\right) \tag{4.5}$$

This equation shows how the plasticity theory allows to describe the dependence of strains in the material on its history. This means that also the yield function is dependent on the loading history through the variable *k* and, as a consequence, it can only expand in the stress space, not translate or rotate. Such hardening is called *isotropic hardening*. The shape of the yield surface at any given loading condition can be determined by the hardening rule. The direction of the plastic strain tensor $\dot{\varepsilon}^{p}$ is determined from the derivative of the plastic potential function as shown in Figure 4.9 (Karihaloo 2003). The parameters in Figure 4.9 are:

$\overline{p}$ the hydrostatic pressure stress, which is a function of the first stress invariant I_1, defined as $\overline{p} = -I_1/3 = -(\sigma_{11}+\sigma_{22}+\sigma_{33})/3$;

$\overline{q}$ the von Mises equivalent effective stress, described as

$$\bar{p} = \sqrt{3J_2} = \sqrt{3\left(\sigma_{11}^2 + \sigma_{22}^2 - \sigma_{11}\sigma_{22}\right)}$$

being J_2 the second deviatoric stress invariant;

ψ the dilation angle, measured in the $\bar{p} - \bar{q}$ plane at high confining pressure.

The connection between the yield surface and the stress-strain relationship is, instead, determined with a *flow potential rule* defined as:

$$\dot{\varepsilon}^p = \dot{k}\frac{\partial G}{\partial \sigma} \tag{4.6}$$

where $\dot{k} \geq 0$ is the scalar hardening parameter which can vary throughout the straining process and G is the plastic potential function. The gradient of the potential surface $\partial G / \partial \sigma$ defines the direction of the plastic strain increment vector $\dot{\varepsilon}^p$ while the hardening parameter $\dot{k}$ determines its length (Chen and Han 1995). The most simple case is when the plastic potential function coincides with the yield surface, which is the case of an *associated flow* because the plastic flow is connected or associated with the yield criterion. Otherwise, when two separate functions are used for defining the plastic flow rule and the yield surface, the potential flow is called *non-associated flow*. The Drucker-Prager hyperbolic plastic potential function illustrated in Figure 4.8 is the one used in the CDP model within the FE program Abaqus.

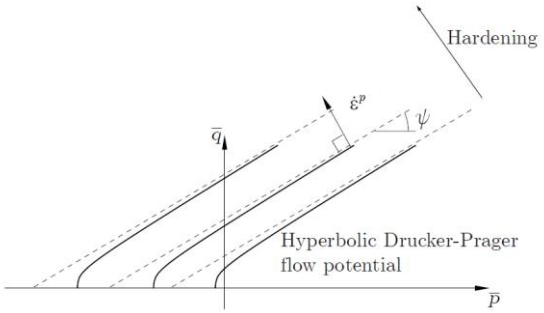

Figure 4.9. The Drucker-Prager hyperbolic plastic potential function in the meridional plane (Hibbitt et al. 2011).

Damage theory. The damage models are very similar to the plasticity theory described in the previous section. They aim at describing the progressive evolution of micro-cracks in concrete by means of a certain number of parameters which modify the elastic and/or plastic behavior of the material at the macroscopic level.

In damage models the total stress-strain relation has the following form:

$$\sigma = D^s : \varepsilon \tag{4.7}$$

where σ and ε are the stress and strain tensors respectively and D^s is the secant stiffness tensor of the damaged material depending on a number of internal variables which can be tensorial, vectorial or scalar. Considering a simplified isotropic model of damage, it can be assumed that the degradation of the matrix D^s is defined by means of a unique damage variable, d, which grows from zero, at an undamaged state, to one, at complete loss of integrity. This leads to the following expression for the stress-strain relationship:

$$\sigma = \left(1 - d\right) D_0^{el} : \varepsilon \tag{4.8}$$

where D_0^{el} represents the stiffness matrix of the undamaged material (De Borst 2002).

Isotropic models are generally considered sufficiently accurate in case of proportional loading of concrete structures where cracking often results from a practically uniaxial tensile stress. On the contrary, according to Grassl and Rempling (2007), isotropic damage models often fail to describe realistic crack patterns in mixed mode fracture tests. In these cases, an anisotropic damage model or damage-coupled plasticity should be adopted. It has to be noted that the strain in Eq. 4.8 is not a permanent strain; it is fully recovered at unloading. As a consequence, in order to couple damage and plasticity concepts, continuum damage mechanics makes generally use of a *scalar damage elasto-plastic model* based on the effective stress concept developed by Ju (1989). First introduced by Kachanov (1958) and further developed by Rabotnov (1969) and Lubliner et al. (1989), the constitutive equation of material with scalar isotropic damage takes the following form:

$$\sigma = (1-d) D_0^{el} : \left(\varepsilon - \varepsilon^{pl}\right) = D^{el} : \left(\varepsilon - \varepsilon^{pl}\right) \tag{4.9}$$

where D^{el} is the damaged stiffness matrix and ε^{pl} is the inelastic strain.

Consequently, also the plastic yield function is formulated in terms of effective stress which is calculated according to the following expression:

$$\hat{\sigma} = \frac{\sigma}{1-d} \tag{4.10}$$

4.3.2 Concrete Damaged Plasticity model

On the basis of what presented in the former section, a brief description of the fundamentals of the CDP model used in the proposed FE analysis is now provided.

The CDP model uses the concept of isotropic damaged elasticity in combination with isotropic tensile and compressive plasticity to represent the inelastic behavior of the concrete. CDP is able to properly account for the concrete confinement effect and assumes that the two main failure mechanisms are the tensile cracking and the compressive crushing. The identification of CDP model parameters for an actual concrete should be carried out starting from uniaxial compression tests, uniaxial tension tests, the knowledge of the failure surface in biaxial plane stress and several triaxial tests of concrete.

As far as in the case of push-out tests carried out by Aiello (2008) the peak resistance of uniaxial compressive tests is the only data available, the concrete behavior within the proposed FE model has been mainly characterized exploiting existing results from the technical literature.

In particular, the concrete compressive behavior has been characterized by using the Saenz model (1964) (Figure 4.10a), while the tensile behavior has been defined as linearly degrading starting from the definition of the fracture energy (Figure 4.10b).

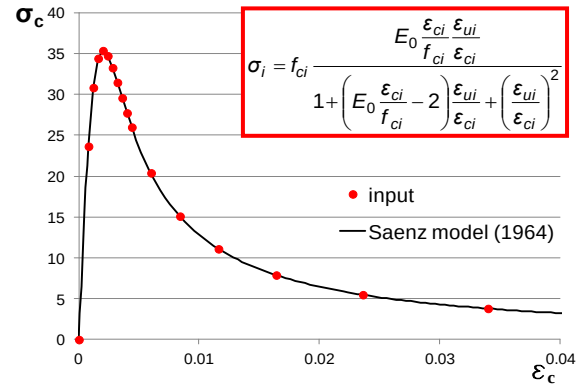

$$\sigma_i = f_{ci}\frac{E_0\frac{\varepsilon_{ci}}{f_{ci}}\frac{\varepsilon_{ui}}{\varepsilon_{ci}}}{1+\left(E_0\frac{\varepsilon_{ci}}{f_{ci}}-2\right)\frac{\varepsilon_{ui}}{\varepsilon_{ci}}+\left(\frac{\varepsilon_{ui}}{\varepsilon_{ci}}\right)^2}$$

a)

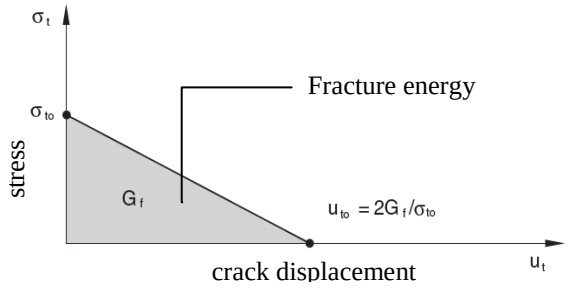

b)

Figure 4.10. Constitutive law of concrete: a) in compression; b) in tension.

As regards the compressive behavior, the CDP model assumes that the uniaxial tensile and compressive response of concrete is characterized by damaged plasticity, as shown in Figure 4.11. Under uniaxial tension the stress-strain response follows a linear elastic relationship until the onset of micro-cracking in the concrete which corresponds to the achievement of the failure stress, σ_{t0}. Beyond the failure stress, the formation of micro-cracks is represented by means of a softening stress-strain response. On the other hand, under uniaxial compression the response is linear until the value of the initial yield, σ_{c0}, is reached. Then, the post-elastic behavior is typically characterized by stress hardening followed by strain softening.

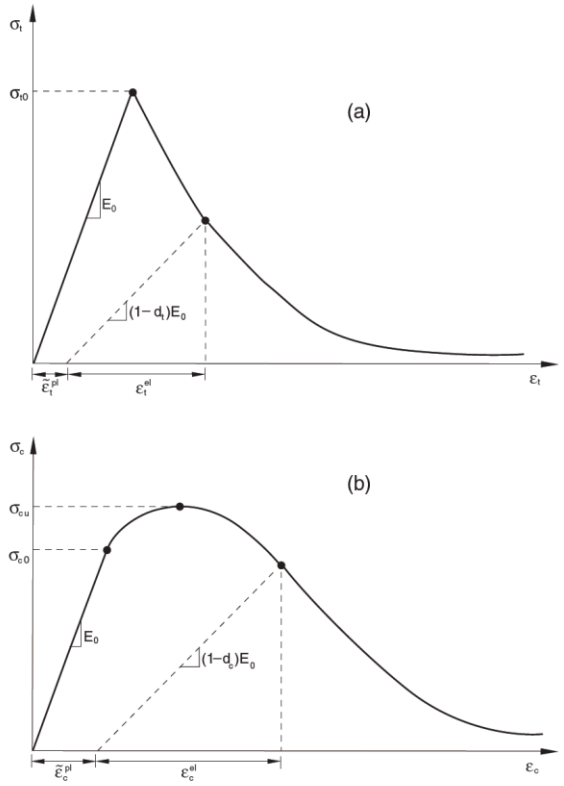

Figure 4.11. Response of concrete to uniaxial loading: a) in tension; b) in compression (Hibbitt et al. 2011).

When the concrete specimen is unloaded from any point on the strain softening branch of the stress-strain curve, the unloading response is characterized by a certain loss of the initial stiffness. Such a degradation of the elastic stiffness is described by means of two *damage variables*, d_c and d_t, which are assumed to be functions of the plastic strains ($\tilde{\varepsilon}_c^{pl}, \tilde{\varepsilon}_t^{pl}$). This means that, according to the symbols introduced in Figure 4.11, Eq. 4.9 assumes the following form if specialized for the cases of tension and compression:

$$\sigma_t = \left(1-d_t\right) E_0 \left(\varepsilon_t - \tilde{\varepsilon}_t^{pl}\right); \tag{4.11a}$$

$$\sigma_c = (1-d_c)\,E_0\left(\varepsilon_c - \tilde{\varepsilon}_c^{pl}\right) \tag{4.11b}$$

In the same way, the "effective" tensile and compressive stresses which determine the size of the yield surface can be defined as:

$$\bar{\sigma}_t = \frac{\sigma_t}{1-d_t} = E_0\left(\varepsilon_t - \tilde{\varepsilon}_t^{pl}\right); \tag{4.12a}$$

$$\bar{\sigma}_c = \frac{\sigma_c}{1-d_c} = E_0\left(\varepsilon_c - \tilde{\varepsilon}_c^{pl}\right). \tag{4.12b}$$

As a consequence, the stress-strain relations for the general three-dimensional multiaxial condition are given by the scalar damage elasticity equation:

$$\boldsymbol{\sigma} = (1-d)\,\boldsymbol{D}_0^{el} : \left(\boldsymbol{\varepsilon} - \boldsymbol{\varepsilon}^{\boldsymbol{pl}}\right) \tag{4.13}$$

where $\boldsymbol{D}_0^{el}$ is the initial undamaged elasticity matrix.

The CDP model assumes *non-associated potential plastic flow*. As previously mentioned in the former section, the flow potential *G* used for this model is the Drucker-Prager hyperbolic function:

$$G = \sqrt{\left(\in \sigma_{t0} \tan\psi\right)^2 + \bar{q}^2} - \bar{p}\tan\psi \tag{4.14}$$

where:

ψ is the dilation angle measured in the $\bar{p}-\bar{q}$ plane at high confining pressure;

σ_{t0} is the uniaxial tensile stress at failure;

$\in$ is a parameter, referred to as the *eccentricity*, that defines the rate at which the function approaches the asymptote (the flow potential tends to a straight line as the eccentricity tends to zero).

This flow potential, which is continuous and smooth, ensures that the flow direction is always uniquely defined.

Finally, the model makes use of the *yield function* of Lubliner et. al. (1989), with the modifications proposed by Lee and Fenves (1998) to take into account the different evolution of strength under tension and compression. The evolution of the yield surface is controlled by the *hardening variables* $\tilde{\varepsilon}_t^{pl}$ and $\tilde{\varepsilon}_c^{pl}$. In terms of effective stresses, the yield function takes the form:

$$F = \frac{1}{1-\alpha}\left(\bar{q} - 3\alpha\bar{p} + \beta\left(\tilde{\varepsilon}^{pl}\right)\left\langle\hat{\bar{\sigma}}_{\max}\right\rangle - \gamma\left\langle-\hat{\bar{\sigma}}_{\max}\right\rangle\right) - \bar{\sigma}_c\left(\tilde{\varepsilon}_c^{pl}\right) = 0 \tag{4.15}$$

with coefficients α, β and γ defined as follows:

$$\alpha = \frac{\left(\sigma_{b0}/\sigma_{c0}\right)-1}{2\left(\sigma_{b0}/\sigma_{c0}\right)-1}; 0 \le \alpha \le 0.5; \tag{4.16a}$$

$$\beta = \frac{\bar{\sigma}_c\left(\tilde{\varepsilon}_c^{pl}\right)}{\bar{\sigma}_t\left(\tilde{\varepsilon}_t^{pl}\right)}\left(1-\alpha\right) - \left(1+\alpha\right); \tag{4.16b}$$

$$\gamma = \frac{3(1-K_c)}{2K_c - 1}. \tag{4.16c}$$

In those expressions

$\hat{\bar{\sigma}}_{\max}$ is the maximum principal effective stress;

σ_{b0}/σ_{c0} is the ratio of initial equibiaxial compressive yield stress to initial uniaxial compressive yield stress;

K_c is the ratio of the second stress invariant on the tensile meridian (T.M.) to that on the compressive meridian (C.M.) at initial yield for any given value of the pressure invariant $\bar{p}$ such that the maximum principal stress, $\hat{\sigma}_{\max}$, is negative;

$\bar{\sigma}_t\left(\tilde{\varepsilon}_t^{pl}\right)$ is the effective tensile stress;

$\bar{\sigma}_c\left(\tilde{\varepsilon}_c^{pl}\right)$ is the effective compressive stress.

Figure 4.12 shows typical yield surfaces for plane stress conditions.

As previously mentioned, this yield function represents a modification of the Drucker-Prager criterion in the meaning that the failure surface in the deviatoric cross-section needs not to be a circle and it is governed by the parameter K_c. This parameter is always higher than 0.5 and when it assumes the value of 1, the deviatoric cross-section of the failure surface becomes a circle, as in the classic Drucker-Prager strength criterion. The CDP model recommends to assume K_c = 2/3. So doing, the shape of the yield surface (a combination of three mutually tangent ellipses) is similar to the one obtained according to the strength criterion formulated by William and Warnke (1975) that is a theoretical-experimental criterion based on triaxial stress test results (Figure 4.13).

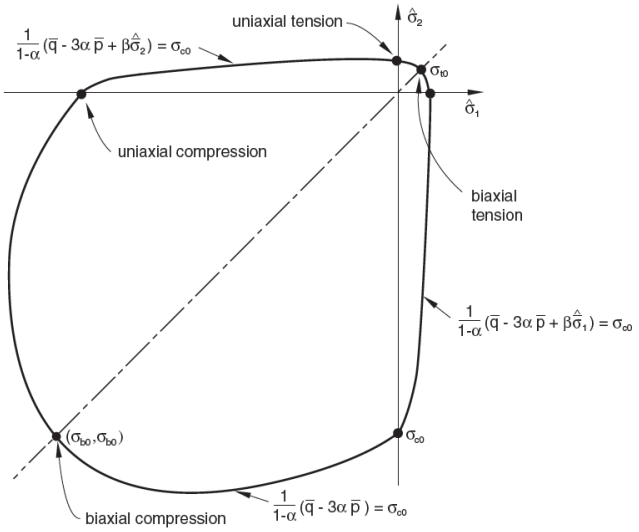

Figure 4.12. Yield surfaces in plane stress (Hibbitt et al. 2011).

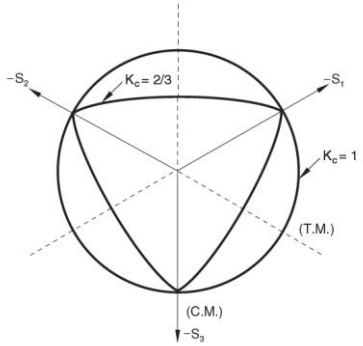

Figure 4.13. Yield surfaces in the deviatoric plane corresponding to different values of K_c (Hibbitt et al. 2011).

4.4 Modeling of the steel - concrete interface

An aspect of paramount importance in the FE simulation of reinforced concrete elements is the definition of the interaction between the bars and the concrete core. Four models characterized by a different implementation of steel-concrete interface are proposed. Particularly two models deal with the case of HSTCBs constituted by ribbed steel truss, conversely the other two concern with the case of smooth steel diagonal bars.

Regarding the case of Ribbed-Steel-Bar-Models (RSBMs), two approaches have been used to define bond: the first one is to provide a simplified modeling of the concrete-steel interaction by tying the nodes of the two surfaces in contact, the second one provides the insertion of cohesive contact elements between the steel bar and the surrounding concrete. The former approach, which is very easy to apply in practice, generates a constraint between the nodes of the meshes of the elements that are rigidly connected each other. The simplified FE model formulated by using this first approach and herein presented will be identified in the follow with the tag RSBM-1. It can be considered as a variation of a previous one proposed by Desiderio et al. (2011). The main difference between the forgoing and the current model consists in the definition of master and slave surfaces involved in the interaction and tied up together; furthermore corner welding between the upper chord and the diagonal bars have been idealized by means of a

coupling interaction between node regions and reference points belonging to steel surfaces.

Such a modeling neglects several aspects of the bonding phenomena and so it can be applied almost only to roughly approximate the behavior of ribbed bars with ideal infinite bond stiffness and resistance. As a consequence, the developing of the latter approach is certainly of paramount importance. This approach, which provides a more detailed description of the bond, requires the insertion of a cohesive interface between the bar and the concrete (Figure 4.14) which establishes a kinematical relationship among the nodes of two surfaces both in the normal and tangential direction.

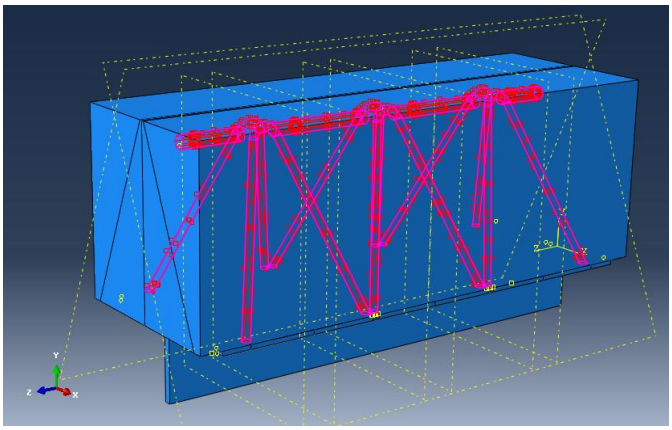

Figure 4.14. Steel-concrete surfaces described through the cohesive behavior.

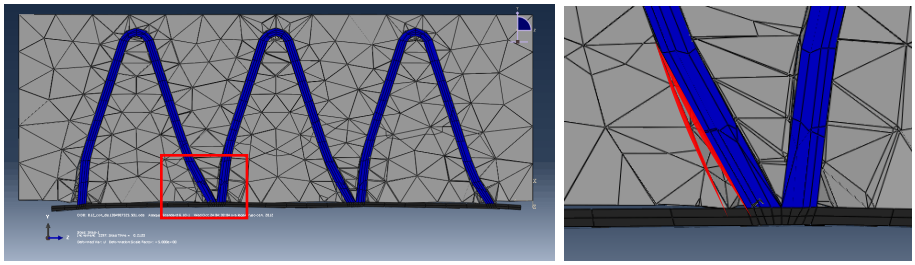

a) b)

Figure 4.15. Separation between steel and concrete surfaces due to the slip force: a) deformed shape of the truss at the end of the analysis; b) zoom of the separation zone.

The adoption of a cohesive interface is necessary in order to model the concrete-rebar tangential bond as well as the traction and separation normal to the bar surface in the zone behind the bar considered in the direction of the steel plate translation during the push-out test (see Figure 4.15).

The cohesive interaction is characterized by the progressive stiffness degradation, driven by a damage process. In the current model (identified as RSBM-2) an elastic uncoupled traction-separation behavior is implemented, whose general representative expression is the following:

$$\boldsymbol{t} = \begin{Bmatrix} t_n \\ t_s \\ t_t \end{Bmatrix} = \begin{bmatrix} K_{nn} & K_{ns} & K_{nt} \\ K_{ns} & K_{ss} & K_{st} \\ K_{nt} & K_{st} & K_{tt} \end{bmatrix} \begin{Bmatrix} \delta_n \\ \delta_s \\ \delta_t \end{Bmatrix} = \boldsymbol{K\delta} \tag{4.17}$$

where $\boldsymbol{t}$ is the vector of the tensile stresses, $\boldsymbol{K}$ is the elastic matrix stiffness and $\boldsymbol{\delta}$ is the vector of the separations. Since the behavior is uncoupled between the normal and the tangential direction, the only terms of the matrix $\boldsymbol{K}$ that are defined are $K_{ss} = K_{tt}$, all other values are zero. This approach represents the simplest specification of cohesive behavior in which pure normal separation by itself does not give rise to cohesive forces in the shear directions, and pure shear slip with zero normal separation does not give rise to any cohesive forces in the normal direction. Furthermore, in order to define the post-elastic cohesive behavior, a damage modeling is introduced by means of the specification of a damage initiation criterion and a subsequent damage evolution law. Damage initiation refers to the beginning of degradation of the cohesive response at a contact point. So, as already remarked, the initial response is assumed to be linear and then, once a damage initiation criterion is met, damage can occur according to an evolution law (see Figure 4.16). In RSBM-2 the damage is assumed to initiate according to the maximum stress criterion, that means that damage is assumed to initiate when the maximum contact stress ratio, as defined in the expression below, reaches a value of one:

$$\max\left\{\frac{\langle t_n \rangle}{t_n^0}, \frac{t_s}{t_s^0}, \frac{t_t}{t_t^0}\right\} = 1 \tag{4.18}$$

where t_n^0, t_s^0, t_t^0 represent the peak values of the contact stress when the separation is either purely normal to the interface or purely in the first or the second shear direction, respectively. Furthermore the symbol $\langle\ \rangle$ represents the Macaulay bracket used to signify that a purely compressive displacement or a purely compressive stress state does not initiate damage.

For the definition of the post peak response the well-known stress-slip relationship developed by Eligehausen et al. (1983) is used.

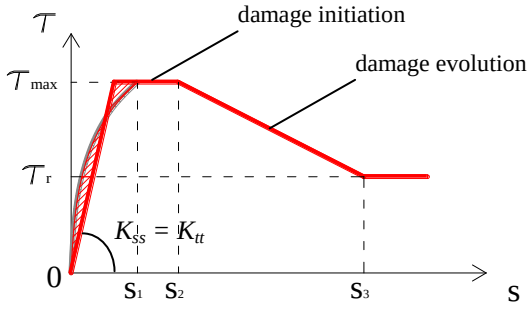

Figure 4.16. Qualitative representation of the bond stress-slip relationship implemented.

Two further models were developed aiming to study the case of HSTCBs constituted by smooth steel truss (Smooth Steel Bars Models - SSBMs). As well as for RSBMs, a simplified approach has been employed to formulate the first model (SSBM-1) where a hard contact frictionless relationship between steel and surrounding concrete were introduced. Afterwards, a cohesive behavior contact property with damage evolution was implemented in the so called SSBM-2 and, in this case, the cohesive behavior was characterized on the basis of the model developed by Verderame et al. (2009).

4.5 Check of the proposed approach

The proposed approach was checked both to verify the ability in simulating the basic dowel mechanism and in representing bond by means of cohesive interface. To this aim, experimental tests carried out by Vintzēleou and Tassios (1990), on one side, and Harajli et al. (1995), on the other side, have been modeled through the FE method.

Aiming to check the ability of the proposed approach to simulate the basic dowel mechanisms, some simpler experimental tests taken from the scientific literature have been preliminary simulated. In particular, the tests carried out by Vintzēleou and Tassios (1990) have been considered. The experimental and analytical study carried out by these authors concerns the prediction of the maximum dowel resistance (D_u) of bars put into a concrete block with different covers and loaded against the core. The scope of these tests was to investigate the influence on the dowel resistance of the concrete due to the cover. The eccentric dowels tested in Vintzēleou and Tassios (1990) could be compared to the diagonals of a steel space truss. The main difference is that the diagonals of the space truss of a HSTCB have a concrete cover that is not constant along the beam depth. Figures 4.17 and 4.18 depict the test arrangement adopted by Vintzēleou and Tassios (1990) and the developed FE model, respectively. In the tests carried out by the authors, twenty-four combinations of side and top covers, denoted as c_1 and c_2 respectively, were selected. The width of the specimens was chosen so that the larger side cover of the dowel was at least five times the bar diameter. In each specimen two reinforcing bars with diameter of 16 mm were embedded. The mean compressive strength of concrete varied from 28.5 to 32.0 MPa. Monotonic displacements were applied to the dowel by a servomechanism through a steel plate so that the dowel was loaded upwards against the concrete core. In all tested dowels, the failure mode was similar: at the end of each test the dowel yielded (a plastic hinge was formed close to the concrete face), while the concrete crushed in the region close to the concrete surface. The typical force versus displacement curves obtained in the tests of Vintzēleou and Tassios (1990), which are not here reported, have an initial linear part and, after the cracking, a progressive loss of stiffness up to failure. For the sake of simplicity, the peak loads obtained through the simulation of only three of the twenty-four tests are presented. The ratio between the covers and the diameter of the bar (d_b) in the considered cases is shown in Table 4.2. The comparison between the maximum dowel experimental versus numerical resistance shows that the numerical model fits satisfactorily the experimental results.

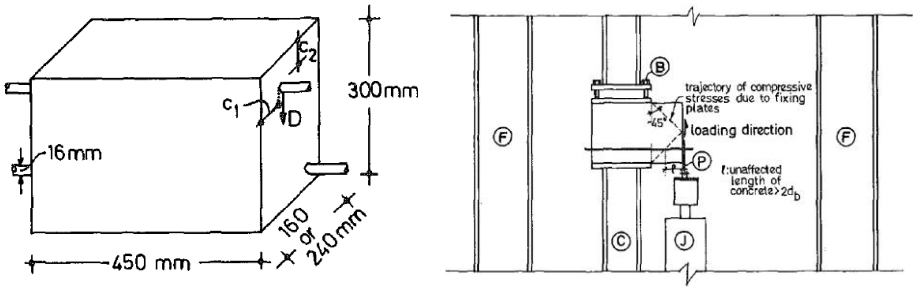

a) b)

Figure 4.17. Geometry of the specimen and test setup (Vintzēleou and Tassios 1990).

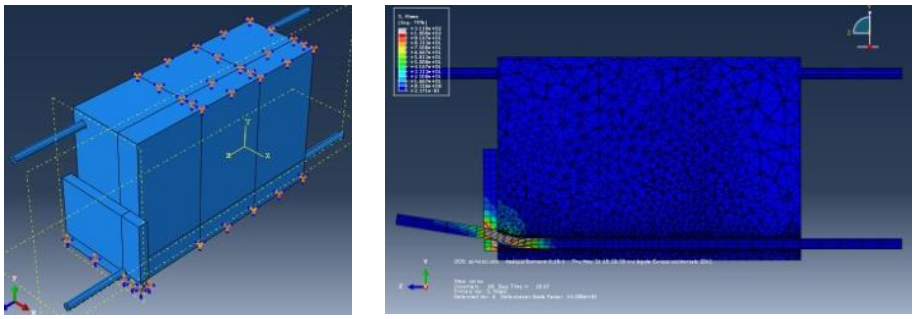

a) b)

Figure 4.18. FE model: a) boundary conditions; b) amplified deformed shape due to dowel action.

Table 4.2. Experimental vs. numerical results.

c_1/ d_b	c_2/ d_b	$D_{u, exp}$ [kN]	$D_{u, num}$ [kN]	$D_{u, num}/ D_{u, exp}$
1	1	25.6	24.43	0.95
2	1	29.6	26.22	0.89
3	3	32.7	33.28	1.02

Then, in order to validate the ability of the developed approach to represent bonding by means of a cohesive element, some experimental pullout tests available in the literature have been numerically simulated. In Harajli et al. (1995) the test specimens consisted of pullout concrete prisms

with reinforcing bars put in the middle of the block. Two series of specimens were tested, Series I and Series II, designed to fail in pullout and splitting modes respectively. Figure 4.19 shows a schematic view of specimen and test setup, on the left, and the corresponding numerical modeling, on the right. For the sake of brevity, only the results concerning one test are herein discussed. The comparison between the experimental and numerical bond stress-local slip curve, represented in Figure 4.20, shows that the cohesive interaction property reproduces the actual behavior satisfactorily.

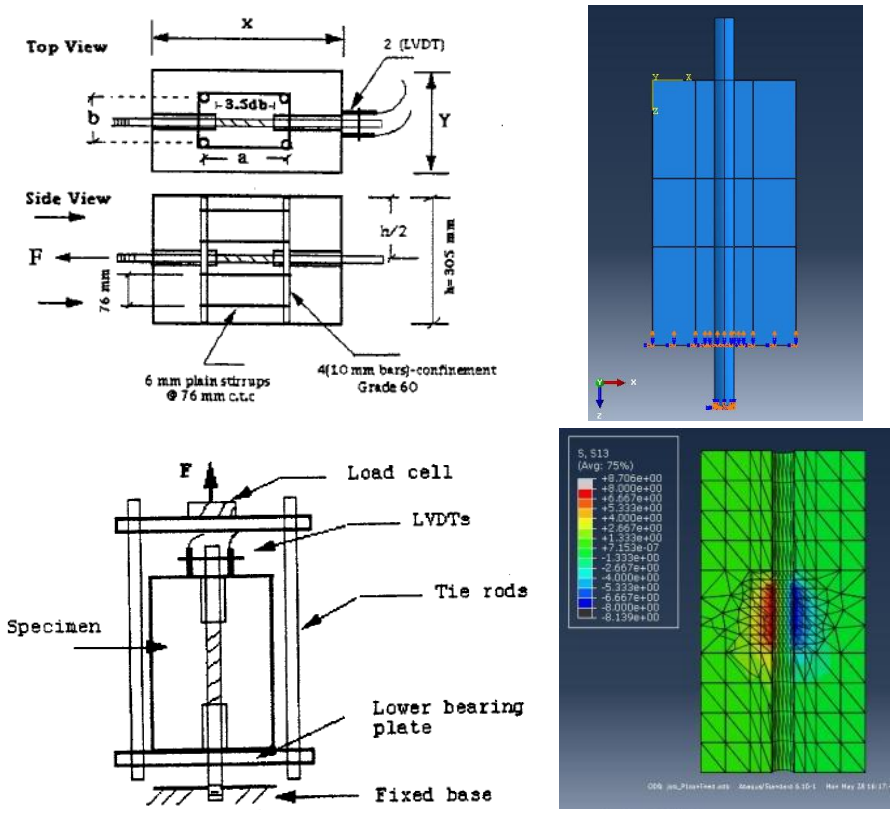

a) b)

Figure 4.19. Pullout test: a) test specimen and schematic view of the test setup (Harajli et al. 1995); b) boundary conditions and bond stress in the FE model.

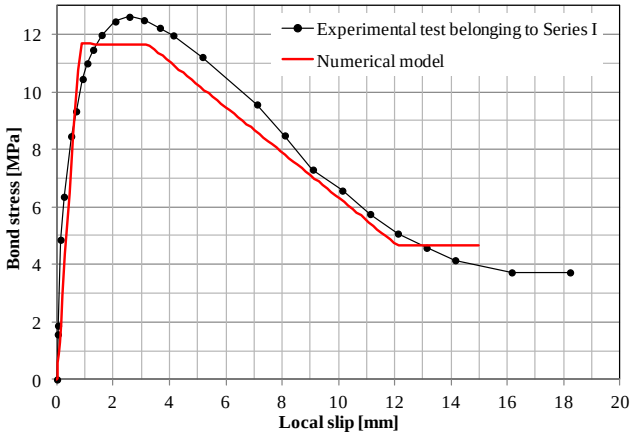

Figure 4.20. Bond stress-local slip curve: comparison between experimental and numerical result.

4.6 Numerical vs. experimental results

The accuracy of the model is checked by comparing the numerical slip-load curves with the corresponding experimental curves of some of the push-out tests carried out by Aiello (2008).

With regard to RSBMs, they have been calibrated on the basis of push-out tests carried out on B12 and B14 specimens (see Table 2.2), the former constituted by diagonal bars of 12 mm of diameter, the latter by a 14 mm truss. As above mentioned, in both cases the specimens are made up of deformed bars.

Figure 4.21 shows a chromatic map of stresses typically resulting from the proposed FE models. The comparison between the slip-load curves in Figures 4.22 and 4.23 shows that RSBMs-1 exhibit, as expected, an overestimation of the maximum strength because of the tie interaction inserted between steel-concrete surfaces. Conversely, the implementation of a cohesive interaction property at the steel-concrete interface in RSBMs-2 allows to obtain a more accurate result which fits satisfactorily the experimental slip-load curves proving that such a contact property better reproduces the actual behavior. Furthermore, as regards the modeling of

HSTCBs having a smooth steel truss, the experimental tests used in order to check the SSBMs concern S12-specimens. The latter are made up of smooth steel ϕ 12 mm diagonal bars, while the upper chord is realized with B450C steel. In Figure 4.24 the comparison between experimental and numerical results demonstrates that both SSBM-1 and SSBM-2 provide force versus displacement curves very close each other and somewhat careful in both cases. Observing the aforementioned curves it can be also appreciate the different behavior of HSTCBs concerning with both strength and stiffness depending on some fundamental parameters such as the diameter of the diagonal bars, steel yielding strength and the constitutive law characterizing all steel surfaces embedded in the concrete core.

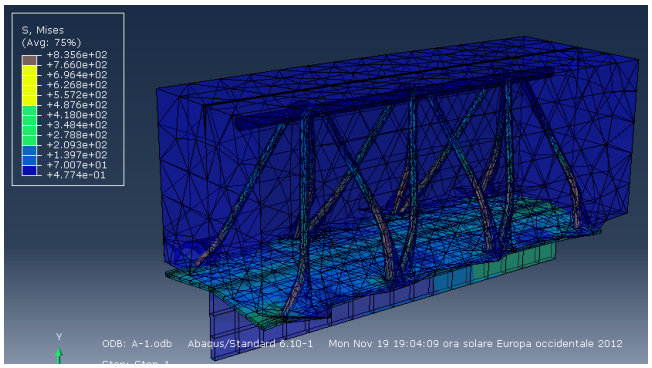

a)

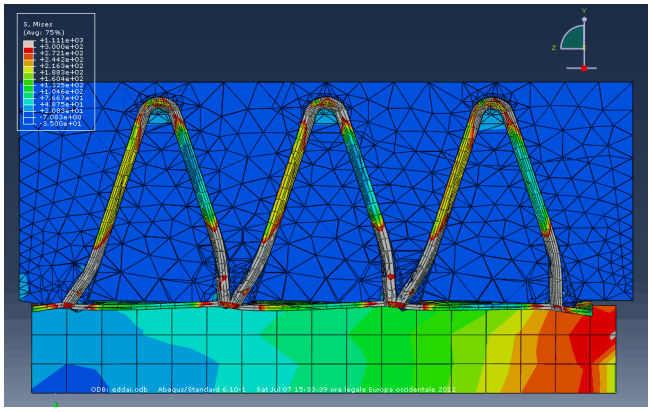

b)

Figure 4.21. Colour mapping of stresses: a) 3D view; b) view in the plane of the web truss.

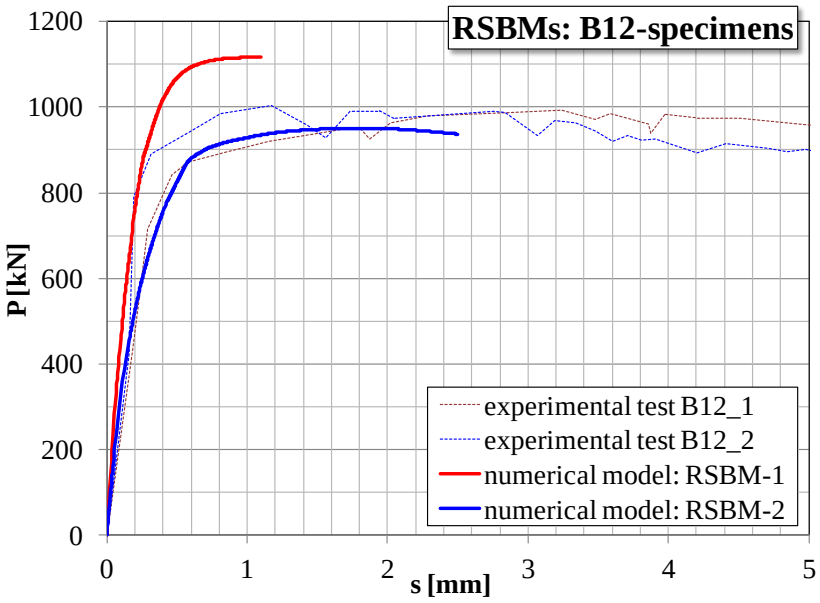

Figure 4.22. Comparison between experimental results and RSBMs of B12-specimens.

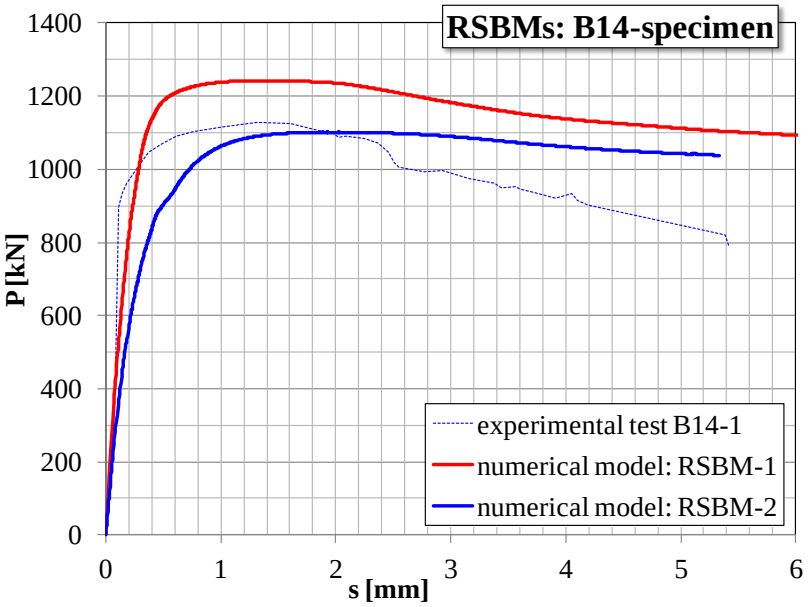

Figure 4.23. Comparison between experimental results and RSBMs of B14-specimen.

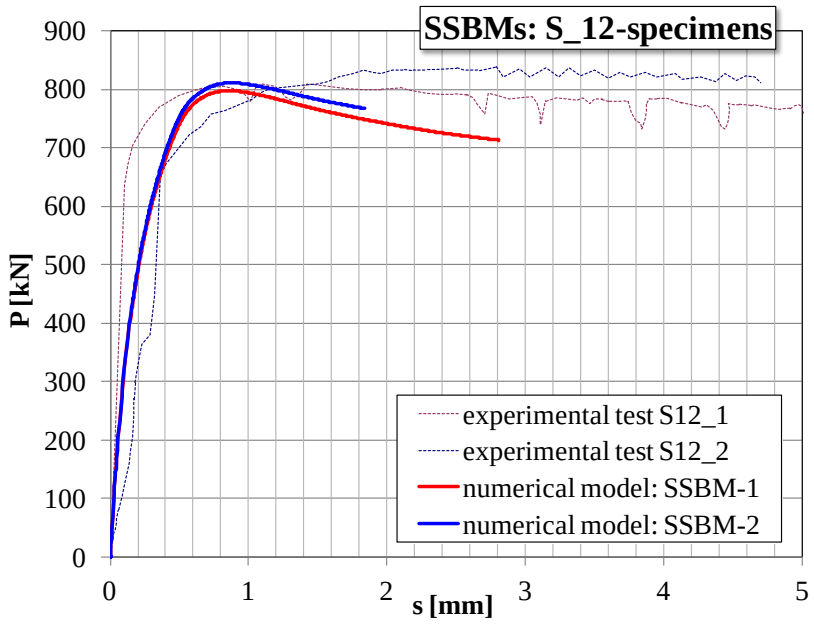

Figure 4.24. Comparison between experimental results and SSBMs of S12-specimens.

Aiming to develop a more detailed investigation of all these issues, a parametric analysis has been carried out. The numerical simulation, in fact, allows evaluating the influence of various single effects also widening the number of parameters which can be investigated with respect to the limits of laboratory experimental tests. In the following paragraph, a synoptic framework of all cases constituting the parametric analysis is presented.

4.7 Parametric simulations of push-out tests

As aforesaid, in order to investigate the main parameters influencing the maximum load that can be transferred from the steel plate to the concrete, a numerical simulation of push-out tests has been developed. The geometrical and mechanical parameters which have been varied have been chosen with reference to the geometry of the typical layout of the tests performed by Aiello (2008). The following four parameters have been varied: the diameter of the diagonal bars; the steel yield stress; the compressive strength of concrete; the bars typology (smooth or ribbed).

4.7.1 Influence of the investigated parameters

Thirty-six simulated tests have been generated. The bottom steel plate and the bar constituting the upper chord are assumed to have a yield stress equal to 355 MPa and 450 MPa respectively. The numerical simulation has been carried out by considering that the bar composing the upper chord has the same superficial finishing of the bars composing the diagonals of the truss, i.e. all the bars composing the truss are always all ribbed or all smooth.

Table 4.3 reports a synoptic scheme containing the identity tags used to individuate all the considered analyses. In particular, letters A, B and C define the concrete cylindrical compressive strength (32, 25 or 16 MPa); numbers 12 or 14 individuate the diameter of the truss diagonals; numbers 2, 3 or 4 identify the steel yield stress (235, 355, 450 MPa respectively) and, finally, the letter "X" has to be read as "R" in case of ribbed bars or as "S" in case of smooth bars.

Besides the analyses, whose tags are reported in the aforementioned Table 4.3, also a preliminary numerical test in which the bottom plate thickness has been assumed equal to 10 mm (instead of 6 mm) has been developed. The comparison of the results has shown a limited influence of this parameter on the strength and a higher influence on the stiffness. In particular, the increase of plate thickness of 4 mm leads to an increase of the resistance and the initial stiffness of about 1.6% and of 28% respectively (Figure 4.25). The attention is now mainly focused on resistance. In Figures 4.26a and 4.26b the influence of the concrete strength is shown for ribbed and smooth bars, respectively, with reference to the case of diagonals of 12 mm and yielding stress equal to 355 MPa. It is worth noting that the peak force raises less than linearly as far as the concrete strength increases and, in the case of ribbed bars, after a certain value of the concrete resistance, it does not increase anymore. In fact, by observing Figure 4.26a it can be noted that, the simulations do not show a significant increase of the peak load for concrete with resistance higher than 25 MPa. An interpretation of this result will be provided in the next section.

In Figures 4.27a and 4.27b the results of the numerical simulations obtained by varying the steel yield stress are reported. Also in this case, it is

easy to note the significant influence that the steel yield stress has on the ultimate load. Furthermore, also the influence of the bars diameter has been investigated. In particular, Figure 4.28 shows the increase of resistance as far as the truss diagonal diameter increases. In Table 4.4 all the results in terms of peak loads are summarized.

Table 4.3. Identity tags of numerical analyses.

	f_y = 235 [MPa]	f_y = 355 [MPa]	f_y = 450 [MPa]
f_c = 32 [MPa]	A12-2X	A12-3X	A12-4X
	A14-2X	A14-3X	A14-4X
f_c = 25 [MPa]	B12-2X	B12-3X	B12-4X
	B14-2X	B14-3X	B14-4X
f_c = 16 [MPa]	C12-2X	C12-3X	C12-4X
	C14-2X	C14-3X	C14-4X

X = R ribbed steel bars; X = S smooth steel bars

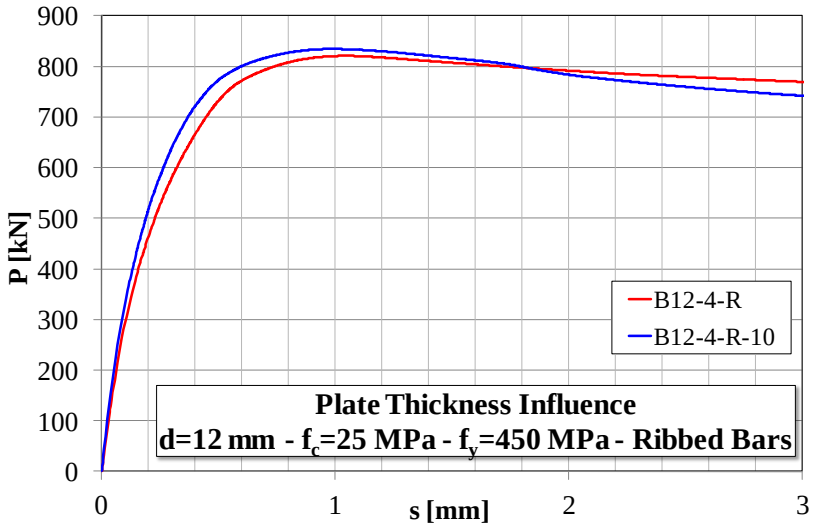

Figure 4.25. Plate thickness influence.

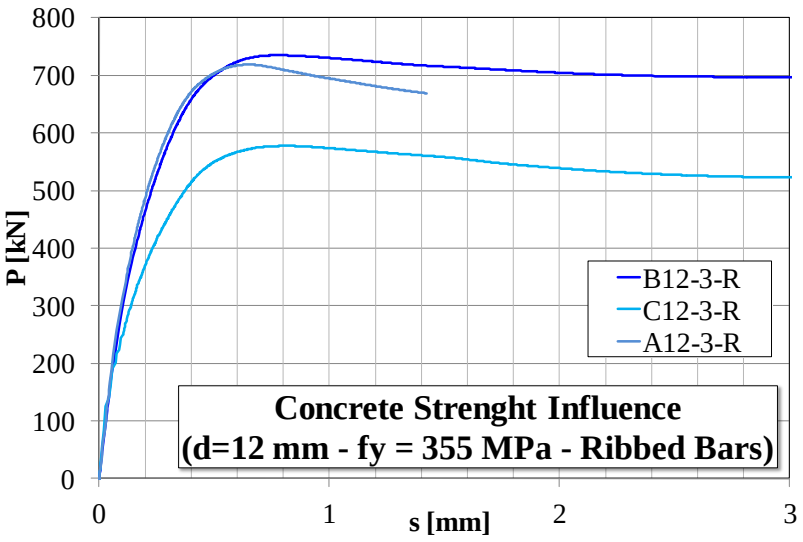

a)

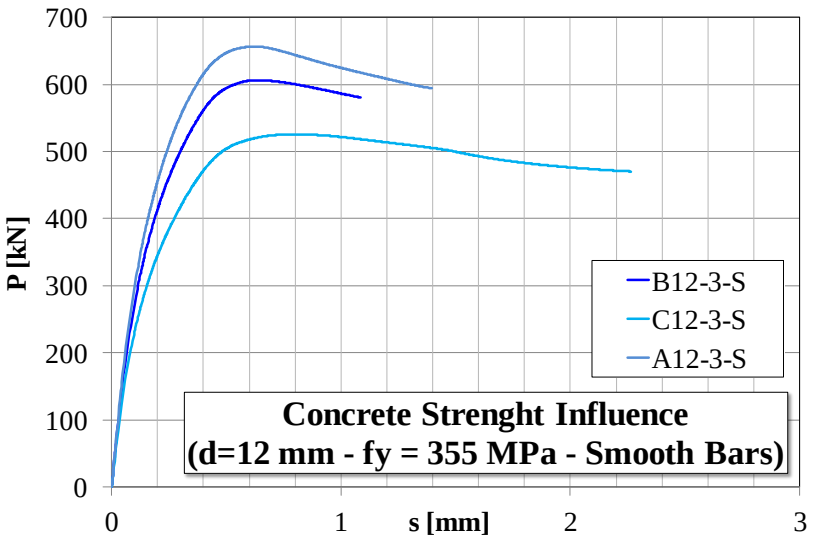

b)

Figure 4.26. Concrete strength influence: a) Ribbed Bars; b) Smooth Bars.

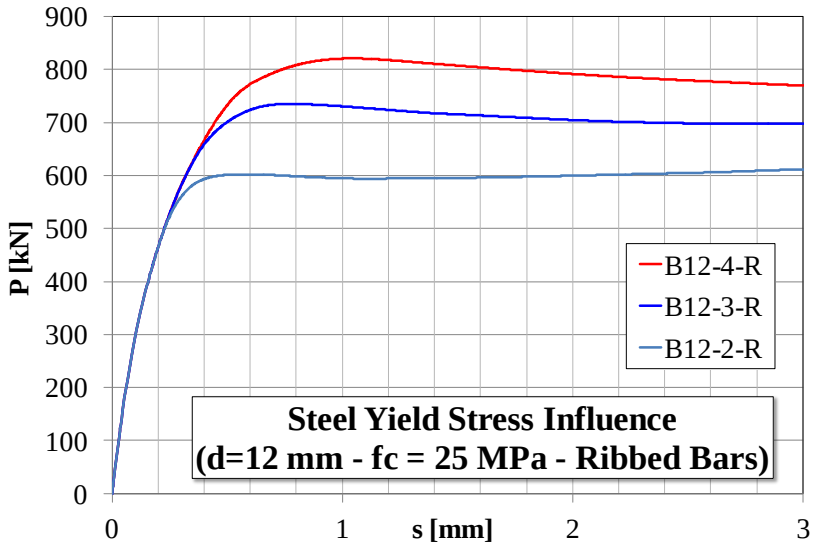

a)

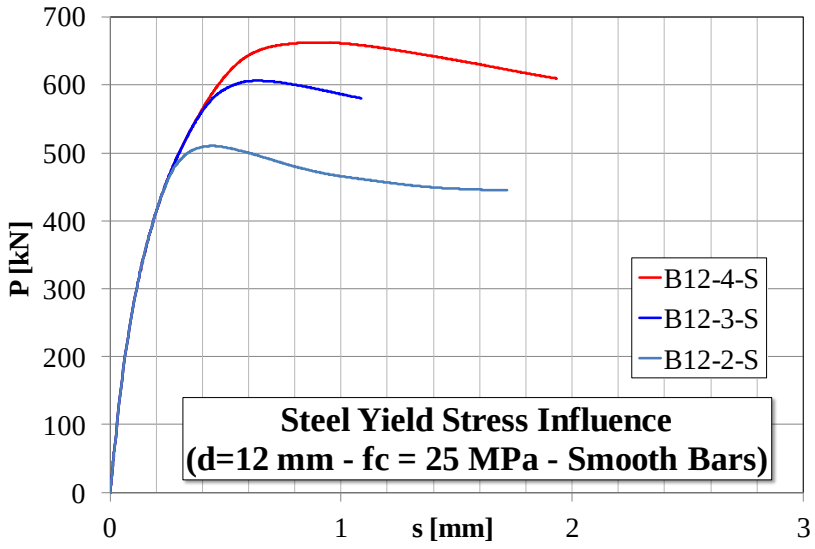

b)

Figure 4.27. Steel yield stress influence: a) Ribbed Bars; b) Smooth Bars.

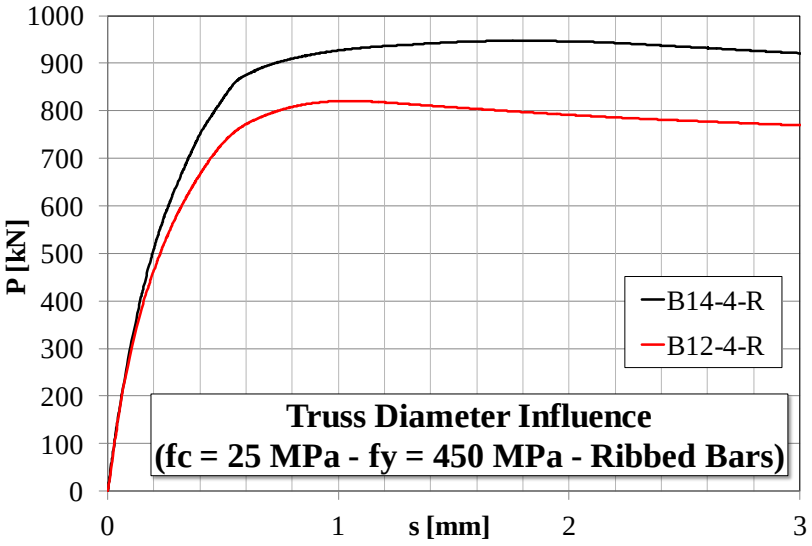

Figure 4.28. Truss diameter influence – Ribbed Bars.

Table 4.4. Peak loads observed in the simulations [kN].

		f_y = 235 [MPa]	f_y = 355 [MPa]	f_y = 450 [MPa]
f_c = 32 [MPa]	***R-12***	592	719	793
	R-14	683	837	939
	S-12	553	657	715
	S-14	662	807	900
f_c = 25 [MPa]	***R-12***	617	735	820
	R-14	669	814	947
	S-12	510	606	663
	S-14	622	765	867
f_c = 16 [MPa]	***R-12***	474	577	645
	R-14	591	726	802
	S-12	441	525	580
	S-14	559	696	782

The developed analyses have provided preliminary results in order to develop, in the future, an analytical model able to predict the ultimate shear load of the steel-concrete connection of HSTCBs starting from the geometrical and mechanical properties of the construction details. To this scope, a more extensive parametric analysis could also be planned for the development of the research.

4.7.2 Interpretation of the numerical results

From the analysis of the load-displacement curves obtained through the parametric simulation of different cases, a trend of the peak load to increase is observed whenever the yielding strength of the steel and/or the compressive resistance of concrete grow. But actually, this trend has shown to change starting from a certain value of the compressive strength of the concrete surrounding the ribbed steel bars: in those cases the maximum load value raises less than linearly.

According to a first interpretation, this result might depend on the ability of concrete to develop the plastic zone (PZ) around the web bars, next to the bottom steel plate, depending on the specific bond law at the steel-concrete interface.

Figure 4.29 and 4.30 show the comparison between two couples of cases: A12-3R vs. B12-3R and A12-3S vs. B12-3S. The markers on the curves represent the peak forces, the moment during the load history in which the PZ begins to develop and the moment in which the process is completed. As can be seen, both in the case of ribbed and smooth truss, the progression of the PZ follows the entire load-displacement curve almost until the peak load is reached.

The development of the PZ begins in the concrete volume around the web bars corresponding to their section next to the bottom steel plate. This section is indicated as "y=0" in Figure 4.31a. Then, the progress of the PZ stops corresponding to another section indicated as "$y=h_{pl}$" in the same figure. The progression of the plasticization has been monitored by means of chromatic maps of stresses in the concrete corresponding to different phases of the analysis, qualitatively represented in Figure 4.31b-c.

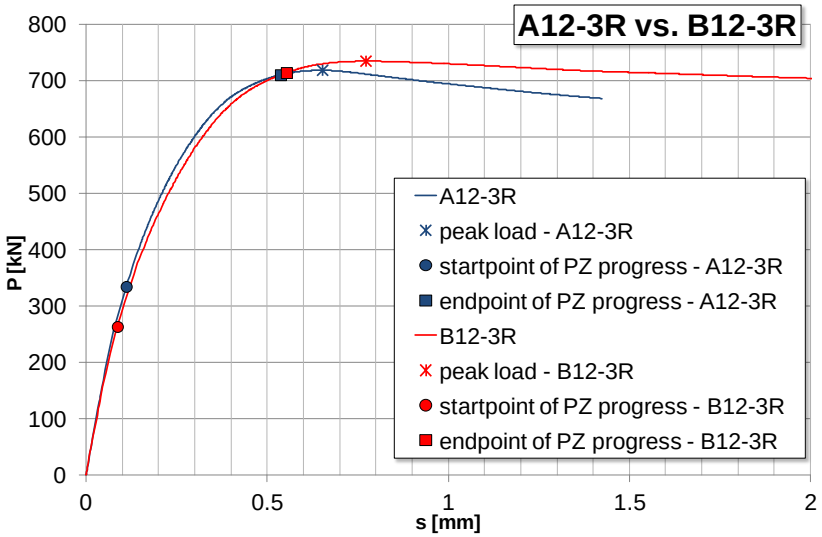

Figure 4.29. Comparison between A12-3R and B12-3R.

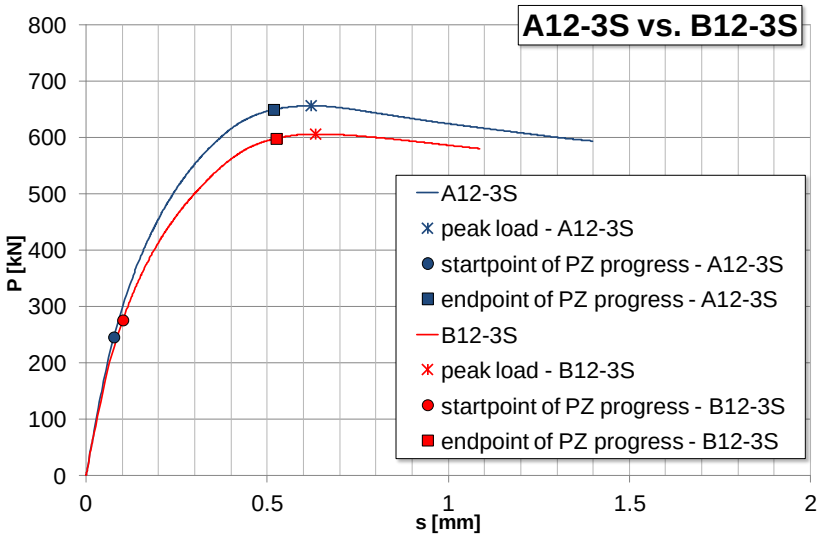

Figure 4.30. Comparison between A12-3S and B12-3S.

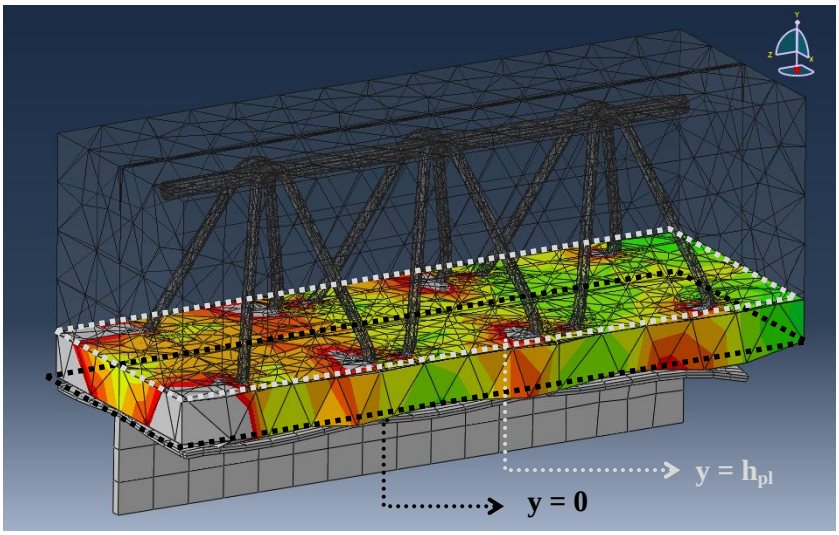

a)

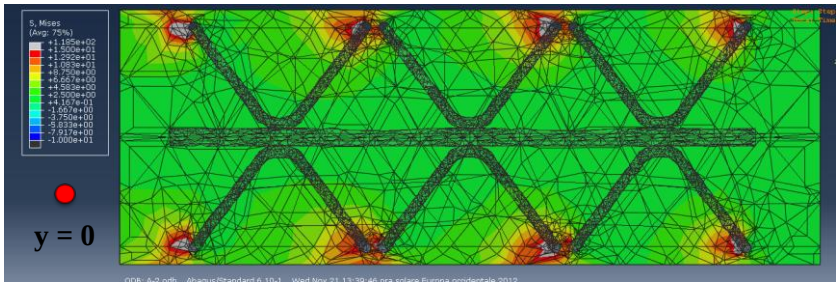

b)

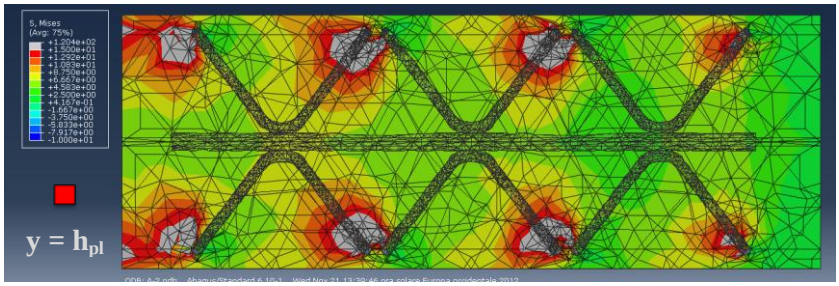

c)

Figure 4.31. Chromatic maps of stresses in the concrete: a) representation of sections at different height levels; b) stresses at the startpoint of the PZ progress at y=0; c) stresses at the endpoint of the PZ progress at y=h_{pl}.

By analyzing those chromatic maps for sections placed at different height levels, it has been observed that, concerning the cases of ribbed bar models, in the analysis B12-3R (ribbed steel truss and concrete compressive strength equal to 25 MPa) the PZ extends along a volume of concrete of about 27 mm depth, i.e. the distance between the section y = 0 and the section y = h_{pl} is almost 27 mm. Conversely, considering the same model in which the maximum compressive strength of concrete is equal to 32 MPa (that is analysis A12-3R), the plasticization of concrete involves a shorter portion of material of about 17 mm depth. As a consequence, it can be deduced that the load-displacement curve exhibits the maximum value in advance with respect to the moment in which it would have exhibited such peak if the PZ had involved a volume of concrete of the same depth than in analysis B12-3R.

In this regard, it is worth to note that in the simulations with smooth steel truss, in which the maximum load always increases with the increase of the compressive strength of the concrete (Figure 4.30), the PZ developed is about 20 mm depth in both cases of 25 and 32 MPa of concrete compressive strength.

Such a result leads to the conclusion that the specific bond stress-slip law at the steel-concrete interface is able to influence the way the PZ in the concrete develops around the web bars, near the section in which the plastic hinge in the bar takes place. Further extensive analyses have been planned for the development of the investigation about this issue.

CHAPTER 5

SHEAR BEHAVIOR OF HSTCBs: THREE POINT BENDING TESTS

In order to study the shear behavior of the HSTCBs, an experimental campaign of three-point bending tests has been carried out on six beams designed such that a shear failure occurs. In this Chapter the description of the specimens, the test setup and the measurement technology, first, and the obtained experimental results, then, are presented and discussed. Finally, an interpretation of the experimental results is provided by means of an accurate FE model and through some existing analytical expressions for the calculation of the shear strength. Furthermore, an analytical formulation of the shear strength mechanism able to predict the shear resistance is formulated with respect to the peculiarities of the tested HSTCBs and it is herein proposed and discussed.

5.1 Experimental program

The three-point bending tests have been performed at the Laboratory of Structures of the Department of Civil Engineering of the University of Palermo. The tests have been carried out on six specimens of HSTCB and executed with a symmetric loading condition. The scope of the experiment is the evaluation of the shear strength in the structural typology object of study.

Two series of specimens have been tested. The first series, named series "A", is subjected to positive bending moment, that is the load is applied so that the bottom steel plate of the beam is in tension. Conversely, the second series, named series "B", is subjected to negative bending moment, that is the load is applied so that the bottom steel plate of the beam is in compression. The scope of the first series of tests is to reproduce the condition of positive bending moment corresponding to the midspan of a beam belonging to a framed structure; similarly, the aim of the second series of tests is to consider the behavior of the beam next to the column where the sign of the bending moment is reversed. The details of the beam geometry are illustrated in the following sections as well as the procedure for the execution of the tests and the mechanical characterization of materials.

5.1.1 Description of the specimens

The basic cross-section of the tested beams is represented in Figure 5.1: it is constituted by three upper bars of 16 mm diameter, a bottom steel plate 5 mm thick and a couple of diagonal bars of 12 mm diameter. The depth of the beam is 250 mm and its width 300 mm.

The six specimens manufactured are geometrically equal in couples and their cross-section differs from the basic typology because of the presence of some other added rebars on the top and/or on the bottom of the beam.

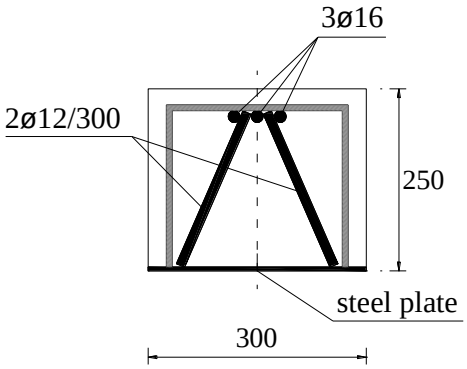

Figure 5.1. Basic cross-section of the tested beams (dimensions in millimeters).

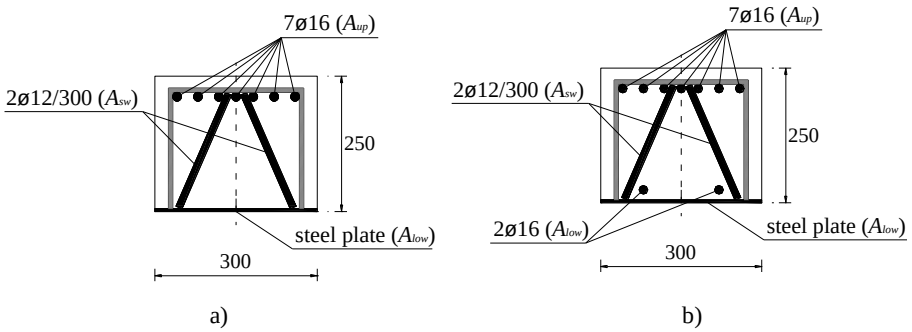

Figure 5.2. Cross-section of specimens series "A" and "B" (dimensions in millimeters): a) specimens A1-1, A1-2, B1 and B2; b) specimens A2-1 and A2-2.

Particularly, the specimens belonging to series "A" and identified with the tag A1-1 and A1-2 present four 16 mm diameter added rebars on the top of the beam (see Figure 5.2a) so that the total area of the upper reinforcement, A_{up}, corresponds to the area of seven bars of 16 mm diameter, while the area of the lower reinforcement, A_{low}, is simply constituted by the area of the rectangular section of the steel plate (300x5 mm^2). As regards specimens whose tag is A2-1 and A2-2, they present both four added rebars on the top and two further rebars on the bottom of the beam. All added rebars are 16 mm diameter. Thus, for this specimens A_{up} correspond to the area of seven bars of 16 mm diameter, while A_{low} is constituted by the sum of the area of the rectangular section of the steel plate and the area of the two added rebars (see Figure 5.2b). In all specimens, the area of the web reinforcement, A_{sw}, corresponds to the area of the cross-section of the two diagonal bars of 12 mm diameter. Finally, specimens of series "B", identified with the tag B1 and B2, present the same cross-section of specimens A1-1 and A1-2.

Concerning the characteristics of materials, the steel constituting the rebars is type B450C, while the steel of the bottom plate is a smooth steel class S355. As regards concrete, during the casting, two different types of mixtures have been adopted since, at a certain point of the procedure, it has been necessary to improve the workability of the material by adding water to the mix. Specimens A2-1, A2-2 and B1 have been cast after the addition of

water. In the following, we will refer to the concrete employed for these beams as concrete "type 1". On the contrary, specimens A1-1, A1-2 and B2 have been manufactured before the addition of water to the mixture. In the following, we will refer to the concrete employed for these latter beams as concrete "type 2".

In Table 5.1 the main characteristics of all specimens are reported.

The longitudinal extension of the beams is shown in Figure 5.3. All specimens have a shear span equal to 600 mm and the bottom steel plate is anchored at the ends of the beam in order to avoid the slip between the plate and the concrete, which is a significant phenomenon influencing the failure mode. Actually, also in practical applications the bottom plate is anchored within the beam-to-column joints of a framed structure by means of special devices which have the aim of prevent a premature failure due to the slip. Finally, in all specimens 8 mm diameter stirrups with 60 mm spacing are placed corresponding to the lateral supports of the beam and the midspan where the load is applied, in order to avoid local crushing.

In Figures 5.4 and 5.5 some pictures of the bare steel trusses before and after the concrete casting, respectively, are shown.

Table 5.1. Characteristics of the specimens.

Series	**ID**	A_{low}	A_{up}	A_{sw}	**Test execution**	**Concrete type**
A	**A1-1**	steel plate 300x5 mm^2	7ϕ16	2ϕ12/300	M+	2
	A1-2					2
	A2-1	steel plate 300x5 mm^2 + 2ϕ16				1
	A2-2					1
B	**B1**	steel plate 300x5 mm^2			M-	1
	B2					2

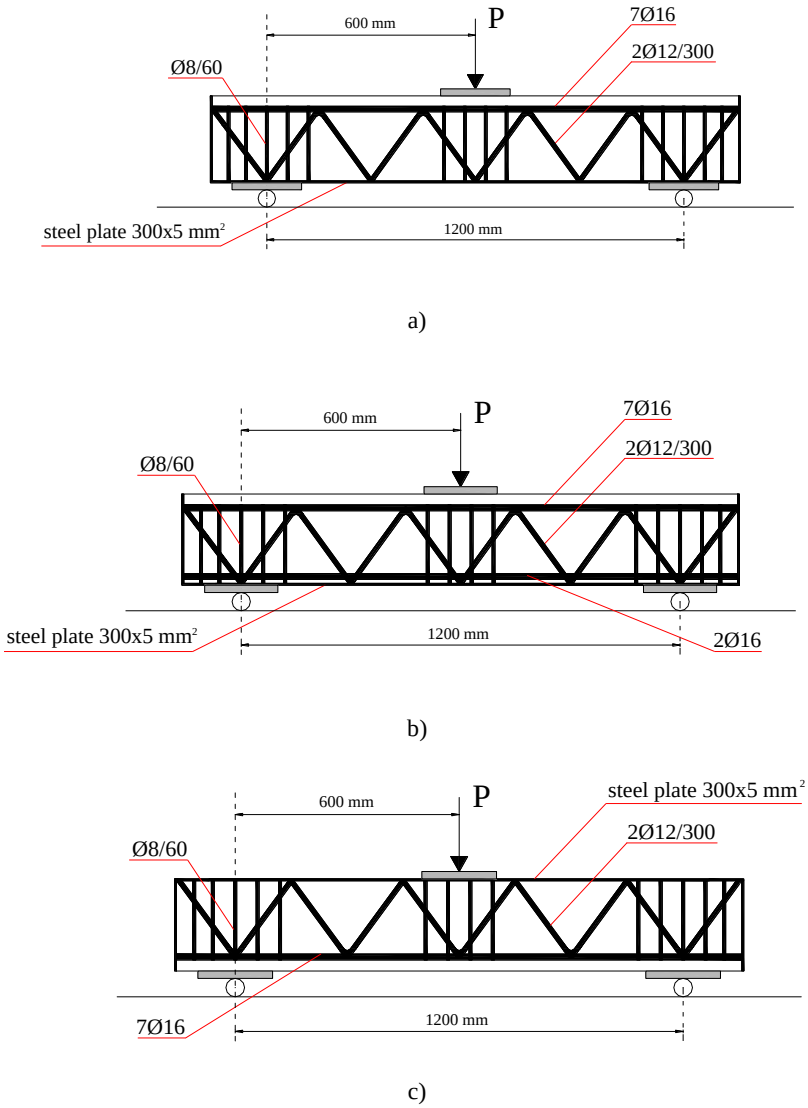

Figure 5.3. Longitudinal extension of the specimens and test scheme: a) specimens A1-1 and A1-2; b) specimens A2-1 and A2-2; c) specimens B1 and B2.

a)

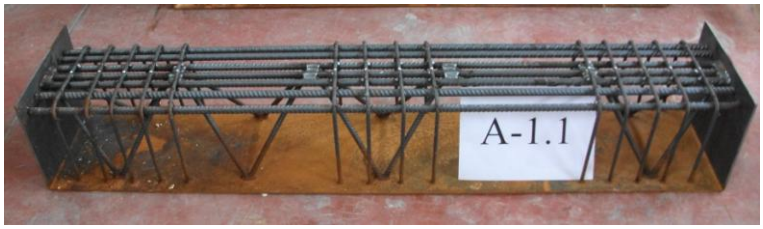

b)

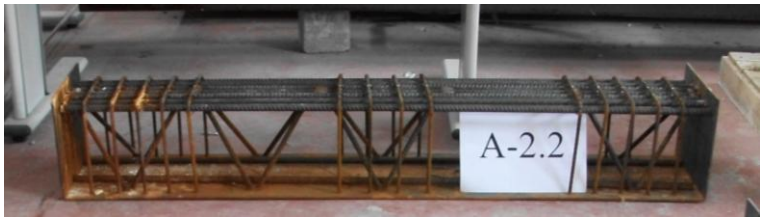

c)

d)

Figure 5.4. Bare steel trusses: a) general view of all specimens; b) specimen A1-1; c) specimen A2-2; d) specimen B2.

Figure 5.5. Specimens after the concrete casting.

5.1.2 Mechanical characterization of materials

Both the steel and the concrete constituting the beams have been mechanically characterized by means of standardized tests all executed with the universal testing machine *Zwick/Roell Z600* owned by the Department of Civil Engineering of the University of Palermo (Figure 5.6).

The machine allows to perform monotonic tensile and/or compression tests, cyclic tests and fatigue tests in load, displacement or deformation control. The type of test and the whole management of the machine is governed by an electronic unit control which is interfaced with the user through a personal computer and by means of the software *TestXpert v.10.11*. The machine has five channels (force, displacement, rigid movable crossbar, Macro-strain gauge and inductive transducer) apt at controlling the test. The mechanical frame is constituted by a basement where the load cell and the clamp or the lower plate, in case of compression tests, are fixed; a crossbeam with the upper clamp which can slide along a guide, consisting in two rods and moved by means of two endless screws of big diameter, with a minimum and a maximum speed of 0.03 and 200 mm/min respectively. The position of the crossbeam is detected by a transducer with a resolution of ± 8 μm.

Figure 5.6. Universal testing machine *Zwick/Roell Z600*.

The maximum distance between the two clamps is 1100 mm. The load cell that detects the value of the force has two resolutions: in class 1, when the load is in the range between 0 kN and 6 kN; in class 0.5 when the range is between 6 kN and 600 kN. For the measurements of the deformations the external strain gauge called Macro or the inductive transducer can be used. They are both produced by HBM industry. The measurement devices are interfaced with the management software and can be directly placed in contact with the specimen providing a real effective measure. The Macro strain gage has a measurement range between 10 to 200 mm, a maximum stroke of 75 mm and a resolution of 0.3 μm; on the other hand the inductive transducer has a stroke of 10 mm and a resolution of 0.1 μm.

Uniaxial compression tests and split tests on concrete and uniaxial tensile tests on steel have been performed. The specimens employed for the compression tests on concrete are cylinders of 121mm diameter and 241 mm depth, leveled in laboratory and monitored by means of three Mitutoyo LVDTs with a measurement range of 13.5 mm (see Figure 5.7). In Table 5.2 the obtained results are reported in terms of maximum compressive strength, f_c, and elasticity modulus, E_c. Figure 5.8 shows the stress-strain curves of the three compression tests with the data recorded by the testing machine. It is worth to remind that the tested concrete is of "type 1" while the mechanical characterization of concrete "type 2" is not available.

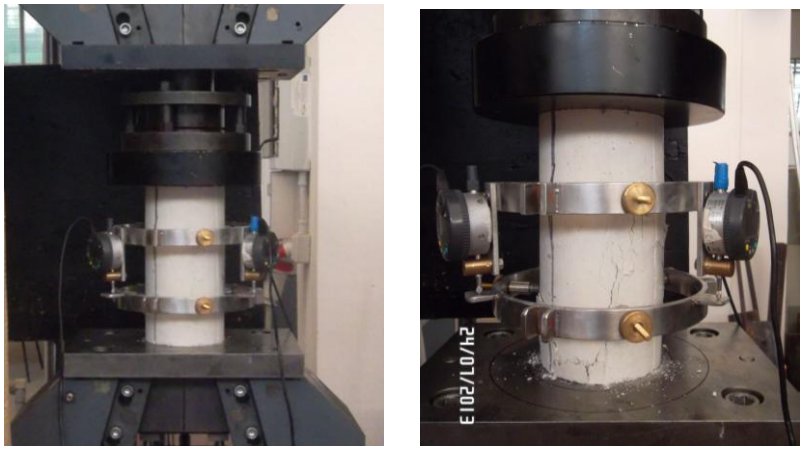

a) b)

Figure 5.7. Cylindrical concrete specimen: a) specimen within the testing machine; b) specimen at the end of the test.

Table 5.2. Measured and average values of the compressive strength and the elastic modulus.

Specimen ID	f_c [MPa]	E_c [MPa]
1	15.66	25170
2	16.57	25600
3	14.75	24721
Average value	15.66	25164

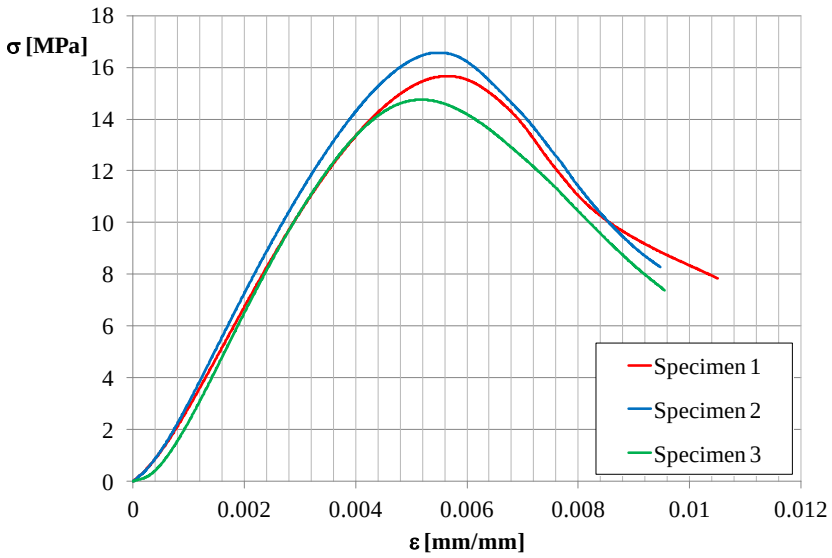

Figure 5.8. Stress-strain curves recorded by the testing machine.

Then also the tensile strength of concrete has been evaluated by means of a standard split tests on cylindrical specimens applying a compression load on two opposite generatrix lines (Figure 5.9). In this way the action of the load determines a state of biaxial tension normal to the direction of the applied load.

Six specimens with 121 mm diameter and a depth-to-diameter ratio of about one were tested. The tensile strength, f_{ct}, is evaluated through the following expression:

$$f_{ct} = \frac{2P_{\max}}{\pi LD} \tag{6.1}$$

where P_{max} is the maximum force, L is the length of the specimen and D the diameter.

In Table 5.3 the values of P_{max} and f_{ct} obtained for each specimen are reported and in Figure 5.10 the corresponding stress-strain curves are represented, being the strains obtained from the displacements recorded by the testing machine.

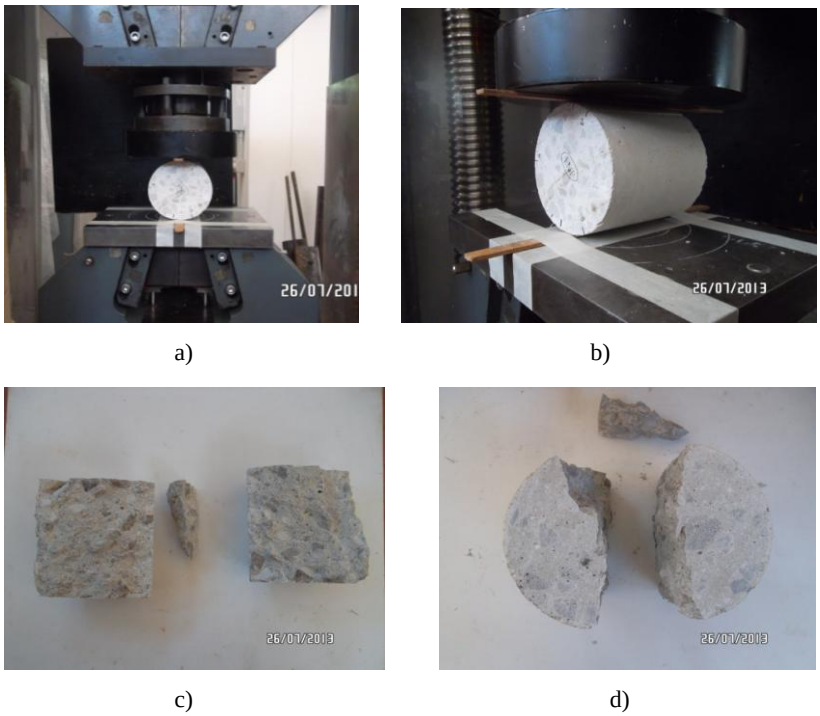

Figure 5.9. Split test: a) frontal view of the specimen within the testing machine; b) lateral view of the specimen within the testing machine; c) and d) details of the specimen after the test execution.

Table 5.3. Measured and average values of the compressive strength and the elastic modulus.

Specimen ID	**P[kN]**	**f_{ct} [MPa]**
1	52.02	2.23
2	51.67	2.23
3	65.67	2.81
4	46.41	1.98
5	50.80	2.19
6	44.15	1.89
Average value	51.79	2.22

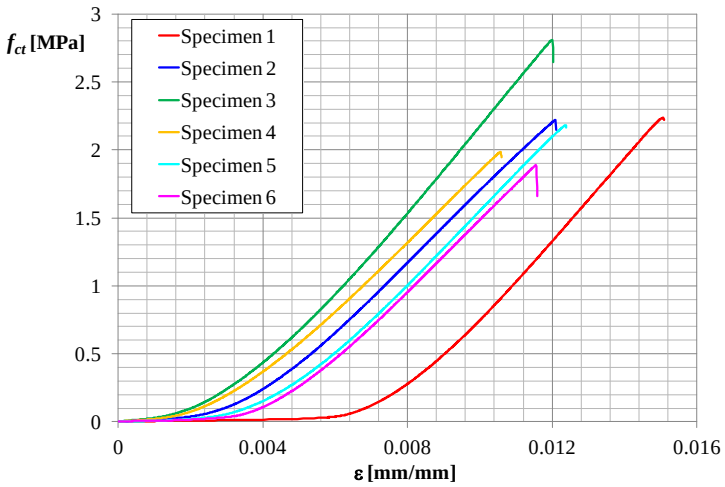

Figure 5.10. Stress-strain curves of the split tests.

a) b)

Figure 5.11. Tensile tests: a) on the rebar; b) on the plate.

Table 5.4. Tensile tests on steel elements.

	plate	**rebar ϕ12**	**rebar ϕ16**
f_y [MPa]	395.44	508.81	489.10
ε_y [%]	0.21	0.27	0.26
f_p [MPa]	463.57	625.94	620.02
ε_p [%]	15.55	9.88	11.33
E_s [MPa]	192193.55	186760.49	184737.97

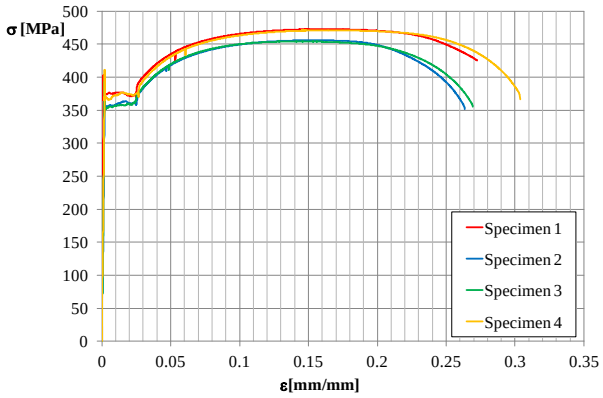

a)

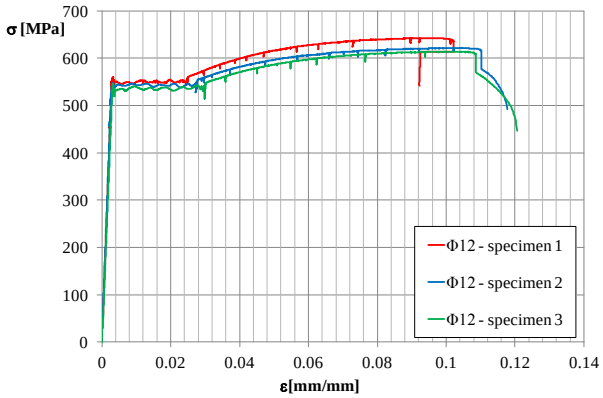

b)

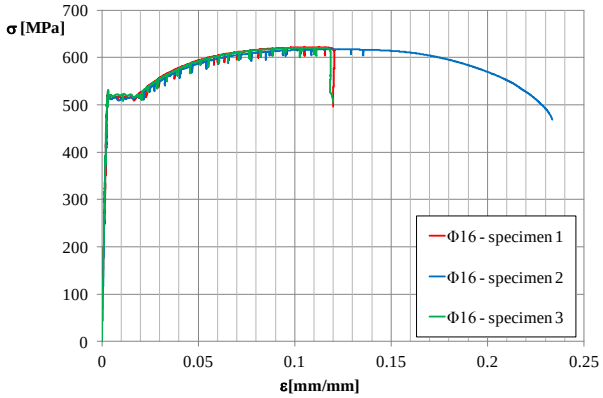

c)

Figure 5.12. Stress-strain curves of the split tests: a) steel plate; b) rebars 12 mm diameter; c) rebars 16 mm diameter.

Concerning the steel, both the 12 and 16 mm diameter rebars and the 5 mm thick plate have been tested (Figure 5.11).

The tests have been performed according to the procedure prescribed in the European standard code "UNI EN 10002-1:2004: Metallic materials - Tensile testing". Three specimens for each diameter of rebars and four specimens of steel plate have been tested. Then, starting from the experimental data collected, the average values of the yielding and peak stress and strain (f_y, f_p, ε_y, ε_p) and the elastic modulus (E_s) have been calculated. Those values are reported in Table 5.4. Figure 5.12 shows all stress-strain curves recorded by the testing machine.

5.1.3 Testing machine and measurement technology

The three point bending tests on the beams have been performed by means of a universal machine by Zwick/Roell & Toni Technik able to apply a maximum load of 4000 kN (Figure 5.13). As well as the one already described in the previous section, this machine allows to perform load, displacement or deformation controlled tests. The type of test and all settings of the machine are managed by an electronic unit control interfaced with the user through a personal computer and by means of the software testXpert v. 7.10. The machine has four channels: force, transducer for the displacements of the piston, external inductive transducer and a couple of external transducers. Tests performed in load control are expected to be controlled through the load cell while tests performed in displacement and deformation control are governed by the piston stroke and the external transducer, respectively.

The frame of the machine is constituted by a lower steel base from which four columns rise; the columns are supposed to be the guide for the upper moveable crossbeam on which a jointed plate is placed. On the lower basement there is the piston in which the load cell is located. Above the piston, a steel plate is placed for the collocation of the structural elements to be tested and, outside from the piston, a displacement transducer with maximum stroke of 100 mm is placed. Tests in displacement control can be performed with minimum speed of 0.25 mm/min. Both the lower and the

upper plate are 420x520 mm and their minimum and maximum distance is 150 and 1500 mm respectively. The load cell that measures the value of the force has a resolution in class 1 in all the load range which is between 0 kN and 4000 kN and the minimum load given to the lock of the upper joint is equal to 24 kN.

The collection of data during the tests has been produced also exploiting the measurements of two different types of external LVDTs with infinitesimal resolution by Mitutoyo. The first type is called "model 460 B" and has a measurement range between 0 and 50 mm. The second type, called "model 250 B", has a smaller measurement range between 0 and 12.5 mm.

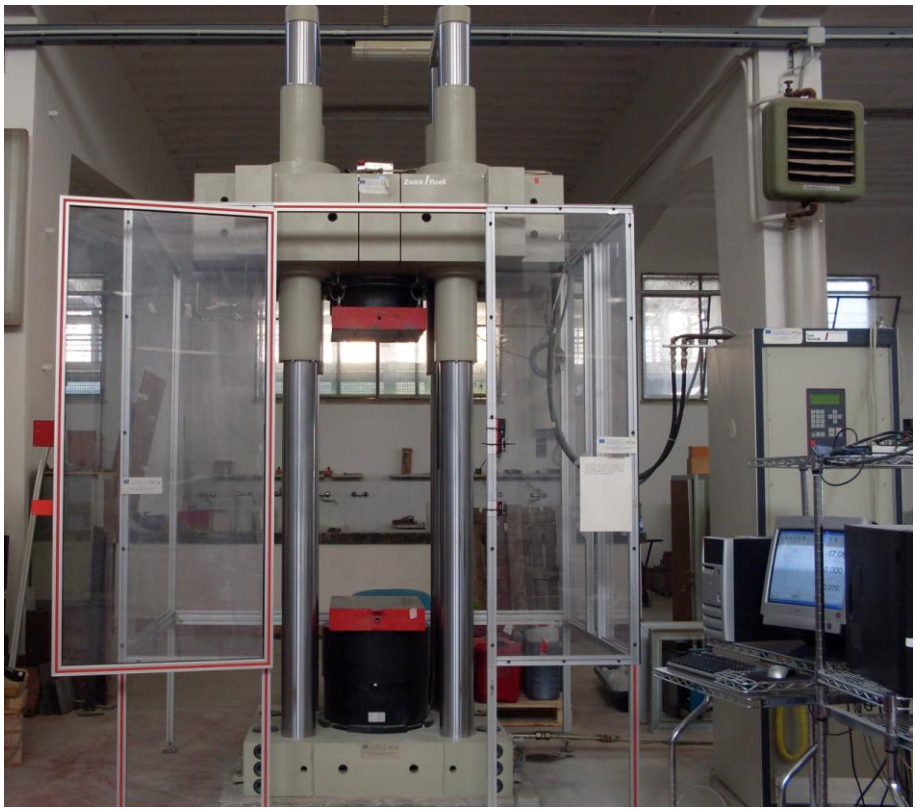

Figure 5.13. Testing machine Zwick/Roell & Toni Technik 4000 kN employed for the three-point bending tests.

Finally also the strain data corresponding to a few steel members of the beam have been collected by means of sixteen Strain Gauges (SG) by HBM industry installed on the beams before the concrete casting. SG are sensors used to monitor the deformations of an element. They are usually constituted by a grid of thin metallic wire which is rigidly fixed to a plastic support, as shown in the schematic diagram of Figure 5.14. Once they are attached to an element, they are able to follow the deformation of the surface. Such deformations vary the electrical resistance of the device which is measured and converted in strains. The SG installed on the beams are identified with the tag "K-LY41-3/120 4" meaning that they are linear SG with 120 Ohm resistance and 3 mm measuring grid, able to record strains in the direction in which the measuring grid is aligned.

The scheme of the typical components of the installation of a strain gauge is showed in Figure 5.15 where "1" is the measuring grid; "2"the plastic rigid support of the grid; "3" is the adhesive used to fix the strain gauge to the steel surface; "4" is the protective coating used in order to protected the device against external effects such as humidity or mechanical damage; "5" are the electrical terminals; "6" is a baseplate and, finally, "7" and "8" are respectively the covering of the cables and the wires.

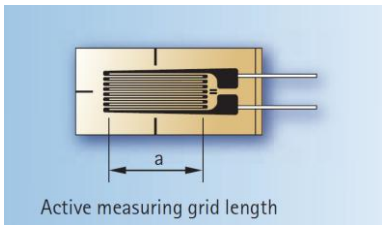

Figure 5.14. Schematic diagram of a strain gauge.

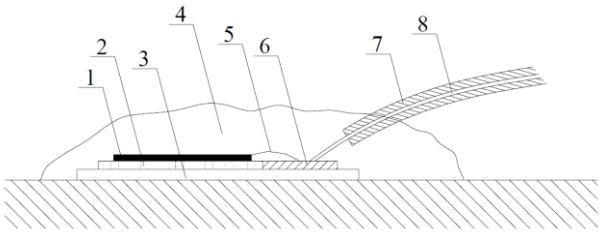

Figure 5.15. Scheme of the installation of a strain gauge.

For a correct installation, the prescriptions of two standardized codes have been followed: UNI 10478-3 "Non destructive testing - Inspection by strain gauges - Strain gauge installation and checking" and ASTM E1237-93 "Standard Guide for Installing Bonded Resistance Strain Gauges". The main steps of such a procedure are the following:

- preparation of the surface with the aim of reducing its roughness as much as possible;
- cleaning of the surface through a specific environmentally-friendly solvent mixture that dissolves all normal contamination (*cleaning agent RMS1-SPRAY*);
- connection of the strain gauge to the surface by means of specific adhesives that are required to free transfer the deformations of the tested object to the active measuring grid, ensuring a stable behavior across a temperature and preventing any chemical attack on both the strain gauge and the object surface (*rapid adhesive Z 70*);
- protection of the installed device against any external attack by means of special material coverings (*silicon rubber SG 250; aluminum foil with kneading compound ABM 75*).

Figure 5.16a shows the steel bar surface whose ribs have been smoothed corresponding to the area interested by the installation of the strain gauge. Figure 5.16b represents the phase of the connection of the device to the surface by means of the rapid adhesive while Figures 5.16c-d show respectively the strain gauge just after the installation and, finally, after the protection.

All SG installed on the specimens are indicated with the identity tag from "SG1" to "SG16". Concerning the beams of series "B", only the deformations of the specimen B1 have been monitored. The detail of the collocation of the SG on the steel members of each beam is reported in Table 5.5 and in Figure 5.17. Particularly, the collocations correspond to the central rebar of the Upper Chord (*UP*), one Tensile Web bar (*TW*), one Compressed Web bar (*CW*) and, finally, the bottom steel Plate (*P*).

Figure 5.18 shows one of the bare steel truss with the SG completely installed before the concrete casting and Figure 5.19 represents the phases of

the collocation of the strain gauge on the bottom steel plate after the maturation of the concrete.

a) b)

c) d)

Figure 5.16. Installation of a strain gauge: a) smooth surface; b) connection to the surface; c) strain gauge installed on the surface; d) final protection.

Table 5.5. Identity tags of SG in the specimens.

specimen	***UP***	***TW***	***CW***	***P***
A1-1	SG1	SG2	SG3	SG4
A1-2	-	SG5	SG6	-
A2-1	SG7	SG8	SG9	SG10
A2-2	-	SG11	SG12	-
B1	SG13	SG14	SG15	SG16
B2	-	-	-	-

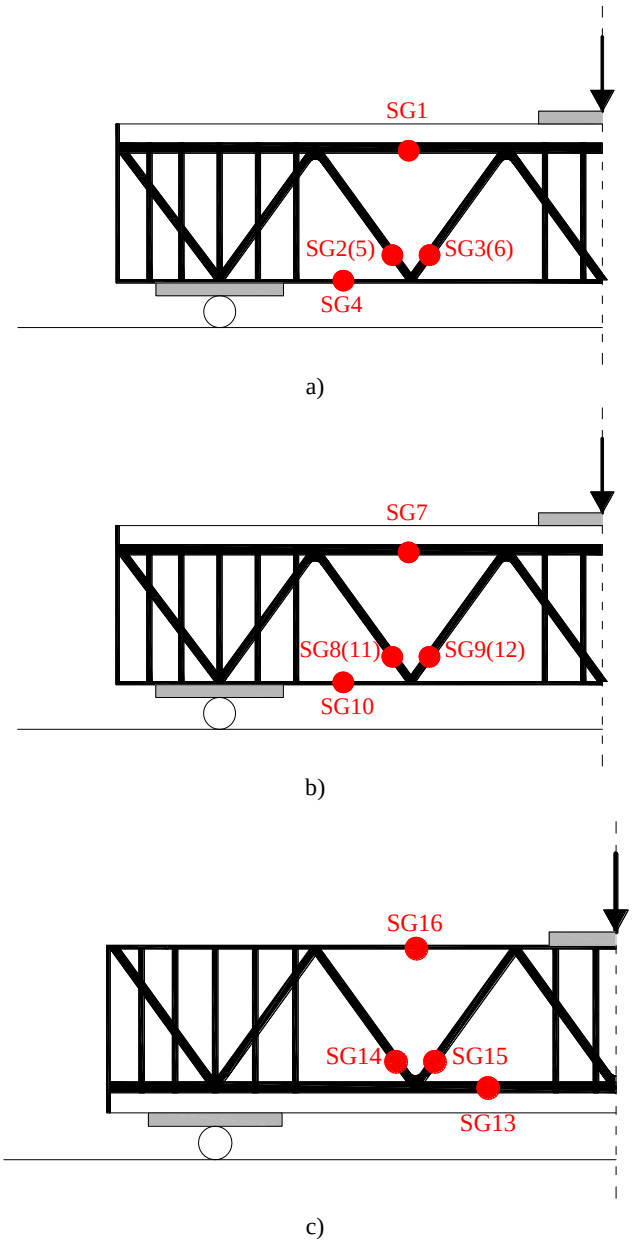

Figure 5.17. Collocation of the SG on the specimens: a) A1-1 and A1-2; b) A2-1 and A2-2; c) B1.

a)

b)

Figure 5.18. Bare steel truss: a) specimen A1-1; b) zoom of the rebars with SG.

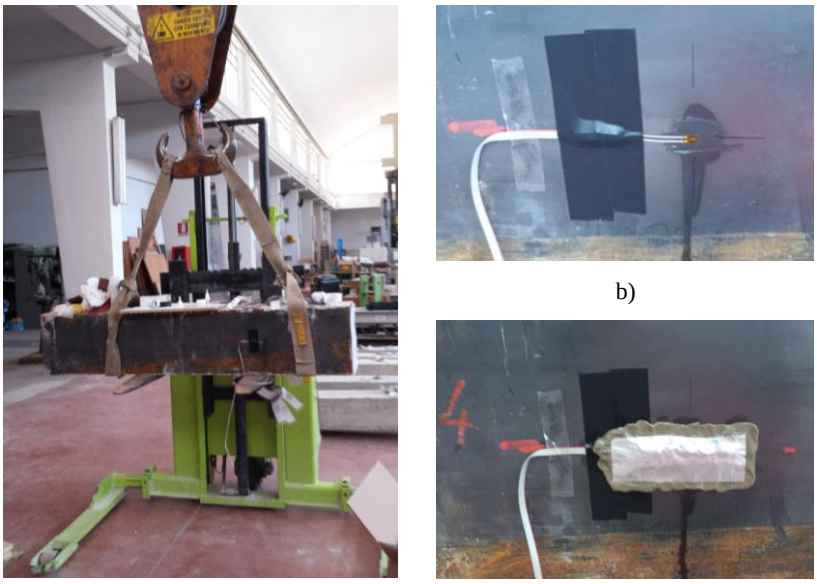

a) b) c)

Figure 5.19. Installation of the strain gauges on the steel plate: a) general view of the specimen; b) strain gauge glued on the surface; c) protection.

5.1.4 Test setup and data acquisition

The configuration of the test setup is schematically represented in Figures 5.20 and 5.21. First of all, a rigid steel HE 240 beam is collocated on the bottom plate of the machine ensuring an appropriate base for the supports of the specimen. As shown in Figure 5.22, in which all constraints are represented, the lateral supports are realized by means of steel cylinders and plates which allow rotations and prevent translations (Figure 5.22b); similarly, the load is applied on the specimen through a steel cylinder placed on the top surface of the beam in order to transform the pressure of the upper plate of the machine into a load distributed on a line (Figure 5.22c). On both sides of the aforementioned rigid HE 240 beam, two steel square hollow profiles are placed as support for the LVDTs. Particularly, six LVDTs are

collocated: two of them (LVDT1 and LVDT2) on both sides of the midspan of the beam (Figures 5.20, 5.21 and 5.22d); two other couple of LVDTs (LVDT-3 and LVDT-4; LVDT-5 and LVDT-6) on both the right and the left side of each one of the lateral supports (Figures 5.20, 5.21 and 5.22b). The LVDTs collocated at the supports of the specimen have the aim of checking that there are no displacements corresponding to the rigid steel beam.

While all data generated by the testing machine are managed by the electronic unit control *Tonitroll* interfaced with the user through the software testXpert v. 7.10, all measurements collected by the transducers are acquired through another unit control by Mitutoyo, indicated as *DMX-16C* in Figure 5.23. The *DMX-16C* is then interfaced with the user by means of a software specifically realized with the program language *LabView by National Instruments*. Finally, the last acquisition system, indicated as *MGCPlus* in the same figure, is able to record all data from the SG. The unit control *MGCPlus* is then interfaced with the user by means of the software *CATMAN* provided by the HBM company.

Figure 5.24 shows the test setup configuration realized in the Laboratory of Structures of the University of Palermo.

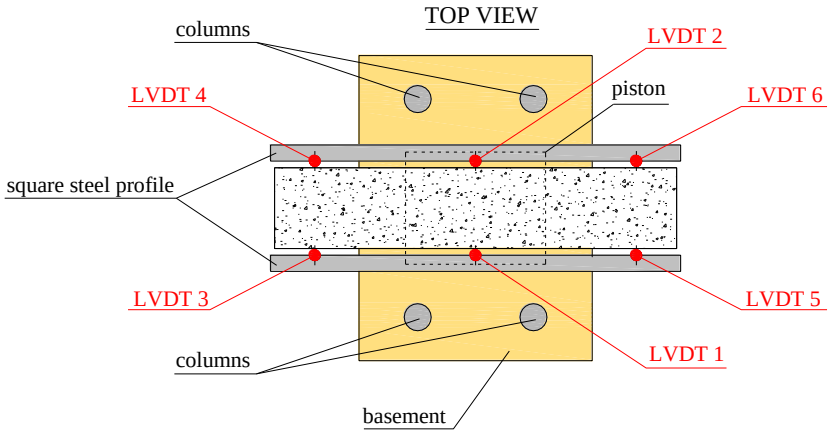

Figure 5.20. Top view of the testing machine and SG collocation on the specimen.

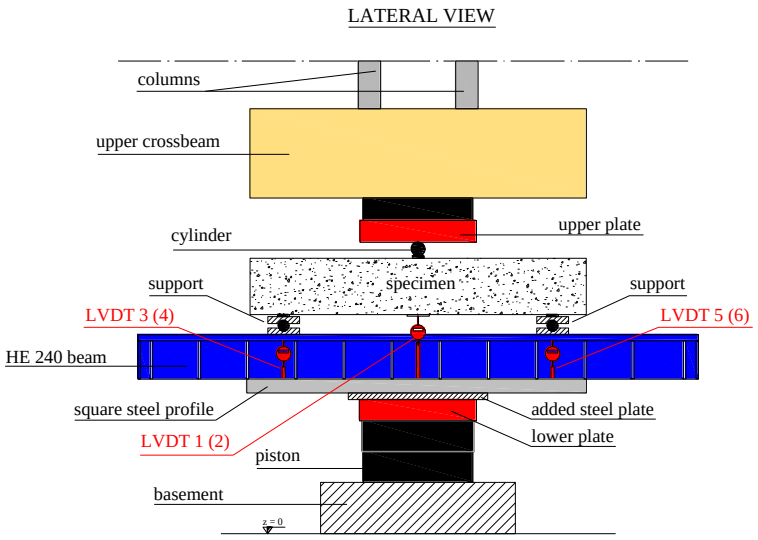

a)

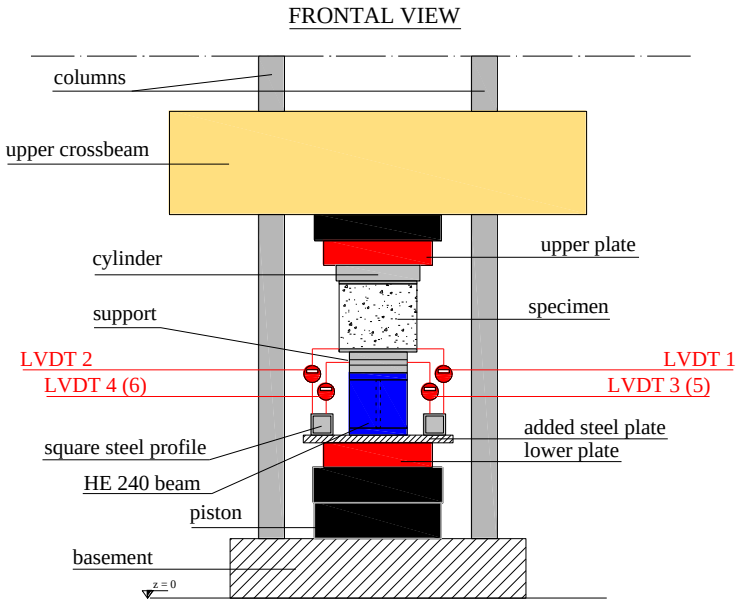

b)

Figure 5.21. Scheme of the test setup: a) lateral view; b) frontal view.

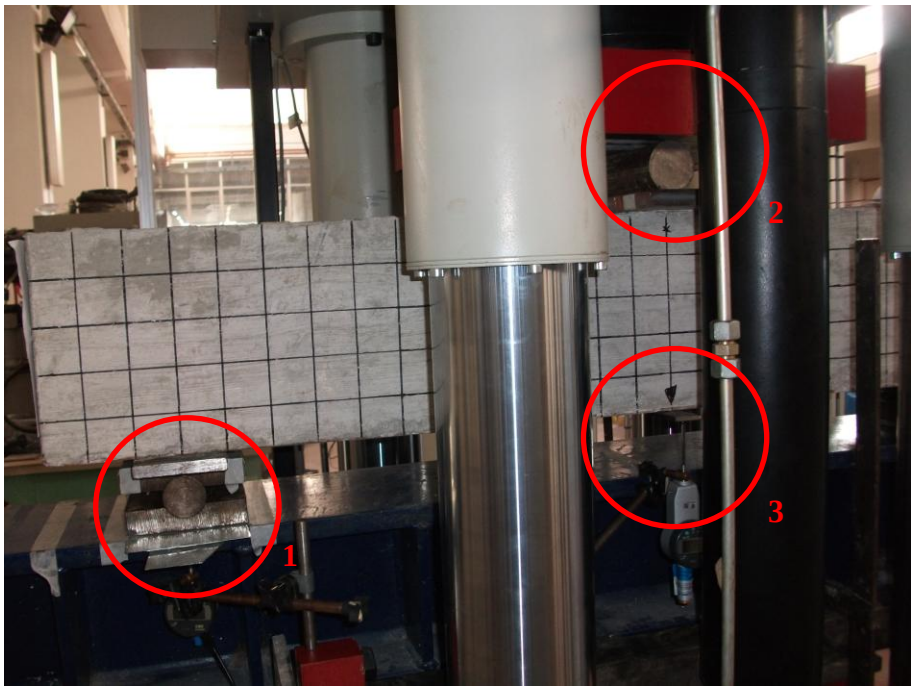

a)

b)

c)

d)

Figure 5.22. Details of the test setup: a) general view; b) support of the beam monitored by the LVDT; c) cylinder and contact plate corresponding to the applied load; d) LVDT placed in the midspan of the beam.

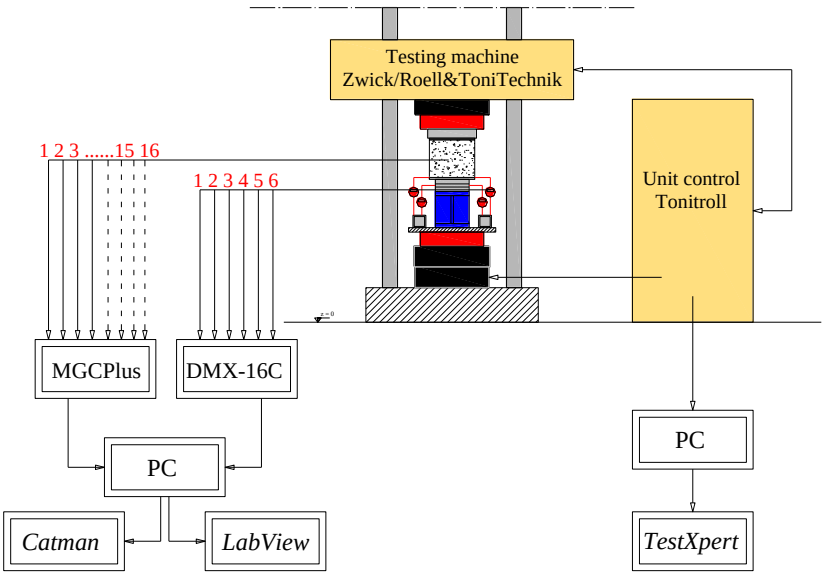

Figure 5.23. Scheme of the hardware and software components of the acquisition system.

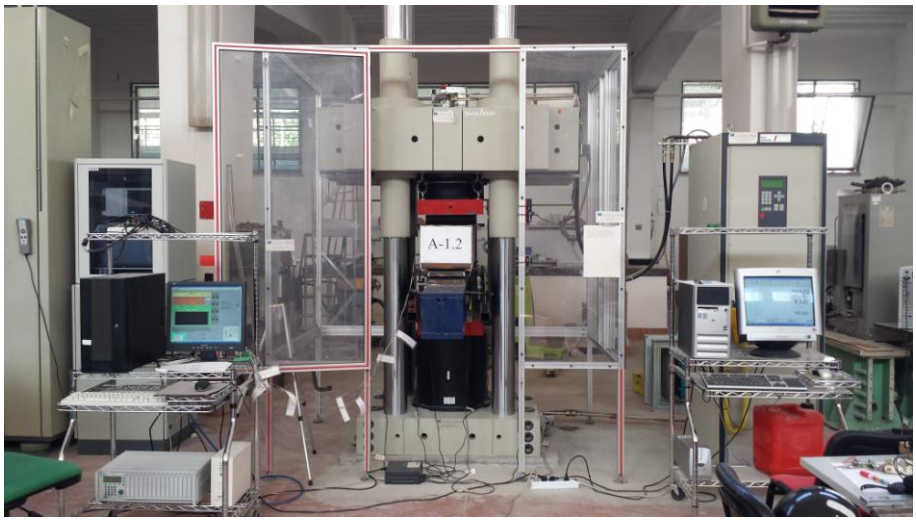

Figure 5.24. Picture of the test setup at the Laboratory of Palermo.

5.2 Experimental results

The tests are performed in displacement control, at a speed of 0.2 mm/min. At the beginning of each test, a 30 kN preload is applied. All data are recorded every 0.5 seconds.

In the follow, for each specimen, the load-displacement curve and the strain gauge measurements are reported.

The load-displacement curves are obtained on the basis of the average value of the measurements recorded by the LVDTs placed in the midspan of the beam minus the mean values of the displacements measured by the LVDTs placed at the lateral supports.

5.2.1 Load-displacement curves

Specimens series "A"

Figure 5.25 shows the load-displacement curve of specimen A1-2. The specimen exhibited a brittle shear failure with a maximum load of 577.74 kN, corresponding to a displacement of 22.35 mm.

During the load history, once the load reaches the value of 190 kN, the first vertical flexural cracks appear in the midspan of the beam (Figure 5.26a). Subsequently, corresponding to a load of about 320 kN, also the diagonal shear cracks begin to develop, as shown in Figure 5.26b. During the test evolution, the separation of the bottom steel plate from the block of concrete is observed (Figure 5.26c).

Before the maximum load is achieved, the behavior of the beam presents a mostly ductile response due to the growth of the flexural sub-vertical cracks. Finally, because of the subsequent evolution of the main diagonal shear crack, a brittle shear failure occurs, after which the load is suddenly almost halved.

Concerning specimen A1-1, unfortunately, because of a technical problem with the testing machine during the execution of the test, the results were definitely compromised and, as a consequence, they are not reported within this thesis.

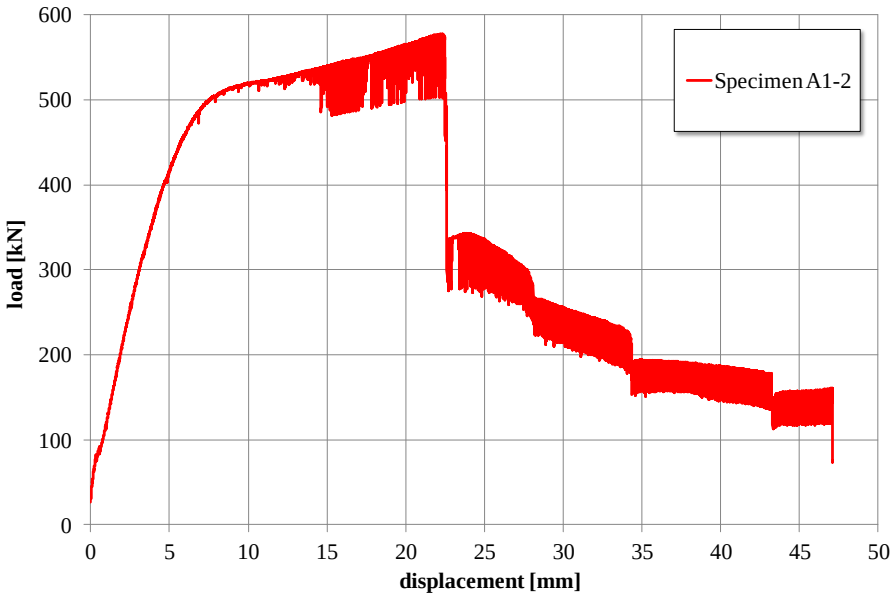

Figure 5.25. Load-displacement curve of specimen A1-2.

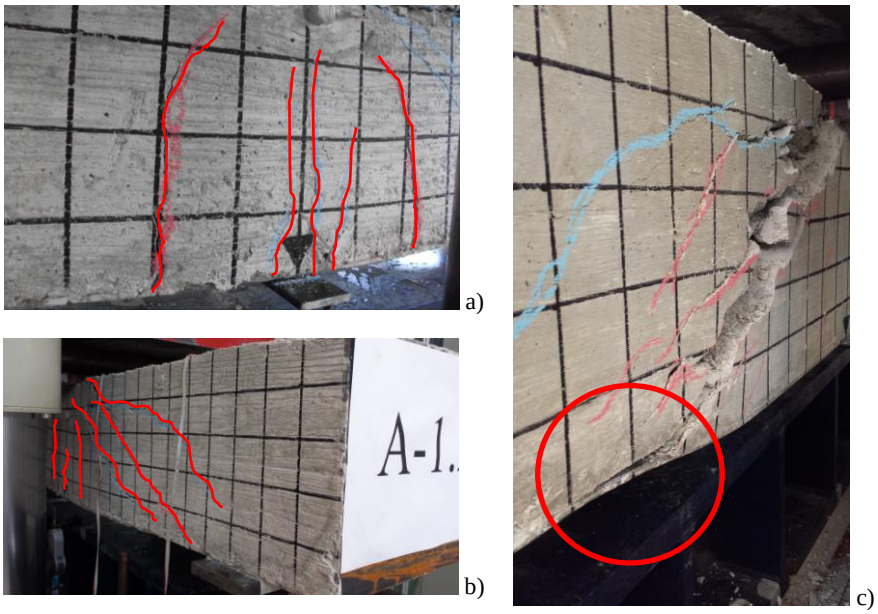

Figure 5.26. Specimen A1-2: a) vertical flexural cracks; b) first diagonal shear cracks; c) separation of the plate from the block of concrete.

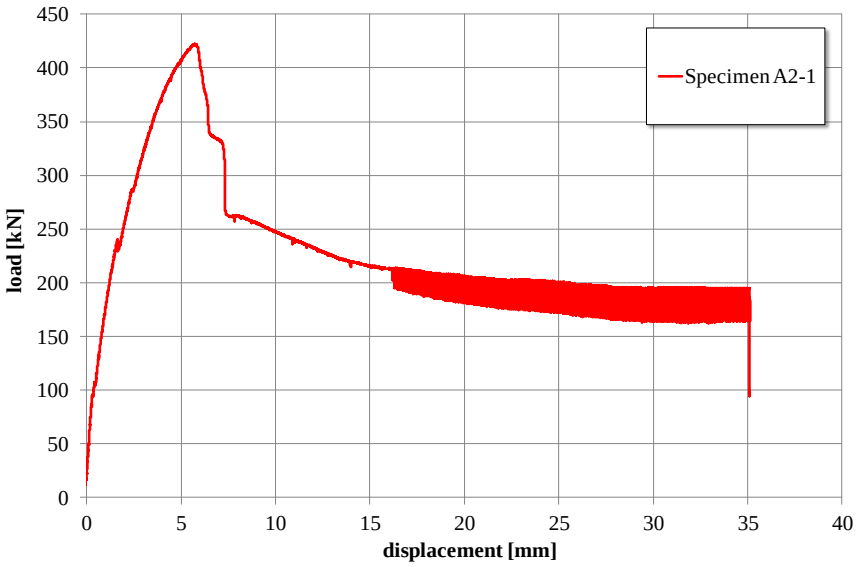

Figure 5.27. Load-displacement curve of specimen A2-1.

a) b)

Figure 5.28. Specimen A2-1: a) main diagonal shear crack; b) view of the upper chord and the tensile web bar of the truss across the diagonal crack.

In a similar way, Figure 5.27 shows the load-displacement curve of specimen A2-1. As it can be observed, in this case the specimen exhibited a clearly brittle shear failure with a sudden loss of load after the maximum value of 422.29 kN is reached corresponding to 5.73 mm of displacement.

During the load history, the first flexural cracks appear when the load reaches approximately the value of 240 kN. In the same time, a partial delamination of the bottom steel plate is observed at a distance of about 20 cm from the midspan of the beam. The failure of the specimen is caused by the evolution of the main diagonal shear crack showed in Figure 5.28a which individuates the compressed concrete strut. Figure 5.28b shows the external bar of the upper chord and the tensile web bar of the truss crossing the main diagonal shear crack.

Figure 5.29 shows the load-displacement curve of specimen A2.2. The specimen exhibited a brittle shear failure, similar to the identical specimen A2-1. The maximum load is 461.29 kN corresponding to a displacement of 7.91 mm.

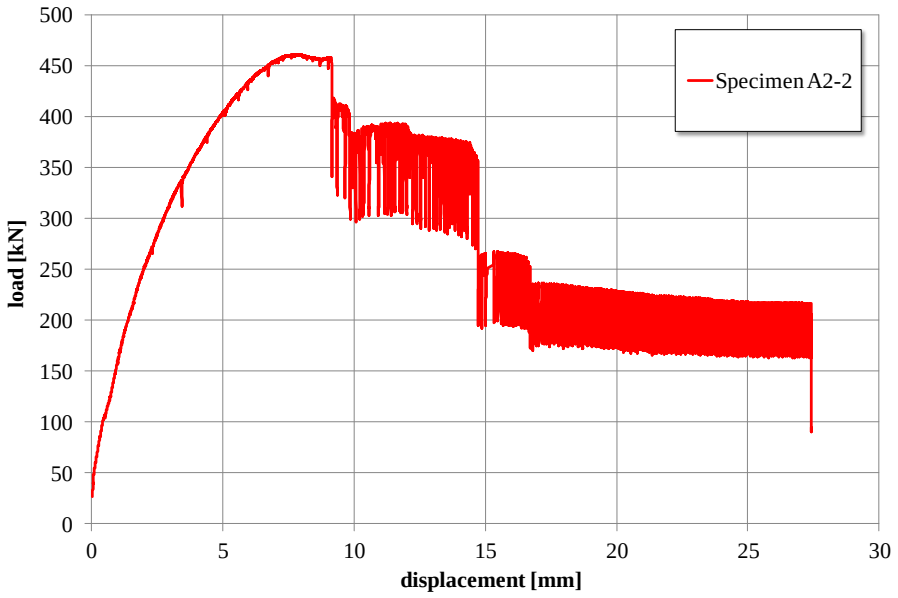

Figure 5.29. Load-displacement curve of specimen A2-2.

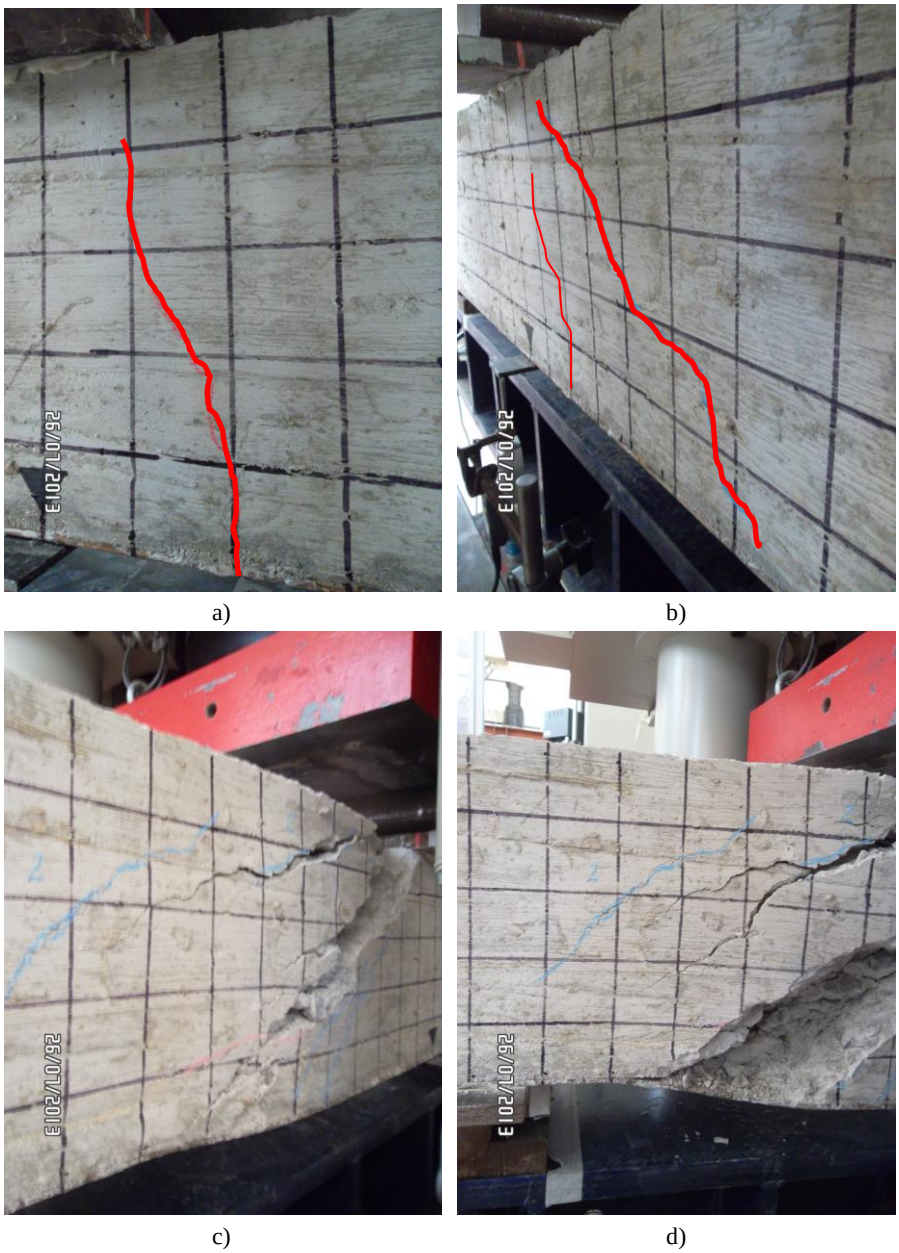

a) b)

c) d)

Figure 5.30. Specimen A2-2: a) vertical flexural crack; b) appearance of the diagonal cracking; c) developing of the main cracks; d) main diagonal crack causing the failure.

During the load history, the first flexural cracks begin to appear when the load reaches the value of 120 kN (Figure 5.30a) while the first diagonal shear cracks start to develop at a load of about 230 kN (Figure 5.30b) and continue growing during the whole test causing the failure (Figure 5.30c-d).

Specimens series "B"

Figure 5.31 shows the load-displacement curve of specimen B1 which has been tested so that the steel plate of the truss is subjected to compression. The specimen exhibited a brittle shear failure with a maximum load of 335.94 kN corresponding to a displacement of 9.17 mm. During the load history, the first flexural cracks appear at a load of about 100 kN (Figure 5.32a); then, corresponding to a load of 300 kN a crack appears and develops through the entire width of the beam in the face opposite to the steel plate (Figure 5.32b). The buckling of the latter can be clearly observed when the load reaches the value of 330 kN and continues developing during the subsequent phases of the test (Figure 5.32c-d).

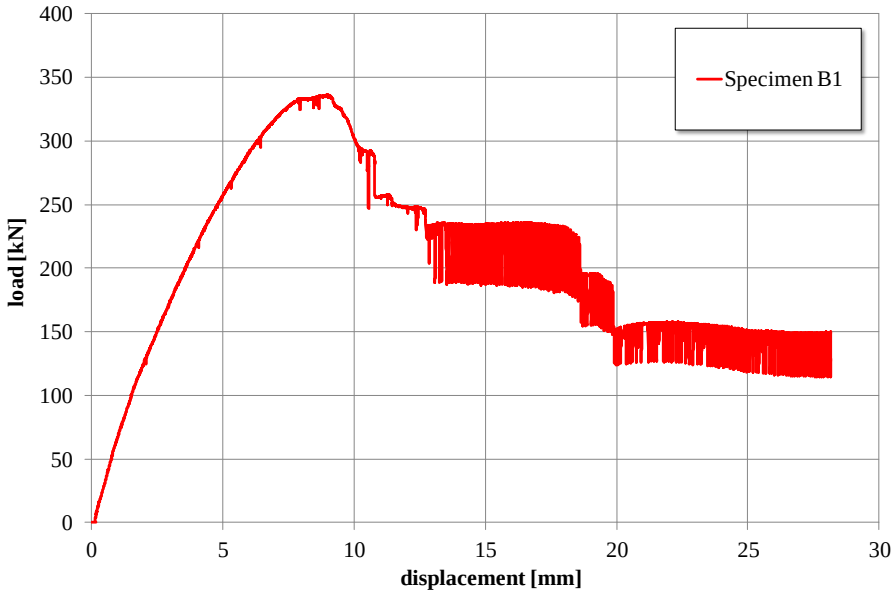

Figure 5.31. Load-displacement curve of specimen B1.

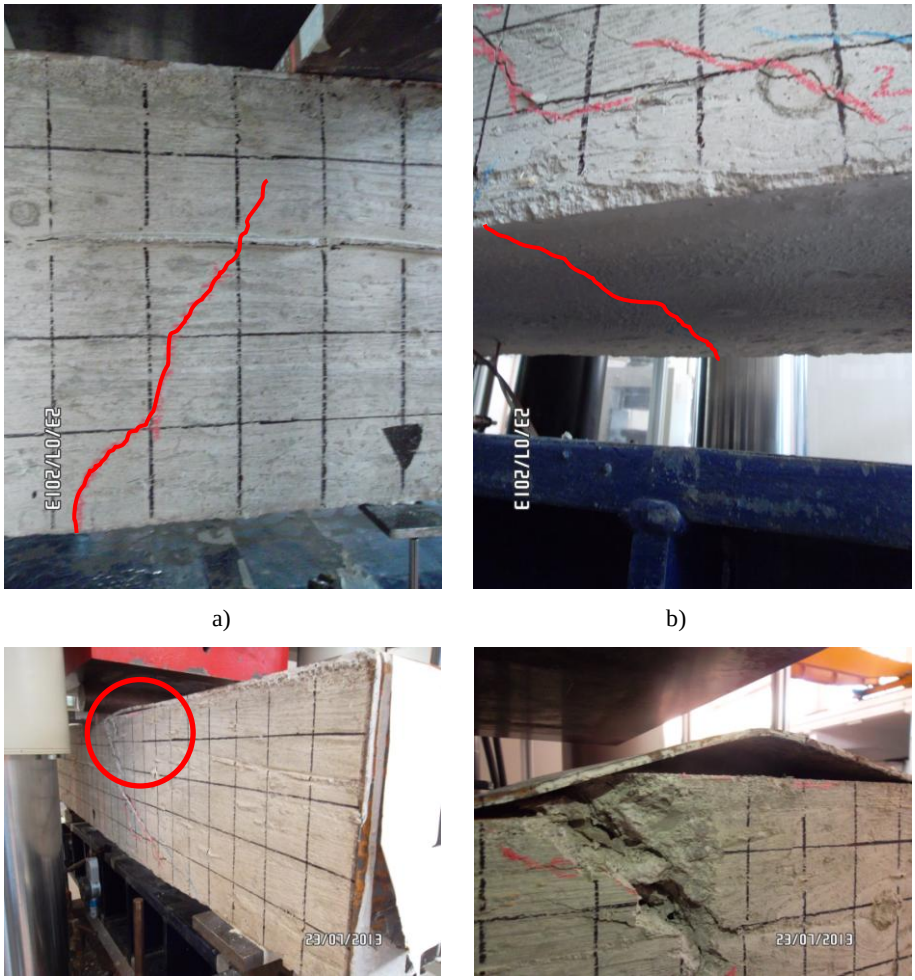

a) b)

c) d)

Figure 5.32. Specimen B1: a) flexural cracks; b) cracking of the face opposite to the steel plate; c) buckling of the compressed plate in the initial phase; d) buckling of the compressed plate at the end of the test.

Figure 5.33. Specimen B1: a) appearance of the diagonal cracking; b) growing of the diagonal shear crack; c) dowel mechanism; d) local crushing of the concrete at the support.

While the main diagonal shear crack is growing (Figure 5.33a-b), the dowel action, typical of a shear mechanism, due to the tensile bars constituting the upper chord of the steel truss, is clearly individuated (Figure

5.33c). Furthermore, a local crushing of the concrete corresponding to the lateral support is observed (Figure 5.33d).

Finally, Figure 5.34 shows the load-displacement curve of specimen B2. In this case the failure mode is not typically brittle, on the contrary, the specimen exhibited a more ductile behavior with a maximum load of 519.53 kN corresponding to a displacement of 8.99 mm.

The first flexural cracks appear at a load of about 190 kN (Figure 5.35a) while the first diagonal cracks at a load of 230 kN (Figure 5.35b). Furthermore, during the load history, in the phase immediately before the peak load, a crack develops through the entire width of the beam corresponding to the face of the specimen opposite to the steel plate (Figure 5.35c), as already observed for beam B1 having the same characteristics, and the local crushing of the concrete corresponding to the lateral support occurs.

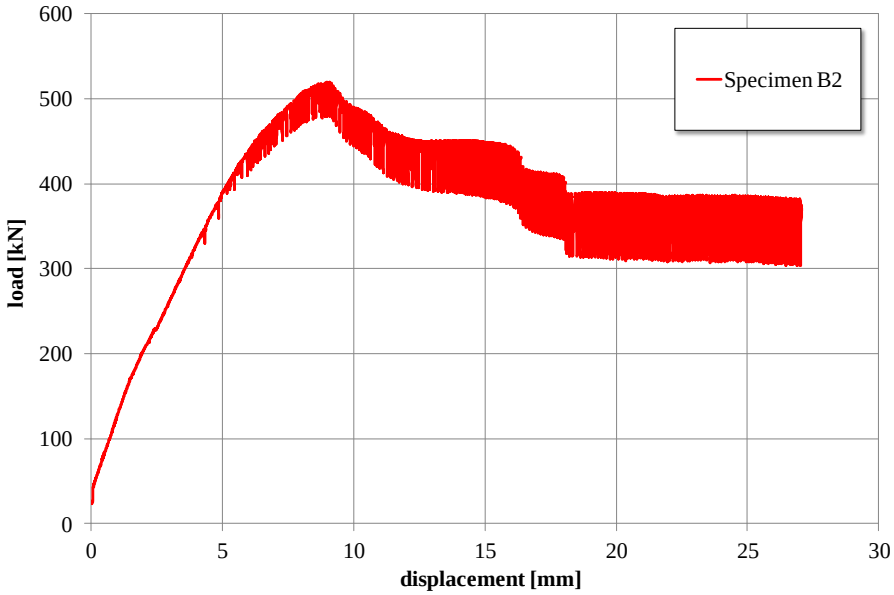

Figure 5.34. Load-displacement curve of specimen B2.

Then, also the separation of the steel plate from the block of concrete is recorded (Figure 5.36a) whit the progressive phenomenon of the buckling (Figure 5.36b-c) corresponding to the area of the steel plate within one mesh of the truss, denoting the effectiveness of the weldings between the diagonal bars and the plate (Figure 5.36d).

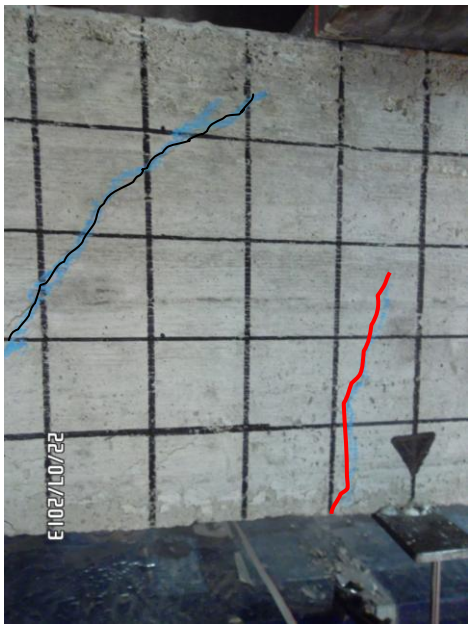

a)

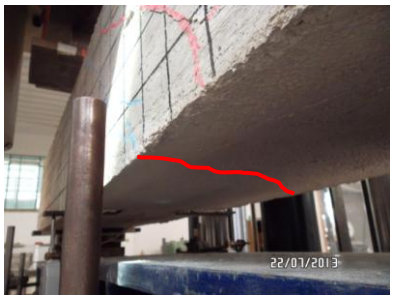

b) c)

Figure 5.35. Specimen B2: a) flexural cracks; b) diagonal cracking; c) cracking of the face opposite to the steel plate.

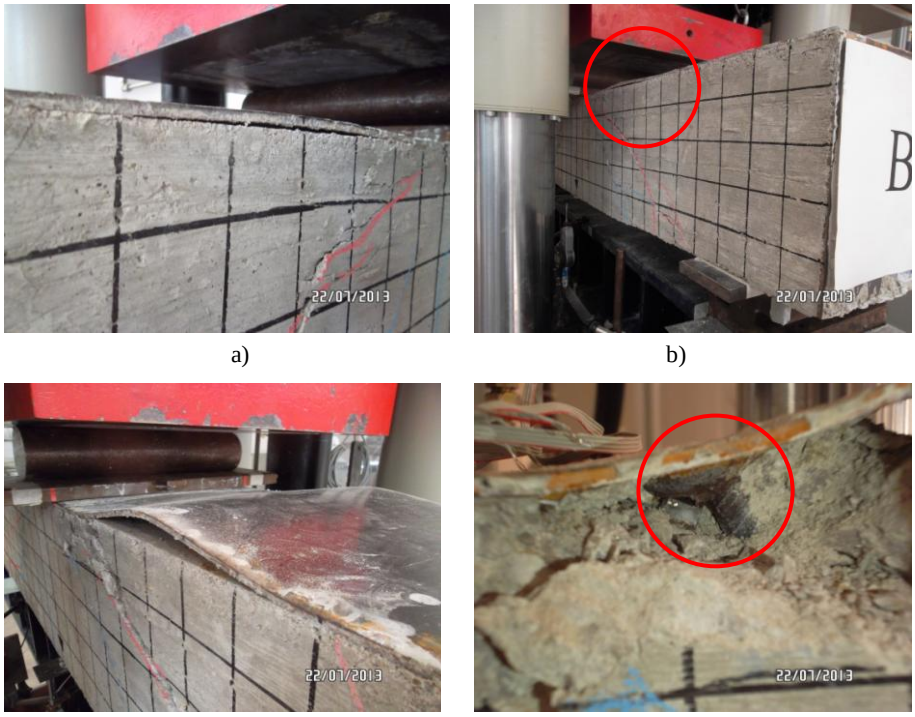

a) b)

c) d)

Figure 5.36. Specimen B2: a) separation of the steel plate from the concrete; buckling of the steel plate; c) top view of the buckling of the steel plate; d) detail of the welding of the web bar to the plate.

5.2.2 Strain gauges measurements

In the following graphs (Figures 5.37-5.40), the measurements recorded by the SG of specimens A1-2, A2-1, A2-2 and B1 are reported. It has to be noted that all curves are stopped corresponding to the strain gauge breakdown which occurred at a certain time of the test execution. In the same plots, the peak load achieved during the test is indicated; furthermore the vertical dashed lines remark the strain values corresponding to the yielding of the steel bars (ε_y = 2.7‰ for the diagonal rebars, ε_y = 2.6‰ for the upper chord bar and ε_y = 2.1‰ for the steel composing the plate - see Table 5.4).

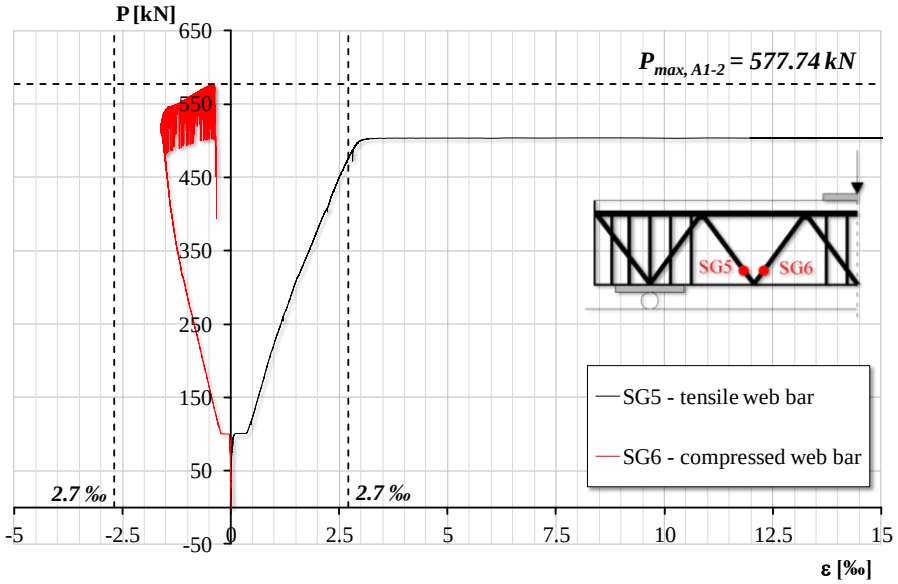

Figure 5.37. Strain gauge measurements of specimen A1-2.

It can be observed that, in all cases, the strain in the tensile diagonal rebars reaches the yielding value before the peak load of the test is achieved (Figures 5.37-5.40). Particularly, for specimens A2-2 and B1 the yielding of the diagonal tensile bar and the achievement of the maximum load occur almost simultaneously (see Figure 5.39 and Figure 5.40a). Concerning the compressed diagonal bars, SG9 and SG15 reach the yielding value (Figure 5.38a and Figure 5.40a) while SG6 and SG12 break before the yielding occurs (Figure 5.37 and Figure 5.39).

It is interesting to note that, for specimen A1-2, the beginning of the plastic deformations field in the load-displacement curve of Figure 5.25 corresponds, with a good approximation, to the moment in which the diagonal tensile bar yields exhibiting the horizontal branch in the load-strain curve of Figure 5.37. By comparing the two abovementioned curves (Figure 5.25 and Figure 5.37) and remembering that the concrete used while manufacturing the specimen was of "type 2" (good mechanical properties), it can be deduced that the ductile branch of the load-displacement plot, until

the peak, is due to the contribution of the yielding and, almost certainly, also the hardening of the steel constituting the diagonals of the truss. It has to be noted, in fact, that the strain gauge in the tensile web bar breaks before the achievement of the maximum load during the test. The quite good mechanical characteristics of the concrete constituting the specimen allow to delay the failure of the compressed strut so that the diagonals are able to let the beam developing a ductile global behavior before the peak load is reached. Then, the fragile loss of bearing capacity, immediately after the maximum load is achieved, corresponds to the incoming failure of the compressed concrete strut.

Conversely, the same mechanism does not occur in specimen A2-1: when the tensile web bar yields (Figure 5.38a), in the load-displacement plot there is not the development of a corresponding ductile branch (Figure 5.27).

In this regard, it is worth to remind that the concrete employed to manufacture the specimen is of "type 1" (poor mechanical properties) and, thus, it is reasonable to assume that the failure of the compressed concrete strut, which determines the sudden fragile decrease of the load, occurs before the steel diagonals are able to develop a ductile branch in the global response. At the end of the test a residual load of about 200 kN is recorded, due to the remaining contribution of the steel members in the bearing capacity.

The behavior of the analogous specimen, A2-2, can be interpreted in a similar way. By comparing the load-strain curves in Figure 5.39 with the load-displacement plot of Figure 5.29, it can be observed that, in this case, after the peak load value is reached, while the tensile diagonals are yielding, there is a very short horizontal branch not followed by a real fragile loss of bearing capacity as in specimen A2-1. On the contrary, before the residual resistance is established at about 200 kN, there is a progressive loss of load attributable to a more gradual failure of the compressed concrete strut with respect to the previous case. Such a slight difference could be due to the normal scatter in the results of experimental tests on specimens made up of heterogeneous materials.

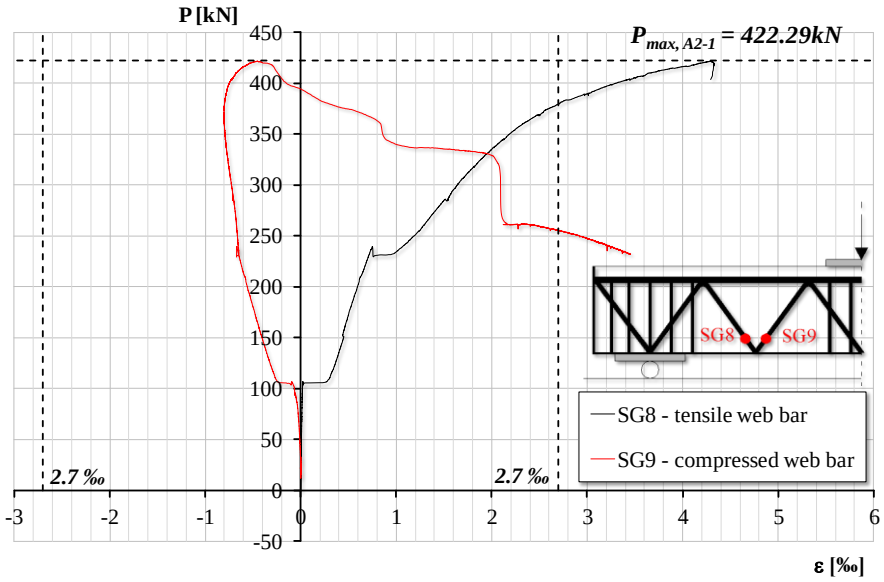

a)

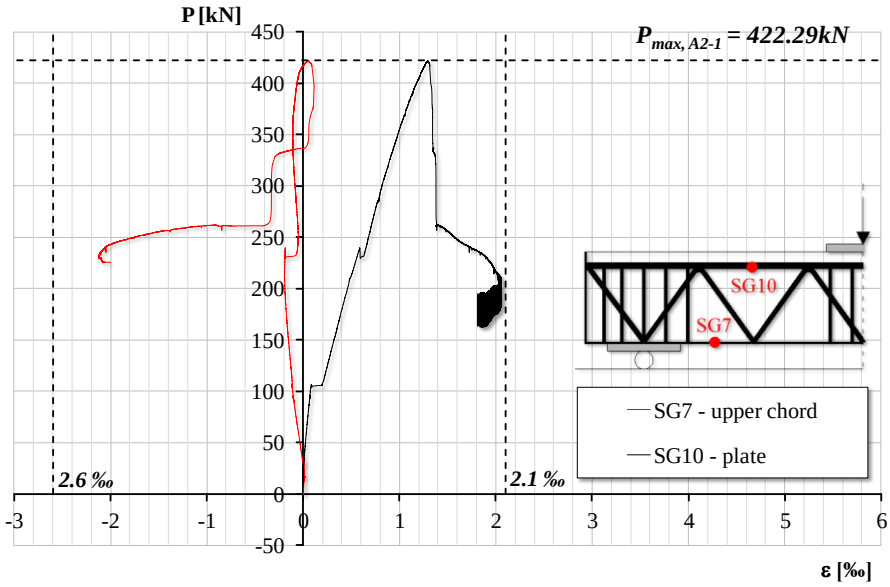

b)

Figure 5.38. Strain gauge measurements of specimen A2-1: a) SG8 and SG9; b) SG7 and SG10.

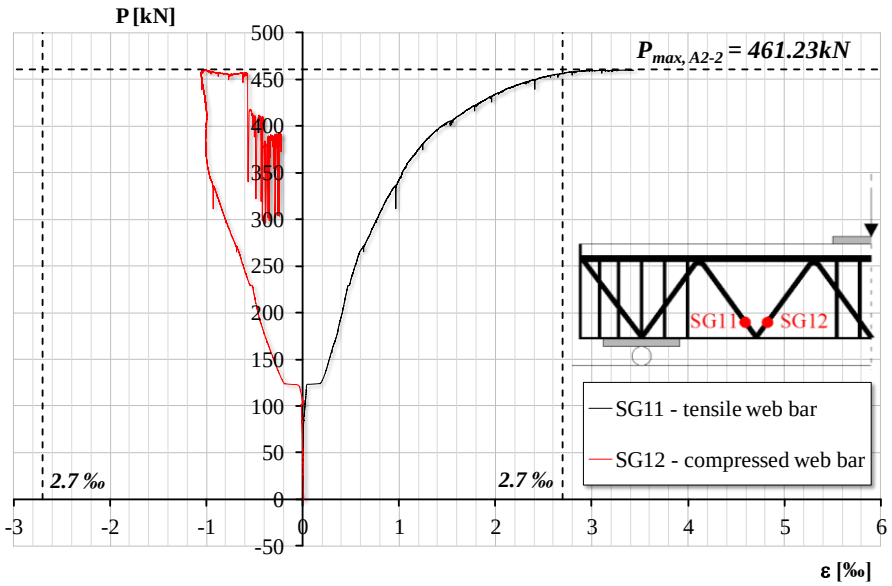

Figure 5.39. Strain gauge measurements of specimen A2-2.

The behavior of specimen B1 proves to be, actually, very similar to the latter two cases. In fact, also in this case, the diagonals yield when the maximum load is achieved (Figure 5.40a). The failure of the steel and the concrete can be considered almost simultaneous: no horizontal branch is able to develop in the global load-displacement curve (Figure 5.31) because the material constituting the beam does not have any characteristic able to delay the crushing of the compressed concrete strut with respect to the failure of the steel. It is worth to remember that, also in this case, the concrete employed to realize the specimen is of "type 1". As a matter of fact, for the case of specimen B2 (Figure 5.34), the behavior proves to be more ductile with respect to the analogous specimen B1. In this regard, it is interesting to note that the maximum load is very similar to the one obtained for specimen A1-2: these two beams are, in fact, equal each other, both for geometry and type of concrete ("type2"); they only differ for the load condition (negative and positive bending moment, respectively). Furthermore, it can be worth to note that the peak load achieved in the test is really close to the analytical load corresponding to the ultimate bending moment of the beam.

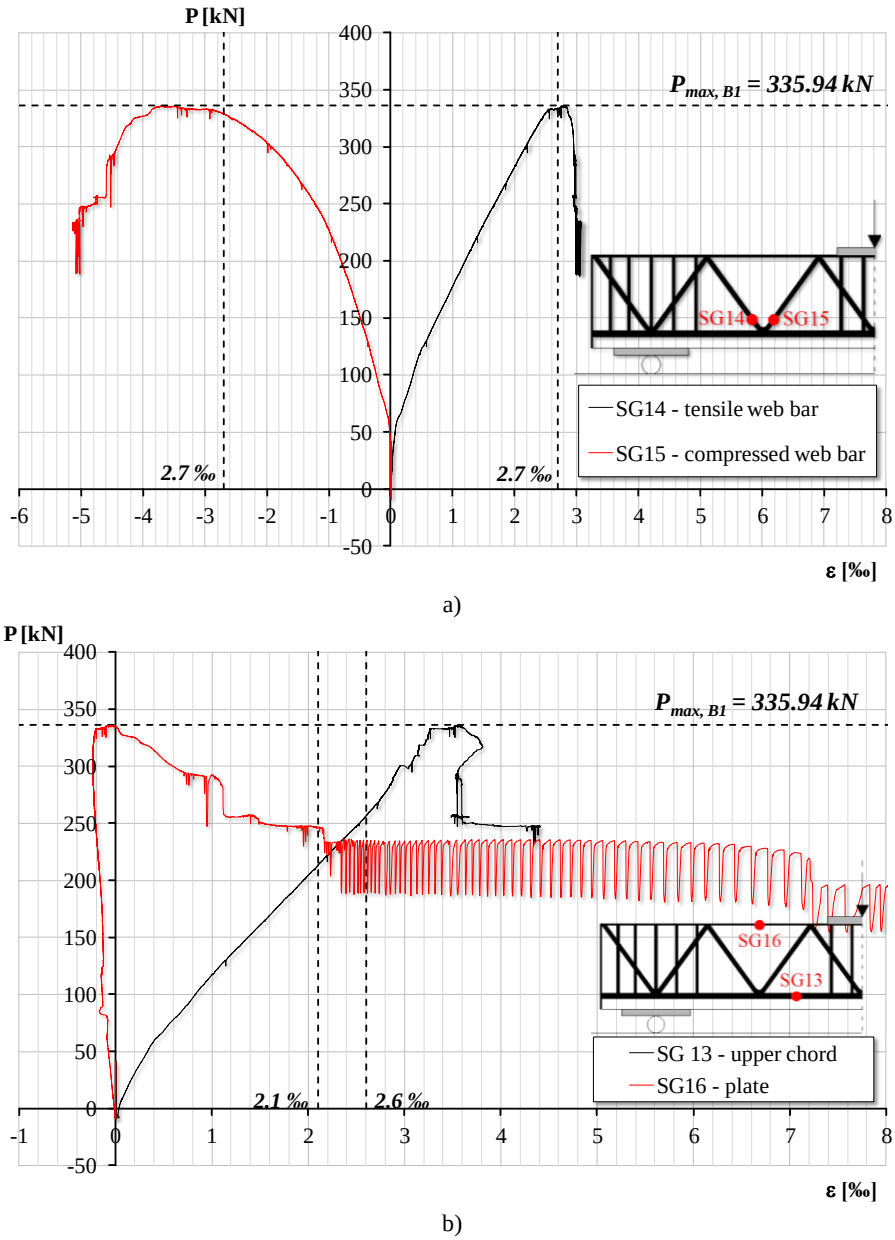

Figure 5.40. Strain gauge measurements of specimen B1: a) SG14 and SG15; b) SG13 and SG16.

Finally, the measurements recorded by the SG on the upper chord of the trusses show that, for specimen A2-1, subjected to positive bending moment, the steel remains elastic during the whole test (Figure 5.38b), while, for specimen B1, subjected to negative bending moment, it starts to yield before the peak load is reached and then highly exceeds the yielding value until about 4.5‰ (Figure 5.40b). Finally, as regards the steel plate, the area where SG10 is placed on specimen A2-1 remains elastic until the peak load is reached achieving the yielding value only when the load decreases till 200 kN in the post-peak branch of the load-displacement curve (Figure 5.38b). As regards the area where SG16 is collocated on specimen B1, it reaches and highly exceeds the yielding value of 2.1‰ (Figure 5.40b). In this regard, it has to be noted that positive strain values are recorded even if the plate is subjected to compression because of the buckling.

5.2.3 Some remarks on the experimental data

In this section some final remarks on the experimental results are reported dealing with the failure mode as well as the shear strength and stress transfer mechanisms. Furthermore, a comparison between the configuration of each specimen at the end of the test and the scheme of the truss geometry and the collocation of the measurement technology is provided aiming at a deeper understanding of the relationship between the beam typology and the corresponding shear response (Figures 5.41-5.45).

Table 5.6 summarizes the maximum loads obtained in each test.

Table 5.6. Synoptic frame of the peak loads.

ID	***P_{max} [kN]***
A1-1	-
A1-2	*577.74*
A2-1	*422.29*
A2-2	*461.26*
B1	*335.94*
B2	*519.53*

As regards all specimens subjected to positive bending moment (A1-2, A2-1 and A2-2), the response to the load history is characterized by the following events:

- before the peak load is achieved, sub-vertical flexural cracks develop on the bottom of the midspan of the beam;
- subsequently, the first diagonal shear cracks start to develop in the direction of the compressed concrete strut (see Figures 5.41-5.43);
- the main diagonal shear crack grows while the sub-vertical flexural cracks remain almost stable (see Figures 5.41-5.43);
- when the maximum compressive strength of the concrete is reached, a brittle shear failure with sudden decrease of the resistance occurs;
- after the achievement of the maximum load, the load-displacement curve exhibits a sub-horizontal branch almost corresponding to the residual resistance due to the steel members;
- the bottom steel plate locally separates from the block of concrete.

Concerning the two specimens subjected to negative bending moment (B1 and B2), the following remarks can be highlighted:

- the behavior of the beam denotes a brittle failure in the case of specimen B1 while it is more ductile in the case of specimen B2 and, in fact, Figures 5.44 and 5.45 show how beam B1 is more damaged than beam B2;
- the flexural and the shear cracks appear and develop as already described for the specimens subjected to positive bending moment;
- other cracks develop through the entire width of the beam in the face opposite to the steel plate;
- a local crushing of the concrete corresponding to the lateral supports is observed;
- the steel plate separates from the concrete block and its buckling occurs in the area comprised within the mesh of the truss (see Figures 5.44 and 5.45), proving the effectiveness of the weldings between the diagonal bars and the steel plate.

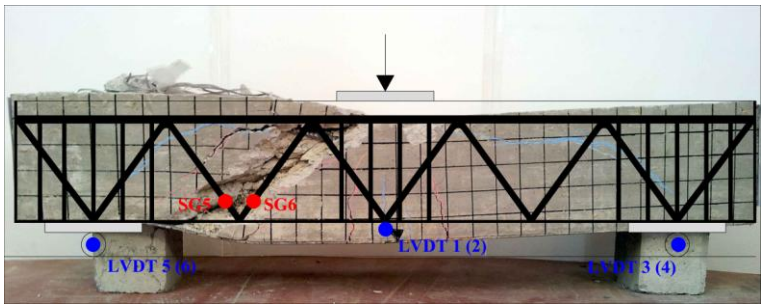

Figure 5.41. Specimen A1-2 at the end of the test with the scheme of the truss and the measurement technology.

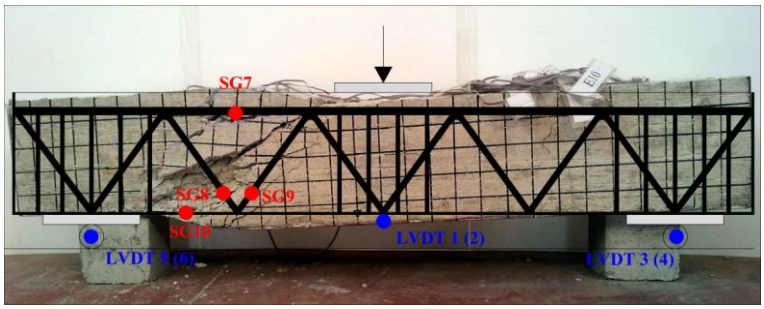

Figure 5.42. Specimen A2-1 at the end of the test with the scheme of the truss and the measurement technology.

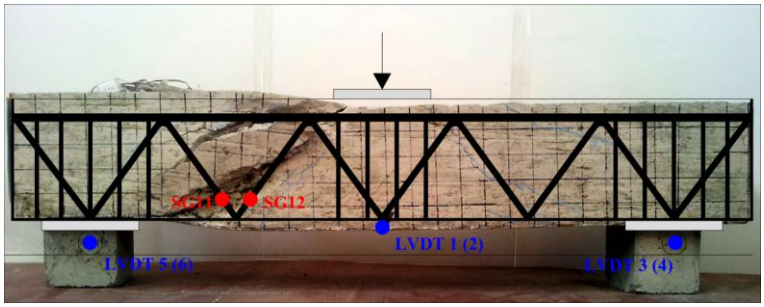

Figure 5.43. Specimen A2-2 at the end of the test with the scheme of the truss and the measurement technology.

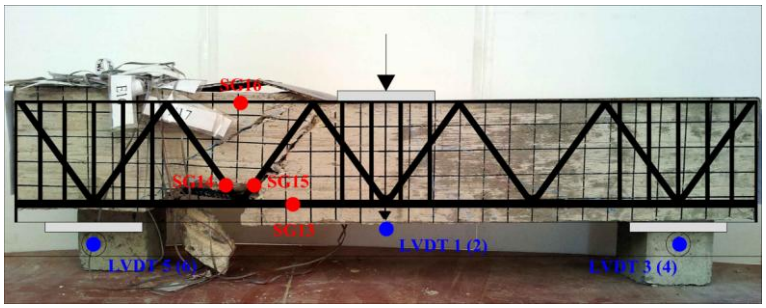

Figure 5.44. Specimen B1 at the end of the test with the scheme of the truss and the measurement technology.

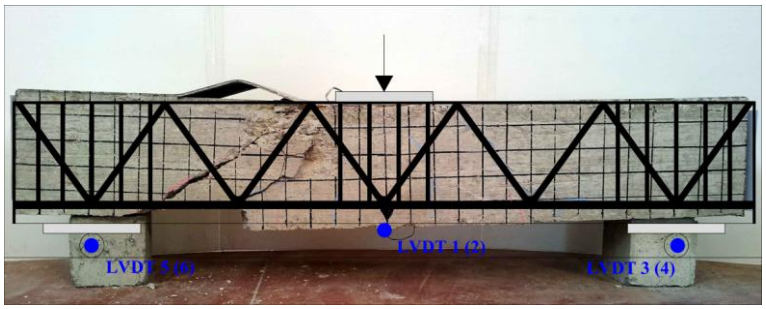

Figure 5.45. Specimen B2 at the end of the test with the scheme of the truss and the measurement technology.

5.3 Interpretation of the experimental results

The obtained experimental data described in the previous sections are herein reproduced by means of an accurate tridimensional FE model. Particularly, the model is representative of the beams belonging to series "A", with tensile bottom plate and in the presence of the added inferior rebars, and to series "B", subjected to negative bending moment.

Subsequently, the experimental data are also interpreted employing some of the expressions for the evaluation of the shear strength existing in the literature and concerning both classical R.C. structures and HSTCBs, previously reported in Chapter 2, with the aim of approximately assess the

degree of accuracy that the existing models are able to provide in the prediction of the shear resistance of the tested typology of HSTCB.

5.3.1 Numerical finite element model

The FE analysis has the aim of simulating the experimental three-point bending tests in order to investigate the shear strength mechanisms occurring in the typology of beam studied in the present thesis. The models are representative of both the beams subjected to positive and negative bending moment, that is beams belonging to series "A" and series "B" respectively, and it is worth to note that they all have the main characteristic features described in the follow.

As already done while developing the models for the push-out tests discussed in Chapter 4, also in the current case the FE models take into account the actual geometry of the specimens, the material nonlinearity and the interaction at the interface between steel and concrete. As a consequence, the steel members, generated by means of sweep and extrusion commands, have been subtracted from the block of concrete obtaining, once again, a volume with empty spaces corresponding to the presence of the rebars. The stirrups in the midspan of the beam and at the lateral supports have been neglected. As regards the mesh, the truss and the bottom steel plate have been discretized by means of linear brick elements utilizing a structured meshing technique while the volume of concrete by means of linear tetrahedra using a free meshing technique (Figure 5.46a-b). In order to improve the convergence of the analyses, a *stabilization parameter* has been introduced within the definition of the contact between the concrete and the steel plate. Moreover, the implementation of a *damage variable* governing the loss of stiffness in the softening branch of the constitutive behavior of the compressed concrete, allows to obtain a numerical load-displacement curve whose post-peak trend fits very well the experimental results.

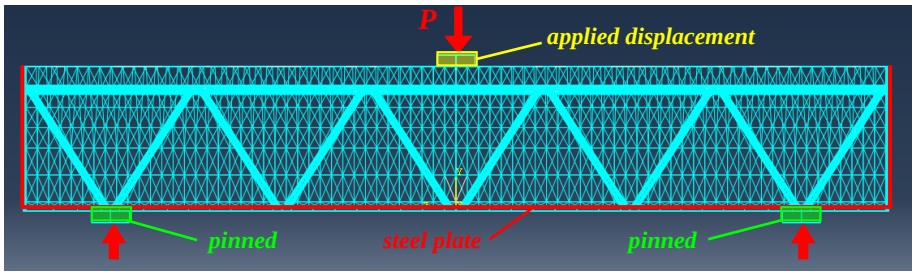

a)

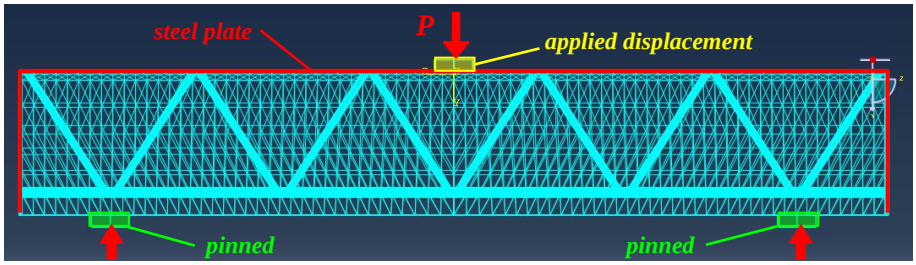

b)

Figure 5.46. Mesh of the elements and boundary conditions: a) beams series "A"; b) beams series "B".

As regards the boundary conditions, the supports have been constrained by means of hinges and a displacement has been imposed on the loading plate (Figure 5.46). Afterwards, the displacement at the midspan of the beam in the direction of the load, *P*, has been evaluated.

In Figure 5.47 the qualitative outcome of the FE simulation concerning the steel truss and the block of concrete is represented for the case of beam subjected to positive bending moment. Particularly, Figure 5.47a shows the qualitative deformed shape of the basic steel truss at the end of the analysis while Figure 5.47b qualitatively represents the distribution of the minimum principal stresses in the concrete corresponding to the achievement of the maximum load. In such a plot, the "arch effect" mechanism is clearly identifiable and it is also interesting to observe the slope of the compressed concrete strut with respect to the diagonal rebars of the truss. Figure 5.48a-b represents the same output dealing with the case of beam subjected to negative bending moment, with compressed steel plate and tensile upper chord.

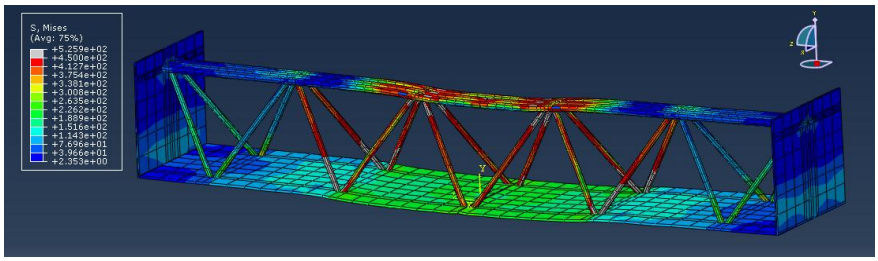

a)

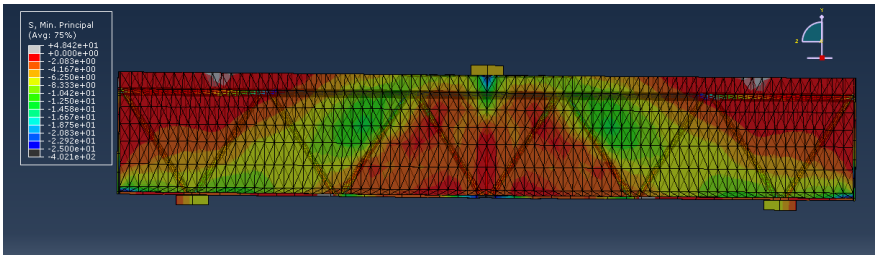

b)

Figure 5.47. Typical qualitative output for positive bending moment simulation: a) deformed shape of the steel truss; b) distribution of the minimum principal stresses in the concrete.

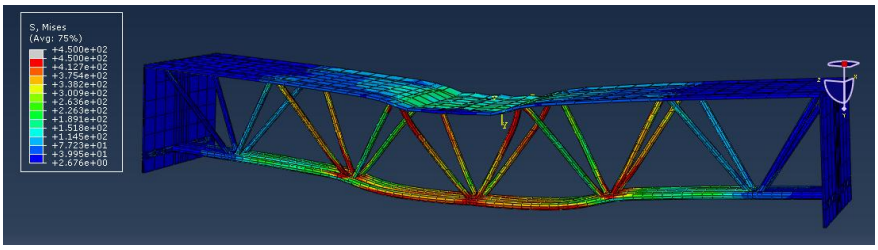

a)

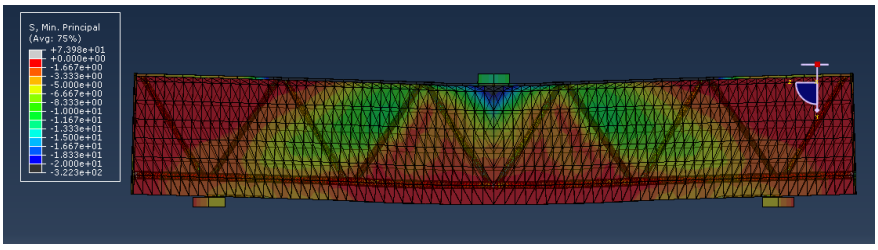

b)

Figure 5.48. Typical qualitative output for negative bending moment simulation: a) deformed shape of the steel truss; b) distribution of the minimum principal stresses in the concrete.

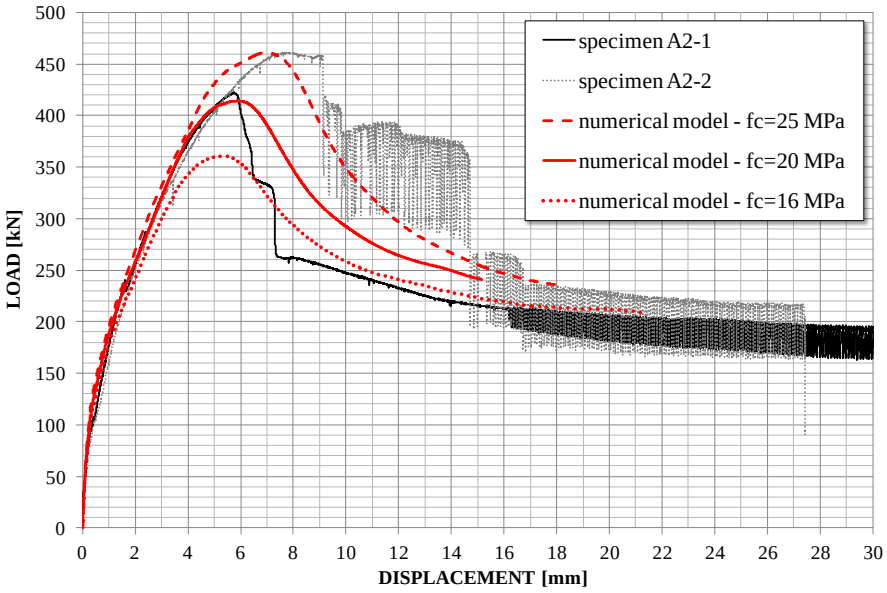

Figure 5.49. Numerical vs. experimental results for beams of series "A2".

The accuracy of the FE models is evaluated by comparing the numerical results with those experimentally obtained for the specimens of both series "A" and "B". The numerical simulations are developed for a range of variation of the compressive strength of concrete between 16 and 25 MPa with the aim of taking into account the uncertainties in the actual resistance of the concrete employed while manufacturing the specimens. Particularly, for both series, analyses assuming f_c equal to 16, 20 and 25 MPa are developed. In the follow, the details of the FE results are showed, first, for beams of series "A", and, then, for beams of series "B".

Concerning series "A", the numerical vs. experimental comparison is showed in Figure 5.49 in terms of load-displacement curve. Particularly, the comparison refers to specimens A2-1 and A2-2 (named as series "A2"). The numerical curves accurately grasp the actual experimental behavior of the beams both in the initial and damaged stiffness until the peak load is reached and also the following softening branch is quite precisely predicted.

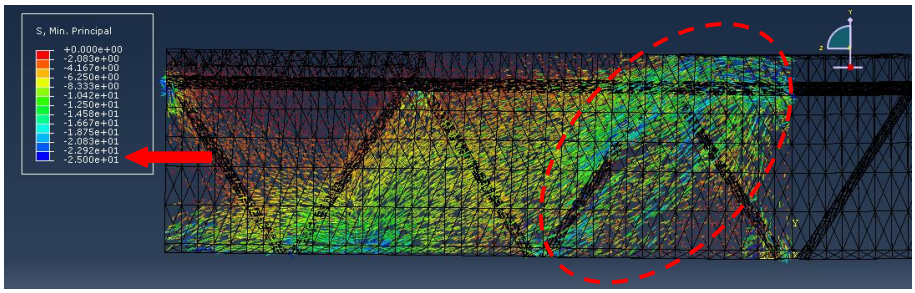

Figure 5.50. FE model series "A2": direction of the compressive principle stresses in the concrete.

The analysis of the FE results allows to individuate the direction of the compressive principle stresses in the concrete: Figure 5.50 shows the direction and the magnitude of such stresses corresponding to the achievement of the peak load during the analysis which simulates a series "A2" beam with an implemented value of the concrete compressive strength equal to 25 MPa. In the plot, the red dashed sign highlights the main directions where the minimum principal stresses are equal to the compressive concrete strength, also allowing to individuate where the damage variable is going to exhibit the maximum value. However, continuing to analyze the FE output, it is also possible to assess the depth and the width of the concrete strut by means of the aforesaid compressed damage variable (Figure 5.51) and associate such parameter with the other one able to predict the crack pattern evolution. In this regard, since the constitutive behavior of the concrete is implemented by means of the Concrete Damaged Plasticity Model (widely described in Chapter 4) which is not based on the smeared crack approach, the crack directions are identifiable through the direction orthogonal to the maximum principal plastic strains (Figure 5.52). With the aim of describing the crack pattern evolution during the numerical simulation of the load history, the direction and magnitude of the maximum inelastic strains are plotted in correspondence of four different phases of the load-displacement curve, represented in the schematic miniatures of Figure 5.52. Particularly, Figure 5.52a represents the cracking of the beam in a intermediate configuration

between the entering of the concrete in the plastic field of its constitutive compressive behavior and the achievement of the maximum load during the analysis (*phase "a"*). Similarly, Figure 5.52b represents the crack pattern corresponding to the peak load (*phase "b"*); then Figure 5.52c shows the evolution of the diagonal cracks in an intermediate phase between the peak and the end of the analysis (*phase "c"*) and, finally, Figure 5.52d represents the cracks configuration at the end of the simulation (*phase "d"*).

By comparing the outcome of the FE model showed from Figure 5.50 to Figure 5.52, it is possible to observe that the compressed strut along which the main diagonal shear crack is developing, causing the failure, is in the direction of the compressed web rebar. On the other hand, the crack pattern evolution shows that the first fractures which develop are the sub-vertical flexural ones (*phase "a"*); then cracks start to appear also in the diagonal direction (*phase "b"*) evolving much more then the first vertical ones (*phase "c"*) till the end of the analysis when other new cracks can be observed further then the diagonal direction, having a quite restrained width.

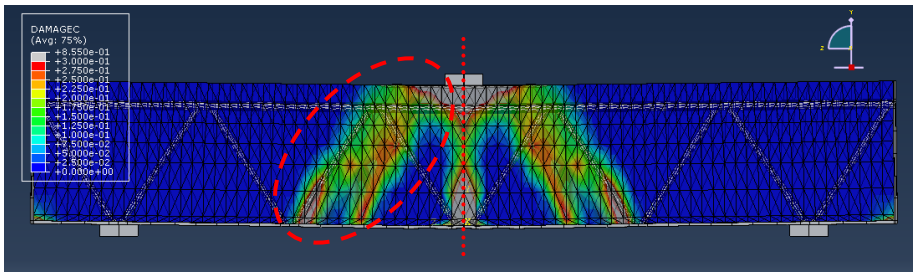

a)

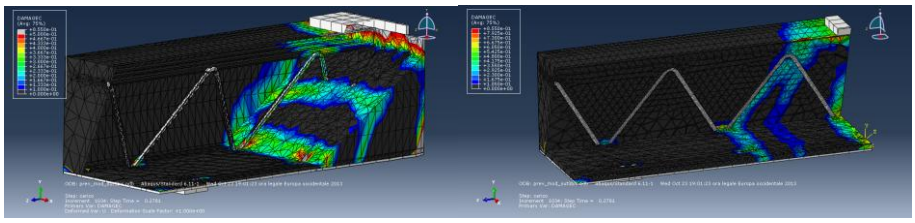

b)

Figure 5.51. Damage variable model series "A2": a) frontal view; b) axonometric cut views.

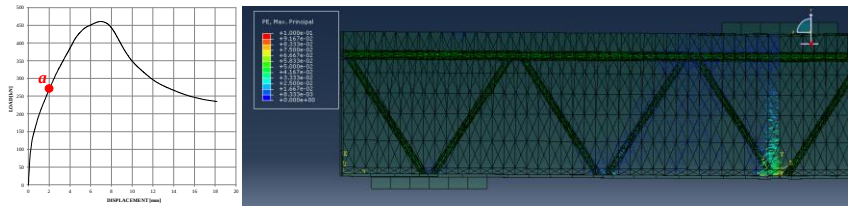

a)

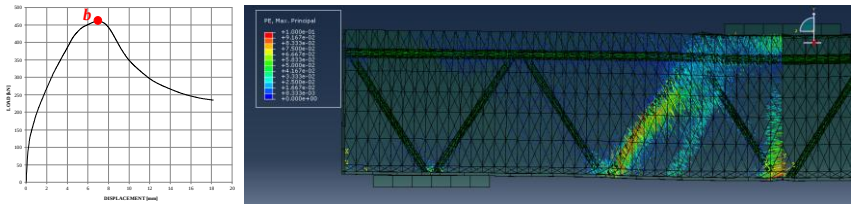

b)

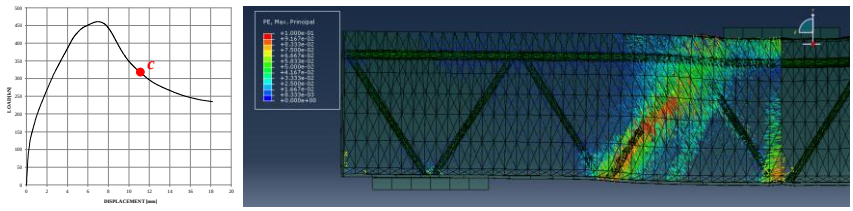

c)

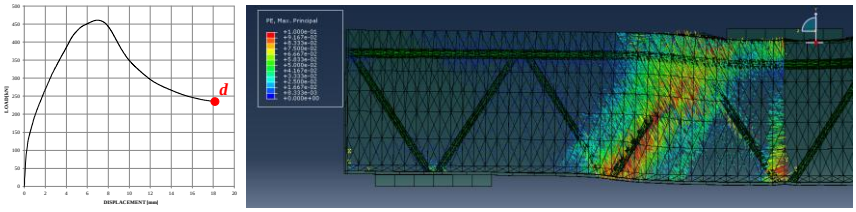

d)

Figure 5.52. Crack pattern: a) before the peak load; b) corresponding to the peak load; c) in the softening branch; d) at the end of the analysis.

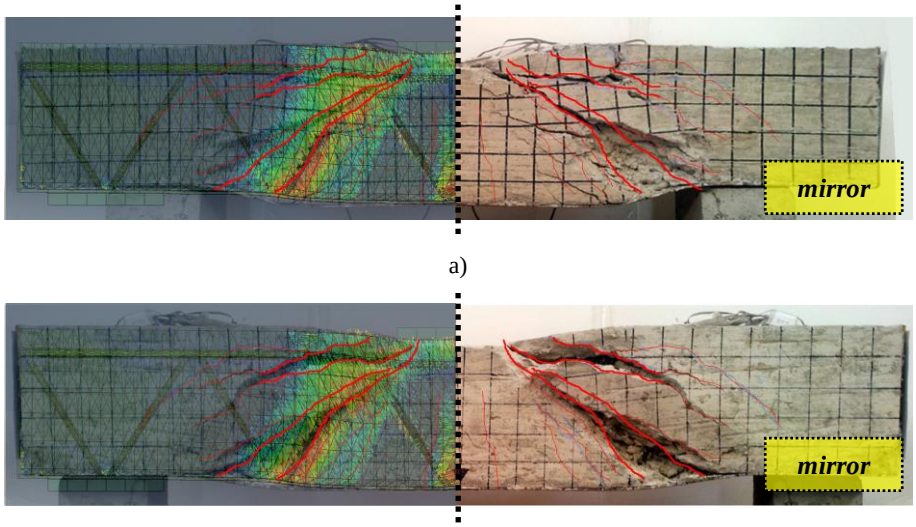

Figure 5.53. Qualitative comparison between crack pattern at the end of the analysis vs. end of the test: a) specimen A2-1; b) specimen A2-2.

The qualitative comparison between the numerical results and the configuration of the real specimens after cracking, at the end of the tests, shows the accuracy of the model in predicting the crack pattern in this typology of HSTCB. Such a comparison is shown in Figure 5.53. Particularly, Figure 5.53a concerns specimen A2-1 while Figure 5.53b deals with specimen A2-2. In those illustrations the configuration of the beam at the end of the experimental test, with the cracks put into evidence, is reported on the right as a mirror image of the main crack pattern, while, on the left, the picture of the aforesaid crack pattern experimentally observed is compared with the direction of the maximum principal strains obtained from the FE model, just showed in Figure 5.52d.

For the case of the beams type "B", the model proves to be quite accurate in catching the resistance of the structural system with reference to the considered range of values of the compressive concrete strength. Figure 5.54 shows the comparison between the load-displacement curves experimentally obtained and those resulting from the FE analyses. As regards the stiffness, it is worth to note that, for specimen B1, such a low value, that is not

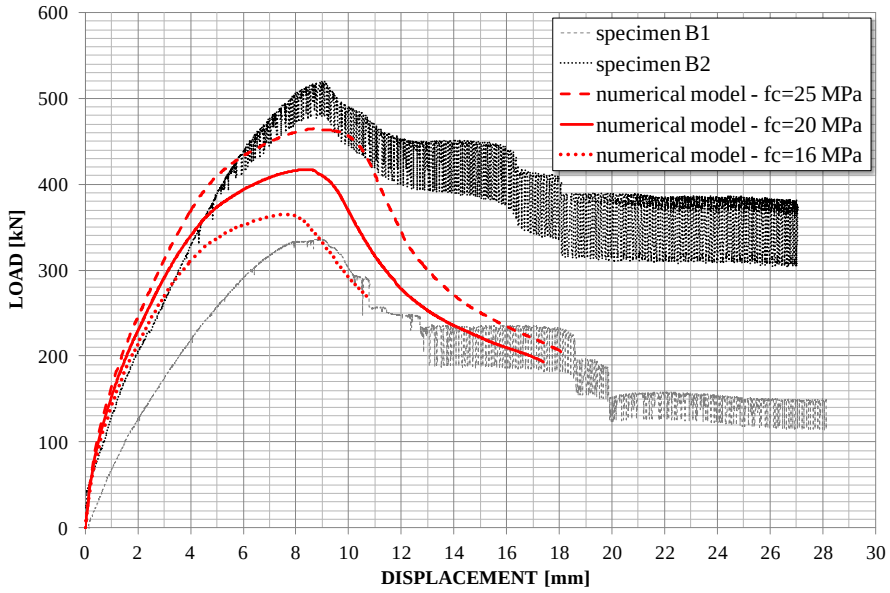

Figure 5.54. Numerical vs. experimental results for beams of series "B".

numerically grasped, can be attributed to the significative crushing of the concrete at the lateral supports occurring during the test execution. Figure 5.55 shows the direction and the magnitude of the compressive principle stresses in the concrete corresponding to the achievement of the peak load during the analysis which simulates a series "B" beam with an implemented value of the concrete compressive strength equal to 25 MPa. To such a distribution of compressive stresses, it corresponds the evolution of the damage variable showed in Figure 5.56 which allows to visualize the compressed concrete strut involved in the shear mechanism. As regards the prediction of the crack pattern evolution, the FE model provides the direction and magnitude of the maximum inelastic strains which are orthogonal to the fractures. As already illustrated for the model of a series "A" beam, Figure 5.57a-d shows the crack pattern in the aforementioned four phases identifiable along the load-displacement numerical curve. Figure 5.57a shows how the cracking of the beam in *phase "a"* is just characterized by the first sub-vertical flexural cracks. At the peak load (*phase "b"*), the

fractures prove to extend to the diagonal direction corresponding to the compressed web rebar, as shown in Figure 5.57b. After the peak load, that is in *phase "c"*, the crack pattern grows mainly in terms of fracture amplitude but it is possible to observe that it also starts to extend till the second mesh of the truss (Figure 5.57c). The increasing length and depth of the cracks is observed until the end of the analysis is reached (*phase "d"*). Such final configuration is shown Figure 5.57d.

The visualization of the chromatic map of the maximum plastic strains before the peak load also allows to individuate the crack which forms on the inferior face of the beam crossing the entire width. Figure 5.58a shows a frontal view of such chromatic map, while in Figure 5.58b the corresponding axonometric view on the right allows to visualize the inferior crack which can be compared with the fracture observed during the experimental test shown in the same figure on the left.

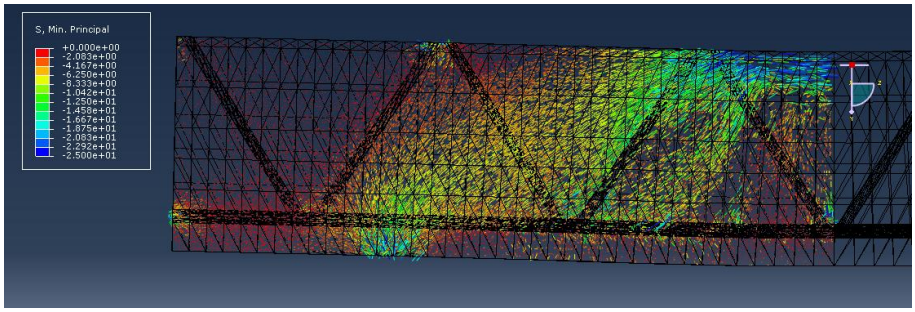

Figure 5.55. FE model series "B": direction of the compressive principle stresses in the concrete.

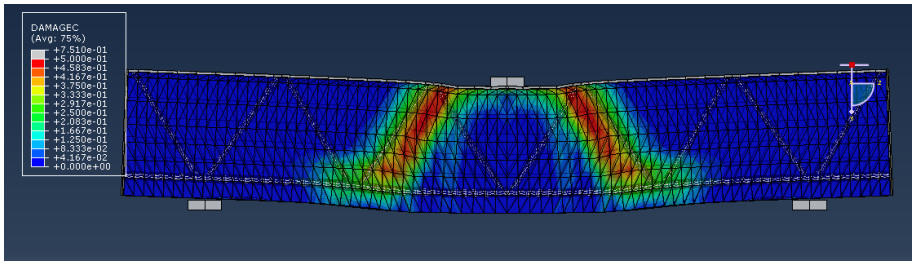

Figure 5.56. Damage variable model series "B".

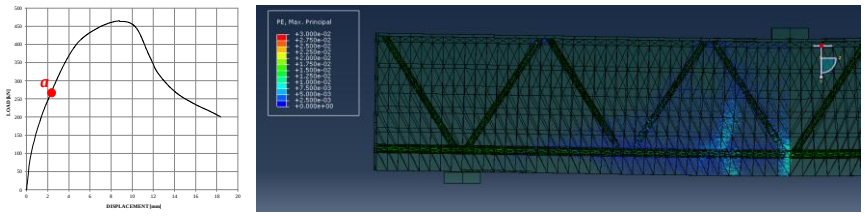

a)

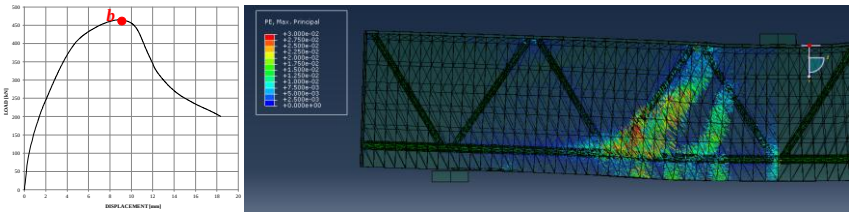

b)

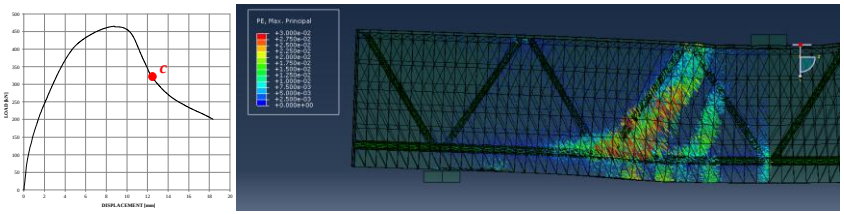

c)

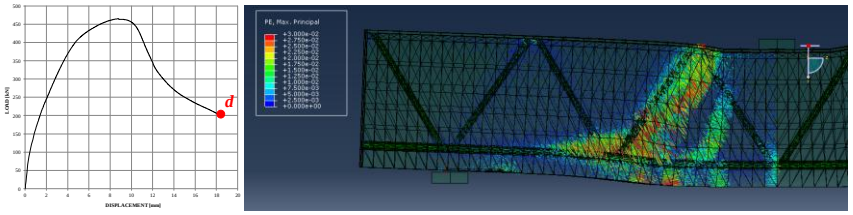

d)

Figure 5.57. Crack pattern: a) before the peak load; b) corresponding to the peak load; c) in the softening branch; d) at the end of the analysis.

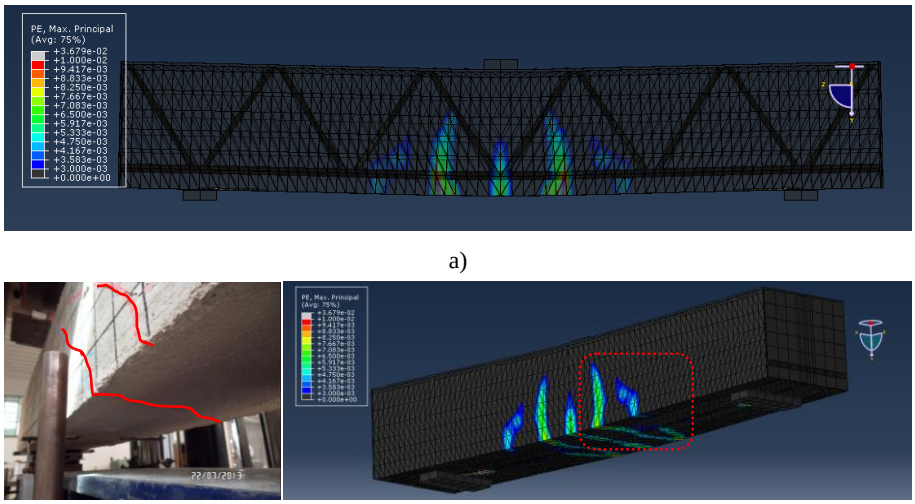

a)

b)

Figure 5.58. Chromatic map of the maximum plastic strains before the peak load: a) frontal view; b) axonometric view vs. experimental evidence.

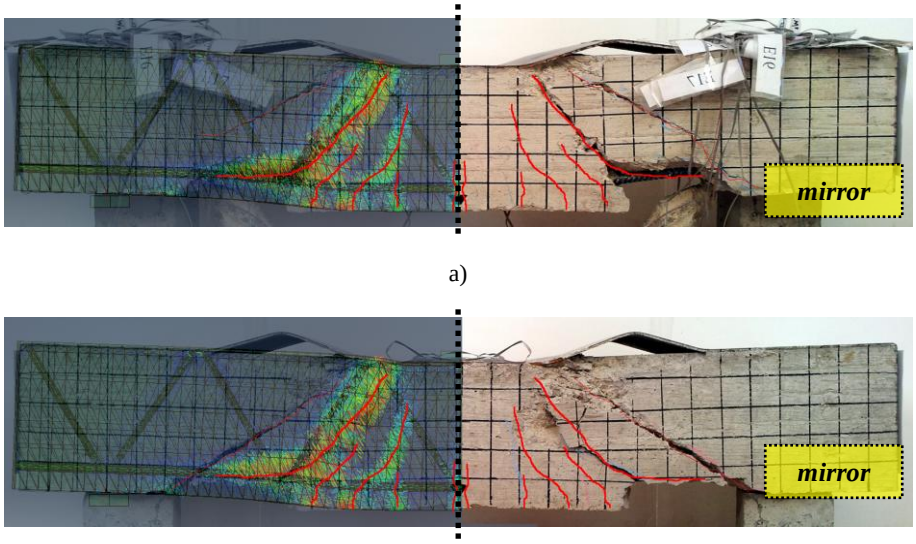

a)

b)

Figure 5.59. Qualitative comparison between crack pattern at the end of the analysis vs. end of the test: a) specimen B1; b) specimen B2.

Finally, the qualitative comparison between the numerical results and the configuration of the real specimens after cracking, at the end of the tests, is showed in Figure 5.59a for specimen B1 and Figure 5.59b for specimen B2. Also in this case, the configuration of the beam at the end of the test, with the cracks put into evidence, is reported on the right as a mirror image of the main crack pattern, while, on the left, the picture of the aforesaid crack pattern experimentally observed is compared with the direction of the maximum principal strains already showed in Figure 5.57d.

The numerical vs. experimental comparison for both specimens of series "A" and "B" proves to be good enough to support the formulation of an analytical model able to interpret the mechanical response of the beam. Before presenting the aforementioned analytical model, the expressions for the assessment of the shear strength available in the literature are employed and the results are shown in the following section.

5.3.2 Analytical expressions for the shear resistance

The experimental data are interpreted employing the expressions for the evaluation of the shear resistance already reported in Chapter 2 and classically conceived for R.C. structures. Particularly, as regards the strut-and-tie models, observing that the EC2-05 and the DM-08 models only differ for the calculation of ν, in the follow, in order to employ the expressions of V_R to interpret the experimental results, it has been chosen to refer only to one of them and, particularly, to DM-08 assuming $\nu = 0.5$.

Table 5.7 shows the ratios between the theoretical value of P_{max} calculated with the abovementioned analytical expressions with respect to the experimental values for each specimen. As it can be observed, the additive models generally underestimate the experimental result of about 20 to 35% with the exception of the analytical model proposed by Amadio et al. 2012 which provides a maximum theoretical load 9% lower than the experimental ones, showing a quite contained dispersion of the theoretical values around their average. A similar observation can be made concerning the truss model with variable strut inclination (DM-08), which provides a

better average prevision of the maximum shear resistance 7.5% lower than the experimental data with a coefficient of variation, CV_r, equal to 0.185.

Table 5.7. P_{the}/P_{exp} ratios.

	EC2-92	DM-96	ACI 318-08	CAN CSA-04	Amadio et al. 2010	Amadio et al. 2012	DM-08
A1-1	-	-	-	-	-	-	-
A1-2	0.719	0.684	0.677	0.565	0.643	0.790	0.772
A2-1	0.860	0.824	0.873	0.709	0.813	0.906	1.033
A2-2	0.787	0.754	0.799	0.649	0.745	0.830	0.946
B1	0.954	0.907	0.950	0.781	0.978	1.139	1.138
B2	0.692	0.652	0.648	0.539	0.675	0.878	0.736
Avg.	***0.802***	***0.764***	***0.790***	***0.649***	***0.771***	***0.909***	***0.925***
CVr	***0.133***	***0.136***	***0.162***	***0.155***	***0.173***	***0.150***	***0.185***

5.4 Proposed analytical model

Considering the FE analysis results, a further interpretation of the shear mechanism occurring in the tested HSTCB typology is formulated by means of analytical expressions derived from a mechanical model based on the two classical shear strength contributions of "arch" and "beam" effect, which also takes into account the peculiarities of the tested beams. A similar analytical approach has been already employed by some authors while studying the shear resistance of R.C. beams with stirrups made up of both lightweight concrete (Campione 2013) and high-strength concrete (Campione et al. 2013a; Campione et al. 2013b).

The model presents an additive formulation in which the HSTCB can be regarded as a R.C. beam with the addition of a steel plate and stirrups inclined in two directions, which are supposed to transfer the stresses from the plate to the concrete. The model differs from the classical additive formulations for R.C. beams because of the way the contribution of concrete is calculated and because it takes into account the contribution of the diagonal web bars both in the direction of the shear force and in the direction of the longitudinal traction. Moreover, in this latter direction, also the contribution of the steel plate is taken into account.

In order to calculate the contribution of the concrete, V_c, in the bearing capacity in shear of the HSTCB, the two classical shear mechanisms occurring in a R.C. beam are considered: the beam action and the arch effect.

According to Bažant and Kim (1984), in fact, the shear strength of a longitudinally reinforced beam can be calculated as the sum of those two resistance contributions by imposing the equilibrium conditions of a portion of the beam between the support and the loaded section corresponding to the shear span *a*, according to the scheme represented in Figure 5.60. With reference to the specific structural typology and considering the case in which the HSTCB is subjected to positive bending moment (that is tensile bottom steel plate), the compressive force *C* is due to the contribution of both the compressed concrete, C_c, and the upper chord of the truss, C_{up}. Similarly, the tensile force *T* is considered as the sum of three different contributions provided, respectively, by the bottom steel plate (T_p), the added inferior reinforcing bars (T_b) and the diagonal tensile web rebars (T_w). As a consequence, the total area of the tensile reinforcement, A_s, is the sum of the area of the bottom plate, $A_{s,p}$, and the area of the cross-section of all inferior rebars, that is $n_b A_{s,b}$, being n_b the number of the added reinforcement.

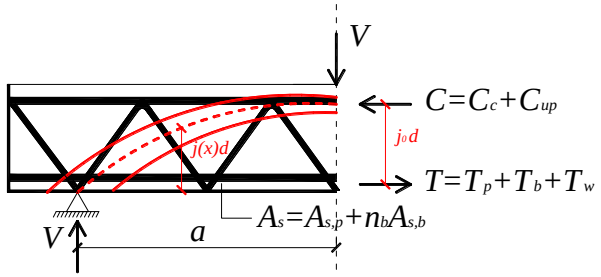

Figure 5.60. Beam and arch effects in the shear span of the HSTCB.

With reference to Figure 5.60, for the equilibrium of every given cross-section, the bending moment, M_c, and the shear force, V_c, can be related to the longitudinal tensile force, *T*, and to the internal lever arm, *j(x)d*, by means of the following relationship:

$$M_c(x) = V_c(x) \cdot x = T(x) \cdot j(x)d \tag{5.1}$$

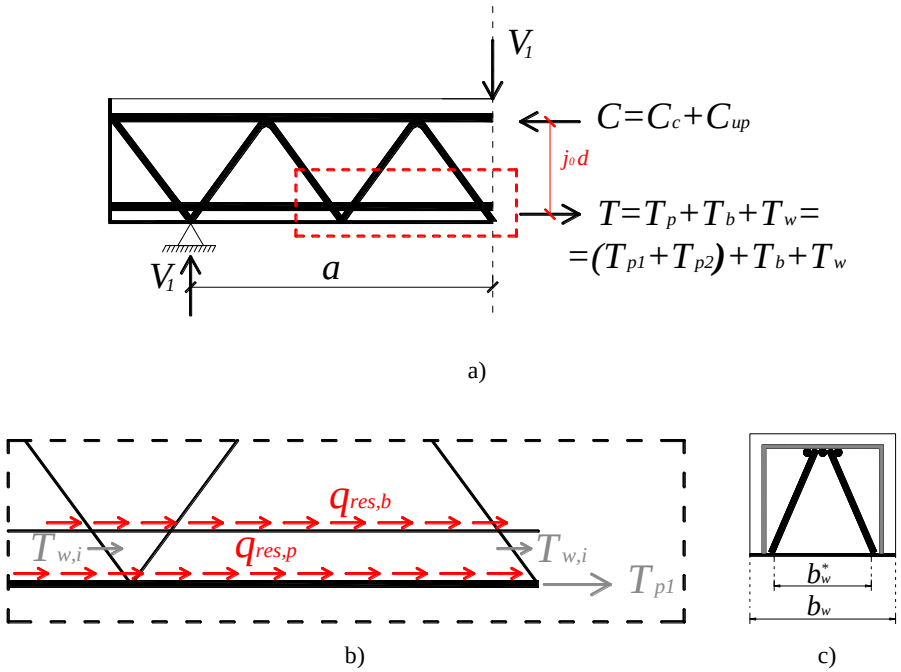

Figure 5.61. Beam effect: a) equilibrium of the forces; b) detail of the single contributions; c) effective width of the bottom plate.

Furthermore, the shear force can be expressed as a function of the variation of the bending moment as follows:

$$V_c(x) = \frac{dM(x)}{dx} = j_o d \cdot \frac{dT(x)}{dx} + T \cdot \frac{d\left(j(x)d\right)}{dx} = V_1 + V_2 \tag{5.2}$$

Eq. 5.2 clearly remarks the two fundamental resistance contributions well known in the literature as *beam effect*, with *jd* constant, and *arch effect*, with *jd* variable. Particularly, the shear resistance due to the beam action is indicated as V_1 while the contribution due to the arch mechanism is denoted as V_2. From Eq. 5.2 it emerges that the resistance contribution due to the beam effect is defined as follows:

$$V_1 = j_0 d \cdot \frac{\mathrm{d}T(x)}{\mathrm{d}x} \tag{5.3}$$

in which j_0 is assumed as a constant and the variation in the bending moment is only due to the variation of the tensile longitudinal force, T.

As already mentioned, with reference to Figure 5.61a, such a traction force can be considered as the sum of three different contributions:

- the traction due to the bottom steel plate (T_p);
- the traction due to the residual bond stress of the lower rebars (T_b);
- the traction due to the tensile diagonal web bars acting as dowels (T_w).

Particularly, the tensile force provided by the bottom plate can be considered as the traction due to the strength of the steel (T_{p1}) plus the resultant of the residual bond stress between the plate and the concrete (T_{p2}).

However, in order to evaluate V_1, it has to be observed that the variation of the total traction force can be expressed only in terms of residual splitting bond stresses transmitted by the longitudinal inferior rebars, $q_{res,b}$, and residual bond stress transmitted by the inferior steel plate, $q_{res,p}$, considering that the other two contributions (T_w and T_{p1}) remain constant. If a linear distribution of $q_{res,b}$ and $q_{res,p}$ is assumed, then the derivate of the force T can be expressed as:

$$\frac{\mathrm{d}T(x)}{\mathrm{d}x} = \pi\, q_{res,b} \sum_{i=1}^{n_b} D_i + q_{res,p} b_w^* \tag{5.4}$$

being D_i the diameter of the i-th bar belonging to the longitudinal reinforcements constituted by n_b rebars and b_w^* the effective width of the plate indicated in Figure 5.61c.

Therefore utilizing Eq. 5.3 and Eq. 5.4 it follows:

$$V_1 = j_o \cdot d \cdot \frac{dT(x)}{dx} = j_o \cdot d \left(\pi \cdot q_{res,b} \cdot \sum_{i=1}^{n_b} D_i + q_{res,p} b_w^* \right) \tag{5.5}$$

The evaluation of $q_{res,b}$ is done according to Harajli (2004):

$$q_{res,b} \cong \frac{1}{3} \cdot \sqrt{f_c'} \cdot \left(\frac{\delta}{D_i} \right)^{2/3} \tag{5.6}$$

where δ is the cover of the longitudinal bars. For simplicity, it is assumed $\frac{\delta}{D_i}=1$ and therefore $q_{res,b}\cong\frac{1}{3}\cdot\sqrt{f_c'}\cong 0.33\sqrt{f_c'}$, being f_c' expressed in MPa. For smooth steel the coefficient 0.33 is reduced to 0.1 and, therefore, the value of $q_{res,p}$ can be assumed equal to $0.1\sqrt{f_c'}$.

Finally the expression of V_1 assumes the following form:

$$V_1 = j_o \cdot d\left(\pi\cdot 0.33\sqrt{f_c'}\cdot\sum_{i=1}^{n_b} D_i + 0.1\sqrt{f_c'}\,b_w^*\right) \tag{5.7}$$

It is worth to note that, for beams without inferior added rebars, the first term of Eq. 5.7 is equal to zero.

In the same way, for beams subjected to negative bending moment, that is in which the bottom plate is compressed, the second term of Eq. 5.7 is null.

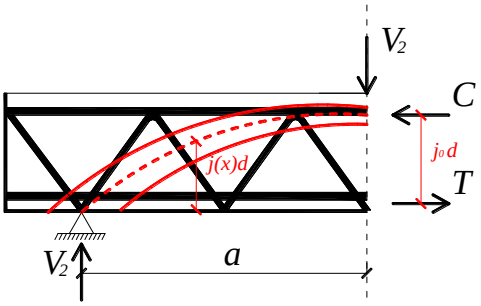

Figure 5.62. Arch effect.

Eq. 5.2 shows that the resistance contribution due to the arch mechanism (Figure 5.62) is defined by relating the shear force V_2 to the variation in j as:

$$V_2 = T\cdot d\cdot\frac{\mathrm{d}\,j(x)}{\mathrm{d}\,x} \tag{5.8}$$

To define Eq. 5.8 it is necessary to establish a possible variation law of $j(x)$. As originally suggested in Bažant and Kim (1984), the following expression can be assumed:

$$j = j_0 \cdot \left(\frac{x}{a}\right)^{\alpha} \tag{5.9}$$

with x measured starting from the support. Deriving Eq. 5.9 with respect to x, the following relation can be obtained:

$$\frac{\mathrm{d}\, j(x)}{\mathrm{d}\, x} = j_0 \cdot \frac{\alpha}{a} \cdot \left(\frac{x}{a}\right)^{\alpha\text{-}1} \tag{5.10}$$

As suggested in Swamy et al. (1993), the exponent α can be assumed equal to 1, that is, the variation law $j(x)$ can be considered linear. As a consequence, the derivate can be simply expressed as:

$$\frac{\mathrm{d}\, j(x)}{\mathrm{d}\, x} = \frac{j_0}{a} \tag{5.11}$$

The FE analysis also confirms that the assumption in Eq. 5.11 is reasonable for the configuration of the HSTCB, as can be observed in Figure 5.63 where the pattern of the principle compressive stresses is represented.

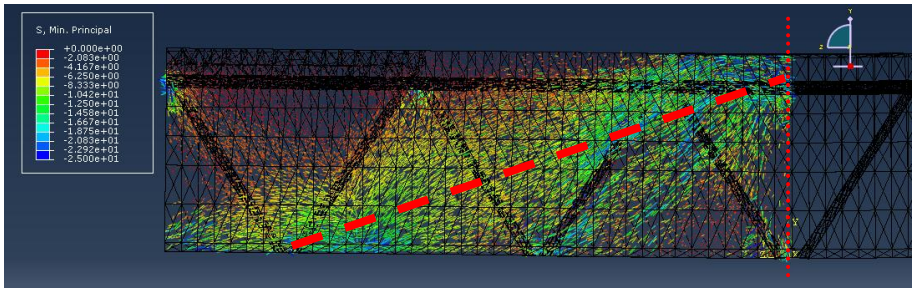

Figure 5.63. Principal compressive stresses from the FE analysis.

Concerning the force T in Eq. 5.8, it can be considered as the sum of the three aforementioned contributions:

$$T = T_p + T_b + T_w \tag{5.12}$$

The tensile force in the steel plate is defined as:

$$T_p = T_{p1} = A_{s,p}\, f_{y,p} \tag{5.13}$$

where $A_{s,p}$ is the area of the steel plate and $f_{y,p}$ is the yielding stress of the steel constituting the plate.

The contribution due to the added rebars is expressed as:

$$T_b = \sigma_b \cdot A_{s,b} \tag{5.14}$$

where σ_b is the stress in the longitudinal bar and $A_{s,b}$ is the area. This stress can be related, then, to the bond residual resistance, $q_{res,b}$, by considering the equilibrium of the internal forces within the crack spacing, s_{rm}, as shown in Figure 5.64.

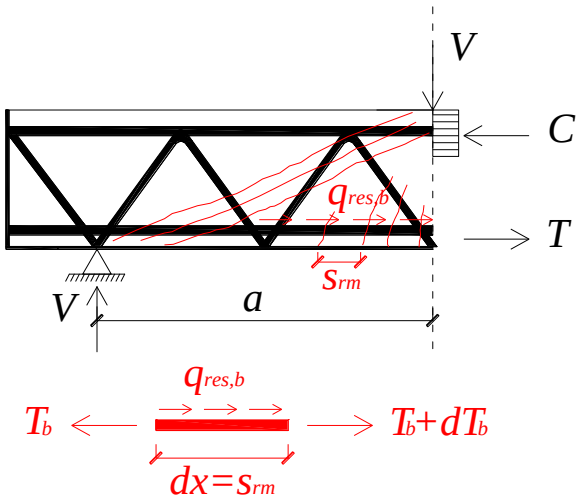

Figure 5.64. Equilibrium of the internal forces between two successive cracks.

The equilibrium is expressed as follows:

$$s_{rm} \cdot \pi \cdot q_{res,b} \cdot \sum_1^{n_b} D_i = \sigma_b \cdot \frac{\pi}{4} \cdot \sum_1^{n_b} D_i^2 \; ; \tag{5.15}$$

$$\sigma_b = \frac{4 \cdot s_{rm} \cdot q_{res,b}}{\sum_i^{n_b} \cdot D_i} \tag{5.16}$$

The length of the crack spacing is evaluated from the FE model by means of the numerical output concerning the maximum principal strains which are able, as already seen, to define the crack pattern.

As a consequence, introducing Eq. 5.15 and 5.16 in Eq. 5.14 it follows:

$$T_b = \pi \cdot s_{rm} \cdot 0.33\sqrt{f_c^{'}} \sum_i^{n_b} \cdot D_i \tag{5.17}$$

The last contribution due to the dowel action of the diagonal web bars, T_w, is evaluated according to the Von Mises strength criterion as follows:

$$T_w = r' n_w \frac{1}{\sqrt{3}} A_{sw} f_{yw} \sin\alpha \tag{5.18}$$

In Eq. 5.18 n_w is the number of dowels in the shear span that is the number of tensile diagonal bars, A_{sw} is the area of the cross-section of the dowel and f_{yw} is the yielding stress. In the same equation, in order to take into account that the diagonal stirrup does not provide the maximum contribution in both the dowel action and the shear resistance (which will be evaluated in the follow), a reduction factor, r', equal to 0.3 is introduced.

Finally, summing Eqs. 5.13, 5.17 and 5.18, considering Eq. 5.11 and substituting in Eq. 5.8, the following expression of V_2 is obtained:

$$V_2 = \left[\left(A_{s,p} \cdot f_{y,p} \right) + \left(\pi \cdot s_{rm} \cdot 0.33\sqrt{f_c^{'}} \sum_i^{n_b} \cdot D_i \right) + \left(r' n_w \frac{1}{\sqrt{3}} A_{sw} f_{yw} \sin\alpha \right) \right] j_0 \frac{d}{a} \tag{5.19}$$

The shear mechanism contribution due to the concrete is, thus, expressed by the sum of Eqs. 5.7 and 5.19:

$$\begin{aligned} V_c = V_1 + V_2 = j_o \cdot d \left(\pi \cdot 0.33\sqrt{f_c^{'}} \cdot \sum_{i=1}^{n_b} D_i + 0.1\sqrt{f_c^{'}} b_w^* \right) + \left[\left(A_{s,p} \cdot f_{y,p} \right) + \right. \\ \left. + \left(\pi \cdot s_{rm} \cdot 0.33\sqrt{f_c^{'}} \sum_i^{n_b} \cdot D_i \right) + \left(r' n_w \frac{1}{\sqrt{3}} A_{sw} f_{yw} \sin\alpha \right) \right] j_0 \frac{d}{a} \end{aligned} \tag{5.20}$$

In order to take into account that the shear mechanism can be governed by the crushing of the compressed concrete strut, an upper limit has to be

imposed for the value of V_c given by Eq. 5.20. For the aim, with reference to Figure 5.65, the maximum compression in the concrete strut is expressed as follows:

$$N_u = \nu f_c^{'} b \cdot x_c \cdot \cos\theta \tag{5.21}$$

where ν is a softening coefficient whose expression can be assumed as in the Swiss design code SIA 262 (2003) in the form $\nu = 0.6\left(\frac{30}{f_c^{'}}\right)^{0.33}$ where $f_c^{'}$ is expressed in MPa. In the same equation, the angle of inclination of the compressed concrete strut, θ, as well as the depth of the neutral axis, x_c, are deduced from the FE results.

From the equilibrium of the forces in Figure 5.65, the expression of the ultimate shear resistance of the concrete, V_{cu}, can be expressed in the following form:

$$V_{cu} = N_u \sin\theta = \nu f_c^{'} b \cdot x_c \cdot \cos\theta \cdot \sin\theta = \nu f_c^{'} b \cdot x_c \cdot \frac{\sin(2\theta)}{2} \tag{5.22}$$

At least, the shear resistance given by Eq. 5.20 should be lower than the value given by Eq. 5.22 to avoid the premature crushing of the compressed strut.

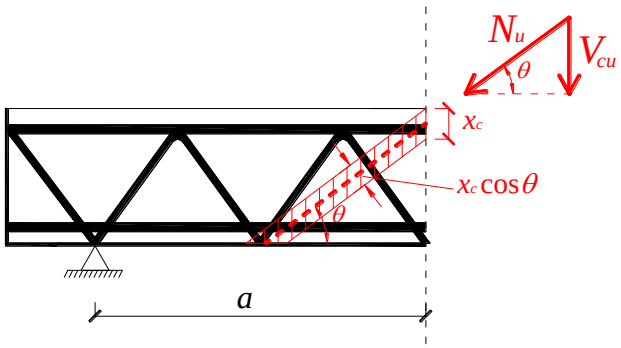

Figure 5.65. Equilibrium of forces corresponding to the compressed concrete strut.

Finally, the contribution of the diagonal web bars is taken into account as the classical shear contribution of stirrups in a R.C. structure but considering the geometry of the HSTCB. In fact the diagonal web bars of the beam, acting as stirrups, are inclined in two directions indicated as α and β in Figure 5.66.

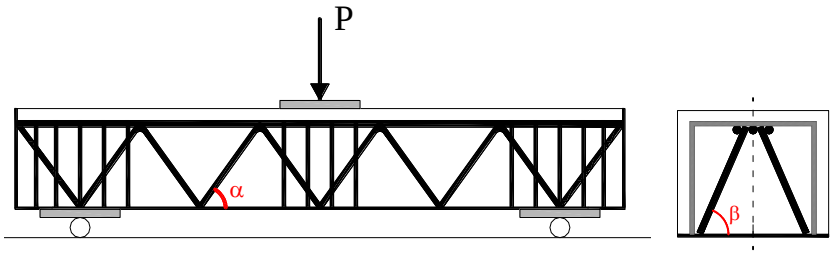

Figure 5.66. Double inclination of the diagonal web bars according to the angles α and β.

As a consequence the contribution of stirrups, V_{sw}, is evaluated as follows:

$$V_{sw} = r'' \frac{A_{sw}}{s} f_{yw} a \sin\alpha \sin\beta = r'' n_w A_{sw} f_{yw} \sin\alpha \sin\beta \tag{5.23}$$

In Eq. 5.23 a reduction factor, r'', complementary to $r' = 0.3$ and, therefore, equal to 0.7, is introduced.

The value of the shear resistance, V_R, is finally calculated by the sum of Eqs. 5.20 and 5.23:

$$V_R = V_c + V_{sw} \tag{5.24}$$

with the condition that $V_c \leq V_{cu}$.

The model is validated, first, with the experimental data of the three-point bending tests on the HSTCBs and, then, with the numerical results obtained from the FE models whose load-displacement curves have been shown in Figure 5.49 and 5.54 for the comparison with the experimental data.

Table 5.8 shows the comparison between the analytical prediction of the maximum load and the experimental values. It can be observed that the analytical prediction is conservative in all cases with the exception of

specimens A2-1 and B1. In the cases in which it is conservative, the theoretical value of the maximum load is -8.5% and -2.2% of the experimental value for specimens A1-2 and A2-2, respectively, while it differs of the 16.7% in the case of specimen B2. In the case in which the prediction proves to be unconservative, it exceeds the experimental peak load of the 6.8% and 13.5% for specimen A2-1 and B1 respectively. The average theoretical load is conservative and differs of 1.4% with respect to the experimental data with a coefficient of variation of 0.121 which represents the accuracy of the predicted results.

Table 5.8. Analytical vs. experimental results.

	P_{exp}	P_{the}	P_{the}/P_{exp}
A1-2	577.74	528.41	0.915
A2-1	422.29	451.28	1.068
A2-2	461.29	451.28	0.978
B1	335.94	381.43	1.135
B2	519.53	432.85	0.833
Avg.			***0.986***
CVr			***0.121***

Table 5.9. Analytical vs. numerical results.

Typology	P_{num}	P_{the}	P_{the}/P_{num}
A2 - f_c=25 MPa	460.88	428.90	0.930
A2 - f_c=20 MPa	414.28	394.94	0.963
A2 - f_c=16 MPa	360.37	373.23	1.035
B - f_c=25 MPa	465.15	432.85	0.931
B - f_c=20 MPa	417.03	406.31	0.974
B - f_c=16 MPa	364.72	383.45	1.051
Avg.			***0.981***
CV_r			***0.053***

By applying the analytical expressions to the numerical simulations previously used to interpret the mechanical behavior of the tested beams, the results in Table 5.9 are obtained. For the models concerning HSTCBs of series "A2", the prediction proves to be conservative for f_c*=25 MPa* and f_c*=20 MPa* obtaining a maximum theoretical value 7%, in the first case, and 3.7%, in the second case, lower than the numerical one. For f_c*=16 MPa* the analytical prediction is 3.5% higher than the numerical peak load. Similarly, for the cases of beams of series "B", the analytical prediction is conservative for f_c*=25 MPa* and f_c*=20 MPa* of 6.9% and 2.6% respectively, while it is unconservative for f_c*=16 MPa*, being the theoretical shear resistance 5.1% higher than the numerical value. Finally, the average theoretical load differs of 1.9% with respect to the numerical data with a coefficient of variation of 0.053 which shows a good accuracy of the prediction with a low scatter of the results. In this regard, it is worth to note that the scatter in the prediction of the shear resistance in the tested beams is related to the scatter in the experimental data themselves because of the uncertainties in the value of the concrete compressive strength. Being such uncertainties not present in the FE modeling, by applying the analytical expressions to the numerical simulations, a lower coefficient of variation is obtained.

As a final remark, it can be interesting to mention that, in all cases, that is for such *a/d* ratio, equal to 2.4, and for such geometrical configuration of the steel members, the contribution of the concrete in the shear mechanism is governed by the crushing of the compressed strut, being the value of V_{cu} expressed by Eq. 5.22 lower than the value of V_c in Eq. 5.20.

CHAPTER 6

SHEAR BEHAVIOR AND SIZE EFFECT INVESTIGATION OF HSTCBs BY NUMERICAL MODELING

The question of scaling is an aspect of paramount importance of every physical theory and it has always occupied a central position in many engineering problems. Particularly, in solid mechanics, the main interest is the study of the size effect of structures on their strength (Bažant 2000; Bažant 2005). Up to the 1980s, the effects of the size experimentally observed in the laboratory were interpreted as a consequence of the material strength randomness. On the contrary, today, it is well known that the one produced by the material strength randomness is just one of the various size effects concerning the structures. On the basis of the long history of studies dealing with this topic, the attention can be focused on three main types of size effect: the already mentioned "statistical size effect", due to the randomness of strength (Weibull 1939); the "energy release size effect", due to the stress redistribution and the fracture energy release occurring during the stable growth of large fractures or large damage zones prior to failure (Bažant 1984); the possible size effect due to the fractality of fractures or microcracks (Carpinteri 1994a,b).

The size effect has been studied with reference to any kind of material (Bažant 1984) above all concrete (Bažant and Kazemi 1988; Ožbolt et al.

1994; Cedolin and Cusatis 2007, 2008; Siroka-Korol and Tejchman, 2012) also with reference to structural high strength concrete (Appa Rao and Raghu Prasad 2004). The influence of the size effect is also widely investigated with regards to further more recent engineering applications such as those dealing with concrete beams reinforced with basalt bars (Korol and Tejchman 2013) or engineered cementitious composite materials (Lepech and Li 2003,2004) and advanced analysis techniques are developed for both classical and new problems (Bažant and Yu 2004; Yasir Alam and Loukili 2010).

With reference to the shear strength of classical R.C. beams, the evaluation of the size effect has been investigated by many authors such as Bažant (1997) and, more recently, Appa Rao and Sundaresan (2012) by means of analytical models supported by the comparison with the available experimental results as well as the elaboration of numerical FE models.

Within this framework, in the present Chapter, the evaluation of the size effect on the HSTCB structural typology is presented. The study is carried out by means of numerical FE simulations on three different sizes of the same beam obtained imposing a two-dimensional geometric similarity.

The details of the scaling criteria of each geometry as well as the main features of the models are reported in the next sections. Then the description of the results concerning the simulations and the comparison between the three different mechanical behaviors is presented and discussed.

6.1 Finite element simulation

For the investigation on the size effect it is necessary to develop numerical simulations whose more and more large geometry produces an increasing computational effort. As a consequence, an highly complex and detailed model of the structure is not suitable for the aim and, therefore, a simplified model capable of retaining the salient features of the response, involving 3D geometry, strain-softening damage of the concrete and plasticity of the steel, is generated. The model has been developed with the guide of Roberto Ballarini, James L. Record Professor at the Department of Civil Engineering of University of Minnesota and Jialiang Le, Assistant

Professor at the same Department. Most of the analyses have been developed using the softwares and the machines of property of *Minnesota Supercomputing Institute*.

6.1.1 Description of the finite element models

Three models of three different sizes of HSTCB are generated with the aim of simulating the load condition of a three-point bending test. In the follow, they are denoted respectively as Model Size 1, Model Size 2 and Model Size 3. Particularly, Model Size 1 refers to the geometric features of the 250 mm depth beam without added inferior rebars, subjected to positive bending moment (type A1) already described in the previous Chapter. Therefore, a qualitative comparison between the experimental result (specimen A1-2) and the numerical outcomes is reasonable as well as suitable. On the other hand, the geometry of Model Size 2 and Model Size 3 is deducted from the geometry of the first size using some specific scaling criteria described in the next sections for each model.

Before developing Model Size 1, whose geometry, as already mentioned, does not include inferior added rebars, also a preliminary simplified modeling of the beam type A2 has been generated in order to qualitatively compare the result of such simplified FE model with the load-displacement curve obtained with the detailed model, containing the cohesive interaction between steel and concrete, previously described in Chapter 5. In Figure 6.1 the comparison between the two numerical models is reported, also showing the qualitative relationship with the experimental results of tests A2-1 and A2-2. As it can be observed, both models are able to catch almost the same value of the peak load: it is equal to 460.88 kN for the detailed model, 452.83 kN for the simplified one. On the other hand, as regards the initial stiffness until the achievement of the maximum load, the simplified model gives an overestimation of the parameter due to the perfect bond hypothesis introduced in the model. However, the post-peak branch well fits the experimental evidence. Since the aim of the development of a simplified model is the investigation of the size effect, the major interest is in the maximum load value rather than in the stiffness of the beam. As a

consequence, comparing the great accuracy of the detailed model with the accuracy of the simplified one, on the basis of the computational effort, the simplified model proves to be more efficient in produce the required simulations.

It is worth to note that Model Size 1 is identical to such model representing the beam type A2 with the exception of the inferior rebars and, as a consequence, it is reasonable to ascribe the same accuracy to both simulations.

The main features of such simplified models consist in the use of simple finite elements that are *beam elements* for the rebars and *shell elements* for the steel plate. Furthermore, no constitutive behavior of the steel-concrete interface is implemented; on the contrary, the simplified hypothesis of perfect bond between the two materials is assumed. The concrete is modeled as a unique block without any void and all rebars are assumed to be embedded within this volume.

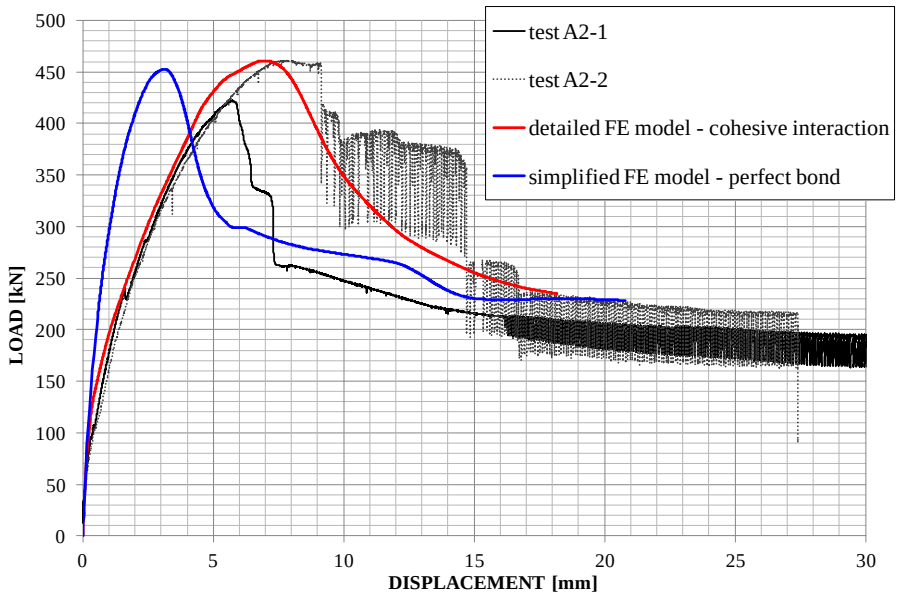

Figure. 6.1. Comparison between detailed and simplified FE models.

As well as for the detailed numerical model described in Chapter 5, also in this case the finite elements employed for the concrete are linear tetrahedra. The boundary conditions are represented by pinned bottom lateral supports and an imposed displacement is applied on the top midspan of the beam. The constitutive behaviors of materials are once again implemented by means of the Concrete Damaged Plasticity Model for the concrete and the Classical Metal Plasticity Model for the steel. The mesh size for the elements is the same in all three models; it has been preliminary chosen by comparing the accuracy of the results of few simulations concerning Size 1 with the time required by the analyses.

6.1.2 Scaling criteria

Table 6.1 reports the data concerning the scaled geometry of each model with reference to the symbols introduced in Figure 6.2.

For the geometry of Model Size 1 the ratio a/D is equal to 2.4. As a consequence, for Model Size 2, chosen D = 555 mm because it represents another value for the depth of the HSTCB usually produced by the industry, it results a shear span, a, equal to 1332 mm so that a/D continues to be equal to 2.4. Furthermore, being the ratio between these two shear spans equal to 1332/600 = 2.22, the spacing between the diagonal rebars, s, is chosen equal to 666 mm so that 666/300 = 2.22 which represents the ratio between the spacing in Model Size 1 (s = 300 mm) and Model Size 2 (s = 666 mm). For Model Size 3, the value of D is chosen so that $D_3/D_2 = D_2/D_1 = 2.22$, where D_1, D_2 and D_3 represent the depth of beam size 1, 2 and 3 respectively. All other dimensions are defined as before. Finally in all cases the quantities b, $\varnothing_{w,}$ $\varnothing_{up,}$ and s_{pl} remain constant.

Table 6.1. Geometric features of Model Size 1, 2 and 3 (dimensions in millimeters).

	a/D	**a**	**D**	b	$\varnothing_w$	$\varnothing_{up}$	s_{pl}	**s**
Size 1	**2.4**	**600**	**250**	300	12	16	5	**300**
Size 2		**1332**	**555**					**666**
Size 3		**2957.04**	**1232.1**					**1478.52**

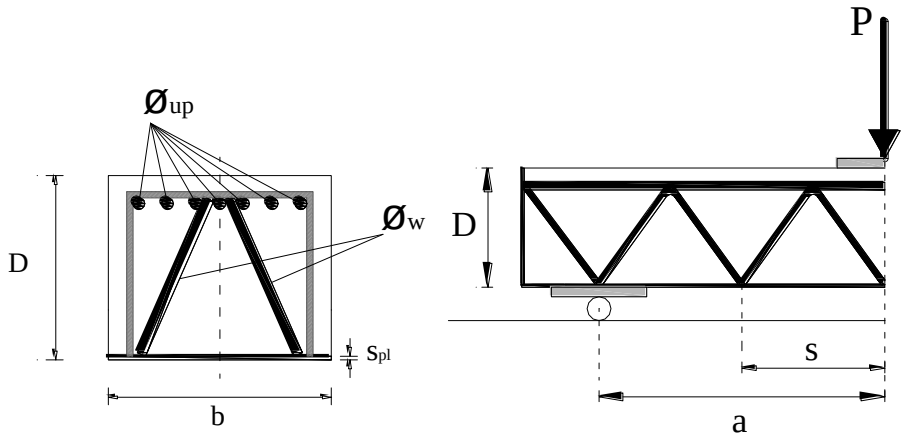

Figure 6.2. Symbols of the geometric parameters of the FE models.

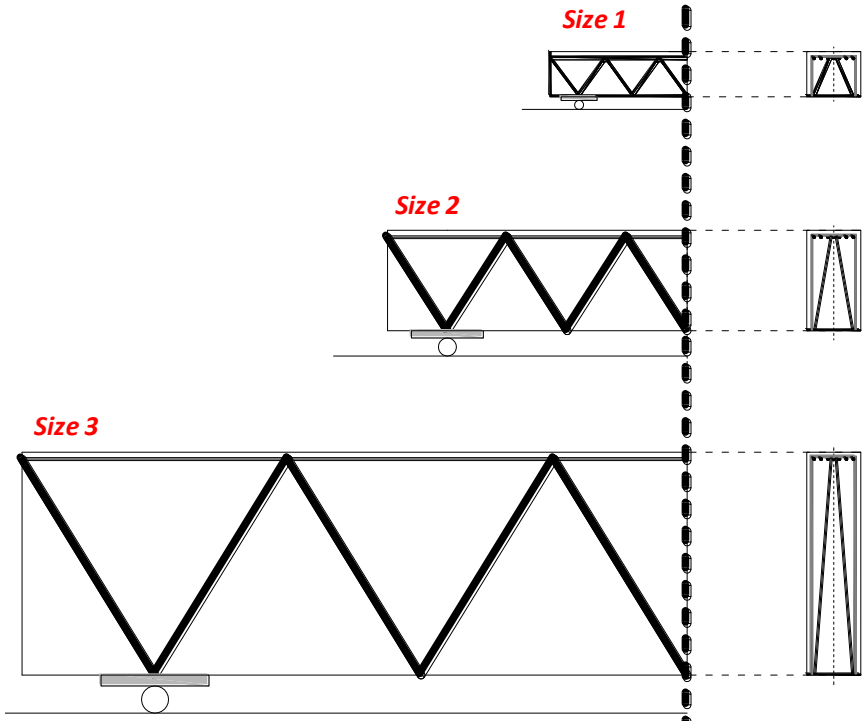

Figure 6.3. Ratio between the geometry of Model Size 1, Model Size 2 and Model Size3.

The ratio between the three different sizes is qualitatively shown in Figure 6.3. It can be observed that, according to this scaling criteria, the resulting cross-sections of the three models are very different each other in terms of the slope of the diagonal rebars which is progressively increasing passing from the first to the third geometric dimension. Particularly, the inclination of the diagonal web bars in the plane of the cross-section is equal to 68° in Model Size 1 while it is equal to 80.8° and 86° in Model Size 2 and Model Size 3 respectively.

6.2 Numerical results

In this section, the results obtained by means of the numerical modeling of the different sizes of beam are presented and discussed. For each FE model the numerical load-displacement curve is analyzed in detail, pointing out some characteristic events occurring during the load history and also suggesting a qualitative comparison between the crack pattern numerically predicted for Model Size 1 with the one experimentally observed for the specimen of HSTCB belonging to the A1 typology described in Chapter 5.

6.2.1 Model Size 1

Figure 6.4 summarizes the geometric features of the model also indicating the so-called "control section" which represents the reference plane where the main crack is going to develop during the analysis.

Observing the load-displacement curve in Figure 6.5, it can be deduced that the beam exhibited a global fragile behavior during the simulation with a maximum load of 432.16 kN.

The markers on the curve represent eight main characteristic steps of the load history that are described in the follow.

STEP N°1 corresponds to an intermediate phase between the moment in which the concrete enters its post-elastic compressive behavior and the moment in which the value of P_{max} is achieved.

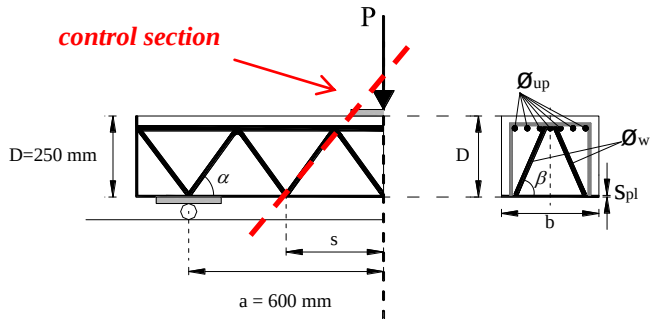

a/D	a	D	b	∅ w	∅ up	s pl	s	α	β
2.4	**600**	**250**	300	12	16	5	**300**	**54°**	**68°**

Figure 6.4. Geometry of the beam and boundary conditions for Model Size 1.

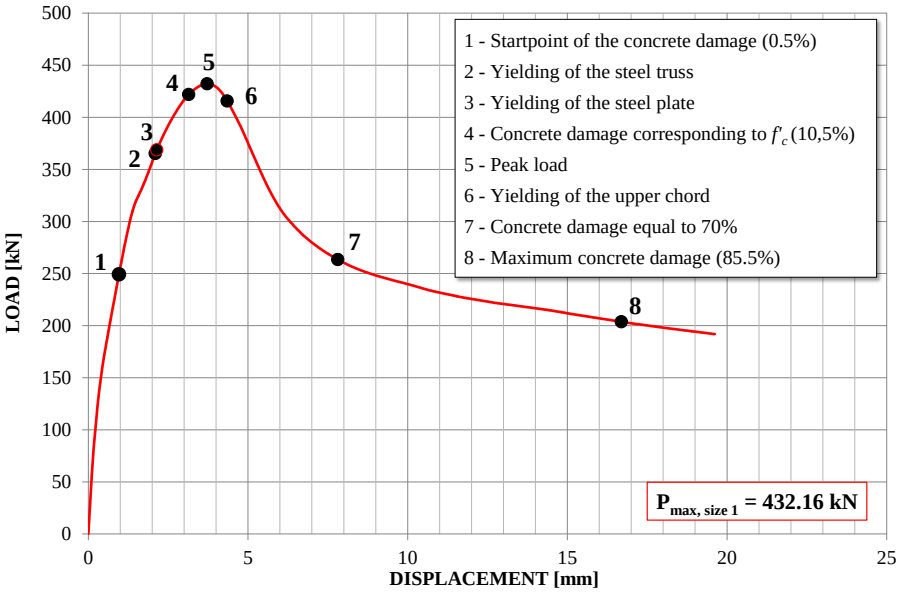

Figure 6.5. Load-displacement curve of Model Size 1.

The inelastic behavior of the compressed concrete is governed by a damage variable whose values are associated to the compressive stresses and the inelastic strains achieved in the concrete during the analysis.

In this configuration all steel members are elastic as shown in Figure 6.6. As regards the concrete, from Figure 6.7 it can be observed that, at the ends of the compressed strut, the stress starts to assume the value of 22 MPa which corresponds to the beginning of the inelastic compressive behavior. According to the definition of the damage in the compressed concrete, this stress value is associated to a rate of damage between 0 and 0.5%. Through the cut three-dimensional view of the beam in Figure 6.8 it is shown how the damage variable starts to locally assume the value of 0.005.

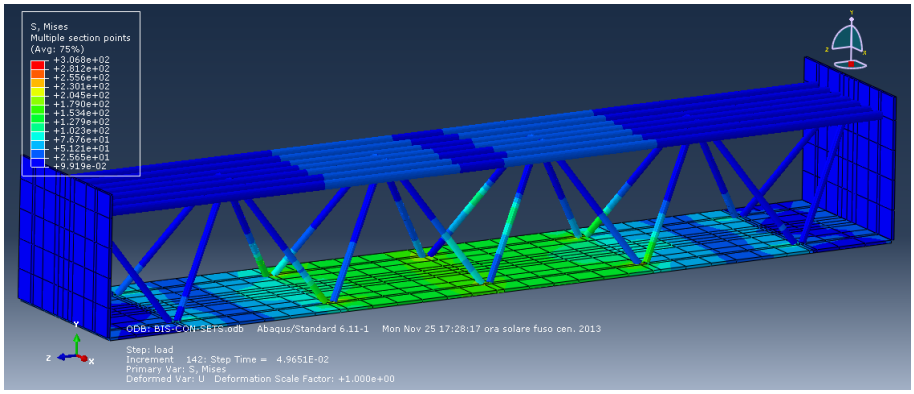

Figure 6.6. Step N°1: magnitude of the von Mises stresses in the steel members.

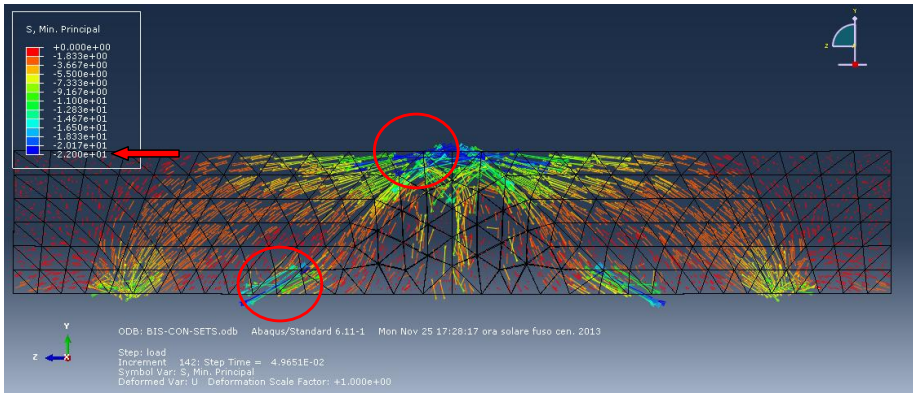

Figure 6.7. Step N°1: direction of minimum principal stresses in the concrete.

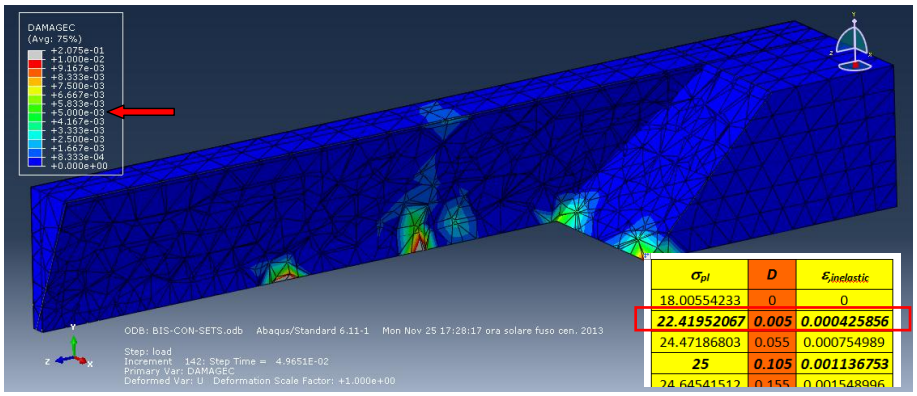

Figure 6.8. Step N°1: damage variable magnitude.

Unlike concrete models based on the smeared crack approach, the CDP model does not have the notion of cracks developing at the material integration point. As a consequence, in order to obtain a graphical visualization of the cracking pattern, it is possible to refer to the direction of the maximum principal plastic strains which is assumed to be parallel to the direction of the vector normal to the crack plane.

Figure 6.9 shows the direction of the maximum principal strains in *STEP N°1*: the first flexural sub-vertical cracks appear in the midspan of the beam and the diagonal cracks begin to symmetrically develop in the bottom of the "control section".

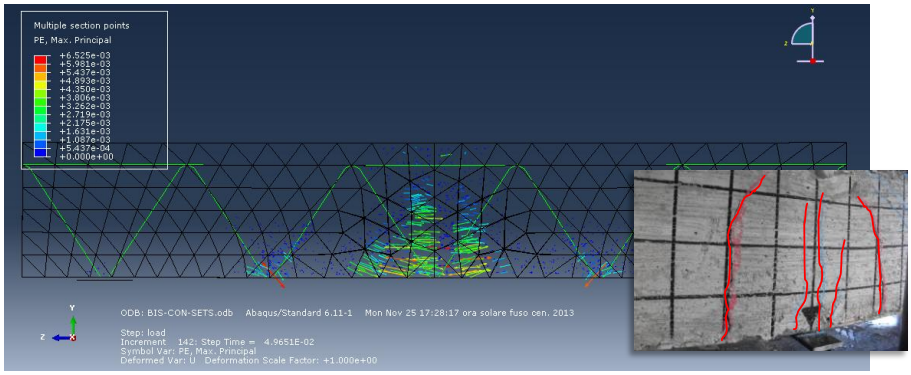

Figure 6.9. Step N°1: direction of maximum principal strains.

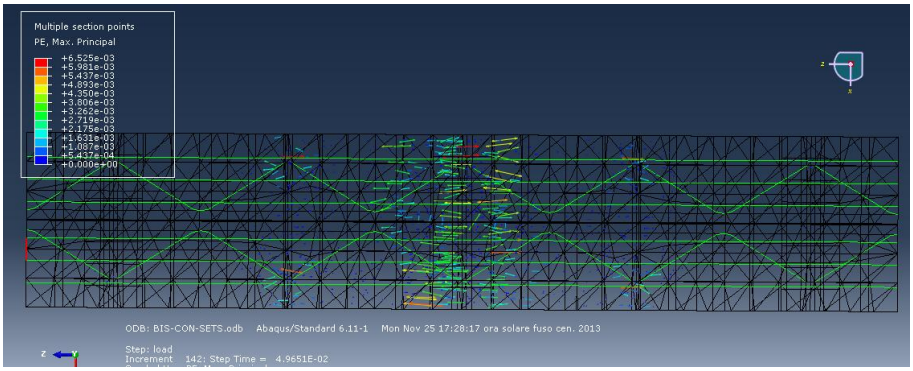

a)

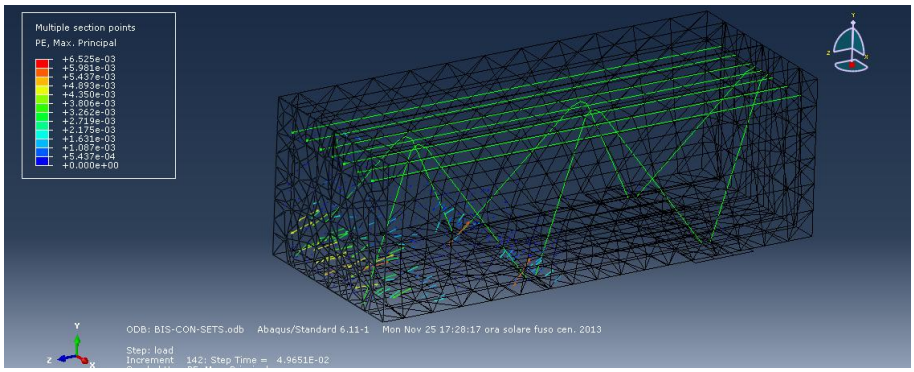

b)

Figure 6.10. Direction of maximum principal strains in Step N°1: a) top view; b) axonometric view.

In the same figure, the crack pattern is also qualitatively compared with a picture of specimen A1-2 showing a good agreement between the numerical prediction and the experimental evidence concerning the first flexural sub-vertical cracks.

Finally, Figures 6.10a and 6.10b represent the crack pattern according to the top and axonometric views of the beam. As it can be observed, the fractures involve the entire width of the beam in the plane of the controlled section.

Since *STEP N°2* is immediately close to *STEP N°3*, only the configuration of the beam corresponding to this latter is described in the follow. *STEP N°3* corresponds to the phase in which both the steel truss and

the bottom steel plate yield, before the value of P_{max} is achieved. Particularly, the truss and the plate yield corresponding to the end of the diagonal bars welded to the inferior plate. The diagonal bars that yield are the tensile ones corresponding to the second mesh of the truss. The configuration of the steel members is represented in Figure 6.11.

As regards the state of stress in the concrete, the volume of concrete in which the minimum principal stresses are equal to 22 MPa is increasing, as shown in Figure 6.12.

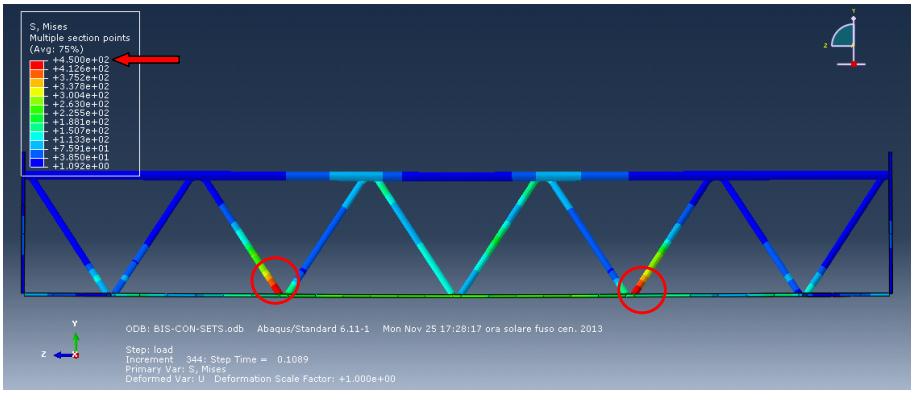

Figure 6.11. Step N°3: magnitude of the von Mises stresses in the steel members.

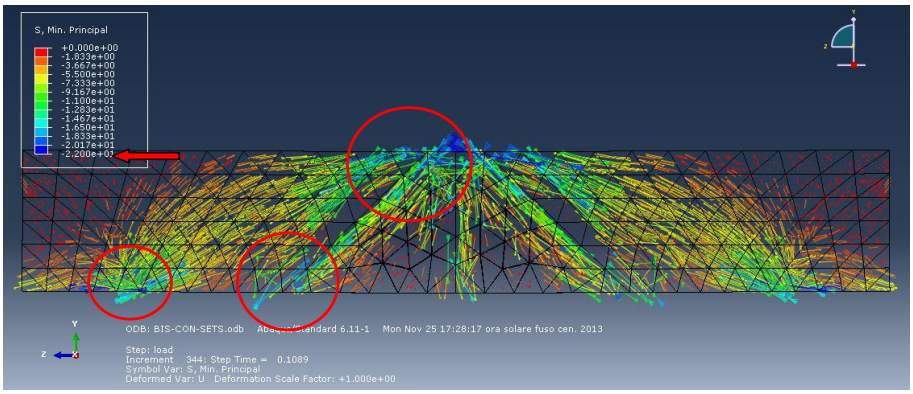

Figure 6.12. Step N°3: direction of minimum principal stresses in the concrete.

In the same time the damage in the compressed concrete evolves corresponding to the volume of concrete surrounding the diagonal compressed bars (see Figure 6.13) and the crack pattern is extending too all around the compressed diagonal bars where the concrete is damaging. The cracks develop in the plane immediately next to the plane containing the diagonal web bars and almost parallel to the latter (see Figure 6.14). With reference to Figure 6.14b, it can be observed that, once again, the numerical prediction of the crack pattern well fits the experimental results.

STEP N°4 corresponds to the configuration immediately before the achievement of the peak load. In this configuration the yielding of the diagonal bars develops involving also the compressed bars and the upper extreme of the tensile bars (Figure 6.15a). Particularly, as regards the yielded areas of the steel plate, the sections subjected to the highest stress state are those corresponding to the first meshes of the truss where the bending moment reaches the highest values because of the load condition (Figure 6.15b). In this step the minimum principal stress in the concrete approaches the maximum value implemented in the compressive constitutive behavior which is equal to 25 MPa (Figure 6.16) and the damage variable reaches the corresponding value (Figure 6.17). A further extension of the cracks is shown in Figure 6.18a with respect to the previous step once again reported in the small frame of the same figure. Particularly, referring to the magnitude of the strain vectors shown in Figure 6.18b, it can be observed that the entity of the strains in the midspan of the beam is smaller than the entity of strains corresponding to the "control section" and that the strains in the control section are wider in the bottom of the beam than on the top. Furthermore, as observed from the beginning of the load history, the plane where the cracks develop is next to the plane containing the diagonal web bars and almost parallel to the latter.

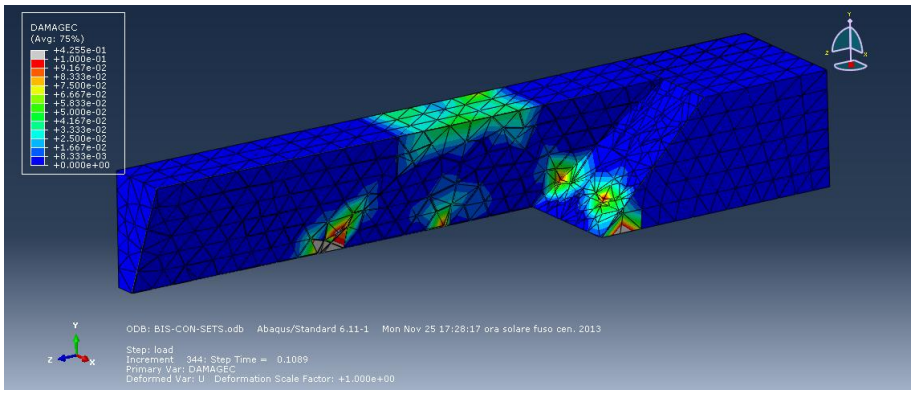

Figure 6.13. Step N°3: damage variable magnitude.

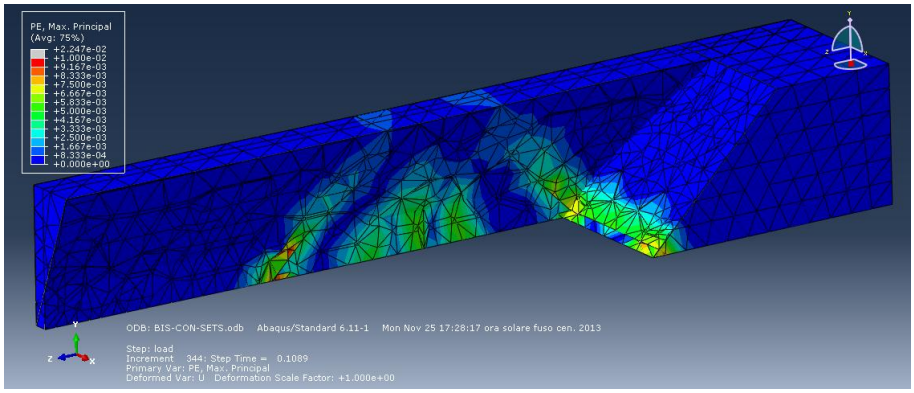

a)

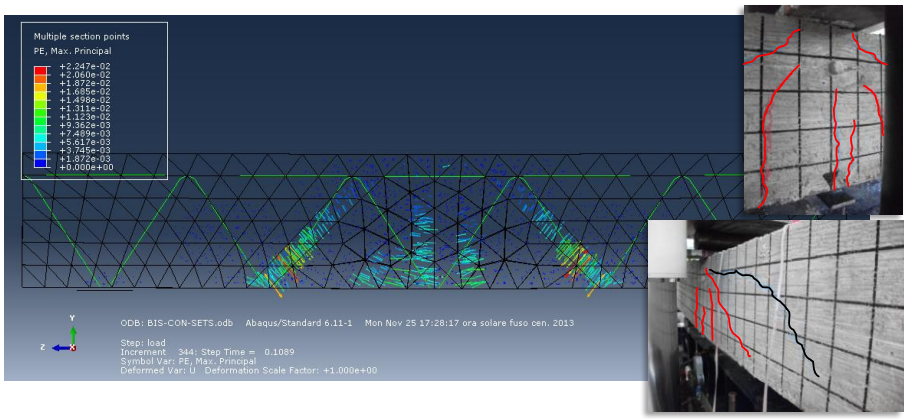

b)

Figure 6.14. Maximum principal strain in Step N°3: a) magnitude; b) direction.

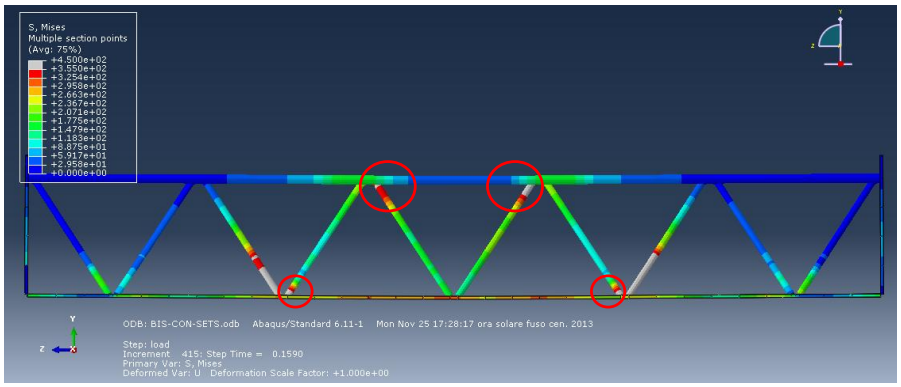

a)

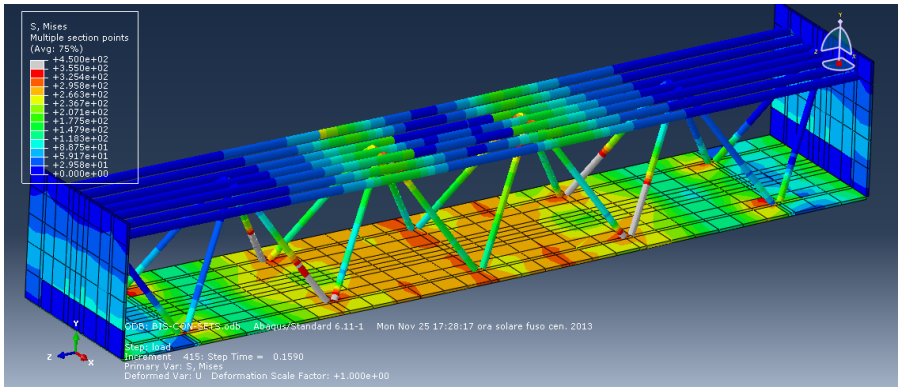

b)

Figure 6.15. Magnitude of the von Mises stresses in the steel members in Step N°4: a) frontal view; b) axonometric view.

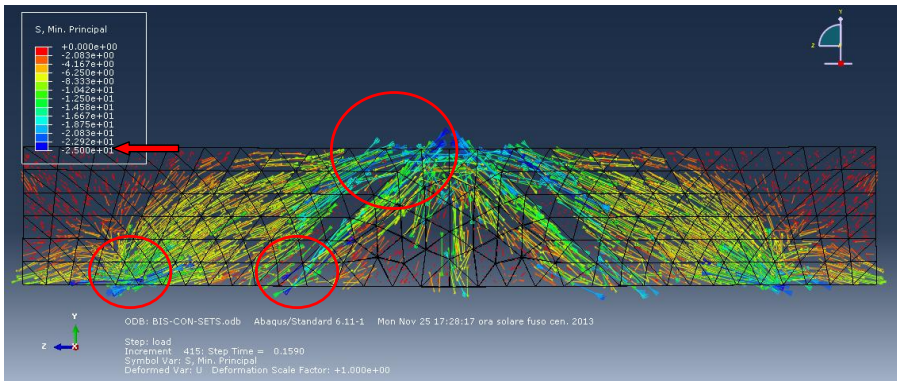

Figure 6.16. Step N°4: direction of minimum principal stresses in the concrete.

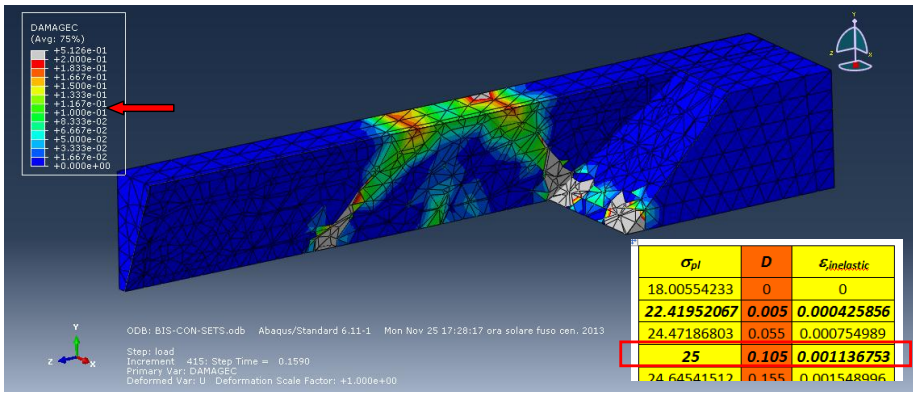

σ_{pl}	D	$\varepsilon_{,inelastic}$
18.00554233	0	0
22.41952067	***0.005***	***0.000425856***
24.47186803	0.055	0.000754989
25	***0.105***	***0.001136753***
24.64541512	0.155	0.001548996

Figure 6.17. Step N°4: damage variable magnitude.

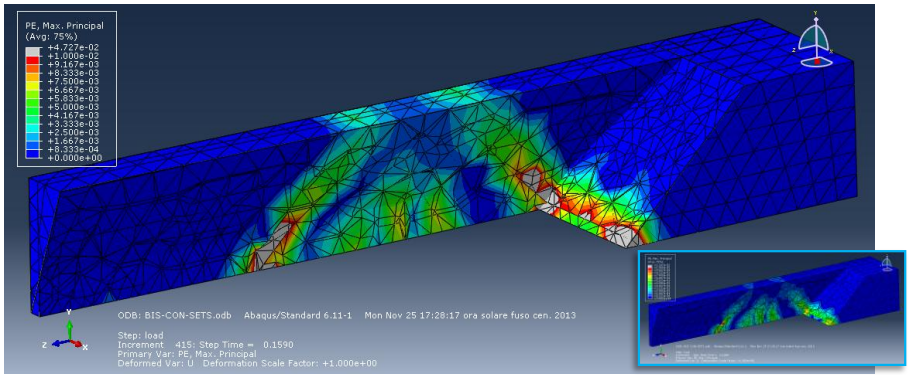

a)

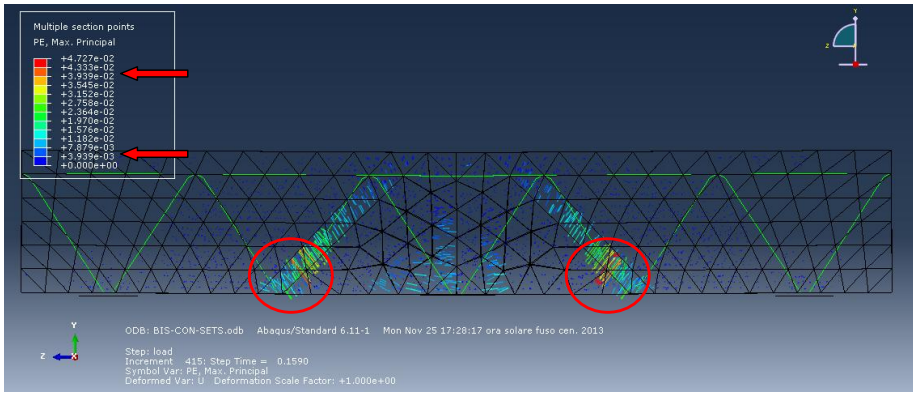

b)

Figure 6.18. Magnitude and direction of the maximum principal strain in Step N°4: a) axonometric view; b) frontal view.

STEP N°5 represents the configuration at failure when the maximum value of the load is achieved. In this phase, as already said, the diagonal web bars and the bottom plate are yielded but not yet in the hardening branch; on the contrary, all rebars constituting the upper chord are still elastic exhibiting stress values in the range between 300 and 338 MPa, being f_y = 450 MPa. Figure 6.19 shows the details of the configuration at failure of the steel members. Concerning the minimum principal stresses in the concrete, they reach the maximum value implemented in the compressive constitutive behavior in almost all the compressed strut (Figure 6.20). The damage variable, whose magnitude is shown in Figure 6.21a, has the value of 0.105 in the volume of the compressed strut (that is where the stress is equal to 25 MPa).

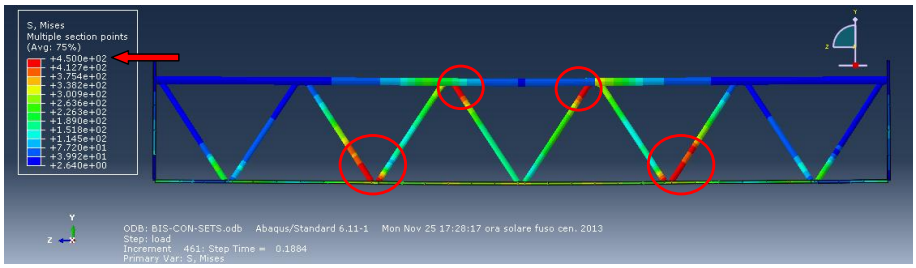

a)

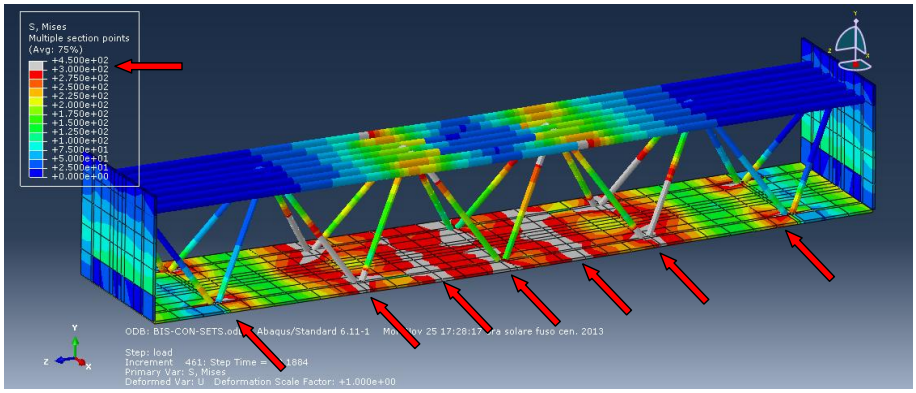

b)

Figure 6.19. Configuration at failure of the steel members (Step N°5): a) diagonal web bars and upper chord; b) steel plate.

In Figure 6.21 it is also possible to observe the extension of the concrete strut and its collocation of with respect to the compressed diagonal bars. Moreover, a tridimensional plot of such parameter shows that at the bottom of the beam the damage in the compressed strut is concentrated in a volume around the diagonal bars and does not involve the all width of the beam (Figure 6.21b-c).

It is also possible to observe that the damage variable reaches higher values locally at the ends of the strut where the damage is bigger due to the action of the bottom steel plate and the upper chord against the concrete strut as shown in Figure 6.22 where the amplified deformed shape (x25) of the steel members is represented.

A further zoom of the amplified deformed shape of the beam also allows to observe the separation of the bottom steel plate from the block of concrete next to the lateral support, phenomenon which is actually observed also in the experimental tests (Figure 6.23).

As regards the crack pattern evolution, Figures 6.24a-b-c represent the maximum inelastic strains direction according to the frontal and top view of the beam as well as the axonometric perspective which remarks the shape of the crack plane in the 3D space.

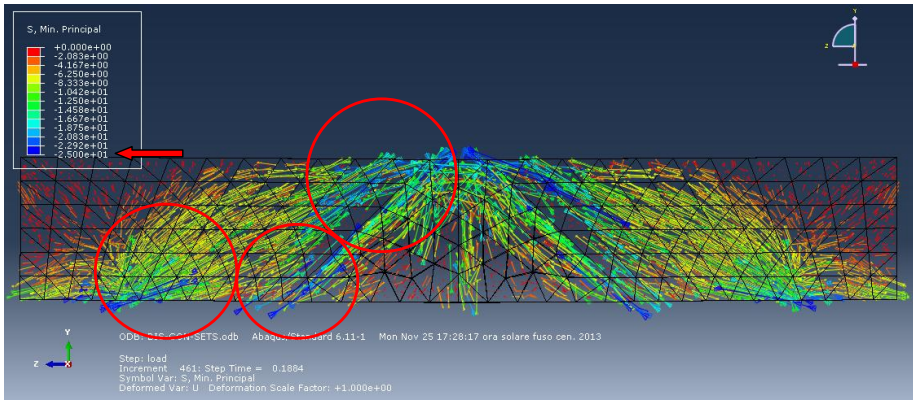

Figure 6.20. Minimum principal stresses in the concrete in the configuration at failure.

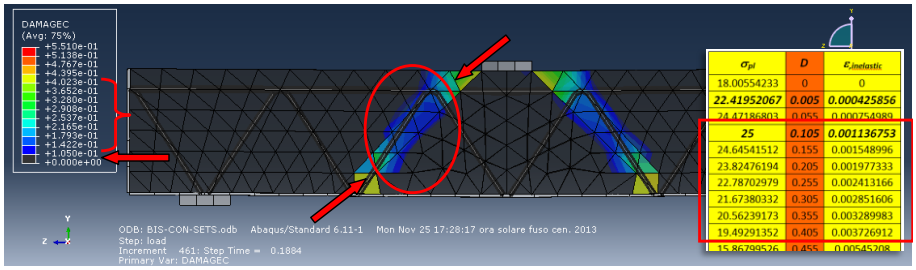

a)

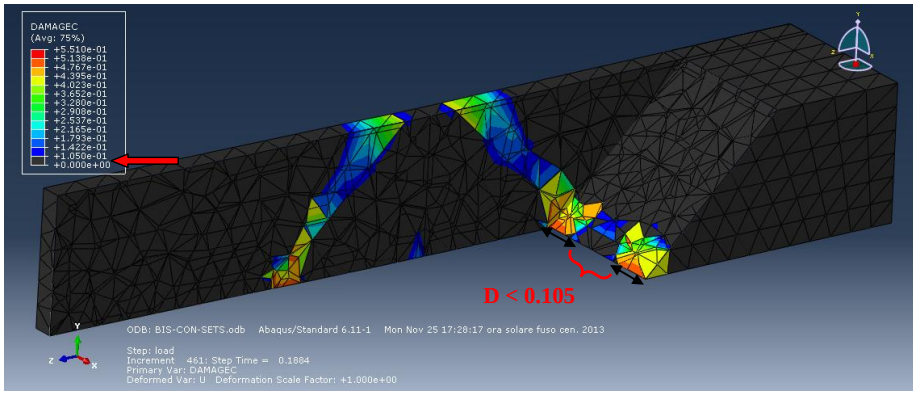

b)

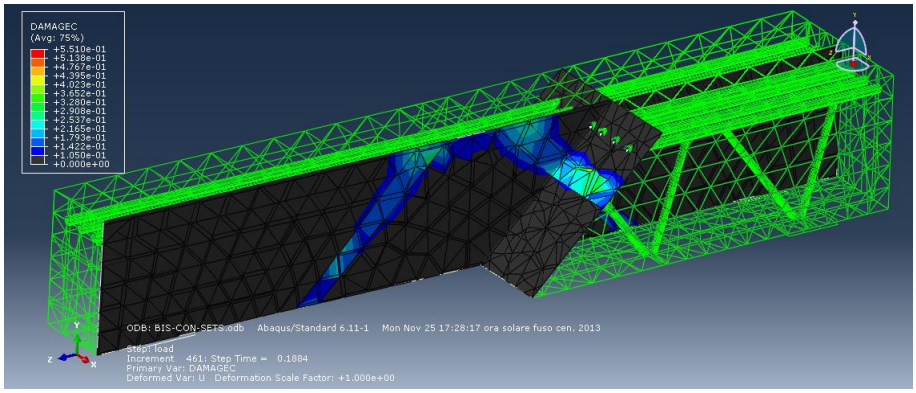

c)

Figure 6.21. Damage variable in the configuration at failure: a) damage magnitude and frontal view of the concrete strut; b) axonometric view of the damage evolution; c) layout of the diagonal bars with respect to the compressed damaged concrete.

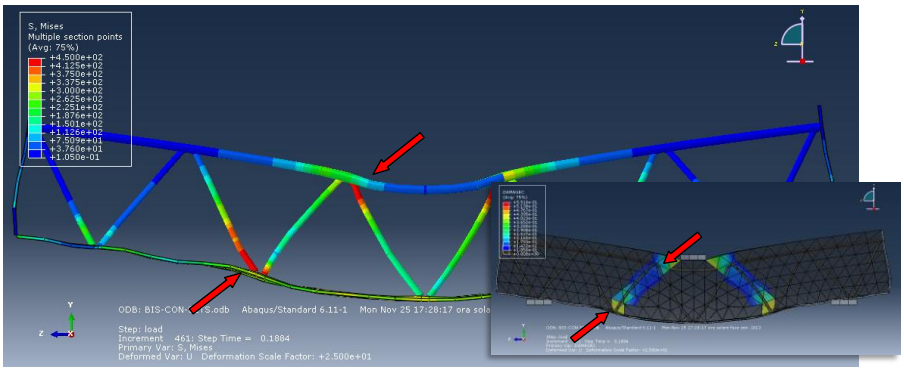

Figure 6.22. Amplified deformed shape of the steel members (x25) showing the action of the bottom steel plate and the upper chord against the concrete strut.

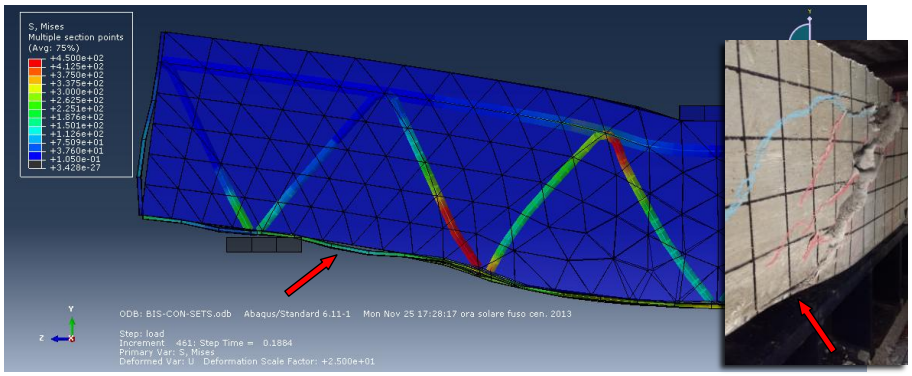

Figure 6.23. Amplified deformed shape of the steel members (x25) showing the separation of the bottom steel plate from the concrete block.

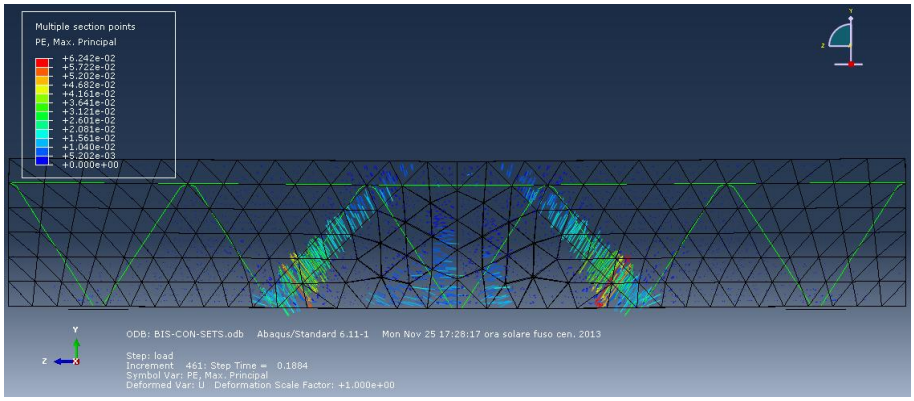

a)

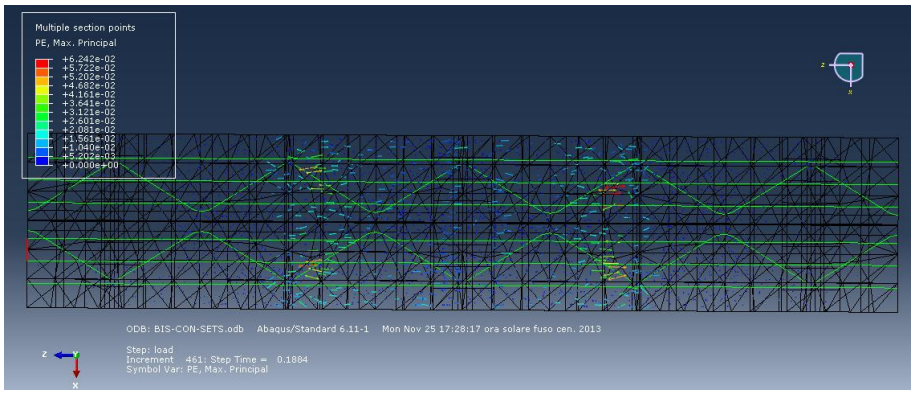

b)

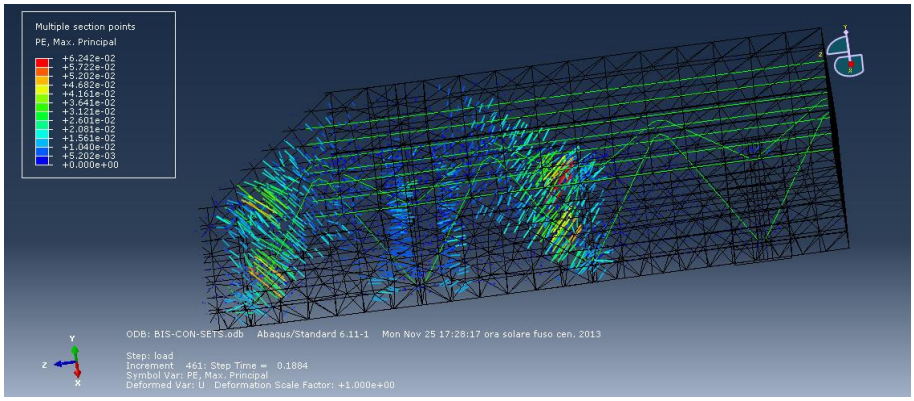

c)

Figure 6.24. Crack pattern at failure: a) frontal view; b) top view; c) axonometric view.

Also the stress state in the concrete corresponding to the control section has been analyzed in order to understand the equilibrium of the free body diagram of the beam in the configuration at failure corresponding to the section in which the main diagonal crack develops. Particularly, Figure 6.25 shows the trend of the tensile stresses in the concrete referred to a local system placed on the plane containing the control section: the tensions are higher on the bottom of the beam where they almost reach the maximum tensile strength equal to f_t = 2.57 MPa implemented in the costitutive behavior of the tensile concrete. The free body diagram of the beam is thus represented in Figure 6.26.

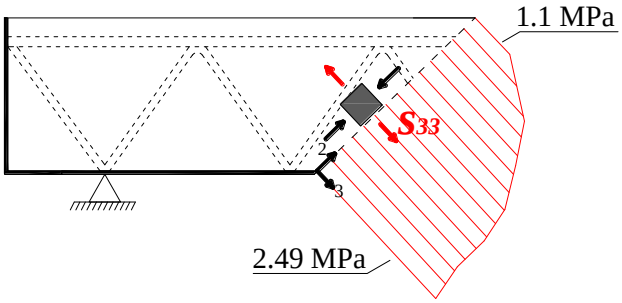

Figure 6.25. Stress state of the concrete in the control section at failure: tensile stresses S33.

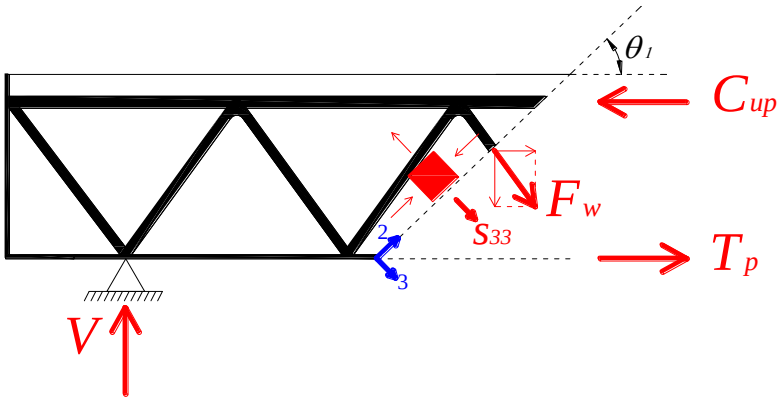

Figure 6.26. Free body diagram of the beam of Model Size 1.

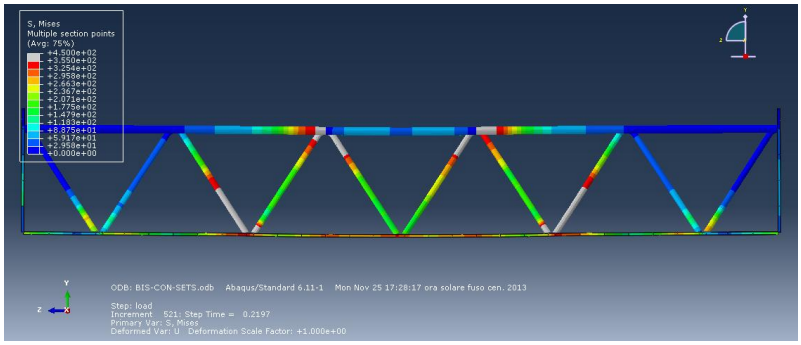

a)

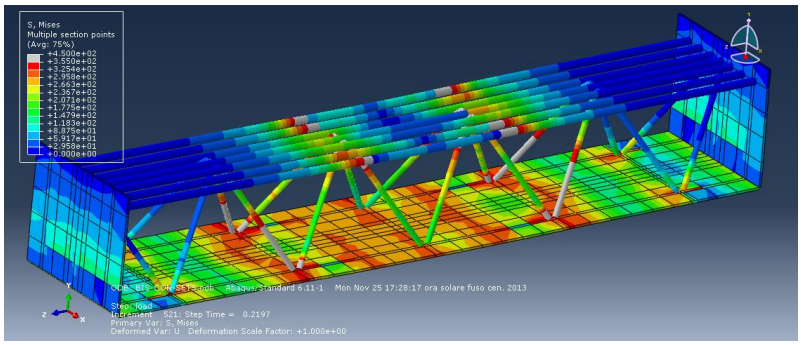

b)

Figure 6.27. Configuration of the steel members in STEP N°6: a) frontal view; b) axonometric view.

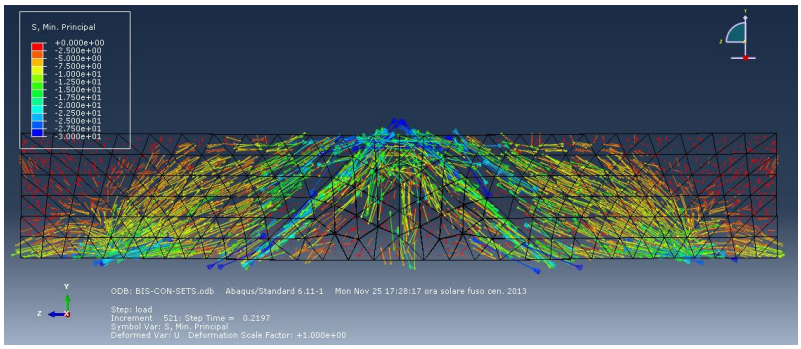

Figure 6.28. STEP N°6: minimum principal stresses.

The following analyzed phase is *STEP N°6* in which the steel constituting the upper chord yields almost immediately after the achievement of the maximum load. Figures 6.27a and 6.27b show respectively the frontal and the axonometric view of the configuration of the steel members: the location of all plastic hinges in the rebars is clearly distinguishable.

In the same time, the progressive reduction of the minimum principal stresses in the concrete is depicted in Figure 6.28 and the corresponding increase of the damage variable is shown in the following Figure 6.29. As well as the damage in the compressed strut, also the maximum plastic principal strains are increasing. Their magnitude and extension is shown in Figure 6.30 and the direction of the strain vectors in Figure 6.31: the diagonal cracks continue growing while the initial sub-vertical flexural cracks assume a width progressively negligible if compared with the diagonal fractures.

STEP N°7 corresponds to an intermediate phase between the moment in which the value of P_{max} is achieved and the end of the analysis. In this configuration the stress in the steel exceeds the yielding stress both in the diagonal bars and in the upper chord, entering in the hardening branch of the constitutive behavior (Figure 6.32). As regards the concrete, the magnitude of the minimum principal stress keeps on reducing (Figure 6.33) and, on the other hand, the damage keeps on increasing both in intensity and extension (Figure 6.34).

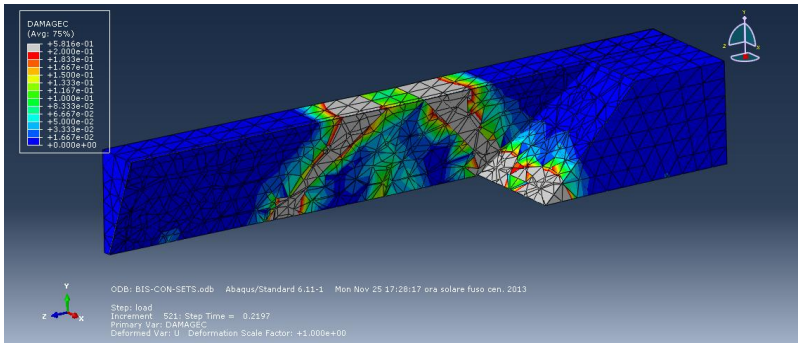

Figure 6.29. STEP N°6: magnitude of the damage variable.

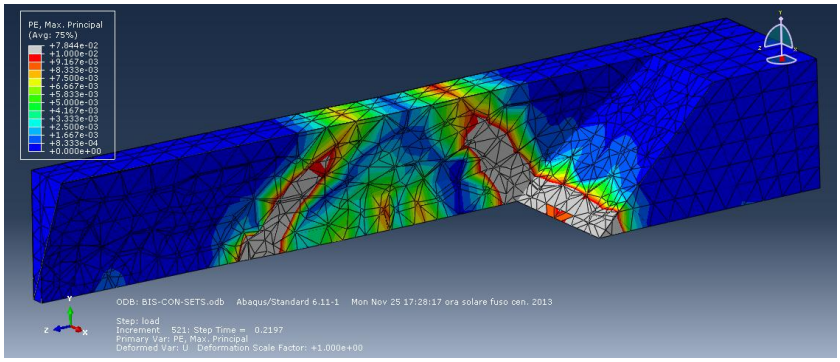

Figure 6.30. STEP N°6: magnitude of the maximum principal strains.

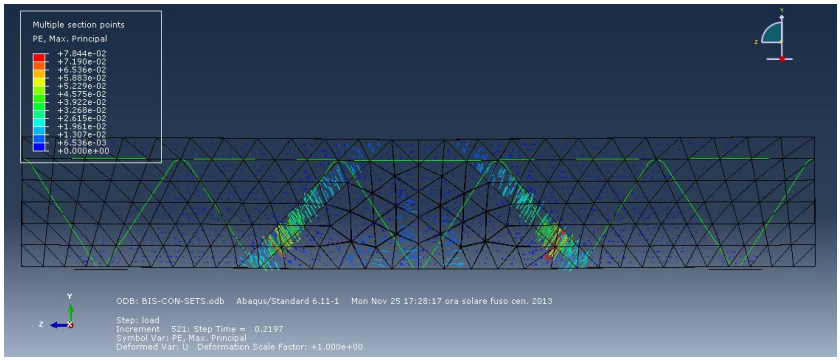

Figure 6.31. STEP N°6: frontal view of the crack pattern.

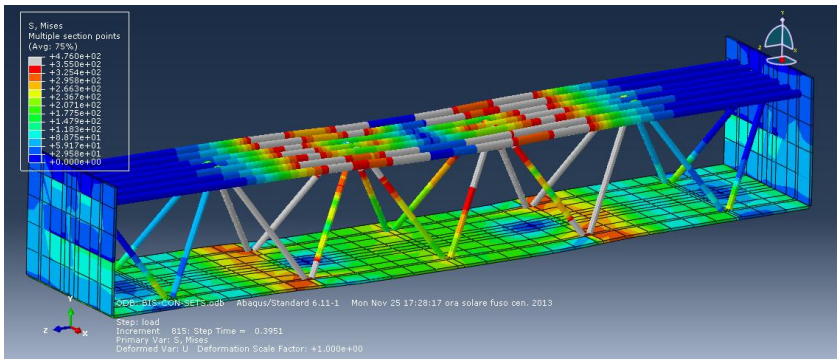

Figure 6.32. Configuration of the steel members in STEP N°7: axonometric view.

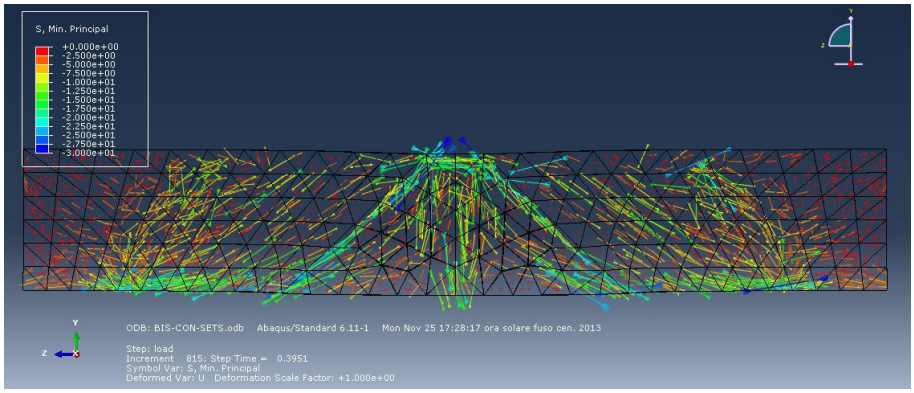

Figure 6.33. STEP N°7: minimum principal stresses in the concrete.

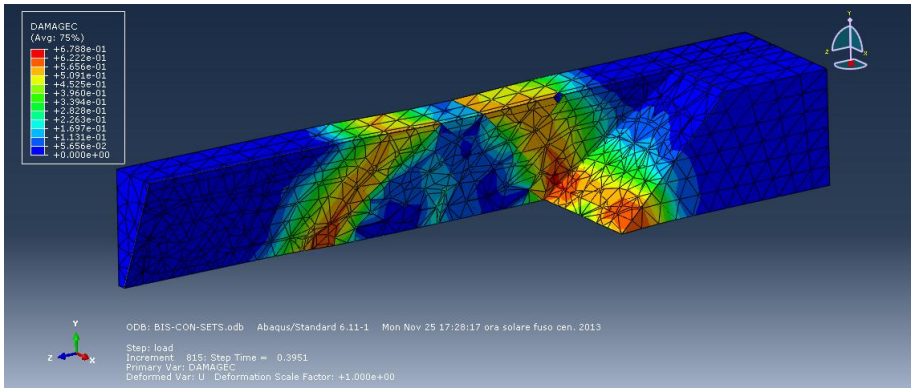

Figure 6.34. STEP N°7: magnitude of the damage variable.

The crack pattern is not significantly changed, the width of the cracks keeping on growing (Figure 6.35a-b-c). Finally STEP N°8 corresponds to the configuration of the beam at the end of the analysis. Figure 6.36 shows the von Mises stresses in the deformed steel members highlighting the diagonal bars that more contribute to the response. The minimum principal stresses decrease (Figure 6.37) and the damage variable reaches the maximum value equal to 0.855 (Figure 6.38). The maximum magnitude of the plastic principle strains is considerably higher than the value achieved in the previous step. The crack pattern is identifiable also further than the main diagonal crack and it is qualitatively comparable with the configuration of the specimen at the end of the experimental test (Figure 6.39a-b-c).

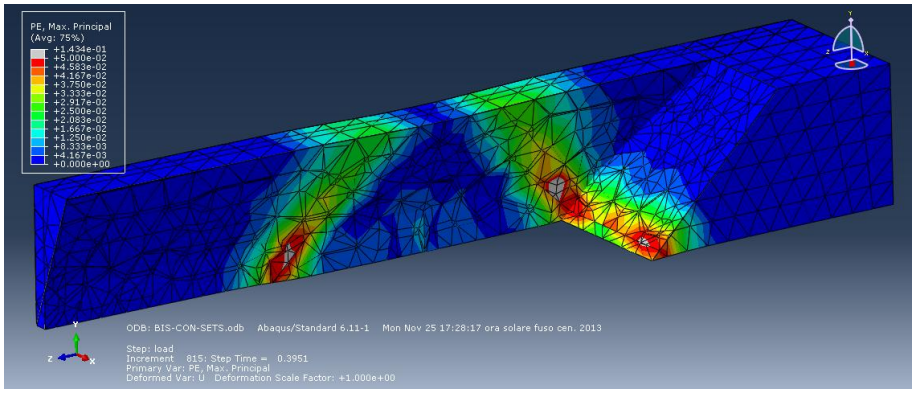

a)

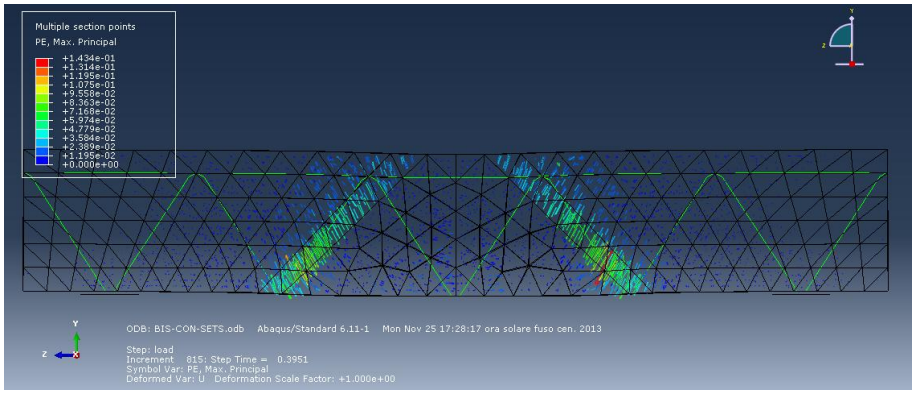

b)

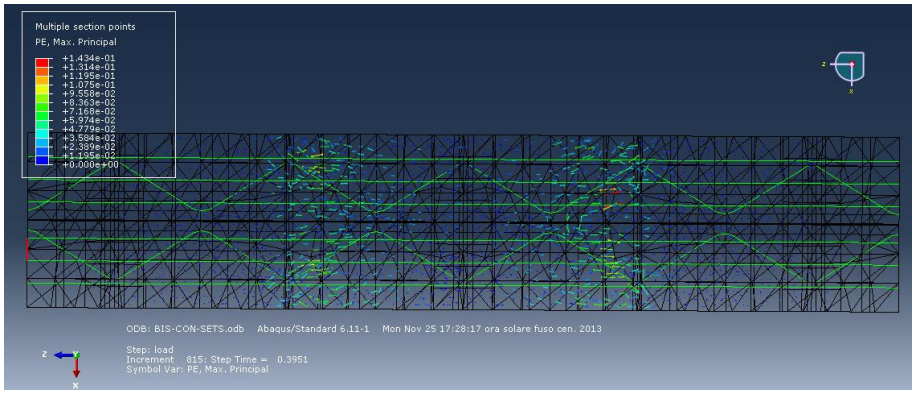

c)

Figure 6.35. Crack pattern in STEP N°7: a) axonometric view; b) frontal view; c) top view.

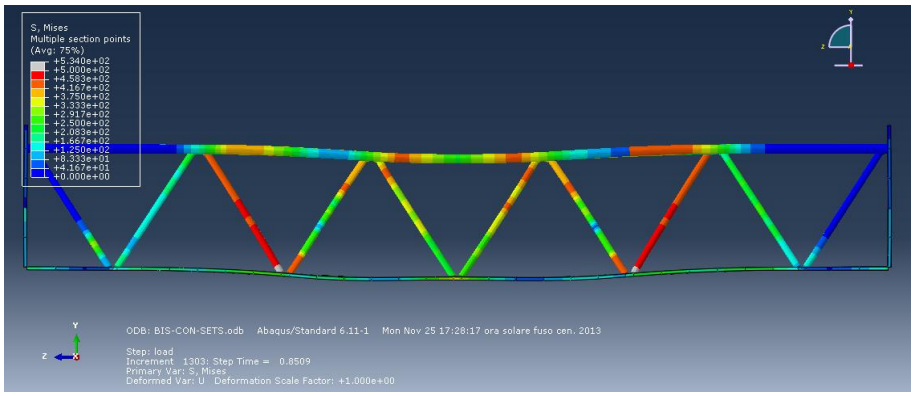

Figure 6.36. Configuration of the steel members in STEP N°8.

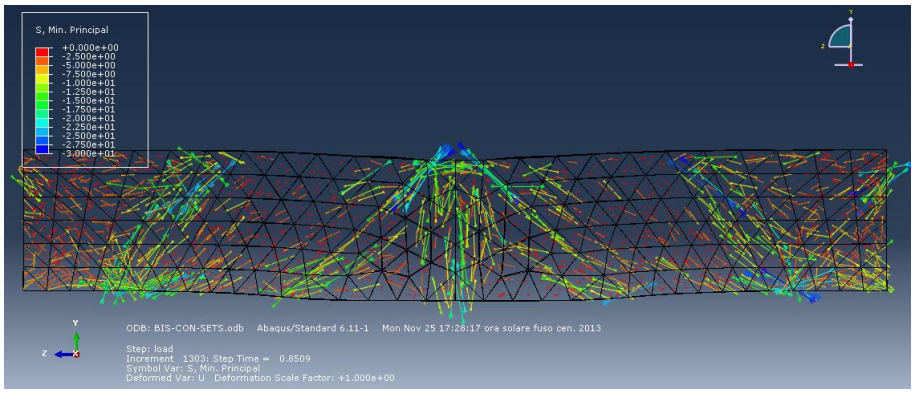

Figure 6.37. STEP N°8: minimum principal stresses in the concrete.

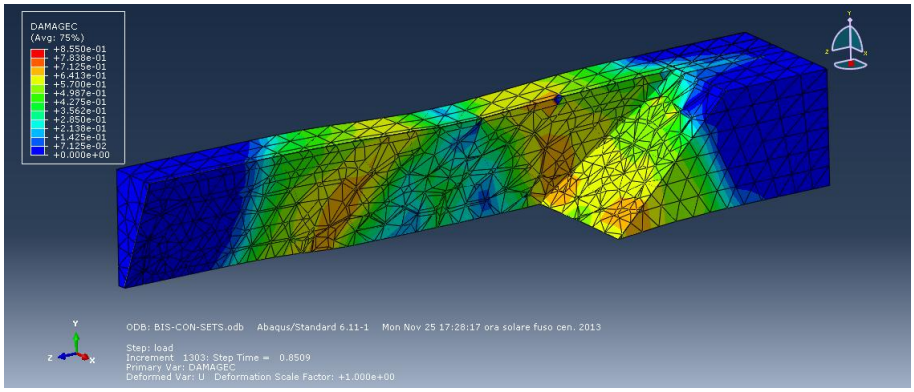

Figure 6.38. STEP N°8: damage variable in the compressed concrete.

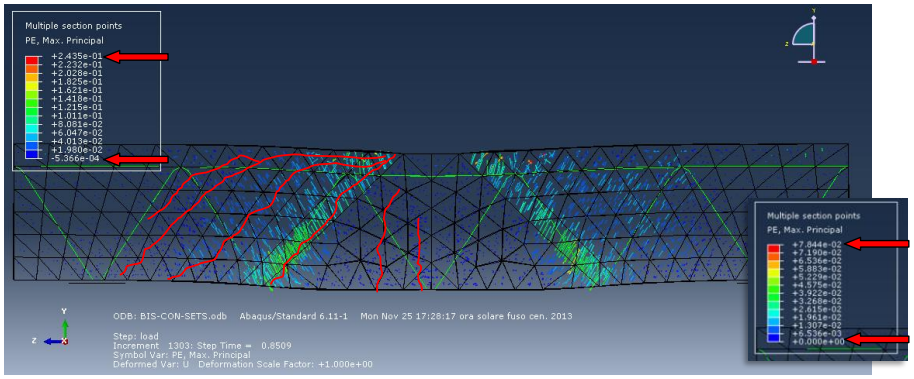

a)

b)

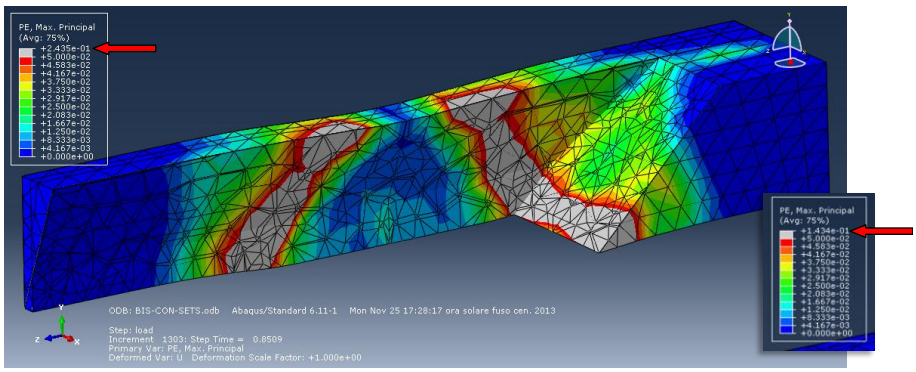

c)

Figure 6.39. Crack pattern at the end of the analysis and comparison with the experimental evidence: a) frontal view of the numerical cracks; b) picture of specimen A1-2 at the end of the test; c) magnitude and extension of the numerically predicted cracks.

6.2.2 Model Size 2

Figure 6.40 summarizes the geometric features of the model also indicating two control sections: "control section 1" corresponds to the midspan of the beam, "control section 2" represents the diagonal direction.

The load-displacement curve in Figure 6.41 shows that, after the achievement of the peak load equal to 540.12 kN, the beam exhibited a large ductile branch until a displacement of about 34 mm after which a sub vertical response is observed with a sudden loss of bearing capacity until a load value of about 180 kN. Such a beam, therefore, exhibits a ductile global behavior followed by a sudden fragile failure.

The markers on the curve represent eight main characteristic steps of the load history that are described in the follow.

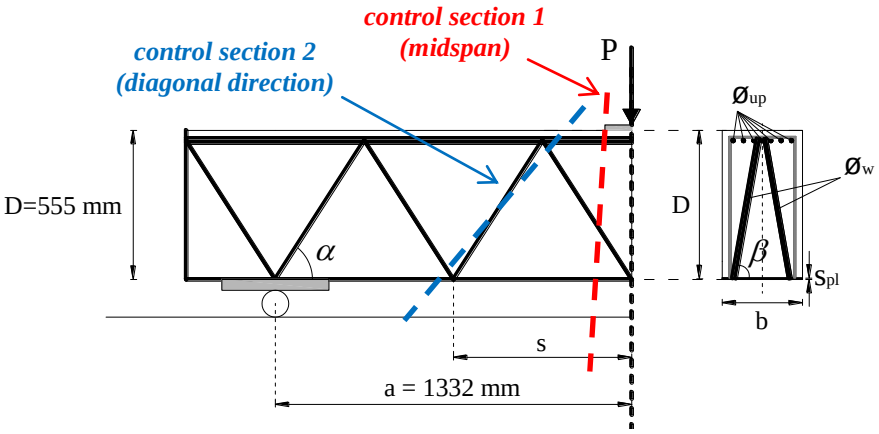

a/D	a	D	b	∅w	∅up	spl	s	α	β
2.4	**1332**	**555**	300	12	16	5	**666**	**57.2°**	**80.8°**

Figure 6.40. Geometry of the beam and boundary conditions for Model Size 2.

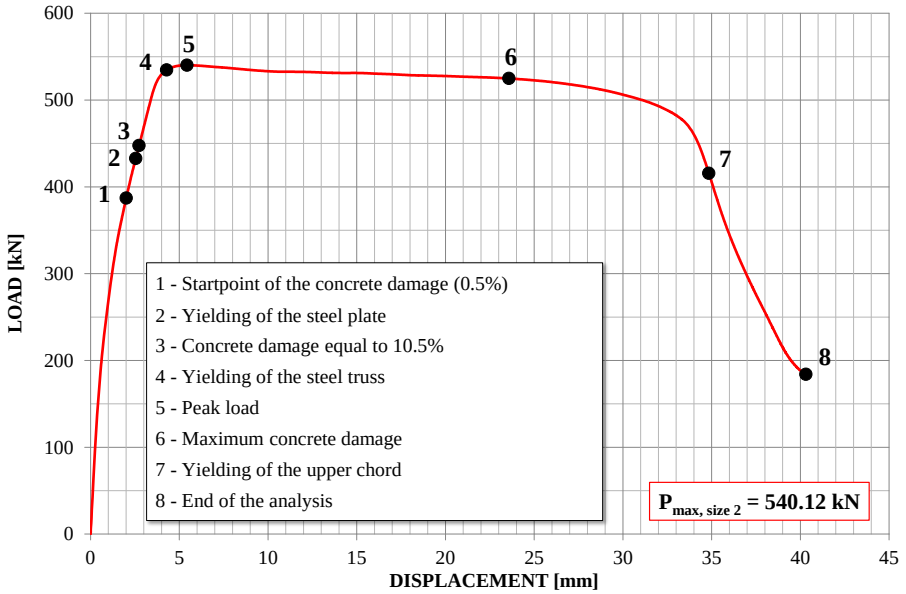

Figure 6.41. Load-displacement curve of Model Size 2.

STEP N°1 corresponds to the phase in which the compressed concrete enters its post-elastic behavior and, thus, the damage variable achieves the corresponding value of 0.005.

In this configuration all steel members are elastic as shown in Figure 6.42. As regards the concrete, from Figure 6.43 it can be observed that, at the end of the compressed strut, corresponding to the applied load, the stress starts to assume the values between 18 and 22 MPa which correspond to the beginning of the inelastic behavior. The damage variable (Figure 6.44) of the compressed concrete, thus, starts to assume values between 0 and 0.5% corresponding to the midspan of beam which are also due to the action of the bottom steel plate against the concrete: the kinematic of truss, in fact, develops so that the steel plate is pulled upward by the two central diagonal bars, inducing a local compression on the concrete (Figure 6.45).

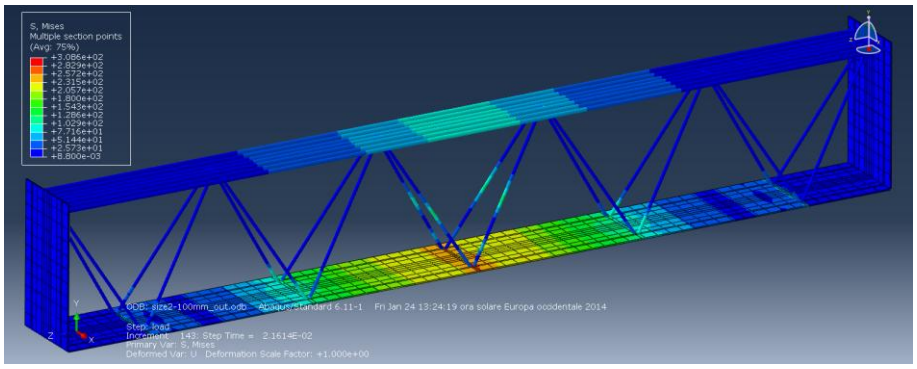

Figure 6.42. Step N°1: magnitude of the von Mises stresses in the steel members.

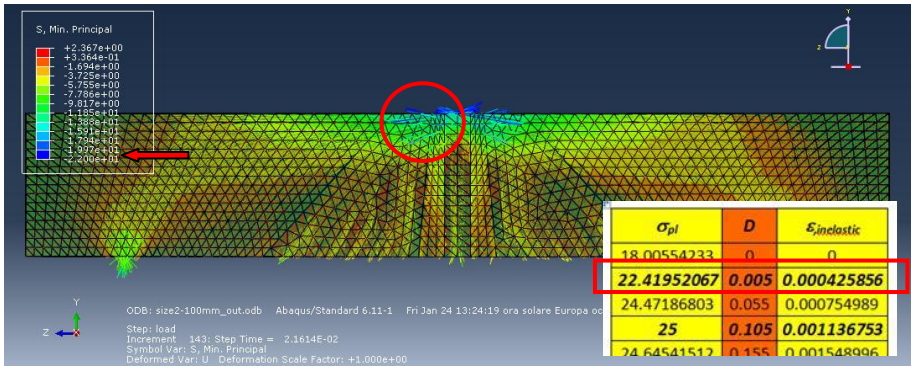

σ_{pl}	D	$\varepsilon_{,inelastic}$
18.00554233	0	0
22.41952067	**0.005**	**0.000425856**
24.47186803	0.055	0.000754989
25	**0.105**	**0.001136753**
24.64541512	0.155	0.001548996

Figure 6.43. Step N°1: direction of minimum principal stresses in the concrete.

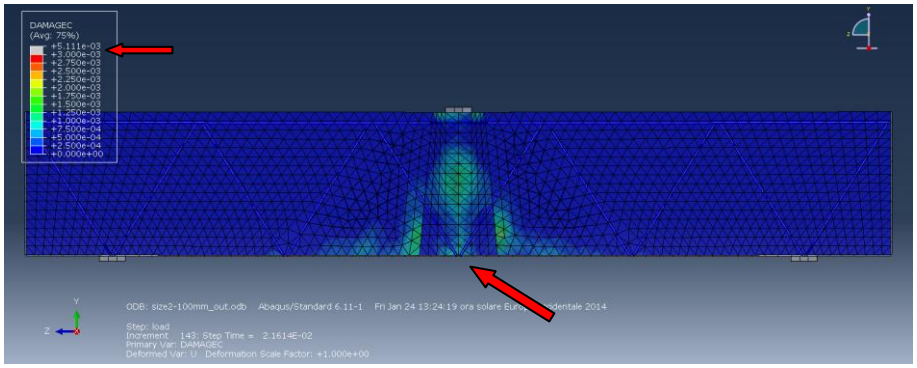

Figure 6.44. Step N°1: damage variable magnitude.

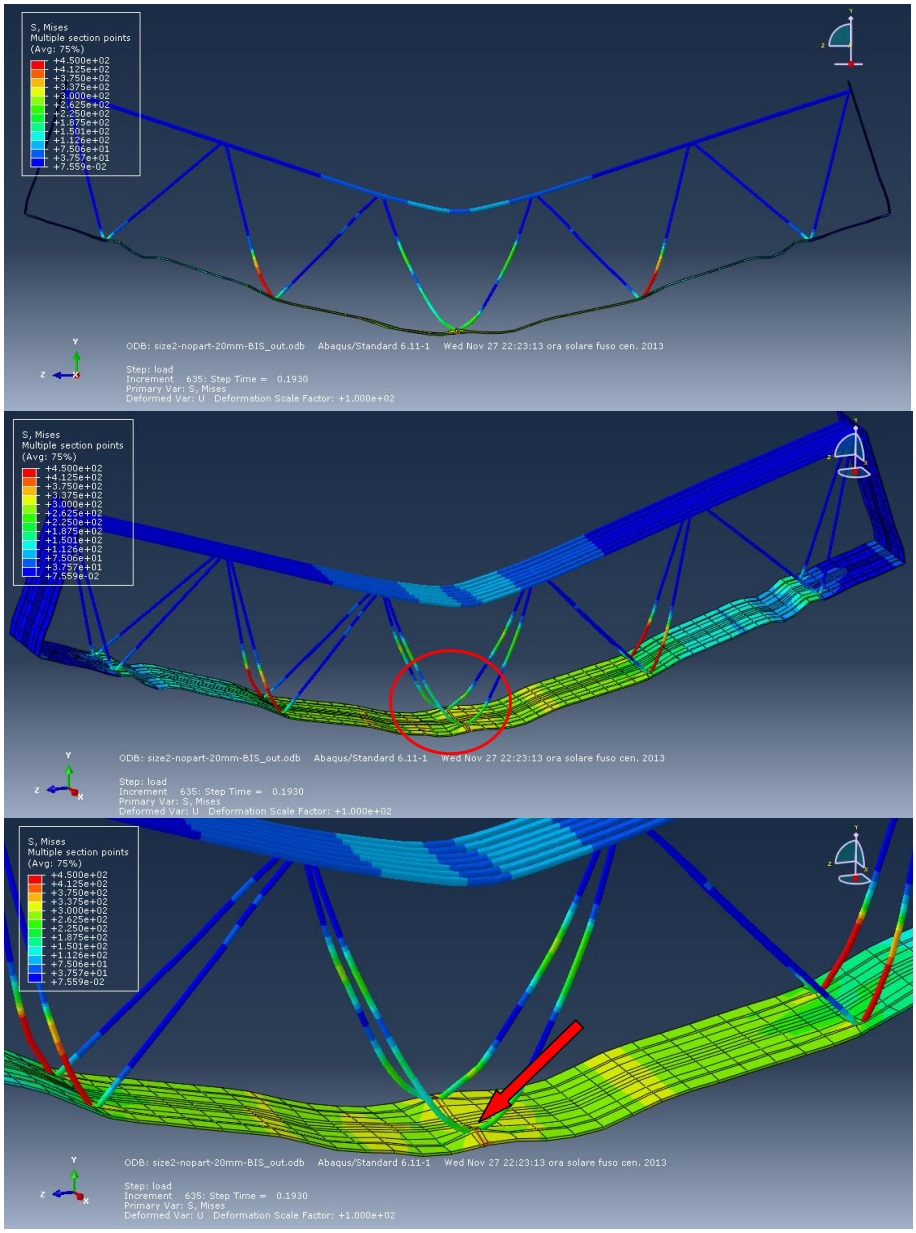

Figure 6.45. Amplified deformed shape of the steel members showing the kinematic of the truss.

The direction of the maximum principal plastic strains represented in Figure 6.46a allows to obtain a graphical visualization of the cracking pattern: as already observed for Model Size 1, the first flexural sub-vertical cracks appear in the midspan of the beam that is corresponding to "control section 1"; furthermore, also the cracks in the diagonal direction are developing but their width is much smaller than the vertical fractures. As shown in the cut 3D view of Figure 6.46b, such cracks cross the entire width of the beam.

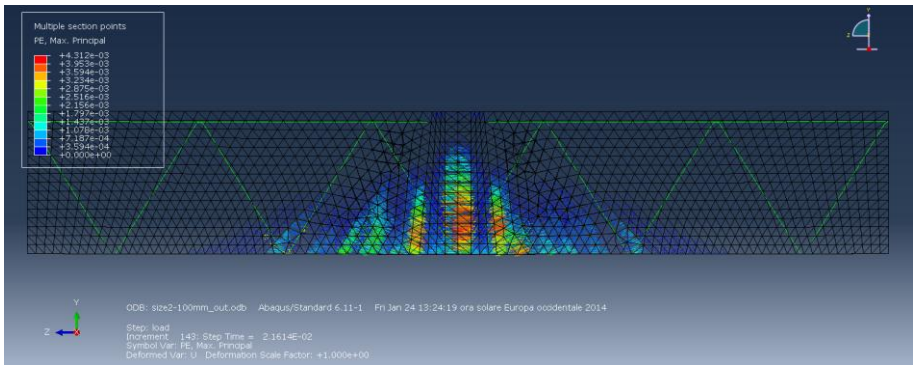

a)

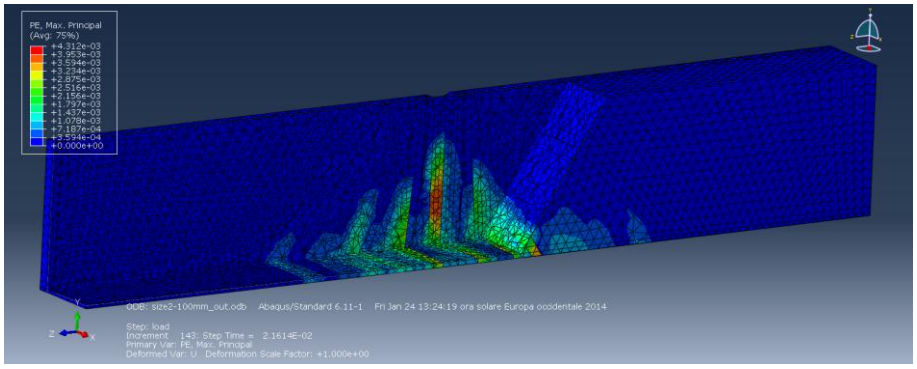

b)

Figure 6.46. Maximum principal strains in Step N°1: a) direction in the frontal view; b) magnitude and extension in the axonometric view.

STEP N°2 corresponds to the phase in which the yielding is achieved in the bottom steel plate. Since such step is close to the following *STEP N°3*, only the latter is herein described.

In *STEP N°3* the stress in the compressed concrete begins to achieve the maximum value of 25 MPa locally next to the point where the load is applied and, therefore, the damage variable starts to assume the corresponding value of 10.5%. In this configuration, the status of the steel members is represented in Figure 6.47, showing how the yielding is achieved only in the midspan of the bottom plate while all other elements are still elastic.

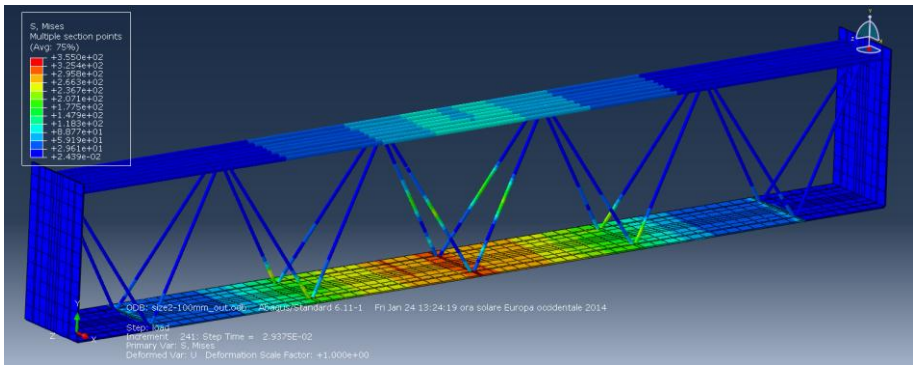

Figure 6.47. Step N°3: magnitude of the von Mises stresses in the steel members.

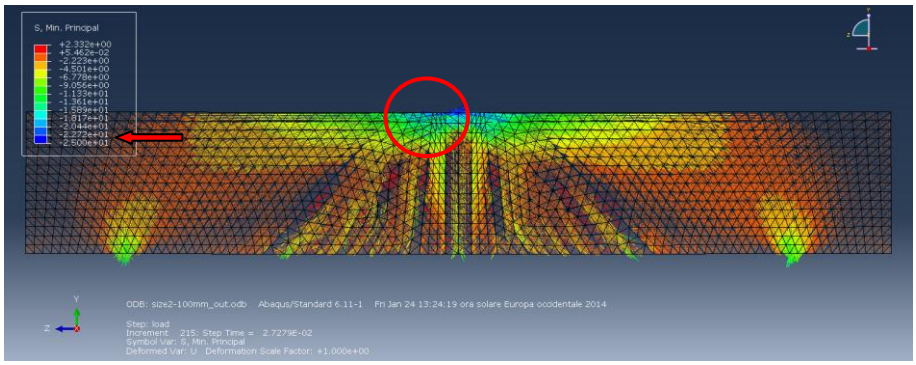

Figure 6.48. Step N°3: direction of minimum principal stresses in the concrete.

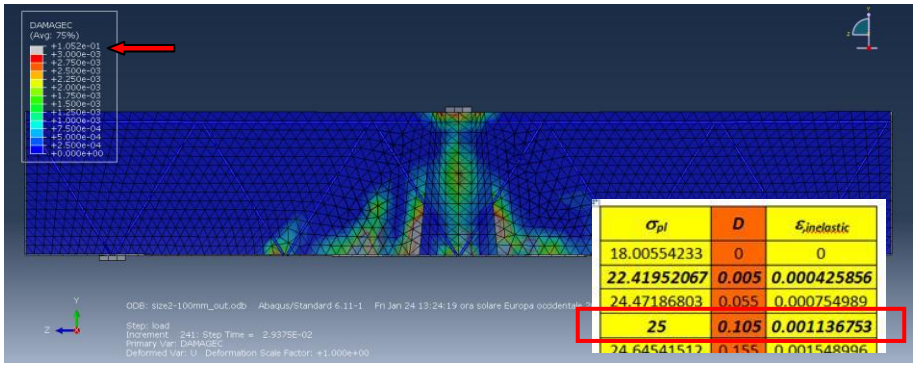

σ_{pl}	D	$\varepsilon_{inelastic}$
18.00554233	0	0
22.41952067	***0.005***	***0.000425856***
24.47186803	0.055	0.000754989
25	***0.105***	***0.001136753***
24.64541512	0.155	0.001548996

Figure 6.49. Step N°3: damage variable magnitude.

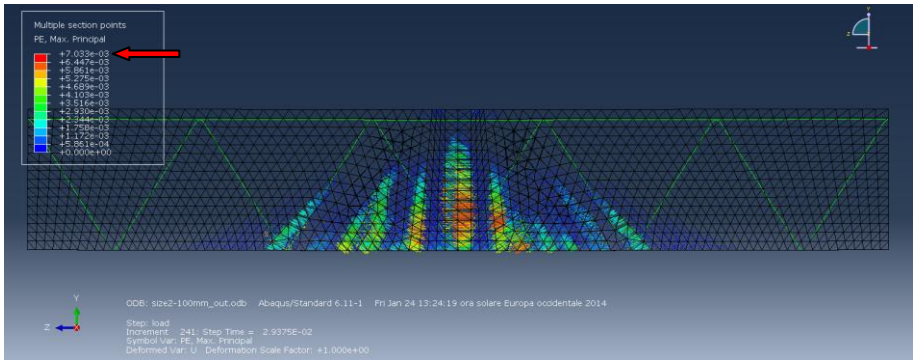

a)

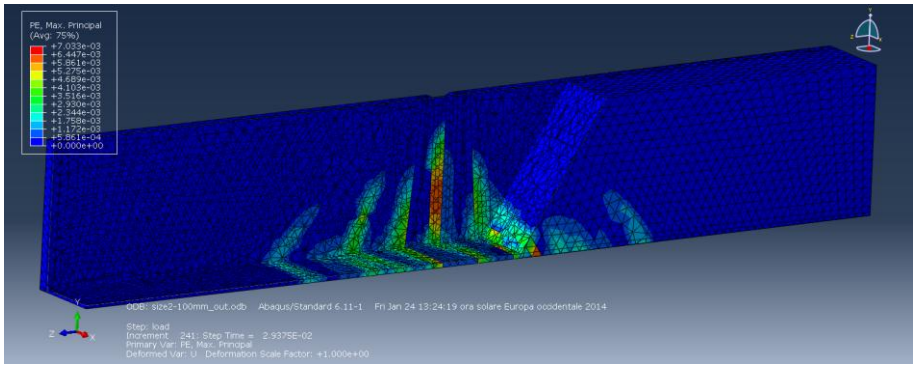

b)

Figure 6.50. Maximum principal strain in Step N°3: a) direction; b) magnitude.

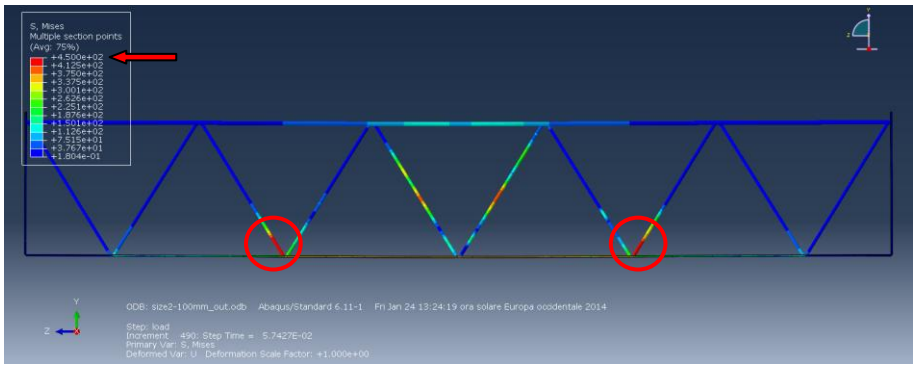

Figure 6.51. Magnitude of the von Mises stresses in the steel members in Step N°5.

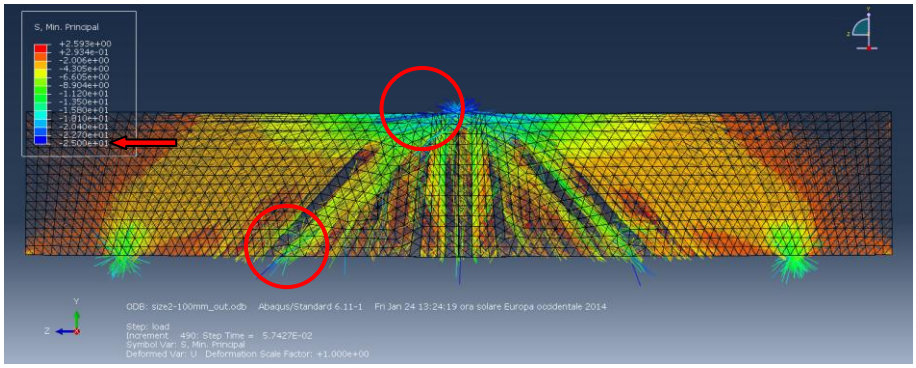

Figure 6.52. Step N°5: direction of minimum principal stresses in the concrete.

The direction and magnitude of the minimum compressive stresses is shown in Figure 6.48 where the portion of concrete in which they are locally achieving the maximum value is indicated. In the same time the damage in the compressed concrete evolves in magnitude and extension (see Figure 6.49) and the sub-vertical cracks grow so that the maximum intensity of the vector of the plastic strains is almost double than in the previous step (see Figure 6.50a). The cut axonometric view allows to observe that the cracks are growing through the width of the beam.

In the following *STEP N°4* the yielding of the steel truss occurs. This step is immediately close to *STEP N°5* in which the peak load is achieved and, thus, in the follow, only the latter will be described.

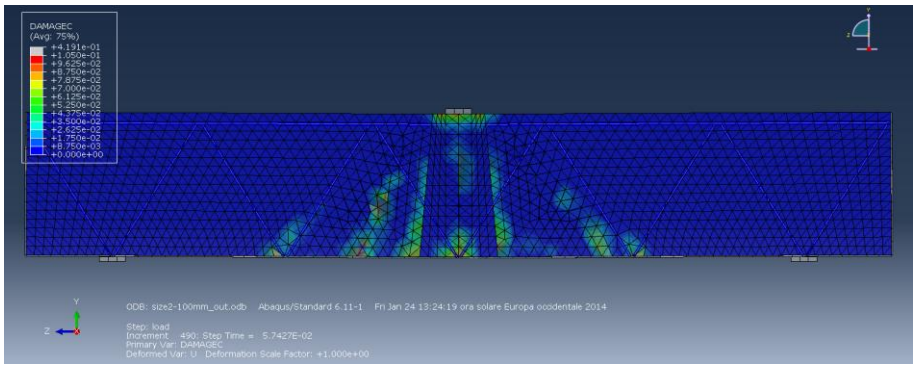

Figure 6.53. Step N°5: damage variable magnitude.

The stress state in the steel members during *STEP N°5* is represented in Figure 6.51: it can be observed that the tensile diagonal rebars of the second mesh of the truss are yielded.

In this step the minimum principal stress in the concrete approaches the maximum value implemented in the compressive constitutive behavior also in the inferior end of the compressed strut (Figure 6.52). The intensity of the damage variable grows with respect to the previous steps corresponding to both the control section 1 and 2 (Figure 6.53) and the same trend can be observed with regard to the crack pattern showed in Figure 6.54. However it is worth to note that the main cracks are the sub-vertical ones in the midspan of the beam (control section 1), being their width higher than the values corresponding to the diagonal direction. Moreover, from Figure 6.54c it can be observed the slope of the planes containing all fractures.

Thus, as well as already done for Model Size 1, the stress state in the concrete corresponding to the main control section (that is control section 1) has been analyzed in order to understand the equilibrium of the beam in the configuration corresponding to the peak load. Particularly, Figure 6.55 shows the trend of the tensions in the concrete referred to a local system placed on the plane containing the control section 1 (midspan): at the bottom of the beam, the tensile stresses reach the value of the maximum tensile strength equal to f_{ct} = 2.57 MPa. The free body diagram of the beam is thus represented in Figure 6.56.

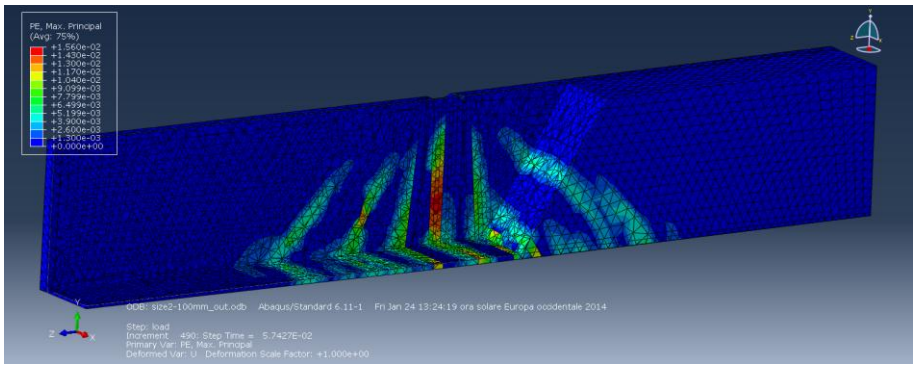

a)

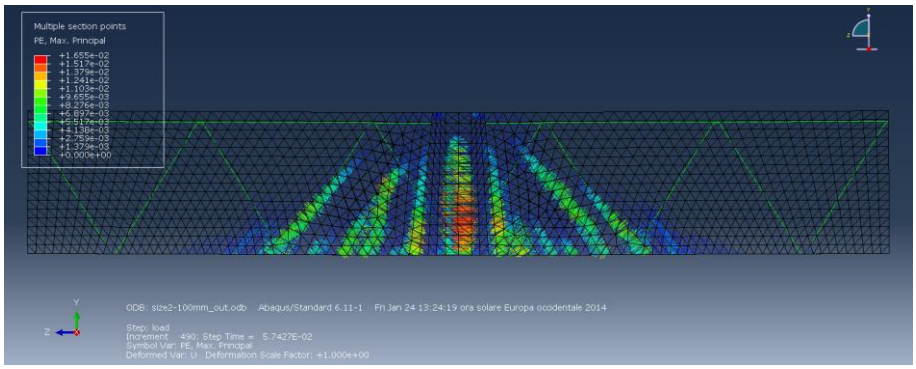

b)

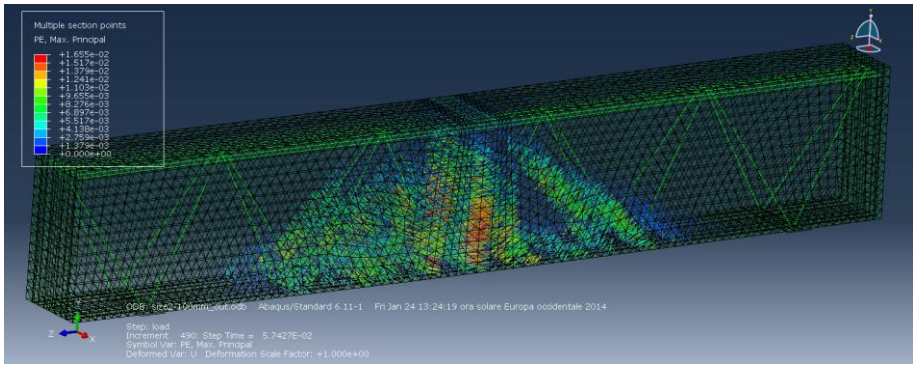

c)

Figure 6.54. Magnitude and direction of the maximum principal strain in Step N°5: a) axonometric view of the magnitude; b) frontal view of the direction; c) axonometric view of the direction.

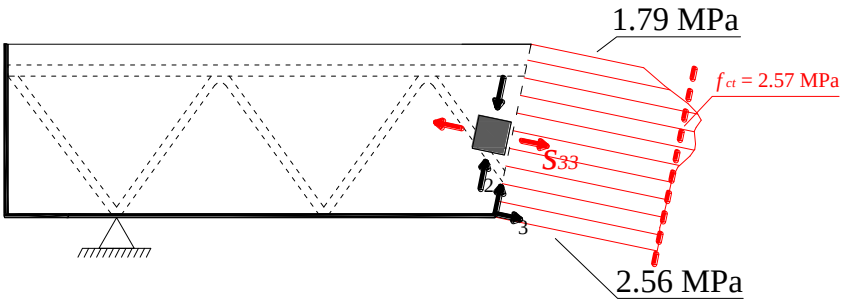

Figure 6.55. Stress state of the concrete in the control section 1 (midspan) corresponding to the peak load: tensile stresses S33.

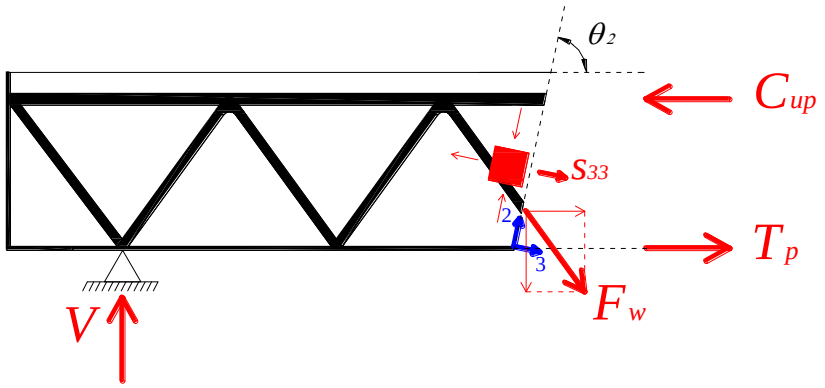

Figure 6.56. Free body diagram of the beam of Model Size 2.

The following analyzed step is *STEP N°6* which corresponds to the phase within the horizontal branch of the load-displacement curve in which the damage in the compressed concrete reaches the maximum value equal to 85.5%.

Figure 6.57 shows the details of the configuration of the steel members: the yielding of the diagonal tensile bars of the first mesh is reached and, furthermore, in some cross-sections the stress already exceeds the yielding value showing that the steel is behaving according to the hardening branch of the constitutive law.

The slope of the compressed concrete strut is clearly identifiable through the plot of the minimum principal stresses in the concrete (Figure 6.58) as well as from the corresponding damage variable which is represented in Figure 6.59a. Figure 6.59b, allows to observe that the damage involves the concrete throughout the whole width of the beam exhibiting the highest magnitude in the midspan.

The crack pattern evolution continues to prove that the main cracks are the vertical ones which correspond to control section 1, developing through all the width of the beam (Figure 6.60).

The following analyzed phase is *STEP N°7* which represents the yielding of the upper chord of the steel truss.

Figure 6.61 shows the detail of the configuration of all steel members while in Figure 6.62 the evolution of the minimum principal stresses in the concrete is represented.

The damage variable in Figure 6.63a-b shows a local crushing of the concrete corresponding to the applied load and proves that the maximum damage is concentrated corresponding to the midspan of the beam even if it can also be observed along the diagonal direction with a lower intensity.

As well as the damage in the compressed concrete, also the maximum plastic principal strains are increasing in the control section 1 and the local cracks next to the loaded plate increase (Figure 6.64a-b).

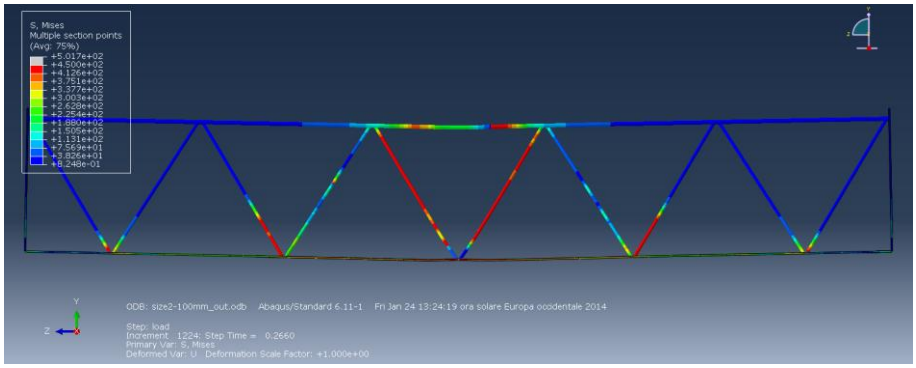

Figure 6.57. Configuration of the steel members in Step N°6.

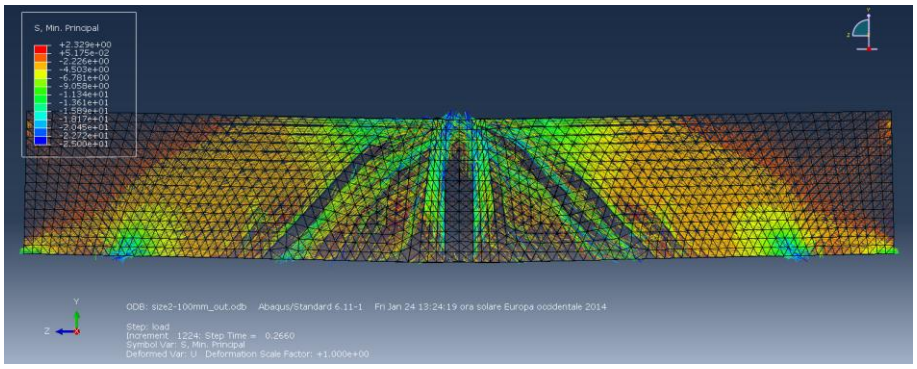

Figure 6.58. Minimum principal stresses in the concrete in *STEP N°6*.

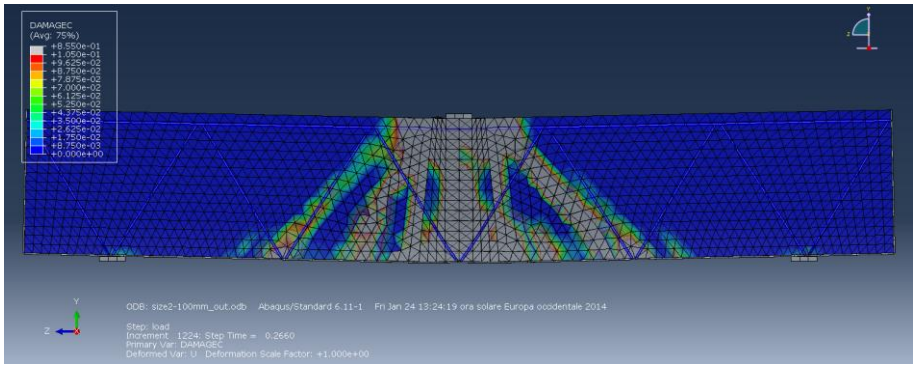

a)

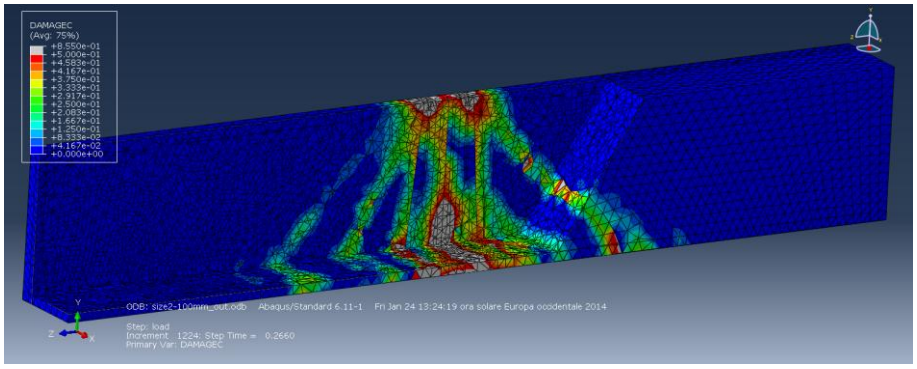

b)

Figure 6.59. Damage variable in Step N°6: a) frontal view; b) axonometric view.

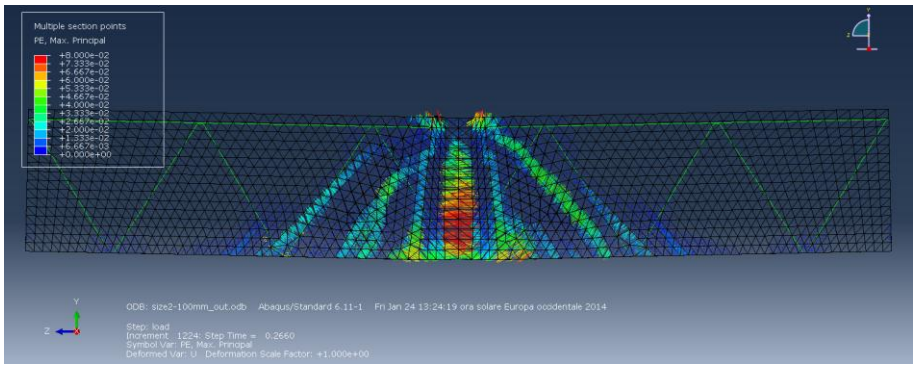

a)

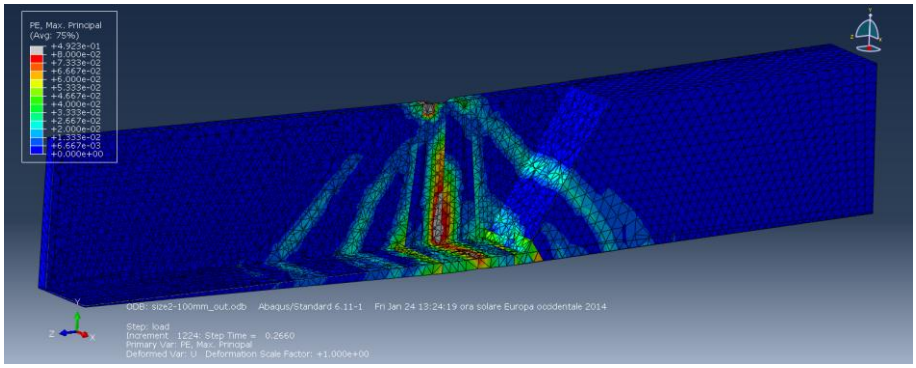

b)

Figure 6.60. Crack pattern in Step N°6: a) frontal view; b) axonometric view.

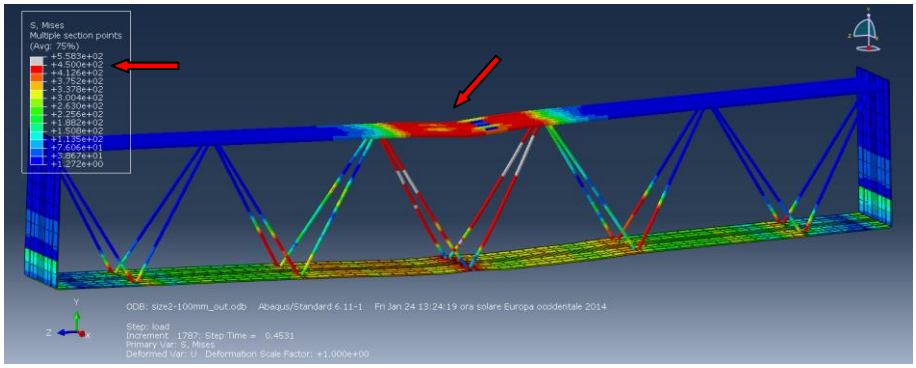

Figure 6.61. Configuration of the steel members in STEP N°7.

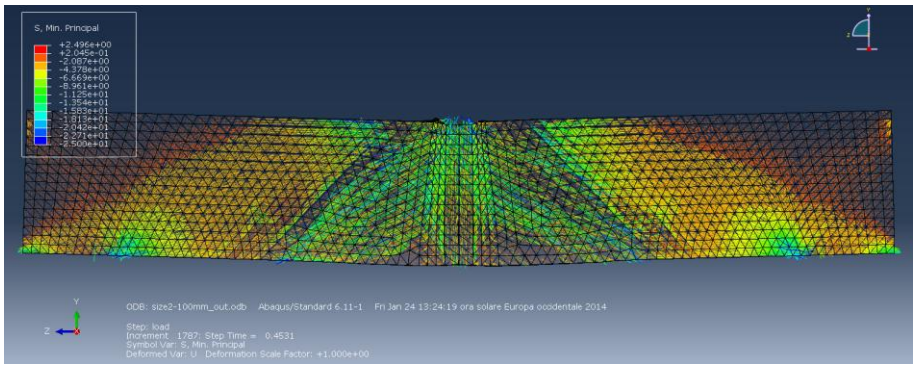

Figure 6.62. STEP N°7: minimum principal stresses in the concrete.

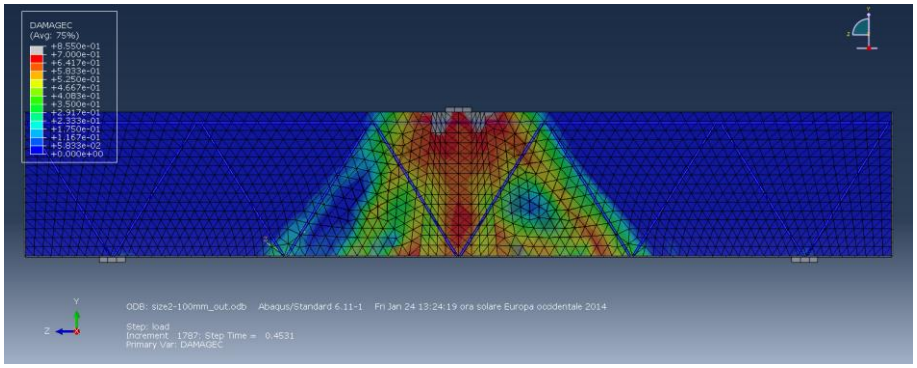

a)

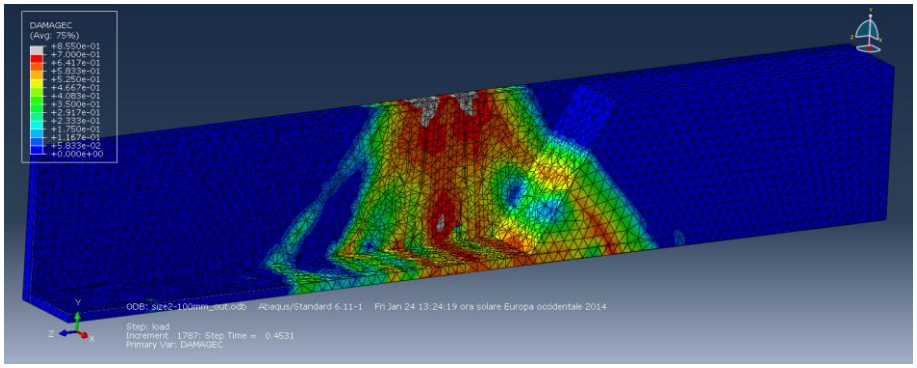

b)

Figure 6.63. Magnitude of the damage variable in STEP N°7: a) frontal view; b) axonometric view.

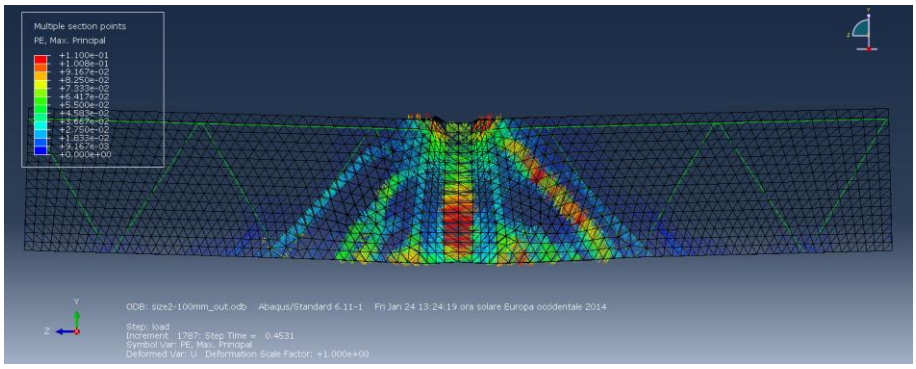

a)

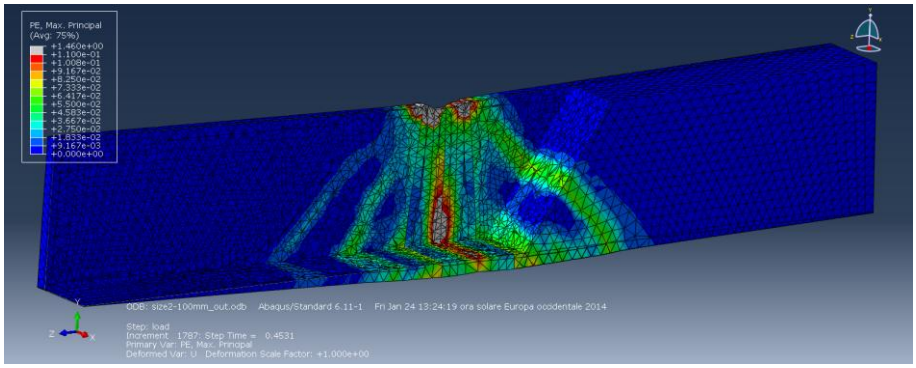

b)

Figure 6.64. Maximum principal strains in STEP N°7: a) directions in the frontal view; b) magnitude in the axonometric view.

Finally, the last phase is *STEP N°8* which corresponds to the end of the analysis. In this configuration the steel of all members is following the hardening branch of the constitutive law (Figure 6.65) which allowed the ductile global behavior of the structural system during the analysis.

Figure 6.66 shows the direction of the minimum principal stresses in the concrete and Figure 6.67 represents the diffusion of the damage with the crushing of the concrete in the midspan of the beam. The corresponding crack pattern is represented in Figure 6.68 in terms of maximum plastic

principal strains. The numerical prediction of the mechanical response of the beam is thus suggesting a crack pattern in the final configuration characterized by wide central fractures caused by the crushing of the concrete, also favored by the kinematic of the truss, with few diagonal cracks of smaller width and length.

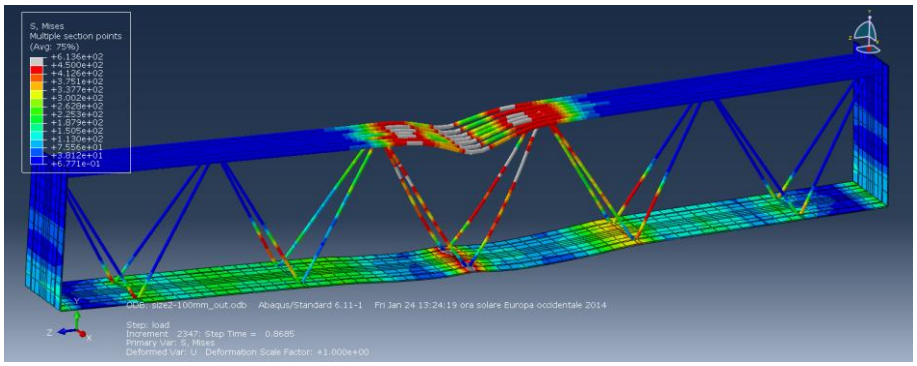

Figure 6.65. Configuration of the steel members in STEP N°8.

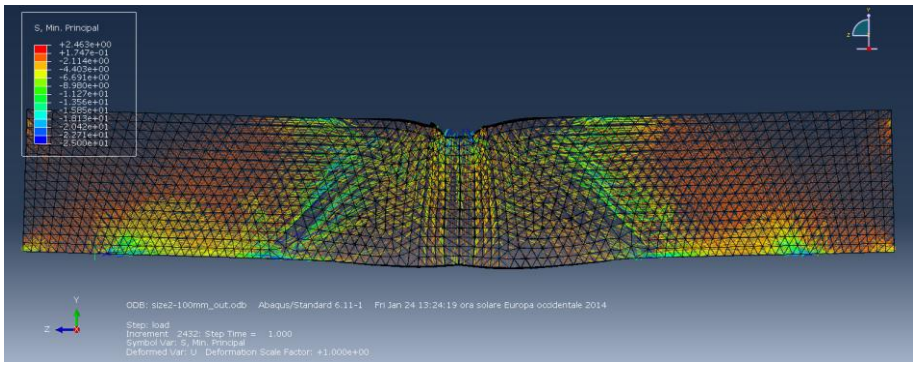

Figure 6.66. STEP N°8: minimum principal stresses in the concrete.

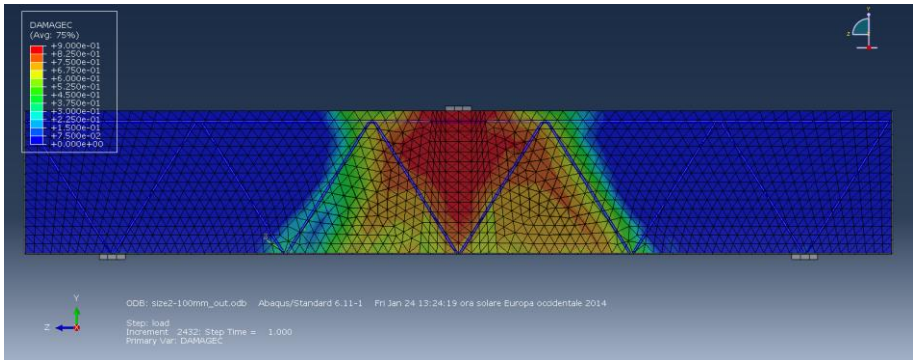

Figure 6.67. Magnitude and extension of the damage variable in STEP N°8.

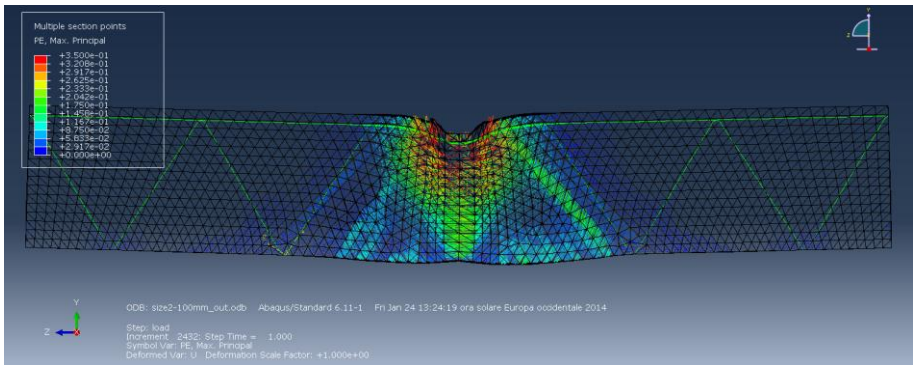

a)

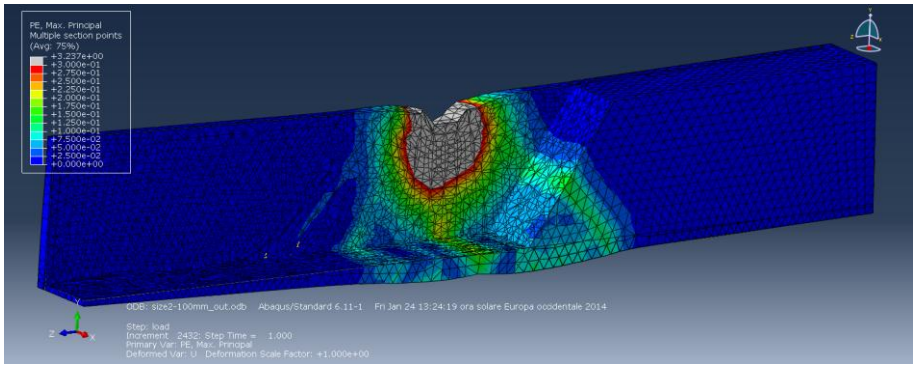

b)

Figure 6.68. Crack pattern in STEP N°8: a) frontal view; b) axonometric view.

6.2.3 Model Size 3

Figure 6.69 summarizes the geometric features of the model and shows the direction along which the main cracks develop.

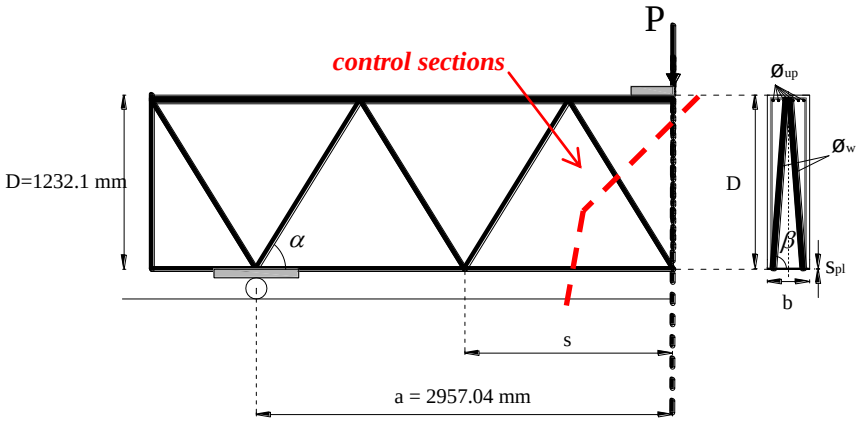

a/D	a	D	b	∅ w	∅ up	s pl	s	α	β
2.4	**2957.04**	**1232.1**	300	12	16	5	**1478.52**	**58.15°**	**86°**

Figure 6.69. Geometry of the beam and boundary conditions for Model Size 3.

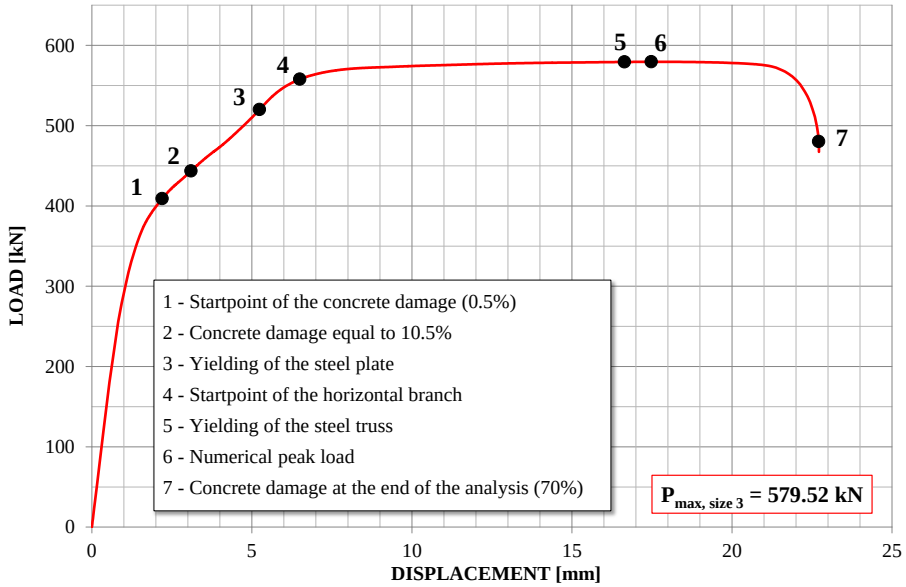

Figure 6.70. Load-displacement curve of Model Size 3.

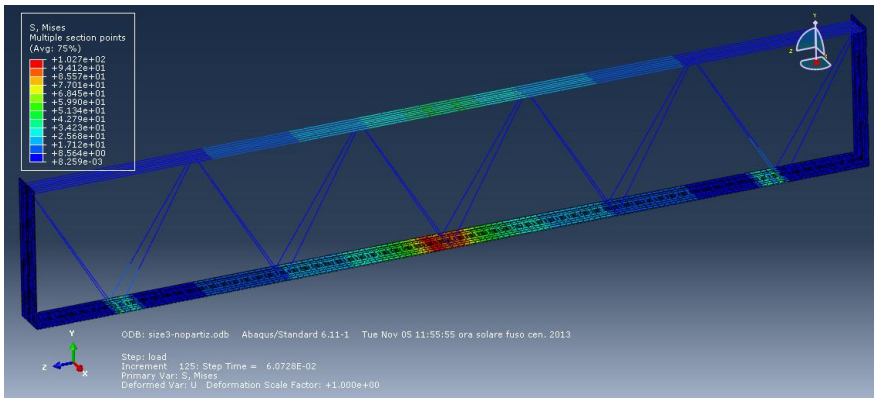

Figure 6.71. Step N°1: magnitude of the von Mises stresses in the steel members.

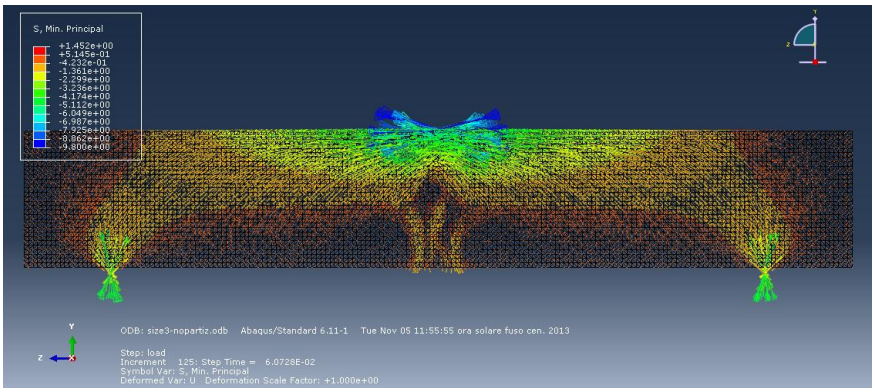

Figure 6.72. Step N°1: direction of minimum principal stresses in the concrete.

The load-displacement curve in Figure 6.70 shows that the beam exhibited a global ductile behavior during the simulation, as already observed also in Model Size 2, but with a maximum displacement of 23 mm after which a sudden loss of load occurred denoting a fragile failure of the structural system. The markers on the curve represent seven main characteristic steps of the load history that are described in the follow.

STEP N°1 corresponds to the phase in which the damage variable locally achieves the value of 0.005. In this configuration all steel members are elastic as shown in Figure 6.71. As regards the concrete, from Figure 6.72 it

can be observed that, at the end of the compressed strut, corresponding to the applied load, the stress is steel lower than 18 MPa which corresponds to the beginning of the inelastic behavior. The damage variable of the compressed concrete (Figure 6.73) assumes a value higher than zero just corresponding to the bottom of beam in the midspan because of the action of the bottom steel plate against the concrete as already observed in Model Size 2. Sub-vertical cracks appear in the midspan of the bottom of the beam crossing the all width (Figure 6.74a). Diffuse microcracks appear on the bottom of the beam corresponding to the first mesh of the truss (Figure 6.74b).

STEP N°2 corresponds to the phase in which the damage variable locally achieves the value of 0.105. The configuration of the steel members, all elastic, is represented in Figure 6.75. As regards the concrete, the minimum compressive stresses are going to locally achieve the maximum value corresponding to the peak of the compressive constitutive behavior, as shown in Figure 6.76. The damage in the compressed concrete, however, is still confined to the midspan of the beam corresponding to the sub-vertical cracks (Figure 6.77) which are considerably growing in magnitude and length (Figure 6.78a): the cut axonometric view allows to observe that the cracks are growing through the width of the beam (Figure 6.78b).

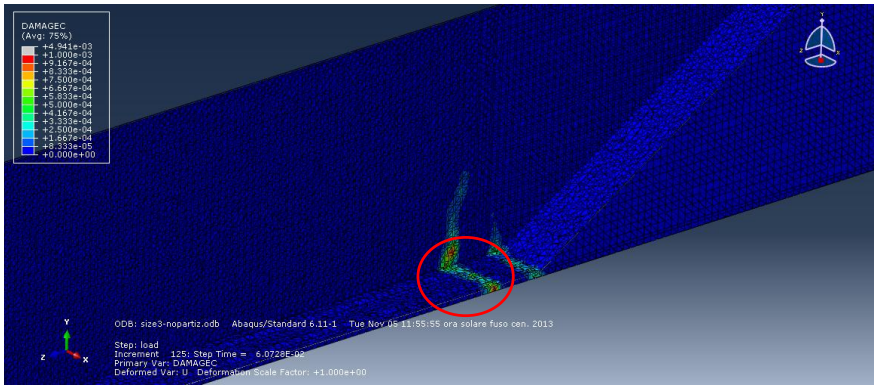

Figure 6.73. Step N°1: damage variable magnitude.

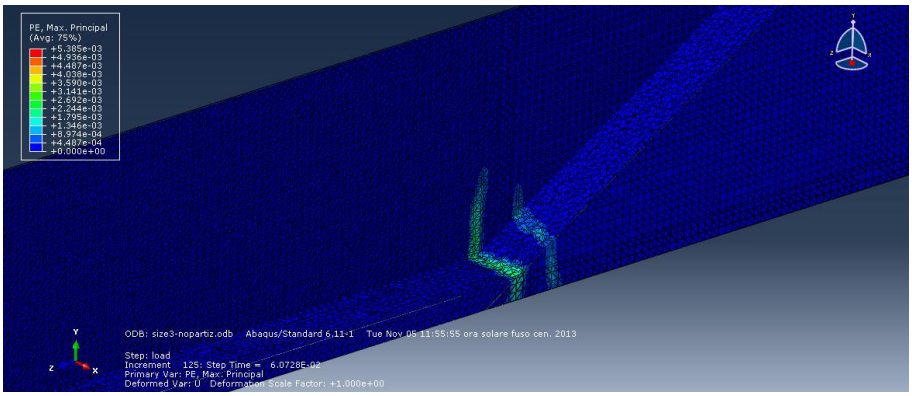

a)

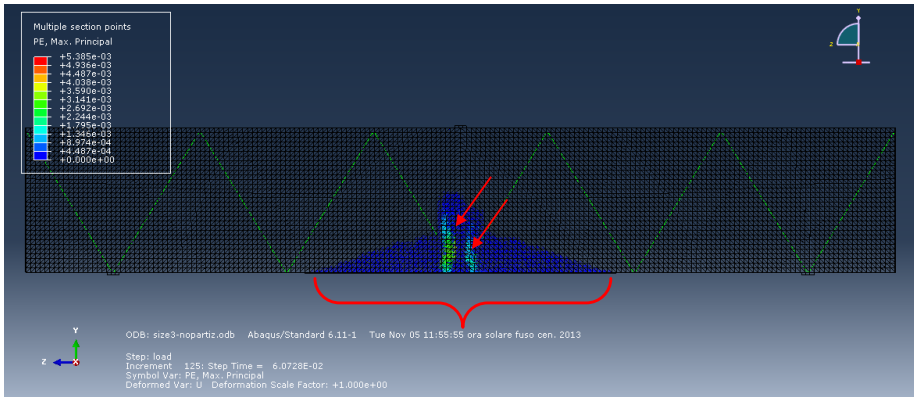

b)

Figure 6.74. Maximum principal strains in Step N°1: a) magnitude and extension in the axonometric view; b) direction in the frontal view.

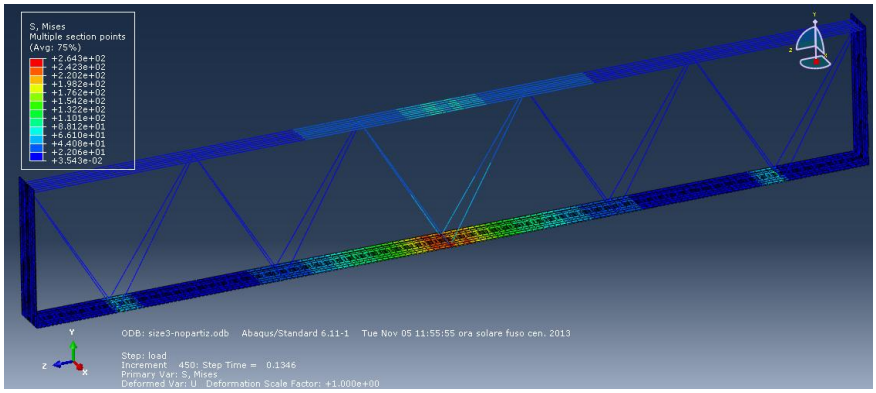

Figure 6.75. Step N°2: magnitude of the von Mises stresses in the steel members.

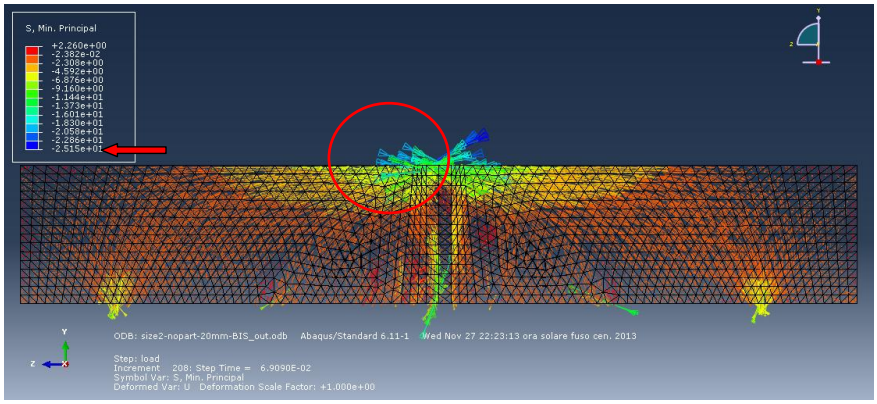

Figure 6.76. Step N°2: direction of minimum principal stresses in the concrete.

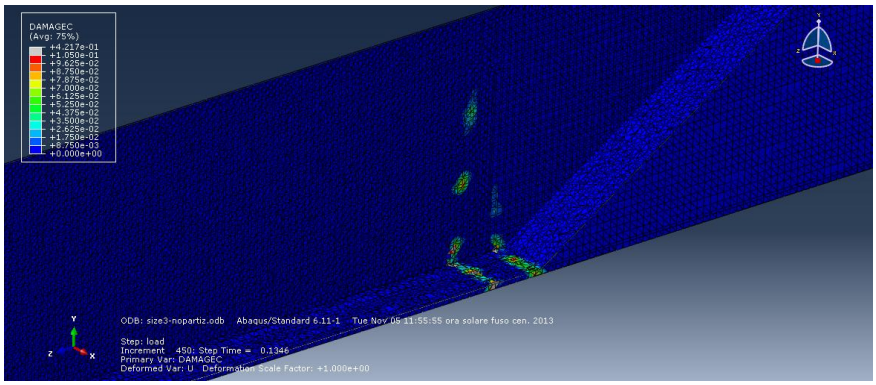

Figure 6.77. Step N°2: damage variable magnitude.

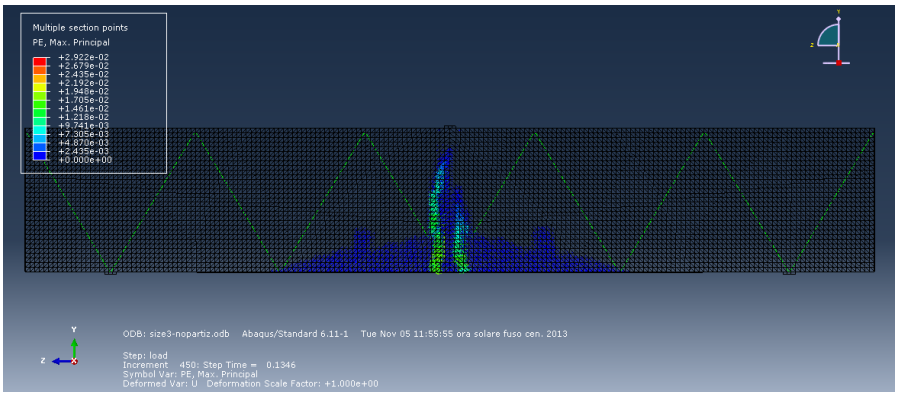

a)

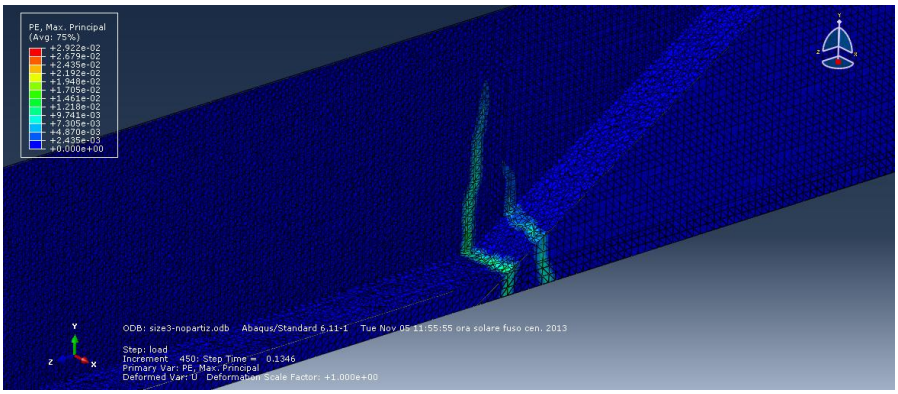

b)

Figure 6.78. Maximum principal strain in Step N°2: a) direction in the frontal view; b) magnitude in the axonometric view.

Since *STEP N°3*, in which the yielding of the bottom steel plate occurs, is close to *STEP N°4*, in the follow, only the description of the latter is presented. *STEP N°4* represents the startpoint of the horizontal branch when the plateau of the maximum load is established. In this step both the diagonal web bars and the upper chord are still elastic.

Figure 6.79 shows the detail of the configuration of all steel members.

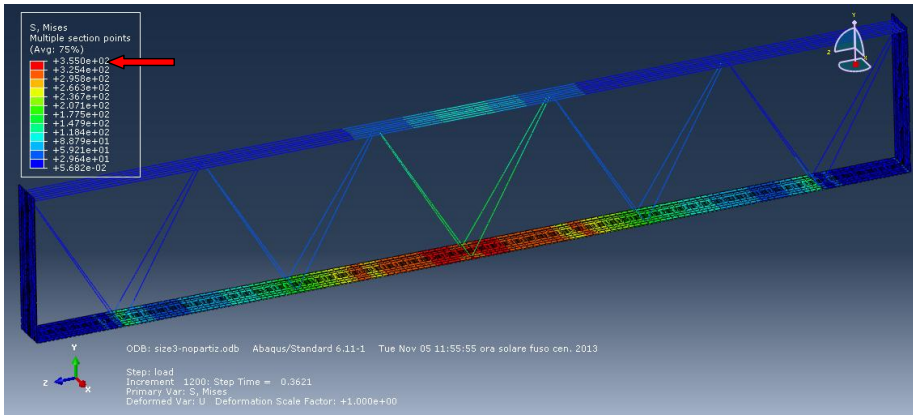

Figure 6.79. Configuration of the steel members in STEP N°4.

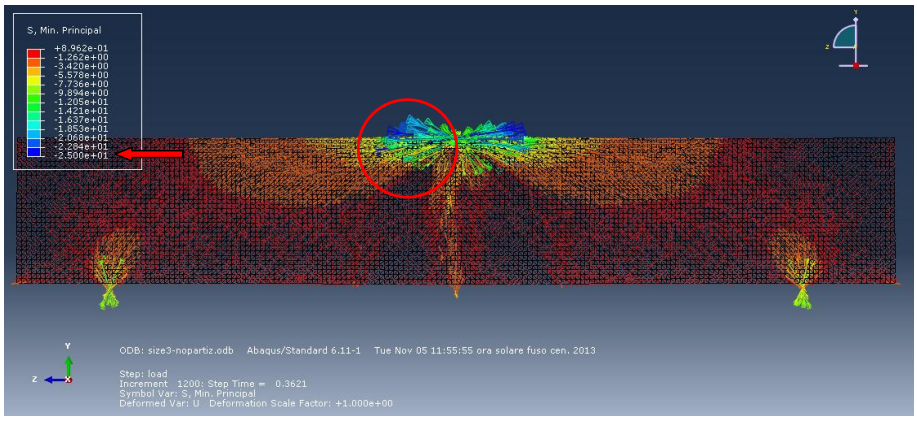

Figure 6.80. STEP N°4: minimum principal stresses in the concrete.

The volume of the concrete in which the minimum principal stress assumes the maximum value implemented in the compressive constitutive behavior (25 MPa) is increasing (Figure 6.80) and the damage variable corresponding to the cracked zone, which, between *STEP N°2* and *STEP N°4*, started to involve also the diagonal direction (Figure 6.81), exhibits values between 0.005 and 0.54 (Figure 6.82). It is worth to note that the width of the cracks in the diagonal direction tends to increase, mainly corresponding to the bottom of the beam, (Figure 6.83a-b) while the central sub-vertical fractures are considerably smaller with respect to the diagonal ones.

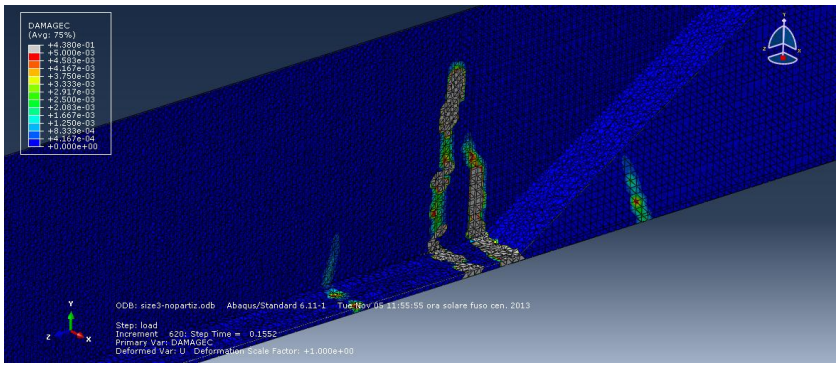

a)

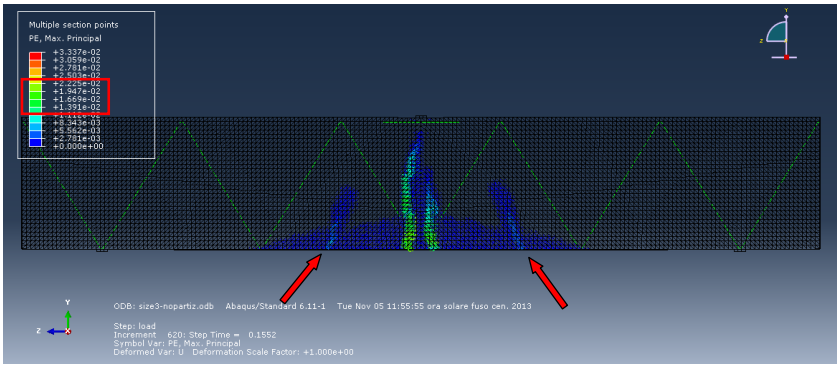

b)

Figure 6.81. Extension of the cracked zone along the diagonal direction between STEP N°2 and STEP N°4: a) damage variable; b) maximum principal strains.

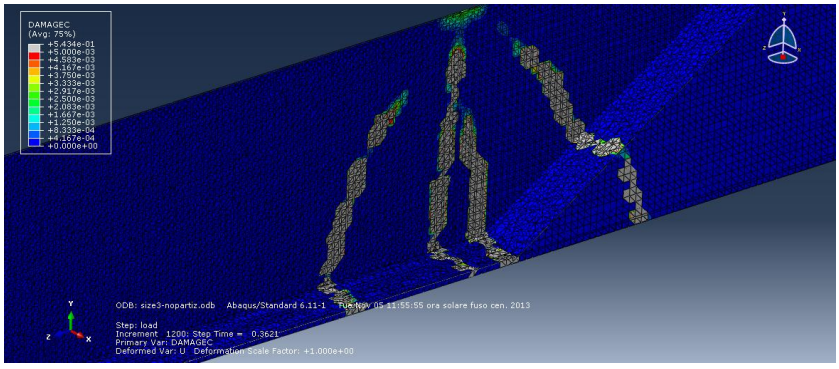

Figure 6.82. Magnitude of the damage variable in STEP N°4.

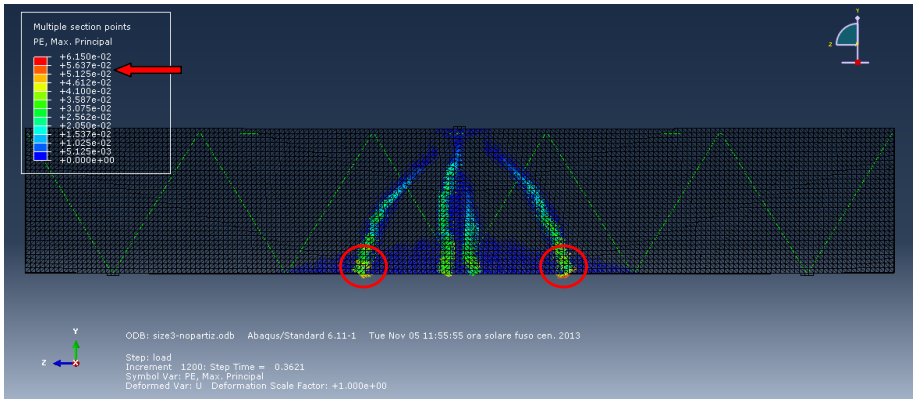

a)

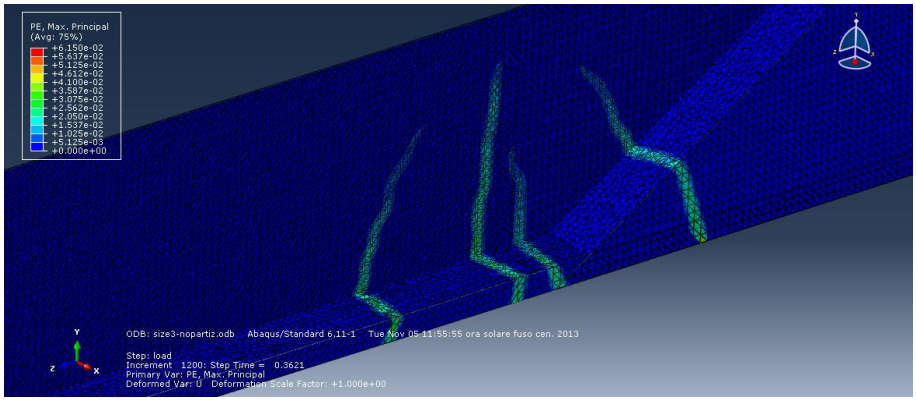

b)

Figure 6.83. Maximum principal strains in STEP N°4: a) directions in the frontal view; b) magnitude in the axonometric view.

STEP N°5, in which the yielding of the steel truss occurs, is immediately close to *STEP N°6* which corresponds to the configuration when the effective numerical maximum load is achieved. Thus, in the follow, only the description of this latter step is presented.

In this configuration the tensile diagonal bars of the first meshes are now yielded (Figure 6.84). Figure 6.85 shows the direction of the minimum principal stress in the concrete and Figures 6.86a and 6.86b the damage variable magnitude and extension. As well as the damage in the compressed strut, also the maximum plastic principal strains in the diagonal direction are

increasing. Particularly, Figure 6.87 shows how the width of the cracks is almost one order of magnitude higher than in the previous step.

The stress state in the concrete corresponding to the control sections is shown in Figure 6.88. It is worth to note that at the bottom of the beam, the tensile stress reaches exactly the value of the maximum tensile strength implemented in the tensile constitutive behavior of the concrete that is equal to 2.57 MPa. The free body diagram of the beam is thus represented in Figure 6.89.

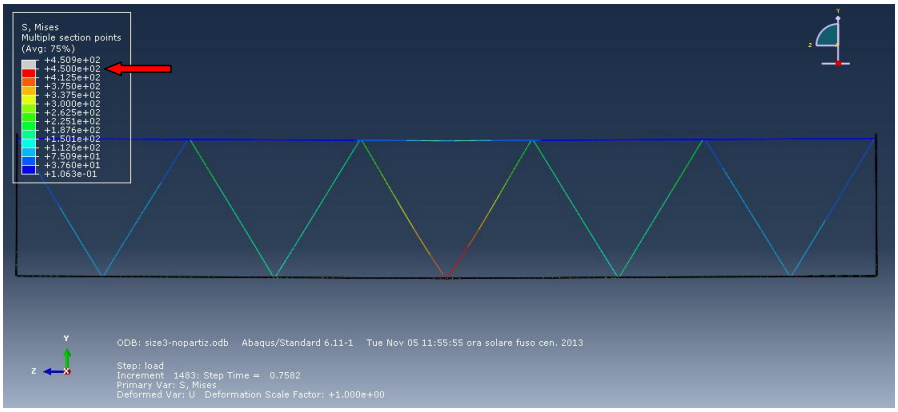

Figure 6.84. Configuration of the steel members in STEP N°6.

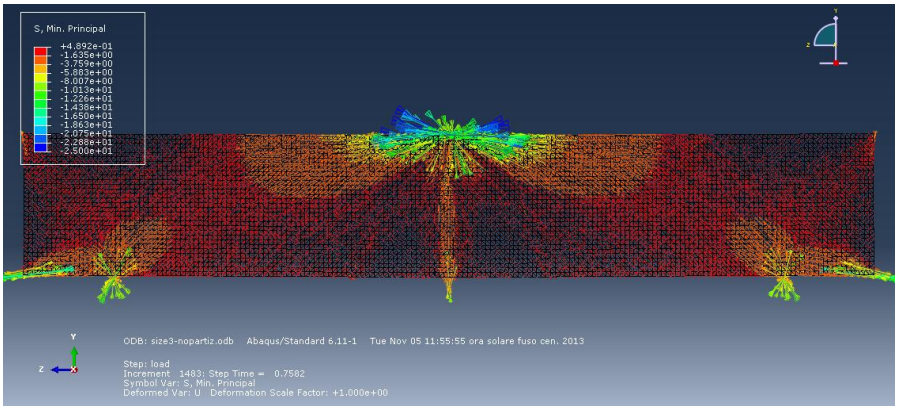

Figure 6.85. STEP N°6: minimum principal stresses in the concrete.

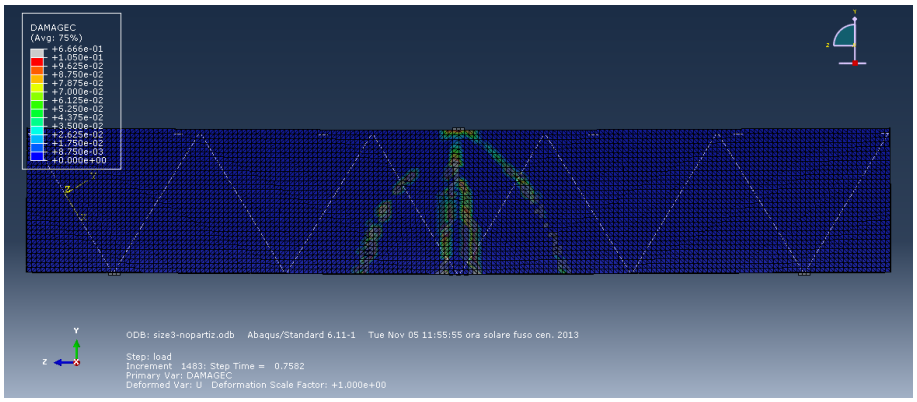

a)

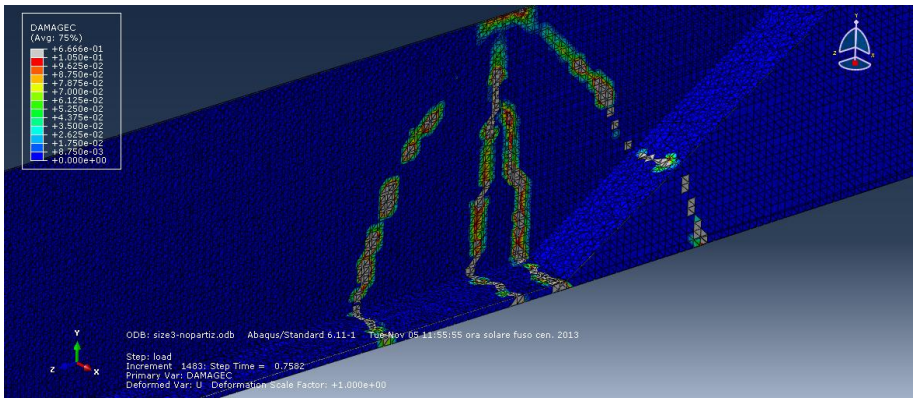

b)

Figure 6.86. Magnitude and extension of the damage variable in STEP N°6: a) frontal view; b) axonometric view.

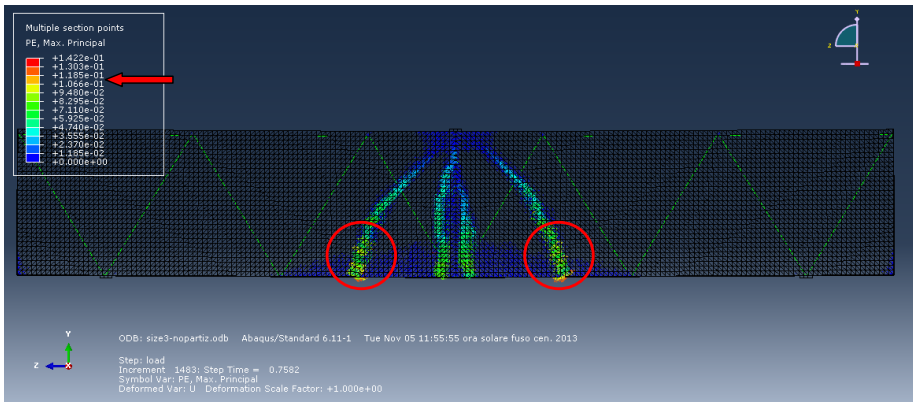

a)

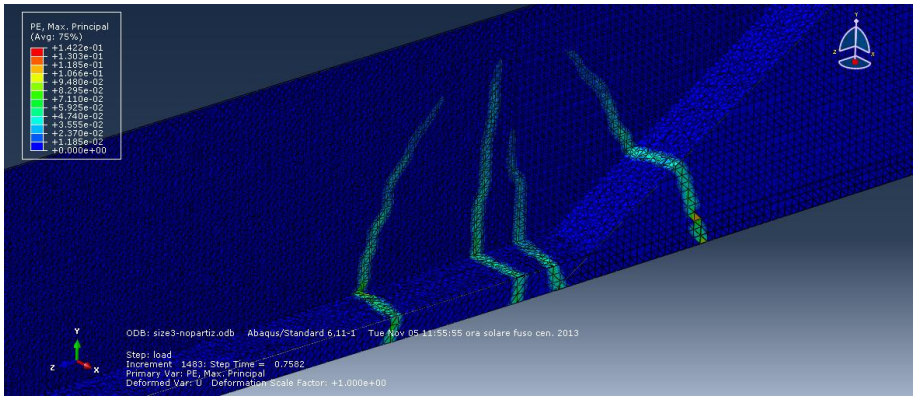

b)

Figure 6.87. Crack pattern in STEP N°6: a) frontal view; b) axonometric view.

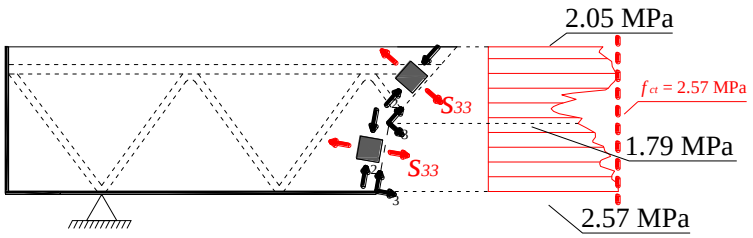

Figure 6.88. Stress state of the concrete in the control sections corresponding to the peak load: tensile stresses.

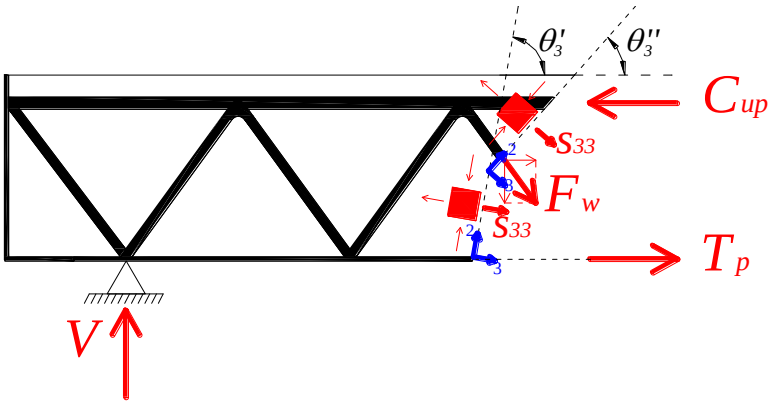

Figure 6.89. Free body diagram of the beam of Model Size 3.

Finally *STEP N°7* corresponds to the configuration of the beam at the end of the analysis. In Figure 6.90 the von Mises stresses in the steel members are represented showing that also the other tensile bars are yielding while the upper chord is still elastic with a maximum stress almost equal to 230 MPa. Figure 6.91 shows the direction of the minimum principal stresses in the concrete: it can be noted that the kinematic of truss develops so that the steel plate is pulled upward by the two central diagonal bars, inducing a local compression on the concrete (see Figure 6.92). There is a local compression also at the end of the beam beyond the lateral support.

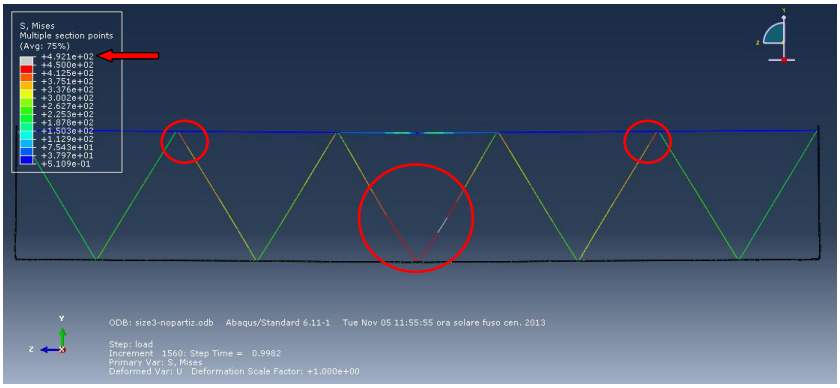

a)

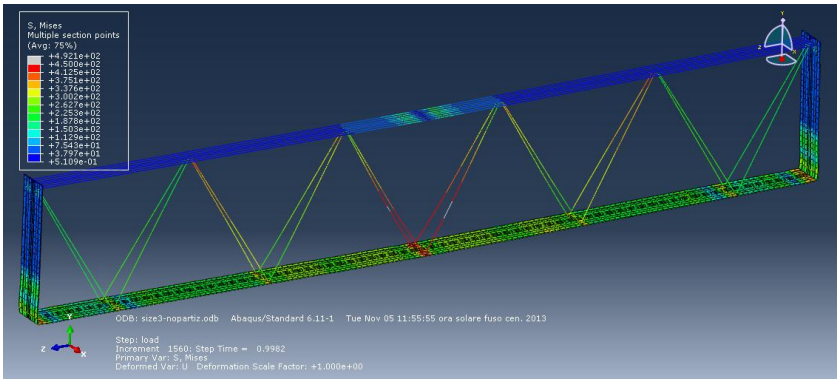

b)

Figure 6.90. Steel members in STEP N°7: a) frontal view; b) axonometric view.

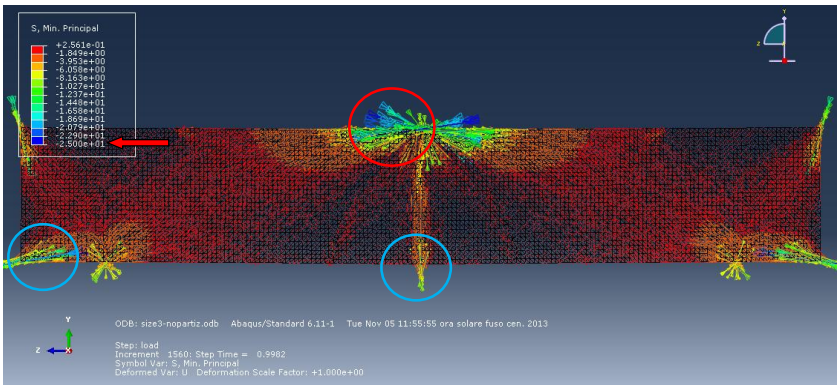

Figure 6.91. STEP N°7: minimum principal stresses in the concrete.

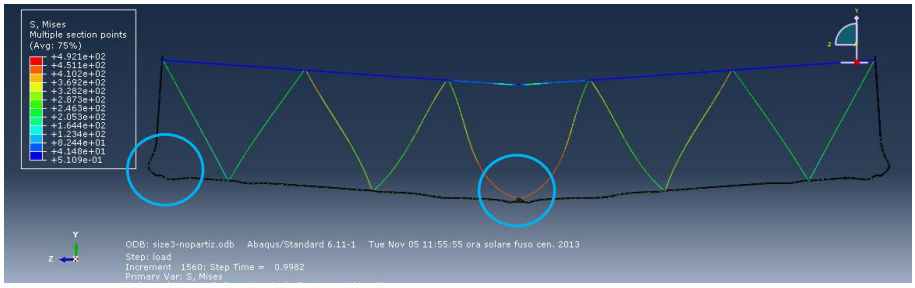

Figure 6.92. STEP N°7: kinematic of the steel truss.

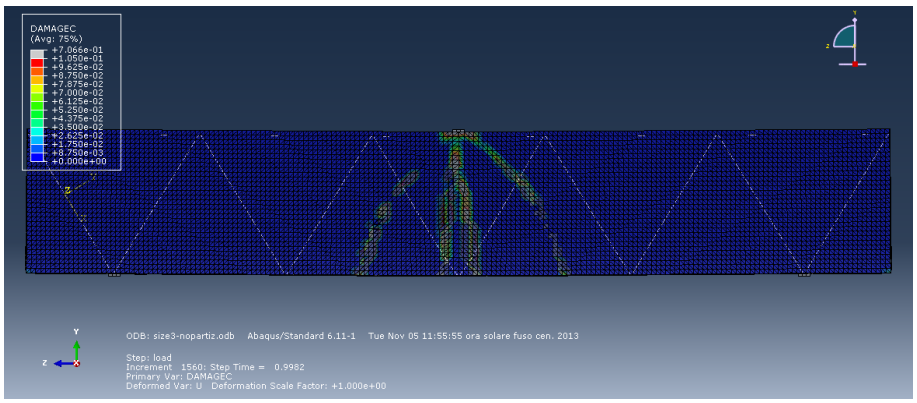

a)

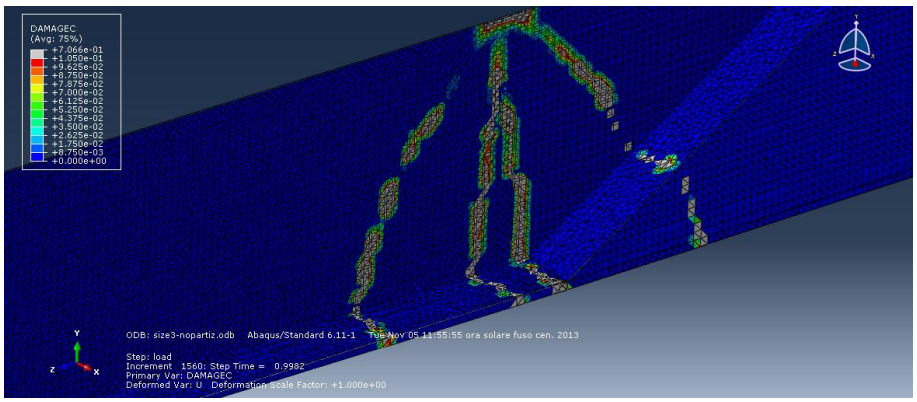

b)

Figure 6.93. Damage variable magnitude in STEP N°7: a) frontal view; b) axonometric view.

In Figure 6.93 the intensity and extension of the damage in the compressed concrete is represented: the damage variable reaches the value 0.77. As regards the cracking, the maximum magnitude of the plastic principle strains keeps on increasing with respect to the value achieved in the previous step. The entity of the cracks in the diagonal direction is about 1.5 times higher than the cracks in the midspan (Figure 6.94a-b).

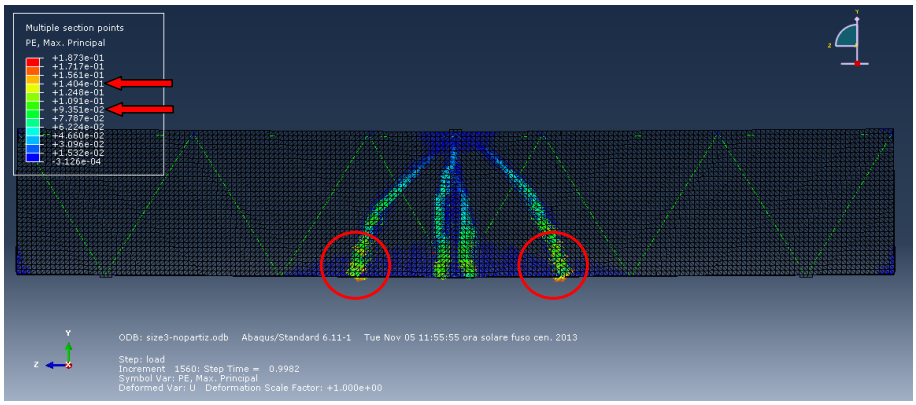

a)

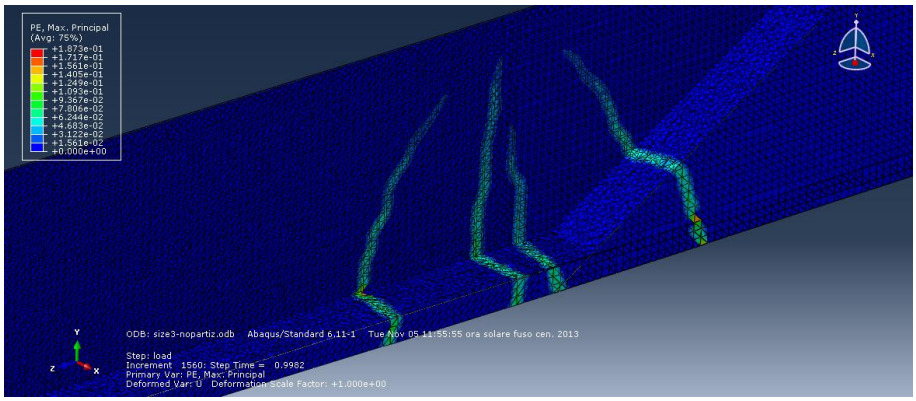

b)

Figure 6.94. Crack pattern at the end of the analysis: a) frontal view; b) axonometric view of the magnitude and extension of the cracks.

6.3 Observations

The comparison between the numerical simulations described in the previous sections is represented in Figure 6.95 where the three load-displacement curves are reported.

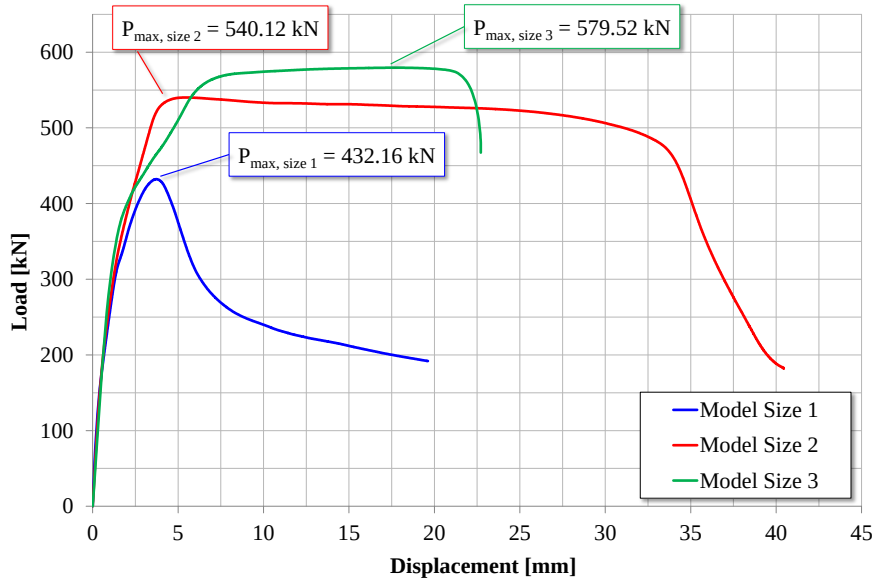

Figure 6.95. Comparison between the numerical load-displacement curves.

As stressed in Table 6.2, where the ratios between the peak load values of the three simulations are reported, the increment of bearing capacity is equal to 25% passing from Size 1 to Size2 and equal to 34% from Size 1 to Size 3. Similarly, the maximum load carried by the beam just increases of 7% passing from Size 2 to Size 3. The comparison between the load-displacement curves also allows to observe the main differences in the global mechanical response of the three sizes of beam.

Table 6.2. Ratios between the numerical peak load values.

$P_{max,\ size3}/P_{max,\ size2}$	1.07
$P_{max,\ size3}/P_{max,\ size1}$	1.34
$P_{max,\ size2}/P_{max,\ size1}$	1.25

Only in Model Size 1 the beam exhibited the typical fragile behavior caused by a shear failure. During the simulation, even if the first cracks which appear are the sub-vertical ones due to the flexural response, then the main fractures develop in the diagonal direction proving that the failure mechanism is governed by the shear; during the load history, the width of the flexural cracks becomes more and more negligible with respect to the diagonal shear fractures. The slope of the compressed concrete strut, which corresponds to the slope of the fracture plane, is almost parallel to the inclination of the compressed diagonal web bars of the truss. The peak in the load-displacement curve corresponds to the achievement of the compressive strength in the concrete strut after which a sudden loss of bearing capacity occurs so that the load-displacement curve exhibits a softening followed by a sub-horizontal branch with a residual load of about 180 kN.

Conversely, in Model Size 2 the beam exhibited a global behavior characterized by a quite wide field of ductility which is suddenly followed by a softening branch denoting a final fragile failure. In fact, the crack pattern evolution corresponding to such a mechanical response is mainly characterized by the growing of sub-vertical flexural cracks during almost all the load history which are then followed by the developing of diagonal shear cracks whose width is inferior with respect to the flexural ones. Furthermore, the failure mechanism is influenced by the kinematic of the steel truss which develops so that the bottom steel plate is pulled upward by the two central diagonal rebars inducing a compression in the concrete in the midspan of the beam. Such a kinematic of the steel members can be ascribed to the geometric features of the cross-section of Size 2 beam whose diagonal rebars are 80.8° inclined in the cross-section plane. Therefore, in such beam the ductile mechanism, mainly allowed by the mechanical response of the steel members, turns into a fragile failure due to the crushing of the concrete and the section governing the failure mechanism proves to be almost corresponding to the midspan of the beam.

Similarly, in the case of Model Size 3, the load-displacement curve exhibits a sub-horizontal ductile branch in which a plateau for the maximum numerical load is established before a sudden fragile loss of bearing

capacity. However, in this case, the maximum displacement achieved by the structural system is lower than the one reached in Model Size 2: the displacement is equal to 23 mm and 34 mm respectively. The numerical outcome shows, one again, how the mechanical response of the system is governed by the steel members during almost all the load history. In Model Size 3 the behavior of the beam is first characterized by a flexural response with diffused sub-vertical cracks mainly concentrated in the midspan; then, the mechanism develops involving the diagonal direction which can be assimilated to a couple of segments crossing the tensile web bars of the first mesh of the truss. While the failure mechanism is developing, the main cracks become the ones in the diagonal direction being their width and length most significant with respect to the flexural fractures. Also in this case the failure mechanism is influenced by the geometry of the truss, being the inclination of the diagonal rebars in the cross-section plane equal to 86°.

In conclusion, the three different models concerning Size 1, 2 and 3, in which the scaled geometry of the beams has been realized according to a two-dimensional criterion, gave rise to two main different mechanical responses of the structural system, characterized or not by a ductile behavior with a final fragile failure. The carried load increases less than linearly passing from Size 1 beam until Size 3 and the crack pattern governing the failure is mainly characterized by the evolution of the diagonal cracks in the case of Size 1 and Size 3 and by the growth of sub-vertical cracks in the midspan of the beam in the case of Size 2. As a consequence, for Size 1 and Size 3 beams it can be individuated a certain shape and slope of the compressed concrete strut involved in the shear mechanism, also highlighting the relation between such slope and the inclination of the web rebars, while for the case of Size 2 the failure is mainly caused by the crushing of the concrete concentrated in the midspan of the beam without an actual developing of a concrete strut in the diagonal direction. In every case, the tensile behavior of the concrete evolves so that the tensile strength of the material is reached corresponding to the bottom of the main crack, being almost constant also along the entire fracture length.

CHAPTER 7

COMPLEMENTARY INVESTIGATIONS ON THE STRUCTURAL TYPOLOGY

In this Chapter two further problems of paramount importance dealing with the behavior of the beam in *phase I*, on one side, and, in *phase II*, on the other side, are presented and discussed within the two sections constituting the Chapter. Particularly, the first issue concerns the interpretation of experimental results of push-out tests in *phase I* available in the literature taking into account the buckling strength of the compressed members as well as the interaction domain between bending moment and axial force.

On the other hand, the cyclic behavior in *phase II* of beam-to-column joints belonging to framed seismic structures, in which HSTCBs are joined to R.C. columns cast in situ, is studied. The investigation is carried out by means of experimental tests herein described and also interpreted employing 2D simplified FE models.

7.1 Behavior of the bare steel truss subjected to push-out test

The behavior of the beam in *phase I* concerns the transient time of the structure construction. In this phase the main problem is the buckling involving the compressed web bars or the upper chord of the steel truss. In Vincenzi and Savoia (2010) three main different buckling modes for the steel truss are presented: 1) the instability of the single rods constituting the

web truss or the upper chord; 2) a wider instability of the compressed upper chord in which the buckling length involves more than one mesh of the truss; 3) the coupled flexural-torsional instability of the entire truss. The classical criteria for the investigation of instability can be employed only in the first case that is when the buckling length can be defined from the distance between the transversal restraints of the upper chord or from the length of the rods constituting the web truss. On the other hand, when the transversal restraints have not stiffness enough to avoid the displacements of the nodes belonging to the upper chord, the latter could collapse involving a buckling length which includes more than one mesh of the truss.

Finally flexural-torsional instability could involve the entire beam and mainly occurs in the case of high depth cross-sections. It has to be noted that, in the latter cases, the critical load value is significantly lower than the Eulerian critical load of single rods. Nevertheless, it has been proved that the critical load inducing the instability increases as the steel truss is a spatial truss rather than a planar truss, so that both the axial and flexural strength of the diagonal web bars can be exploited in the response mechanism.

Aiming to better understand the behavior of the HSTCBs in *phase I*, Badalamenti et al. (2008b) carried out monotonic push-out tests in displacement control on specimens realized as in the scheme of Figure 7.1. The test is similar to that suggested in Eurocode 4 (2005) for push-out tests on classical composite steel-concrete beams. Two tests were carried out on specimens S1 and S2. Specimen S1 consists of two pieces of truss symmetrically coupled along the bottom plate middle lines by means of a connecting steel plate 8 mm thick, placed perpendicularly to the plates of the steel trusses. Each truss beam is constituted by an upper chord composed by three coupled 16 mm diameter rebars, a bottom chord constituted by 5 mm S355 steel plate and B450C 12 mm diameter web rebars formed at reverse V. The depth of the truss beam is 210 mm.

At the top of the specimen an 8 mm thick plate is placed orthogonally to the specimen axis and properly stiffened to apply the load through the testing machine.

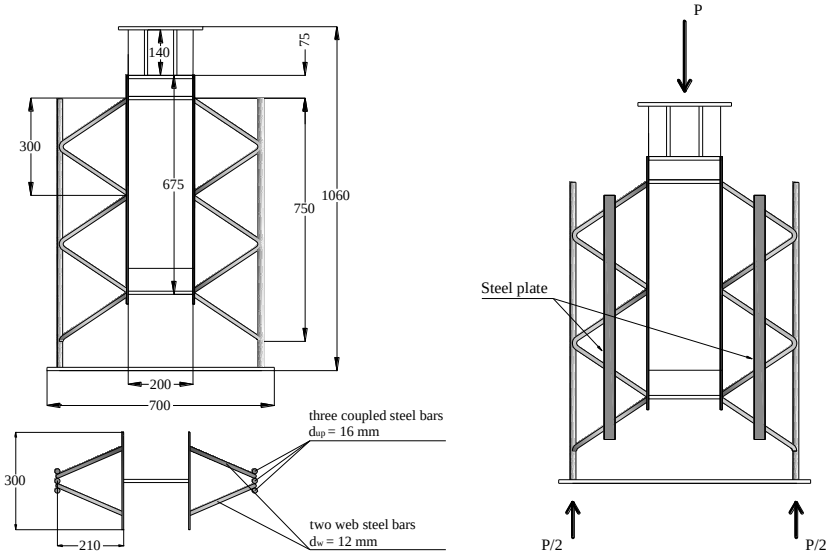

a) b)

Figure 7.1. Push-out test in *phase I* (dimensions in mm): a) specimen S1; b) specimen S2.

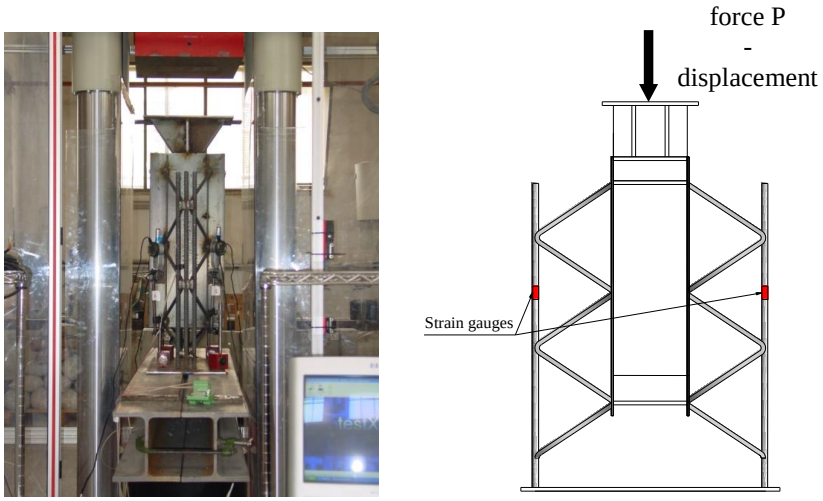

a) b)

Figure 7.2. Test-set-up for push-out test in *phase I*: a) testing machine; b) instrumentation.

Specimen S2 (Figure 7.1b) is different from specimen S1 (Figure 7.1a) only for two longitudinal plates, 40 mm width and 5 mm thick, welded to the web bars placed in order to reduce the web bar slenderness to avoid buckling phenomena. The load was applied by a press with 4000 kN load carrying capacity shown in Figure 7.2a used in displacement controlled mode by means of an electronic device recording the reaction force and the applied displacement. The strain rate utilized for the tests was 0.1 mm/min. Two electric strain gauges were put on the upper chords of the two coupled trusses as it is shown in Figure 7.2b, in order to evaluate the top chord strain during the test.

7.1.1 Experimental results available in the literature

The results of the aforesaid experimental campaign are herein summarized aiming at providing their interpretation in the following paragraph by means of analytical expressions. In Figure 7.3 the load-displacement curves obtained by push-out tests on S1 and S2 specimens are shown; the displacement is the one recorded by the testing machine.

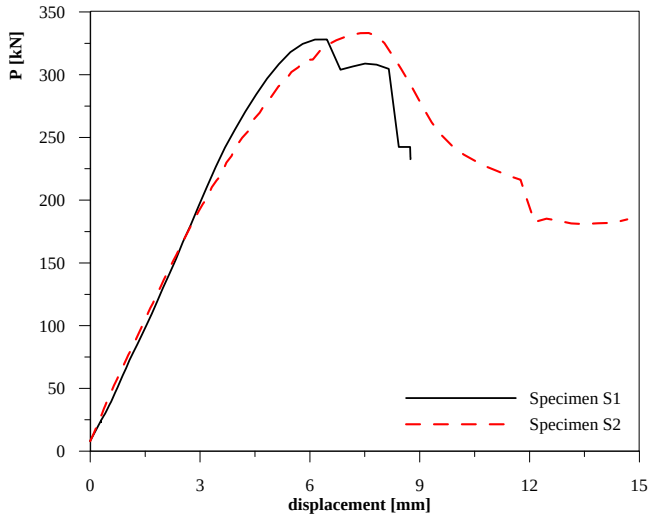

Figure 7.3. Load-displacement curves for push-out test in phase I.

a) b)

c) d)

Figure 7.4. Specimens of push-out tests in phase I at the end of the test: a) specimen S1; b) zoom of web bars in specimen S1; c) specimen S2; d) zoom of upper chord in specimen S2.

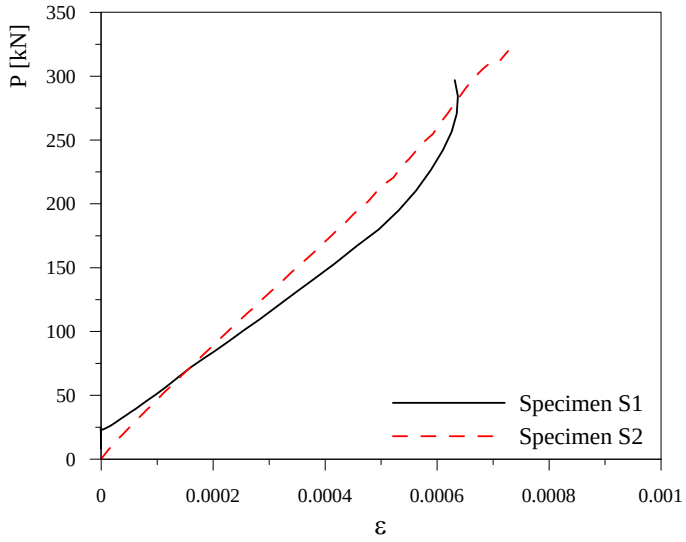

Figure 7.5. Load-strain curves of the strain gauge put on the upper chord.

Both curves in Figure 7.3 show a similar response in the first linear branch; then, the nonlinear part preceding the peak value (328 kN for S1 and 333 kN for S2) is characterized by an increasing loss of stiffness due to geometric nonlinearity and buckling phenomena, the latter arising in the compressed bars subjected to both axial force and bending moment. In specimen S1 the buckling occurred in the compressed web bars, while in specimen S2 the presence of the added plates made it possible to delay the instability of the diagonal rebars, modifying the failure mechanism. As abovementioned, the peak load values are similar in both specimens while the post-peak branch of specimen S2 showed a slower strength reduction than in specimen S1. In specimen S2 the buckling occurred in the upper chord which showed a better post-critical behavior than the one of the web rebars. Thus, larger deformations in the plastic range with a slower decrease in strength have been achieved. In both two tests the weldings did not fail. Figures 7.4a-d show the specimens configuration at the end of the test.

The results recorded by the strain gauges, reported in Figure 7.5, underline that, during both the tests, the upper chord remained in the elastic field with a maximum stress of about 165 N/mm^2. In specimen S2 the load-

deformation curve is linear until failure, while in specimen S1 the trend was non-linear for load values greater than 200 kN due to the buckling occurring in the web bars that modified the stress transfer mechanism.

7.1.2 Analytical interpretation of the experimental results

In order to interpret the experimental behavior, an approximate evaluation of the specimen strength is made in this section (see Colajanni et al. 2014).

According to Eurocode 3 (2005) the buckling strength of a compressed member, N_b, is expressed as follows:

$$N_b=\chi N_y; \qquad N_y=A f_y \tag{7.1}$$

with A the cross-section area of the member and χ the reduction factor for the buckling mode. In order to evaluate the reduction factor χ for the bars in which the buckling occurs, the non-dimensional slenderness is evaluated and the buckling curve is chosen. For the web bar having diameter d_w=12 mm, and length l_w=250 mm in the specimen S1, the buckling length is assumed to be 175 mm, by considering a semi-rigid connection (reduction coefficient 0.7), the slenderness 58.3 and the non-dimensional slenderness $\bar{\lambda}=\sqrt{A f_y / N_{cr}}=0.96$, being the bar cross-section of class 1, and the elastic flexural buckling force N_{cr}=67.6 kN. Referring to the buckling curve *c*, the imperfection factor is equal to 0.49 and the reduction factor $\chi=1\Big/\left[\Phi+\sqrt{\Phi^2-\bar{\lambda}^2}\right]=0.56$, in which $\Phi=0.5\left[1+0.49\left(\bar{\lambda}-0.2\right)+\bar{\lambda}^2\right]=1.15$.

Therefore, the reduced axial strength in Eq. 7.1 is N_b=35.2 kN.

By approximating specimen S1 behavior to that of a simple truss in which shear forces and bending moments are neglected at the joints, an approximate estimation of the maximum load can be obtained taking into account the contribution of 16 web bars only (8 of them compressed and the other 8 in tension), assuming that the web bars at the bottom are unloaded. In

this way the maximum load can be evaluated by assuming a linear behavior up to the buckling of the compressed web rebars, by adding the contribution of 16 bars with axial strength N_b calculated as in Eq. 7.1. Thus the maximum load P = 16×35.2×cos(α^*) = 306.74 kN is obtained, α^*=57° being the angle of inclination of the web bar axis with the longitudinal axis of the specimen (see Figure 3.1a). In Table 7.1 the comparison with the experimental maximum load for the specimen S1, P=328 kN, shows that the simplified evaluation provides an effective assessment of the experimental load.

A more accurate evaluation, however, has to take into account the stiffness of the truss joint connections. Therefore, due to the presence of the bending moments in the truss members, the *M-N* plastic domain has to be considered. At this aim a simplified expression of the domain proposed by Millard and Johnson (1984) is utilized:

$$M_u = \frac{d^3}{6} f_y \left(1 - \frac{N_u^2}{N_y^2}\right) \tag{7.2}$$

in which d indicates the diameter of the cross-section of the circular member. This simplified curve is reported in Figure 7.6 and compared to the other curve which represents the correct form proposed by Campione et al. (2012) already presented in Chapter 3 (Eq. 3.8) and herein again reported indicating with d the diameter of the cross-section:

$$N_u = \frac{1}{4} f_y d^2 \left\{ \pi - 2\arcsin\left[\frac{1}{d}\sqrt[3]{\frac{6M_u}{f_y}}\right] + \sin\left[2\arcsin\left(\frac{1}{d}\sqrt[3]{\frac{6M_u}{f_y}}\right)\right]\right\} \tag{7.3}$$

The figure shows how the two formula provide almost coincident results.

Moreover, for compressed bars the reduction due to buckling has to be taken into account. To this aim the *M-N* buckling domain proposed by Eurocode 3 (2005) can be considered:

$$\frac{N}{N_b} + k\frac{M}{M_u^0} \le 1 \tag{7.4}$$

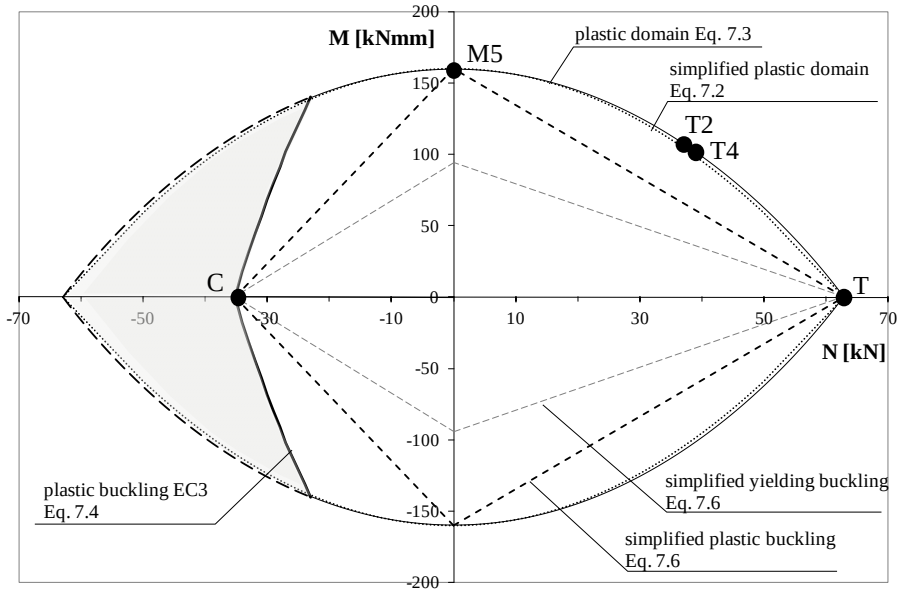

Figure 7.6. *M-N* domains for web bar with d_w= 12 mm.

in which k is an interaction factor, and $M_u^0 = W_{pl}\, f_y$ is the plastic bending moment corresponding to a zero axial force (W_{pl} = plastic section modulus).

The k factor can be evaluated, for plastic cross-sectional properties, class 1, as suggested in Eurocode 3 (2005) (Method 1 in Annex A) as:

$$k = C_m \frac{\mu}{1-\frac{N}{N_{cr}}} \frac{1}{C} \tag{7.5}$$

with

$$\mu = \frac{1-\frac{N}{N_{cr}}}{1-\chi\frac{N}{N_{cr}}}; \quad C_m = \; 0.79 + 0.21\psi + 0.36(\psi - 0.33)\frac{N}{N_{cr}}; \quad \psi = -1;$$

$$C = 1 + (w-1)\left[\left(2 - \frac{1.6}{w} C_m^2 \overline{\lambda} - \frac{1.6}{w} C_m^2 \overline{\lambda}^2\right)\right]\frac{N}{N_u} \geq \frac{W_{el}}{W_{pl}}; \quad w = \frac{W_{pl}}{W_{el}} \leq 1.5;$$

in which ψ takes the shape of the moment diagram into account and W_{el} is the elastic section modulus. In this case ψ = -1 is chosen considering the same restraint conditions at the bar ends. The interaction curve obtained is also represented in Figure 7.6 for the web bar with d=d_w=12 mm.

With the aim of representing simplified linear domains considering buckling effects in compression, in the same figure, also the curves corresponding to the following equation are reported:

$$\frac{N}{N^*}+\frac{M}{M^*}\leq 1 \tag{7.6}$$

where N^*= N_y in tension and N^*= N_b in compression, M^*=W_y f_y (where W_y is the elastic modulus) has to be read as M_y in the case of the yielding domain while it has to be read as M_u^0 in the case of the plastic domain. Furthermore, in Figure 7.6 the points C and T correspond to the N_b and N_y values respectively.

All the statements and expressions in the follow refer to one half of the steel truss belonging to the plane which contains the axis of the web bars of the truss itself.

Aiming at estimate the maximum load value, taking into account the axial force redistribution in the web bars allowed by shear forces and related flexural moments in the web bars, the equilibrium equations of the planar system represented in Figure 7.7 can be written assuming the following hypotheses:

a) the upper chord bar remains elastic, as it had been observed by the measurements recorded by the strain gauge during the test (Figure 7.5);

b) the web bars have reached their maximum capacity, that is in the tensile bars the flexural moments and axial forces are linked by Eq. 7.2, while in the compressed bars by Eq. 7.6 (by assuming a stable post-buckling behavior);

c) the distribution of internal forces in node B (see Figure 7.7c) of the upper chord is anti-symmetric; thus bending moments M_{BC}=M_{BA};

d) the bending moment diagrams in the web bars is anti-symmetric;

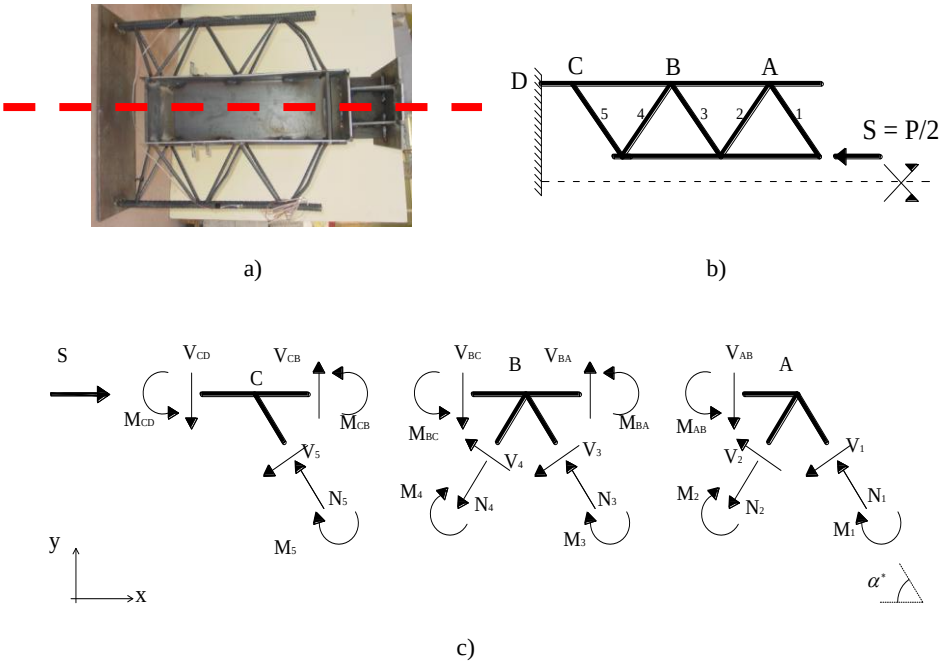

Figure 7.7. Simplified model: a) real system; b) planar system; c) equilibrium of the upper chord at each joint.

e) axial force in bar n°5 vanishes, and therefore the bending moment is the plastic one;

f) the bending moment in the rod BC vanishes at a distance of one third of the bar length from the node C.

On the basis of the aforementioned assumptions and referring to the symbols introduced in Figure 7.7, the following equilibrium equations are derived:

$$(N_1 - N_2)\sin\alpha^* - \frac{2}{l_w}(M_1 - M_2)\cos\alpha^* + \\ -\frac{2(M_1 + M_2) + M_3 + M_4}{2l_c} = 0 \tag{7.7a}$$

$$(N_3 - N_4)\sin\alpha^* - \frac{2}{l_w}(M_3 - M_4)\cos\alpha^* - \frac{3M_5}{l_c}\frac{\rho_{CB}}{\rho_{CB}+\rho_{CD}} + \\ + \frac{2(M_1+M_2)+M_3+M_4}{2l_c} = 0 \tag{7.7b}$$

$$S = \left(\sum_{i=1}^{5} N_i\right)\cos\alpha^* + \frac{2}{l_w}\left(\sum_{i=1}^{5} M_i\right)\sin\alpha^* \tag{7.7c}$$

being ρ_{CB} and ρ_{CD} the flexural stiffness of CB and CD rods respectively; l_w and l_c the length of the web and the upper chord bars respectively. Particularly, with reference to the coordinate system in Figure 7.7c, Eqs. 7.7 represent the equilibrium of node A in the y-direction, the equilibrium of node B in the y-direction and the equilibrium of the entire system in the x-direction, respectively.

In order to find the maximum value of the external force S that the system is able to withstand, the lower bound theorem of plasticity is used, according to the equilibrium Eqs. 7.7 and the admissible plastic and buckling conditions expressed by Eq. 7.2 and Eq. 7.6. Thus, the estimated analytical value of the maximum load, P, is obtained from the maximum value of S considering the couple of two trusses constituting the beam. In this way, the value P = 326.64 kN is obtained (this value with respect to the experimental one is reported in Table 7.1), corresponding to the internal forces values indicated in Figure 7.6 by the point C for the compressed web bars n° 1 and 3, points T2 and T4 for the tensile bars n° 2 and 4 and the point M5 for the bar n°5 in pure bending.

Table 7.1. Comparison between theoretical and experimental results (*phase I*): $P_{u,theo}/P_{u,exp}$.

ID	Truss Model	Frame Model
S1	0.935	0.996
S2	1.198	-

For specimen S2, due to the presence of the stiffening plate, a different collapse mechanism is expected, involving the buckling of the more compressed top chord bar, i.e. bar BC. The buckling load of the top chord bar, having diameter 16 mm and length 300 mm, is evaluated as follows: the buckling length is assumed to be 210 mm by considering a semi-rigid connection (reduction coefficient 0.7), the slenderness 52.5 and the non-dimensional slenderness $\bar{\lambda} = 0.84$, being the bar cross-section of class 1 and the elastic flexural buckling force N_{cr}=148.3 kN. Referring to the buckling curve *c*, the imperfection factor is 0.49 and the reduction factor χ=0.64, calculated assuming for the coefficient Φ the value 1.01. Thus, the reduced axial strength is N_b = 66.5 kN.

On the basis of the reduced strength, and taking into account that each one of the two symmetrical beam top chords is made up of 3 rebars, an upper bound of the expected specimen strength, related to the top chord rebar buckling, can be predicted as $P = 6 \times N_b = 399$ kN.

A more effective prediction of the specimen strength should be obtained by reducing the latter value taking into account the presence of the bending moment on the top chord rebars transmitted by the web bars. However, in this case it is not easy to achieve this goal in a simplified way, since both the web and the upper bar not involved in the buckling remain in the elastic field. Finally it is worth noting that, even if in the top chord the buckling represents one of the most relevant failure modes for the trussed beam in *phase I*, the experimental value obtained for specimen S2 is influenced by the setup geometry that is not able to effectively reproduce the restrain condition of the actual beam before the cast phase.

7.2 Shear behavior of beam-to-column joints under cyclic loading

In this section the results of an experimental investigation on the cyclic behavior of joints in framed seismic structures, where HSTCBs are connected to R.C. columns cast in situ, are presented (see Colajanni et al. 2012). The specimens are representative of four-way joints made up with a

particular type of beam produced by the Italian industry Sicilferro Torrenovese in Torrenova (ME) called SER beam. The typology of the steel truss is the same already described in Chapter 2 for the push-out tests in *phase II* carried out at the University of Palermo by Badalamenti (2010). Studies in the literature on the cyclic behavior of the connection between HSTCBs and columns point out that, in the absence of specific technological solutions, a rapid degradation of the stiffness of the connection can arise starting from the first loading cycles and the shear failure of the metallic truss of the beam or a remarkable "pinching" of the hysteresis cycles, resulting in poor energy dissipation, can occur (Sanpaolesi et al. 1987, 1988). Furthermore, because of the difficulties in developing analytical models aiming at interpreting the complex mechanical behavior of the system, many authors carried out their researches by means of design-by-testing procedures (La Mendola et al. 2009; Badalamenti et al. 2009; Amato et al. 2010). In consideration of the aforesaid issues, the nodes object of the experimental testing are representative of portions of framed seismic structures and, thus, the test setup is realized in order to simulate the stress state in the joint induced by seismic actions. The objective of the investigation is to check the strength capacity and ductility of the beam-to-column joint in accordance with the requirements provided in the Italian code (D. M. LL. PP. 14 Jan 2008) and to determine the global behavior of the connection as well as the stress transfer mechanisms between the steel truss and the concrete in the proximity of the joint.

7.2.1 Experimental program and description of the specimens

The SER beam used to manufacture the specimens object of the experiments is made up of a metallic spatial truss obtained with inclined steel bars for R.C. structures type B450C which represent the transverse reinforcement of the beam; these web bars are then connected superiorly to an upper chord constituted by coupled rebars of the same type of the truss through fillet weldings and inferiorly butt-welded to a metal plate of smooth steel type S355. The described truss, manufactured in the industry, is then

completed in situ with the concrete casting. Figure 7.8 shows an example of the type of steel truss described. The truss of the SER beam is not provided with bearing devices and, as a consequence, it does not exploit the self-bearing capacity. It is worth to note that, for this reason, the elements of the truss are interrupted before the section next to the column and integrated with added rebars to ensure the transmission of the stress to the column.

For the execution of the experimental tests three specimens are manufactured. They all have the same geometric features and executive details which have been deduced from the calculation report produced by Sicilferro industry dealing with the design of a three-story building.

The specimens are representative of four-way nodes; a compressive force of magnitude equal to the load obtained by the structural calculation is induced on the column. It is applied through four outer bars connected to a 1000 kN hydraulic jack: in particular, on two specimens, representative of an internal node, a 800 kN force has been applied while in the third specimen, representative of an external node, the applied axial force was equal to 400 kN. In all three tests there is no confinement to the joint, actually provided by the cross beams of the 3D frame. Because of the purpose of the test, the load applied and the constraints imposed are such as to simulate a seismic stress state in the specimen.

The truss used for the SER beams is constituted by a lower steel plate 5 mm thick, three coupled bars 16 mm diameter which constitute the upper chord of the truss and diagonal web bars 12 mm diameter placed at a 300 mm spacing. The mechanical properties of the materials have been deducted from the certifications made by the Laboratory DISMAT of Canicattì (AG) who also managed the execution of the tests.

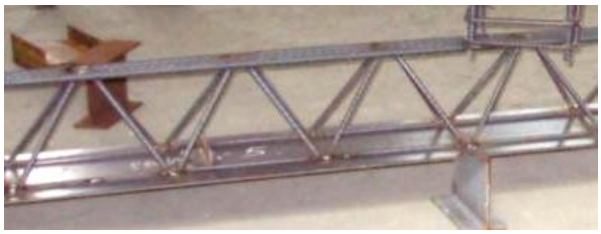

Figure 7.8. Truss of the SER beam.

The compressive strength of the concrete is assumed as the average value of the results of three tests conducted at 23 days since it is a fast-setting concrete; the obtained value is 36.52 N/mm^2. Tensile tests on reinforcing bars with steel type B450C and on elements extracted from the plate, whose steel is S355, provided the average values of the yield and ultimate stress, f_y and f_t respectively, reported in Table 7.2.

The SER beam presents reinforcing bars in number and position as shown in Figure 7.9. The cross-section of the beam is 300 mm width and 250 mm depth. As reported in some previous studies about the *SER beam*-to-column joint carried out at the University of Palermo (La Mendola et al. 2009), in the section of the beam next to the column it is possible to take into account the resistance contribution of only the added reinforcing rebars neglecting the contribution of the truss. Therefore the upper and lower areas of the reinforcement in the sections next to the joint are equal to 1808 mm^2 and 904 mm^2 which are due to 4Φ24 and 2Φ24 respectively.

In order to calibrate the test set-up, the ultimate moment in the end sections of the beam, only considering the added rebars, has been calculated as follows. In the case of positive moment, the tensile reinforcement is constituted by 2Φ24 with a side cover δ of 24 mm, while the compressed reinforcement is made up of 4Φ24 with a cover δ' of 40 mm. In the calculations, the average values of the strength of steel and concrete have been considered equal to f_y = 500.40 N/mm^2 and f_c = 0.83 • 36.5 = 30.31 N/mm^2, respectively.

Table 7.2. Characteristics of steel.

steel	Φ_b / s_p [mm]	f_y [N/mm^2]	f_t [N/mm^2]
B450C	16	498.46	596.32
	20	540.94	629.95
	24	500.40	614.85
S355	5	400.60	530.69

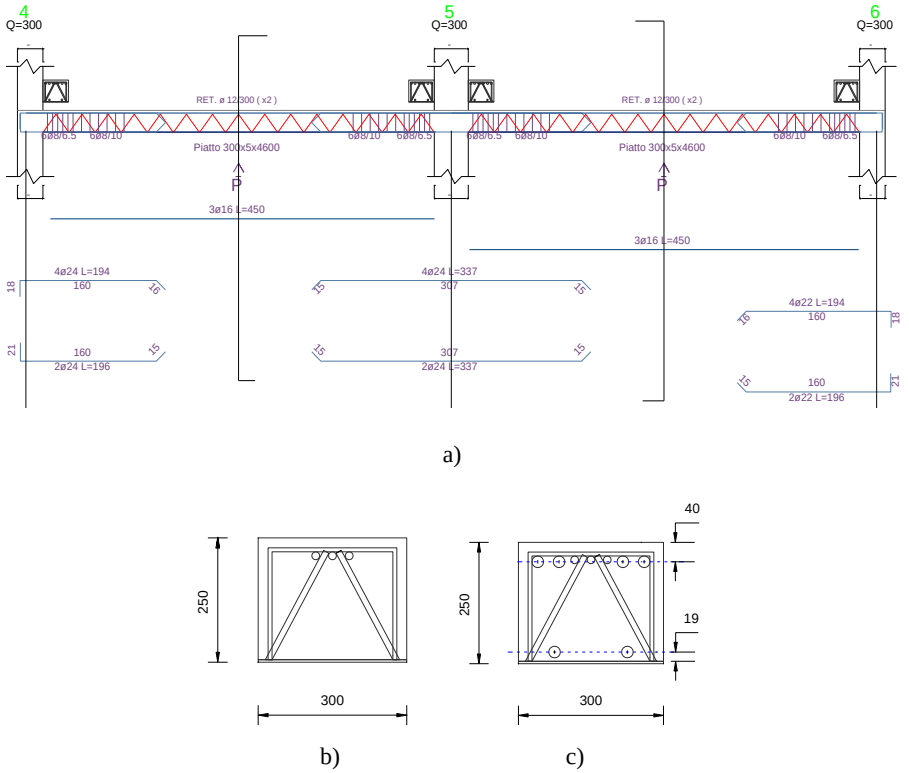

Figure 7.9. Executive details of the beam: a) longitudinal section and reinforcement (dimensions in cm); b) cross end section (dimensions in mm); c) cross-section corresponding to the midspan of the beam (dimensions in mm).

Therefore, the actual resisting moment is equal to 91.10 kNm with x_c = 44.39 mm and x_c/d = 0.20, being x_c the neutral axis position and d = h- δ = 226 mm the effective depth of the beam.

Similarly, in the case of negative bending moment, the effective resisting moment is equal to 166.83 kNm, with x_c = 67.64 mm, x_c/d = 0.32 and d = 210 mm.

R.C. columns cast in situ converge to the joint object of the experimental test. The cross-section of the column has dimensions 300x400 mm and the reinforcement resulting from the calculation consists of 10 rebars of 20 mm diameter. The total length of the column is 300 cm.

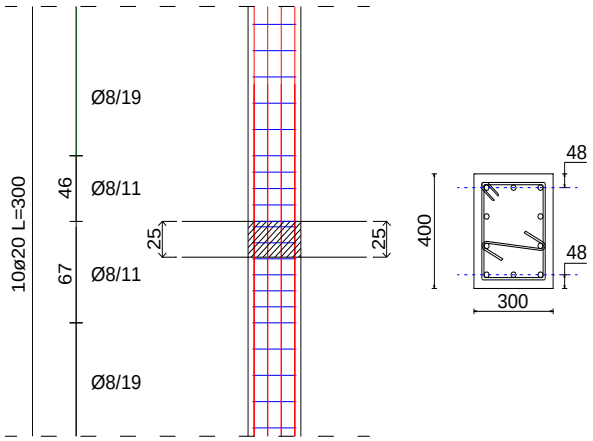

a) b)

Figure 7.10. Executive details of the column: a) longitudinal section (dimensions in centimeters); b) cross-section (dimensions in millimeters).

Figures 7.10a and 7.10b show the longitudinal and cross-sections of the column with the layout of the reinforcement.

Finally, Figure 7.11 shows the details of the reinforcement and the geometry of the test specimen consisting of two semi-beams and two semi-columns, as well as the location of the measurement technology.

As already mentioned, the two semi-beams of the specimen are of type SER made up with the truss described above. This truss is interrupted few centimeters before the joint and, therefore, the connection is made up by the addition of rebars, as it usually occurs in R.C. structures. Two of the top added bars have also been extended to the end of the beam and properly folded at the bottom to prevent unwanted premature shear failure. Inside the panel zone there are three stirrups placed at the same spacing they have within the column in the area next to the panel while, in the beams, the stirrups have a smaller spacing in the proximity of the joint.

In each one of the three specimens, strain gauges have been placed before the concrete casting: four strain gauges on both the upper and the lower added rebars, at a distance of 15 cm from the edge of the column. After the concrete casting two other strain gauges have been placed on the plate, one

in the middle of the first mesh and the other one in the middle of the next mesh.

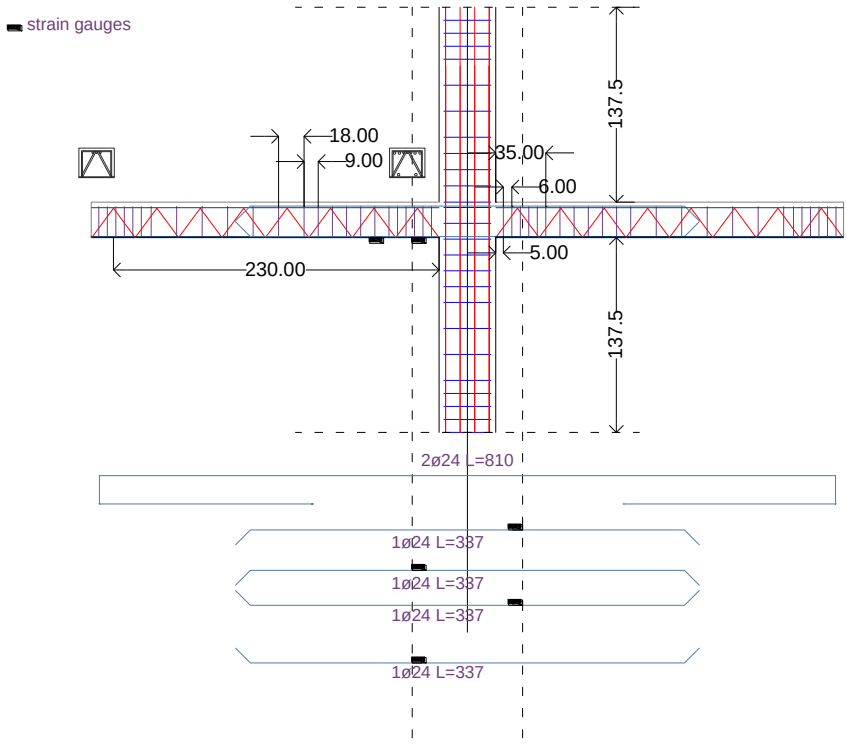

Figure 7.11. Executive details of the joint and position of the strain gauges on the steel rebars.

7.2.2 Test set-up and measurement technology

Figure 7.12 shows the scheme of the specimen with the constraints and the force provided in order to reproduce the load condition induced by the earthquake. In particular a bilateral sliding support at the ends of the beam and a fixed hinge on the top of the upper semi-column are realized. The horizontal load is applied by means of 170 kN hydraulic jacks collocated corresponding to the end of the inferior semi-column. The test is carried out in displacement control. The length L of the semi-beam is equal to 230 cm,

the length of the upper semi-column, h_2, until the center of the fixed hinge, is equal to 141 cm while, as regards the length of the lower semi-column, h_1, it differs depending on the point of application of the horizontal force and is given in the follow with the description of the three tests.

Before starting the test, a prestressing axial force has been applied by means of hydraulic jack of 1000 kN and four steel rebars type B450C 30 mm diameter threaded at the ends. The application of two LVDTs with 400 mm stroke and 0,01 mm precision allows to determine the global response of the structural system. Particularly, one LVDT is placed corresponding to the loaded section of the inferior semi-column and another transducer has been collocated for the measurement of the horizontal displacements of the semi-beam also with the aim of verifying that the friction was negligible (see Figures 7.12 and 7.13). The local response was determined through the application of the aforementioned six strain gauges with basis of measurement equal to 6 mm, collocated as described before.

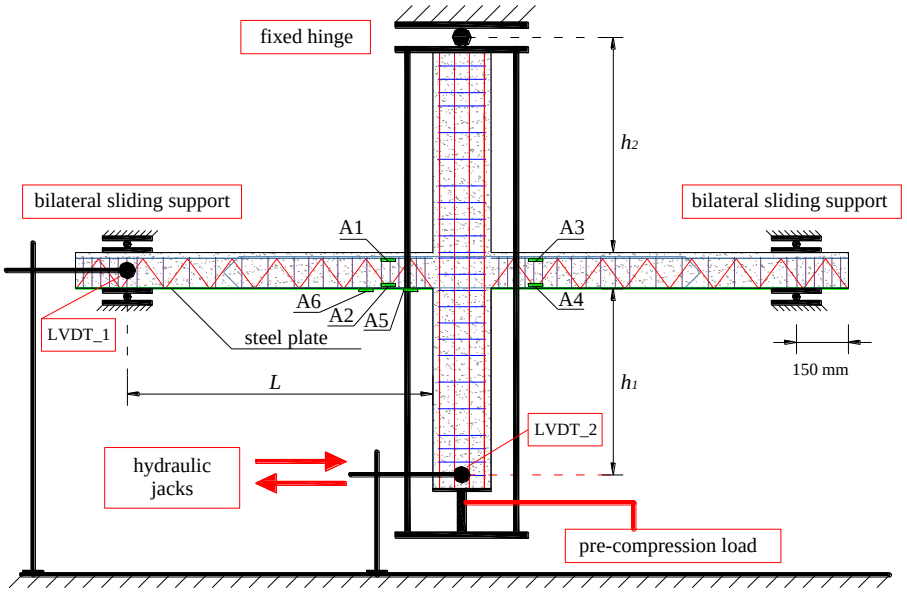

Figure 7.12. Scheme of the constraints and load condition of the specimen.

Figure 7.13. Test set-up in the laboratory and specimen placed in the contrast frame.

7.2.3 Experimental results

In the follow, the load-displacement curves and the measurements of some of the strain gauges are shown with the aim of interpreting the behavior of the joint under cyclic actions. In the first phase, loading cycles (whose results are not always shown in the diagrams) until the value of ± 25 kN are imposed to allow the arrangement of the specimen. The amplitude of the cycles has been established on the basis of both the prediction of the yield strength and the maximum resistance carried out, first, through simplified calculations based on equilibrium relationships in the joint and, then, through a more accurate modeling realized with a non-linear FE code. In the second phase, three cycles with increasing intensity of the load, up to approximately ± 50 kN, ± 75 kN and ± 100 kN, are imposed in order to reach the sub-horizontal branch of the load-displacement curve. Finally, few cycles in displacement control are imposed in different ways depending on the response of the specimen.

Test n°1. The test was carried out by imposing a pre-compression load of 800 kN on the column. The horizontal force was applied through 600 kN hydraulic jacks. With reference to the symbols in Figure 7.12, the distance h_1 of the point of application of the force from the intrados of the beam is equal to 107 cm. In Table 7.3 the values of the force and the displacements corresponding to the point where the load is applied (LVDT_2) as well as the drift expressed as the ratio in percentage between the displacement imposed and the length of the specimen (distance between the point of application of the load and the top hinge) are reported. In Table 7.4 the analogous values with reference to the displacement of the end of the beam (LVDT_1) and the drift calculated as the ratio between the displacement of the beam and the length of the upper semi-column, evaluated starting from the hinge to the axis of the beam, are shown. Finally in Figures 7.14 and 7.15 the corresponding load-displacement curves are reported.

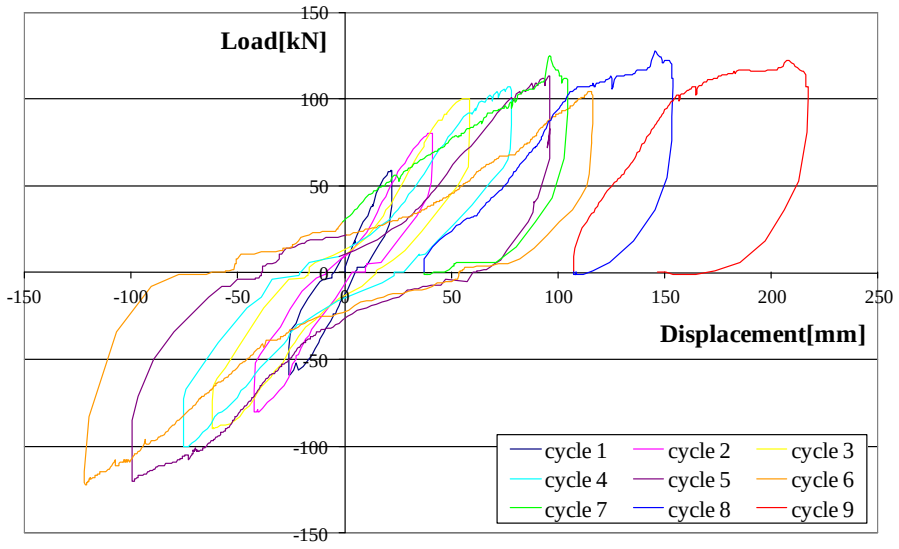

Figure 7.14. Test N°1: load-displacement curves corresponding to the point of application of the load (LVDT_2).

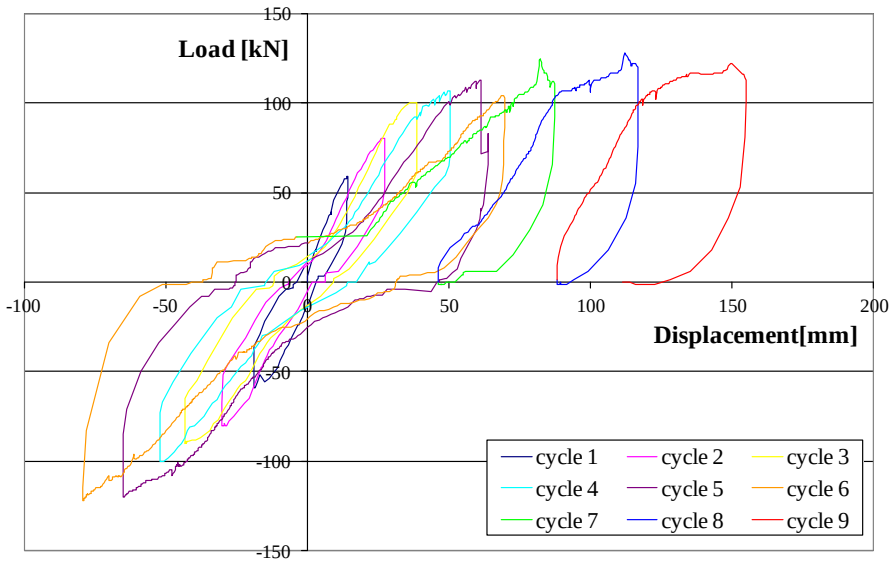

Figure 7.15. Test N°1: load-displacement curves corresponding to the axis of the beam (LVDT_1).

The load history shows that, in the first three cycles, the specimen exhibits no significant damage with limited stiffness reduction due to the cracking of the end sections of the beam. At the third cycle, for positive displacement equal to 59 mm and 2.16% of drift, the load of 100 kN is reached. This load is higher than the maximum theoretical load (equal to 94.48 kN) evaluated analytically on the basis of the resisting moments neglecting the hardening of the steel. For negative displacements, in consideration of the response of the specimen and with the aim of avoiding a strong asymmetry of the displacements, the load was limited to 90 kN in correspondence of which a displacement of 62 mm is measured. In the subsequent cycles number 4 and 5, the imposed displacement was increased of about 20 mm per cycle recording, for positive displacement, a load increasing of 7% in the 4th cycle and 13% in the 5th cycle while, for negative displacement, the increase obtained is of 11% in the 4th cycle and 33% in the 5th cycle. This latter loading cycle has a non-negligible pinching due to the cracking of the panel zone. In the next 6th cycle in which the

displacement varies in the range [-122 mm, +116 mm] the response exhibits a significant pinching without appreciable loss of strength, having reached a maximum load of 122 kN, for the negative displacement of 122 mm, and 104 kN, for the positive displacement of 116 mm. Starting from these conditions, increasing loading cycles without sign inversion have been imposed. In spite of a considerable reduction of stiffness, a negligible loss of strength is observed, with a maximum load of 128 kN reached at the 8th cycle, 35.5% greater than the theoretical conventional resistance. The specimen exhibited a good capacity to dissipate energy with displacements up to 217 mm corresponding to a drift of 7.95%, condition in which the test was finally stopped. In Figure 7.16 are presented some details of the specimen at the end of the 6th cycle and at the end of the test.

In the following Figure 7.17, with reference to the position shown in Figure 7.18, the load vs. strain curves measured by the four strain gauges placed on the beam at 150 mm from the faces of the column are shown. For the first two cycles the behavior of the reinforcement is elastic, being the strain smaller than the yield one, equal to 0.25%, in all strain gages.

Table 7.3. Test N°1: load cycles and corresponding displacements of the point of application of the load.

Cycle	P_{max} (kN)	spt_{max} (mm)	Drift (+) (%)	P_{min} (kN)	spt_{min} (mm)	Drift (-) (%)
1	59	22	0.81	-59	-26	0.95
2	80	41	1.50	-80	-42	1.54
3	100	59	2.16	-90	-62	2.27
4	107	78	2.86	-100	-75.6	2.77
5	113	96	3.52	-120	-100	3.66
6	104	116	4.25	-122	-122	4.47
7	125	105	3.85	0	37.2	1.36
8	128	154	5.64	0	107.7	3.95
9	122	217	7.95	0	148	5.42

Table 7.4. Test N°1: load cycles and corresponding displacement of the axis of the beam.

Cycle	P_{max} (kN)	spt_{max} (mm)	Drift (+) (%)	P_{min} (kN)	spt_{min} (mm)	Drift (-) (%)
1	59	14	0.91	-59	-19	1.24
2	80	27	1.76	-80	-30	1.95
3	100	39	2.54	-90	-43	2.80
4	107	51	3.32	-100	-52	3.39
5	113	64	4.17	-120	-65	4.23
6	104	70	4.56	-122	-79	5.15
7	125	87	5.67	0	46	2.99
8	128	117	7.62	0	88	5.73
9	122	155	10.10	0	111	7.23

When the maximum positive displacement of the third cycle is achieved and the load produces the yielding of the tensile upper and lower reinforcement corresponding to the section next to the column, the plastic strains are still limited to the area next to the column and the strain gages, placed at 150 mm from the face of the column, do not record deformations higher than the yielding strain.

In the subsequent cycles, the plastic deformations propagate along the entire length of the plastic hinge reaching, for negative loads, high values in the bottom tensile rebars (strain gauges A4) and values close to the yielding in the upper tensile bar (strain gauge A1). The maximum tensile strains in the strain gauges A2 and A3 are lower than those corresponding to the yielding and show that, for positive displacements, the plastic deformations of the reinforcement do not reach the monitored section.

In Figure 7.19 the curves of the strains recorded by the strain gauges A5 and A6 placed on the bottom steel plate are shown. In particular, strain gage A5 is placed within the first mesh of the truss next to the panel while strain gage A6 is collocated in correspondence of the following mesh, at 450 mm of distance from the face of the column.

The values of the deformations in the strain gauge A5 show that, in the proximity of the panel zone, the bottom steel plate, not enough anchored

within the joint, does not participate significantly to the strength of the panel, while the increase of the magnitude of the deformations recorded by strain gauge A6, compared to a corresponding reduction of the bending moment, shows that the diagonal bars of the truss are effective in the stress transferring to the bottom plate.

a)

b)

c)

Figure 7.16. Test n°1: a) the configuration of the specimen at the end of the 6th cycle; b) cracking of the panel zone at the end of the test; c) plasticization of the end of a beam**.**

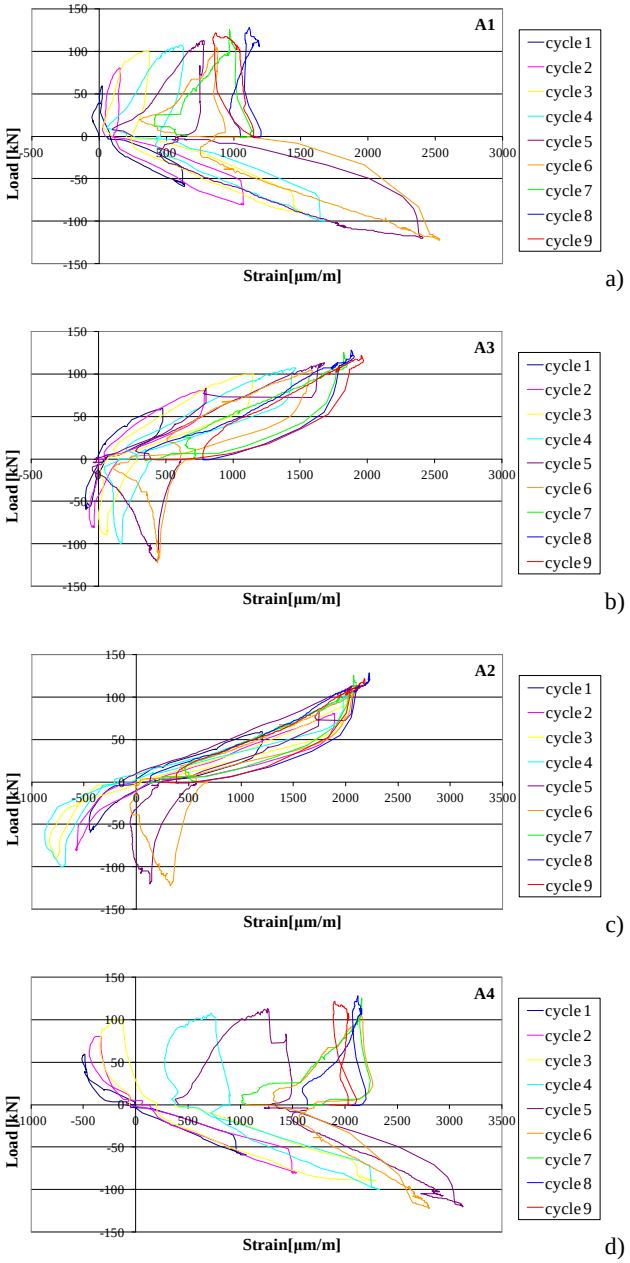

Figure 7.17. Load-strain curves of the longitudinal reinforcement in Test N°1: a) strain gauge A1; b) strain gauge A3; c) strain gauge A2; d) strain gauge A4.

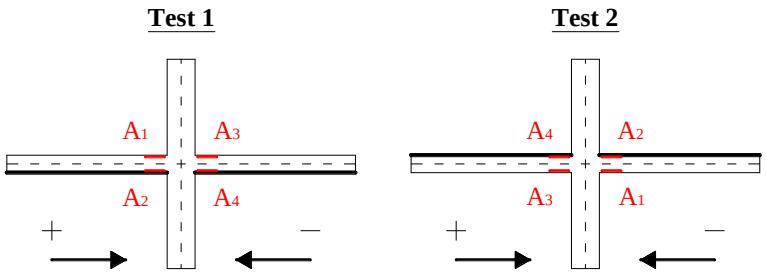

Figure 7.18. Schematic position of the strain gauges on the longitudinal rebars and sign of the applied force in tests N°1 and N°2.

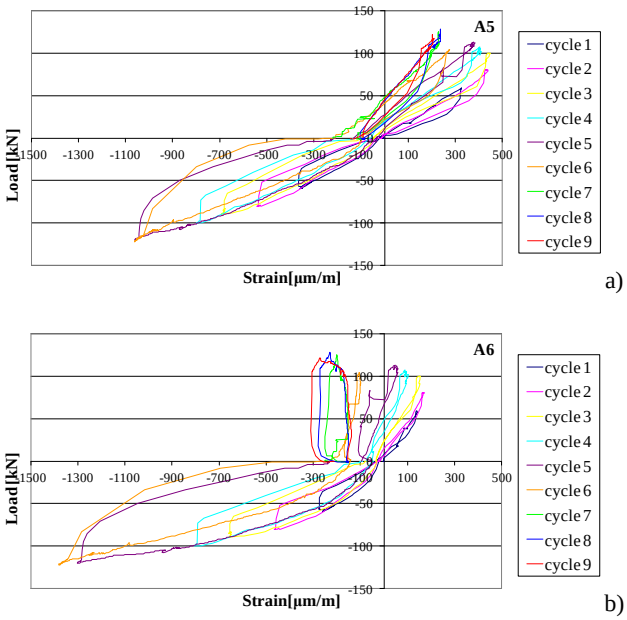

Figure 7.19. Load-strain curves of the bottom steel plate in Test N°1: a) strain gauge A5; b) strain gauge A6.

Test n°2. The second test is carried out with the steel plate of the specimen placed on the top. The applied prestressing load is equal to 800 kN. The horizontal force is applied at a distance h_1 = 128 cm using 170 kN hydraulic jacks with a maximum stroke of 400 mm. In Figure 7.20 the load-

displacement curves of the point of application of the load recorded by LVDT_2 are shown and in Table 7.5 the corresponding values of load and displacement at the extremes of the cycles are reported together with the values of drift. In Figure 7.21, with reference to the position indicated in Figure 7.18, the measurements of the strain gauges A1, A2, A3 and A4 are shown. After the first two cycles of adjustment of the specimen, three cycles in load control, with values of the force equal to ± 26 kN, +52, -51 kN and +75, -77 kN, are imposed; in all three cycles the response of the structure is elastic as it can be seen from the maximum deformations measured by the strain gauges A2 and A4 equal to 0.18% and 0.12%, respectively. The next 4th cycle for positive load was led up to the yielding of the tensile reinforcement of both plastic hinge sections next to the column, achieving a load of 104 kN that is 18.5% higher than the conventional resistance analytically estimated (equal to 87.73 kN). During the test the displacements grew up to the value of 84 mm (corresponding to a drift of 2.85%).

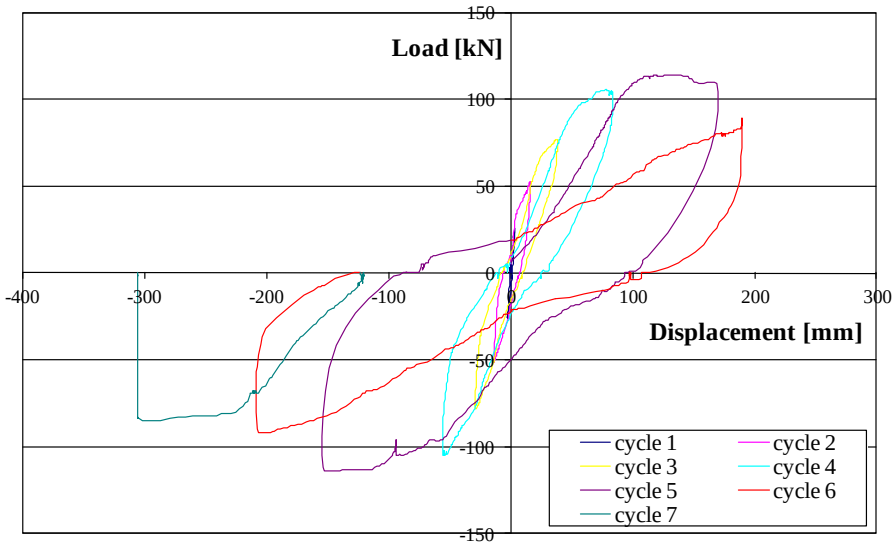

Figure 7.20. Test N° 2: load-displacement curves point of load application (LVDT_2).

Table 7.5. Test N°2: load cycles and corresponding displacements of the point of load application.

Cycle	P_{max} (kN)	spt_{max} (mm)	Drift (+) (%)	P_{min} (kN)	spt_{min} (mm)	Drift (-) (%)
1	26	3	0.11	-26	-2	0.08
2	52	16	0.55	-51	-13	0.46
3	75	38	1.30	-77	-29	0.99
4	104	84	2.85	-105	-56	1.90
5	104	170	5.78	-112	-154	5.24
6	81	189	6.45	-90	-208	7.08
7	0	-123	4.20	-82	-306	10.42

At the reversal of the sign of the load, the same resistance (-105 kN) has been achieved for a lower displacement equal to -56 mm, showing a negligible damage of the specimen. Also the crack pattern corresponding to the 4th cycle shows the opening of cracks of appreciable amplitude only in the areas of the beam next to the column and small cracks in the panel zone. The value of the strain equal to 0.30% recorded by the strain gauge A2 for positive loads (see Figure 7.21c) shows that the plastic deformations in the reinforcement are widespread, stating an appropriate extension of the area of the plastic zone. On the contrary, for negative loads, no significant plastic deformations are observed.

During the 5th cycle, carried out in the field of the large plastic displacements [-154 mm, +170 mm] in correspondence of values of drift [-5.24%, +5.78%] the specimen exhibited a further increase in resistance to negative loads and no loss of resistance to positive loads, with loads of +104 kN and -112 kN; the latter maximum value reached in the test is 27.73% greater than the conventional resistance. The shape of the hysteresis loop was characterized by a modest pinching showing good capacities of dissipation. The plastic deformations in the monitored sections have grown of 12.24% and 12.33% in the strain gauges A1 and A2 respectively (Figures 7.21a and 7.21c).

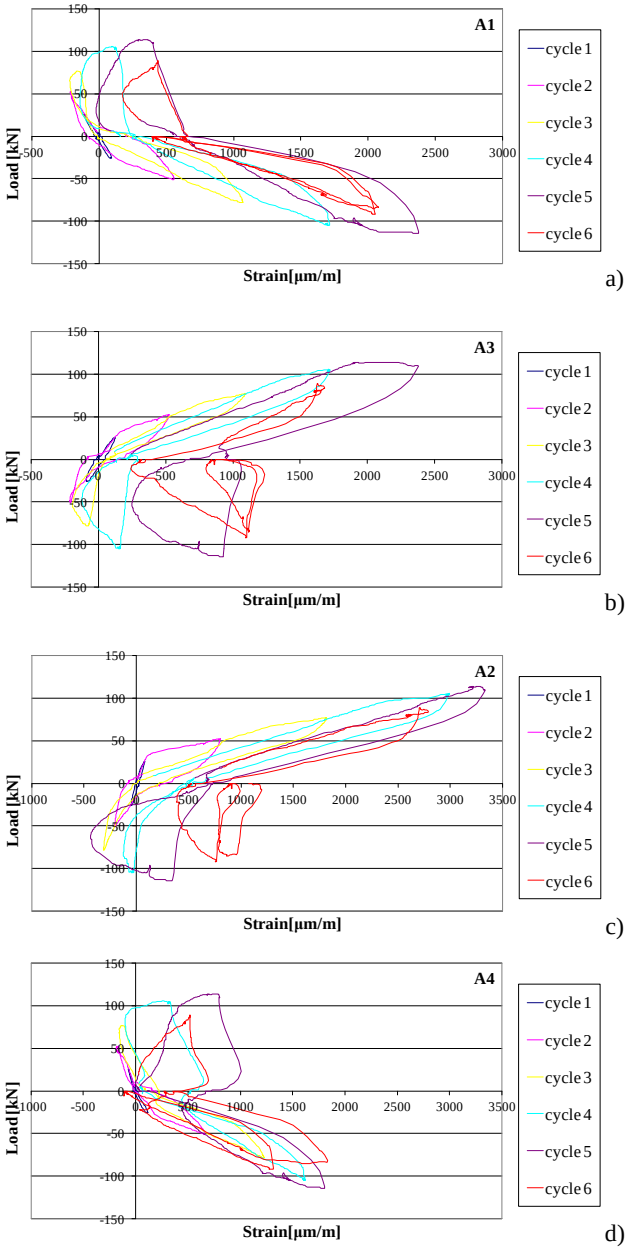

Figure 7.21. Load-strain curves of the longitudinal reinforcement in Test N°2: a) strain gauge A1; b) strain gauge A3; c) strain gauge A2; d) strain gauge A4.

Figure 7.22. Test N°2: configuration of the specimen at the end of the test.

In the 6th cycle, carried out once again in displacement control, by increasing the displacements [-208 mm, +189 mm] corresponding to drift [-7.08%, +6.45%], a reduction of the stiffness and strength of the specimen has been observed, with a maximum load of -90 kN and 81 kN corresponding approximately to the 80% of the maximum loads achieved in the previous cycles and, in any case, exceeding the limit of the theoretical yielding. The reduction of the dissipation capacity in the field of high ductility requirements is proved by the observed significant pinching.

Figure 7.22 shows the configuration of the specimen at the end of the test, characterized by a drift of 10.42% and a residual strength equal to the 73% of the maximum strength, higher than the maximum predicted value.

Test n°3. In the third test both the position of the specimen and the point of application of the load used in Test n° 2 have been assumed. A pre-compression load equal to 400 kN is applied in order to simulate the behavior of an internal joint of a perimeter frame.

In Figure 7.23 the load-displacement curves of the point of application of the load are reported. As it can be seen from Table 7.6, after having imposed the first two cycles of adjustment of the specimen, three cycles in load

control have been imposed with values of +28 kN, -27 kN; +46 kN, -47 kN; + 75 kN, -74 kN during which the response of the structure was elastic.

In the next 4th cycle a positive load of 100 kN was applied, almost equal to the maximum resistance of the specimen exhibited in the previous test, observing a displacement of 69 mm corresponding to a drift of 2.34% and, then, a negative load, able to yield the tensile reinforcement of both sections where the plastic hinges form in beam next to the column, obtaining a minimum load of -103 kN and a displacement of -84 mm (2.86% drift). In the next 5th cycle, carried out in the range of the large plastic displacements [-190 mm, +177 mm] corresponding to drift of [-6.48%, +6.01%], the specimen exhibited a further increase of resistance under positive loads until the maximum load of 108 kN and the minimum load of -95 kN are reached, corresponding respectively to the 124% and 108% of the predicted resistance, exhibiting a perfectly stable behavior in the field of the large plastic deformations. During this cycle a significant cracking of the panel zone is observed.

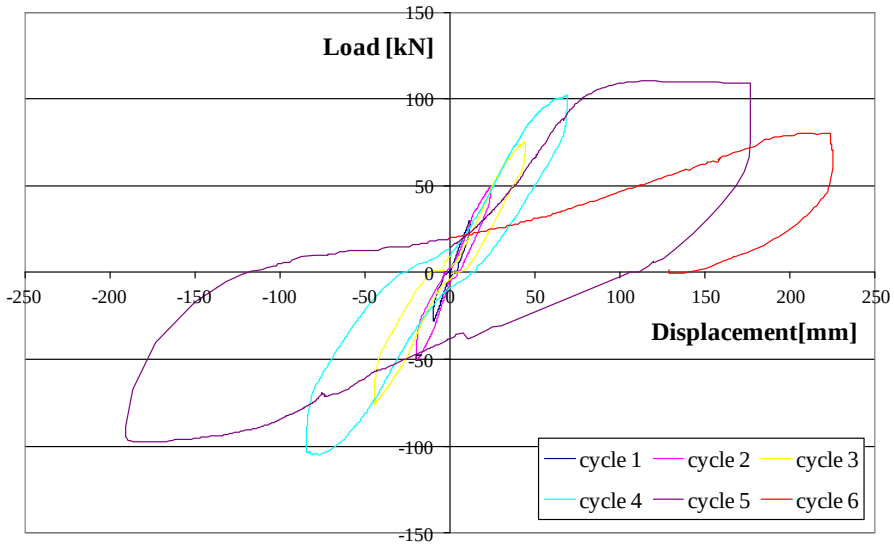

Figure 7.23. Test N°3: load-displacement curves of the point of load application (LVDT_2).

Table 7.6. Test N°3: load cycles and corresponding displacements of the point of load application.

Cycle	P_{max} (kN)	spt_{max} (mm)	Drift (+) (%)	P_{min} (kN)	spt_{min} (mm)	Drift (-) (%)
1	28	12	0.41	-27	-10	0.33
2	46	24	0.81	-47	-19	0.66
3	75	44	1.51	-74	-44	1.51
4	100	69	2.34	-103	-84	2.86
5	108	177	6.01	-95	-190	6.48
6	80	224	7.61	20	0.28	0.01

In the 6th cycle a loss of stiffness and strength of the specimen is recorded, with a residual strength of 80 kN equal to the 74% of the maximum load achieved in the previous cycles and, in any case, greater than the theoretical value. Once the maximum value of the cycle is reached, however, the specimen exhibits the ability to undergo further plastic deformation increments without significant reductions of resistance and with a sub-horizontal branch up to a drift of 7.61% corresponding to a displacement of 224 mm when the test was stopped.

7.2.4 Numerical models

For the prediction and interpretation of the results of the tests, two models are developed. In the first extremely simplified model, by exploiting the symmetry of the specimen and on the basis of simple equilibrium relationships, the yielding and the failure loads, F_y and F_u, are estimated for each specimen.

For Test n°1, the equilibrium proves to be the following (in the absence of hardening):

$F_y = 2M_{min} / (h_1 + h_2 + h_{beam})$ = 2x91.10 / (1.07 +1.41 +0.25) = 66.74 kN;

$F_u = (M_{max} + M_{min}) / (h_1 + h_2 + h_{beam})$ = (91.10 +166.80) / (1.07 +1.41+ +0.25) = 94.48 kN;

where M_{min} = 91.10 kNm is the smaller of the resisting moments of the beam in the proximity of the joint (lower tensile fibers) while M_{max} = 166.80 kNm is the biggest resisting moments of the beam in the proximity of the joint (upper tensile fibers), h_1 = 1.07m and h_2 = 1.41m is the length of the columns and h_{beam} = 0.25 m is the depth of the beam.

In a similar way, for the other two tests the values F_y = 61.92 kN and F_u = 87.73 kN are obtained, being h_1= 1.28 m and h_2 = 1.41 m. Therefore, the prediction of the maximum load obtained is conservative.

A second modeling is realized by means of a non-linear FE code using a fiber model for predicting the behavior of the resistant elements of the specimen. In such a model, in the proximity of the beam-to-column joint, the resistant section is considered to be made up only of concrete and the longitudinal reinforcement, neglecting the contribution provided by the upper chord and the bottom plate of the steel truss. The truss is considered to be effective in providing strength and stiffness to the beam starting from the third mesh. The constitutive material behavior employed is a simplified bilinear behavior for steel and a five points relationship for the concrete; the stress-strain curves have been calibrated on the basis of the experimental tests. The tensile strength of the concrete has been neglected. In the model the overstrength capacity of the panel zone is assumed. Such a numerical model provides the curves for monotonic load which represent the envelope of the cyclic behavior. The yield strength F_y and the ultimate load F_u as well as the corresponding displacements of the point of application of the load (LVDT_2) and the axis of the beam (LVDT_1) are assessed in correspondence with the formation of the first plastic hinge and the formation of the collapse mechanism. The values are reported in Table 7.7.

Table 7.7. Results obtained by the numerical model.

Specimen	F_y (kN)	LVDT_2,$_y$ (mm)	LVDT_1,$_y$ (mm)	F_u (kN)	LVDT_2,$_u$ (mm)	LVDT_1,$_u$ (mm)
1	75.6	34.0	19.8	94.9	51.1	29.5
2	71.9	33.2	17.1	90.2	49.7	25.5
3	71.2	35.9	18.6	90.3	53.8	27.8

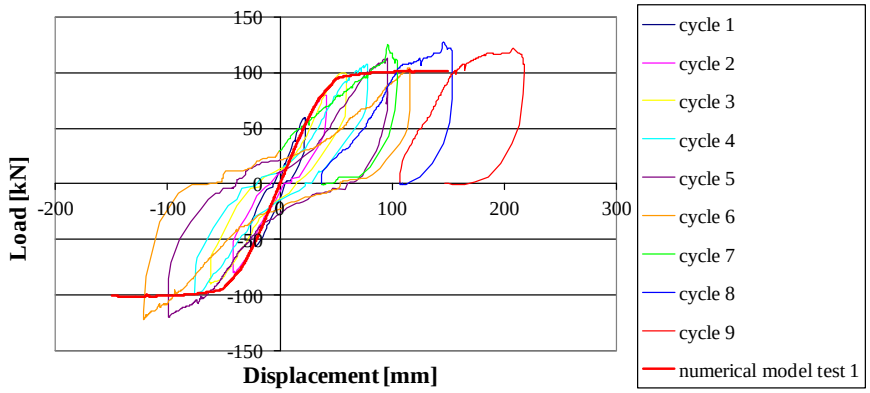

a)

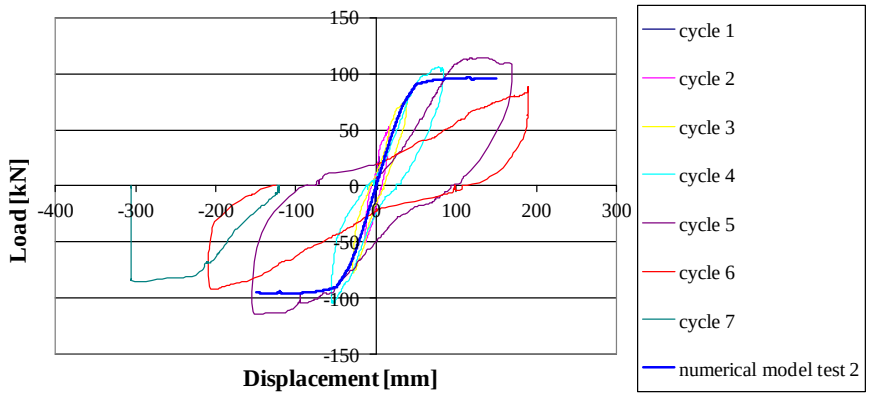

b)

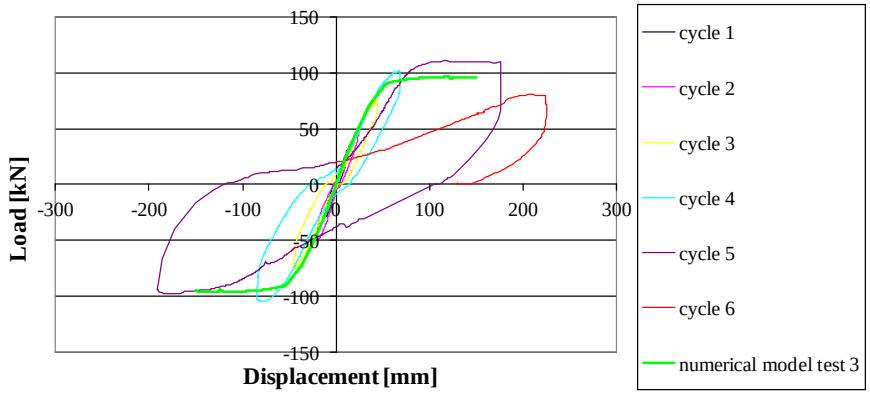

c)

Figure 7.24. Interpretation of the force-displacement cycles of the point of application of the load with the numerical model: a) Test N° 1; b) Test N° 2; c) test N° 3.

The analyses performed have also allowed to verify that the columns remain in the elastic range satisfying the capacity design criteria. Figure 7.24 shows the comparison in terms of load-displacement curves of the point of application of the load between the theoretical model and the experimental results for each one of the three tests.

7.2.5 Observations

The main observations arising from the analysis of the results obtained from the three tests can be summarized as follows.

- For the first loading cycles, carried out in order to not exceed the threshold of the yielding, the joint does not exhibit any significant damage and the specimen does not undergo significant reductions in stiffness, except those attributable to the cracking of the end sections of the beams.
- The subsequent cycles, obtained by increasing the displacement in the plastic range, exhibit a not negligible pinching due to the cracking of the panel zone but without a significant resistance reduction.
- For cycles with high values of displacement in the plastic range, the cracking of the specimen mainly involves the connection between the beam and column and a more limited area of the panel zone. The plots show a good capacity of the specimen to dissipate energy and an almost negligible loss of strength in spite of a reduction in stiffness. In this condition the panel zone of the tested specimen does not appear significantly damaged despite the lack of confinement that, in the real system, is ensured by the transverse beams converging at the joint.
- Under failure, reached for high values of displacement (of the order of magnitude of 20-30 cm, corresponding to drift of about 7-10%), the loss of strength of the system is contained and the joint is able to transmit loads in excess of those corresponding to the formation of the first plastic hinge.

Furthermore, the measurement of the horizontal displacement has allowed to exclude the hypothesis of concentration of the relative displacements in only one of the two semi-columns, revealing the absence of formation of plastic hinges in the columns and the respect, therefore, of the capacity design criteria.

The simplified calculations, carried out by exploiting the symmetry of the specimen and based on simple equilibrium relationships, leads to reliable values of load at yielding and ultimate state even if they are reduced with respect to those observed during the tests.

Finally, the more accurate modeling, realized by using a non-linear FE code, shows that the envelope curve, obtained in terms of load-displacement of the point of application of the load, well fits the experimental results of the cyclic tests giving a good assessment of the stiffness exhibited by the specimens both in the initial and cracked phase, although slightly underestimates the resistance.

CONCLUSIONS

In the present thesis the shear behavior of the *Hybrid Steel Trussed Concrete Beams (HSTCBs)* has been investigated focusing on the resisting mechanisms and the transfer of stresses between the steel truss and the surrounding concrete. Two main issues have been analyzed: the study of local problems of stresses transfer from the steel members to the concrete matrix, on one side, and the evaluation of the global shear behavior of the beam subjected to three-point bending test, on the other side.

From the local problems standpoint, experimental results of push-out tests in *phase II* on specimens of HSTCBs available in the literature have been considered. First, simplified numerical and analytical models for the interpretation of the resisting mechanism have been developed and, then, accurate FE simulations of the experimental tests have been generated.

The results of both the analytical strut-and-tie and dowel-mechanism models, as well as the outcomes of the simplified FE modeling, have shown that the attempt of interpreting the resisting mechanism occurring in the push-out test by means of simplified hypotheses, introduced in a 2D geometrical scheme, proves to be difficult since the mechanical response of the beam is highly influenced mainly by the 3D features of the geometry and the material non-linearities. As a consequence, the research has been continued elaborating more detailed FE models representative of the abovementioned experimental tests and able to grasp the complex stress transfer mechanism between the steel and the concrete. The numerical simulations, thus, take into account the actual geometry of the space truss of the beam and simulate the mechanical properties of the materials by means of accurate constitutive models mainly able to provide the strain-softening

damage of the concrete, the plasticity of the steel and the constitutive behavior of the steel-concrete interface. A preliminary check of the ability of the numerical model to grasp the basic dowel and bonding mechanism has been carried out by simulating some standard tests taken from the technical literature. Afterwards, the developed model has been verified against the push-out tests carried out by Aiello (2008). Lastly, the FE model has been used to provide a parametric analysis aimed at individuating the main geometrical and mechanical parameters influencing the maximum load that is possible to transfer from the steel diagonals to the concrete. The developed analyses have shown the significant influence of the following three principal factors: the concrete and steel class, the diameter of the diagonals of the truss, the type of the bars superficial finishing. Particularly, the mechanism has proved to be governed by the interaction between the steel and the concrete mainly depending on the constitutive behavior of the interface. In fact, even if in the simulated load-displacement curves a general trend of the peak load to increase is observed whenever the yielding strength of the steel and/or the compressive resistance of the concrete grow, then, starting from a certain value of the compressive strength of concrete, and depending on the bond stress-slip law implemented in the steel-concrete interface, such a trend has shown to change, denoting a less than linear increase of the maximum load value. Particularly, it has been showed that such numerical evidence might depend on the ability of the concrete to develop the plastic zone around the web bars, next to the bottom steel plate and near the section in which the plastic hinge in the steel takes place.

From the global shear behavior standpoint, an experimental campaign of three-point bending tests has been performed on specimens of a specific typology of HSTCB. The results showed that, in almost all cases, both for positive and negative bending moment, a fragile shear failure occurred, evidencing the crisis of the compressed concrete strut involved in the mechanism. Concerning the steel members, they are devoted in providing ductility to the system in those cases in which the mechanical properties of the concrete are sufficiently adequate and allow the failure of the strut to be delayed. However, in almost all cases, after the maximum load carried by the

beam is reached and the crisis of the concrete achieved, the steel contributes in providing a residual bearing capacity to the entire system until high values of displacement. The numerical simulation of the experimental tests allowed to confirm and clarify the resisting mechanism, giving further information on the distribution of the stresses in the concrete, the inclination and the width of the compressed strut, the formation of the plastic hinges in the web bars and the progressive qualitative evolution and quantitative extension of the crack pattern. Moreover, an analytical interpretation of the mechanical behavior of the tested beams has been proposed with the aim of obtaining a mathematical formulation for the assessment of the shear resistance. For the purpose, the sum of the two classical shear mechanisms contributions occurring in the R.C. structures have been considered and specialized with respect to the current problem: the "beam effect" and the "arch effect" mechanism. Then, also the contribution of the diagonal web bars and the bottom steel plate have been considered.

The global shear behavior has been further investigated also with reference to the evaluation of the size effect through FE simplified models on three different sizes of beam which, however, are capable of retaining the salient features of the response, involving 3D geometry, strain-softening damage of the concrete and plasticity of the steel. The models do not take into account the actual constitutive behavior of the steel-concrete interface; they have been generated, instead, exploiting the hypothesis of perfect bond between the rebars and the surrounding concrete. The comparison between the three numerical results on the 2D scaled geometry of the beams showed that the larger is the size of the beam the more ductile is the global response but, in every case, the system undergoes to failure with a fragile loss of the carried load. Moreover, the maximum load increases less than linearly passing from the smallest size of beam until the biggest. The accurate analysis of the numerical results pointed out that the mechanical response is governed by the formation of a principal crack which evolves along the diagonal direction whose inclination changes depending on the size of the beam. Such inclination proved to be almost vertical for the case of the intermediate size of beam. In the cases in which the global behavior of the

beam exhibited a certain ductility, the crack pattern evolution is significantly characterized by the presence of sub-vertical flexural cracks with a not always negligible amplitude. The scaled geometry of the truss highly influences the distribution of the stresses as well as the width and inclination of the compressed concrete strut involved in the response.

All achieved results that have been presented and discussed in the thesis, together with the accurate detail of the investigations carried out, allow possible further insights on the covered topics to be developed. For instance, concerning the study of the stress transfer mechanism, a wider parametric analysis could be planned with the purpose of generating simulations in which other parameters, such as the slope of the diagonal rebars, the number of bars constituting the upper chord or the depth of the beam, not yet considered, are taken into account. Moreover, the results of such numerical analyses could be exploited to formulate a more accurate analytical model for the assessment of the shear connection resistance in the beam typology.

Concerning the researches carried out on the size effect, instead, the execution of an experimental campaign on few different sizes of beam, compatible with the laboratory capacity, could represent an important tool of investigation which could be also exploited for the validation of further FE models. Furthermore, it could be significant to investigate the influence of different scaling criteria (such as a 3D criterion) also involving the steel members geometry and taking into account further sizes of beam in order to widen the covered cases. Finally, the results of the simulations could be used to formulate and validate an analytical model able to predict the shear strength of the HSTCB depending on the size effect.

In addition to the investigations which represent the main subject of the thesis, other studies have been developed as complementary researches dealing with two specific issues: the behavior of the bare steel truss under push-out test in *phase I*, aimed at investigating the buckling phenomenon which may arise in the compressed bars, and the experimental cyclic response of beam-to-column joints in framed seismic structures made up of HSTCBs connected to R.C. columns.

With reference to the interpretation of the push-out tests in *phase I*, the results have shown that the failure is governed by the buckling of the compressed web or upper chord bars. Under standard conditions, the failure occurred in the diagonal bars while the presence of stiffeners placed in order to inhibit instability made it possible to achieve a slight increase in the ultimate load, due to the buckling of the upper chord bars. For the assessment of the maximum load carried by the bare steel truss under standard conditions, the axial force redistribution in the web bars, allowed by shear forces and related flexural moments, has been taken into account and the equilibrium of the planar system has been considered. Conversely, in the presence of stiffeners, both the web and the upper bar not involved in the buckling remain in the elastic field, making the prediction of the specimen strength more difficult.

As regards the cyclic behavior of the beam-to-column joints, the study allowed to point out that, in the proximity of the panel zone, where the connection with the column is ensured almost only by the added inferior rebars, the bottom steel plate of the beam, not enough anchored within the joint, does not participate significantly to the strength of the panel. On the contrary, the diagonal web bars proved to be effective in the stress transferring to the bottom plate. In correspondence to the cycles with high values of displacement in the plastic range, the cracking of the specimen mainly occurred next to the connection between the beam and the column, involving a limited area of the panel zone. The system exhibited a general good capacity to dissipate energy with negligible loss of strength with respect to the corresponding reduction in stiffness and without significant damage. Furthermore, the absence of formation of plastic hinges in the columns and the respect of the capacity design criteria has been observed and confirmed by the numerical FE model of the beam-to-column joint which allowed to obtain the monotonic envelope of the experimental cyclic curves.

REFERENCES

Abaqus 6.10 Theory Manual, Dassault Systèmes Simulia Corp., 2010.

ACI Committee 318 (2008). “Building code requirements for structural concrete and commentary”, American Concrete Institute USA P.O.BOX9044-Framington Hills, MI 48333.

Aiello, M. A. (2008). "Analisi sperimentale della connessione acciaio-calcestruzzo nelle travi reticolari miste. (Experimental analysis of steel–concrete connection in hybrid truss beams)." *Proc., 7th Italian Workshop on Composite Structures,* Benevento (Italy), October 23-24, 33-42 (in Italian).

Amadio, C., Chisari, C., Plizzari, G., and Minelli, F. (2012). "Indagini preliminari sul comportamento a taglio delle travi PREM (Preliminary Investigations on the shear behavior of PREM beams)." *Proc., 19th C.T.E. congress,* Bologna (Italy), November 8-10, 101-112 (in Italian).

Amadio, C., Macorini, L., and Suraci, G. (2008). "Structural performance of a new hybrid RC-encased steel joist system. Advances in Reinforced Concrete and Precast Constructions." Marco di Prisco, eds., Strarrylink, Milan, 19-29.

Amadio, C., Macorini, L., Sorgon, S., and Suraci, S. (2011). "A novel hybrid system with RC-encased steel joists." *EJECE*, 15(10), 1433-1463.

Amadio, C., Sorgon, S., and Suraci, G. (2010). "Criteri di verifica per un sistema costituito da elementi tralicciati in acciaio inglobati nel calcestruzzo. (Verification criteria of a system constituted by steel trussed elements embedded in the concrete)." *Proc., 18th C.T.E. Congress,* Brescia (Italy), November 11-13 (in Italian).

Amato, G., Badalamenti, V., P. Colajanni, and La Mendola, L. (2010). "Comportamento ciclico delle connessioni tra travi prefabbricate reticolari miste e pilastri in c.a. (Cyclic behavior of the connection between hybrid trussed beams and R.C. columns)." *Proc., 18th C.T.E. Congress*, Brescia (Italy), November 11-13, 3-12 (in Italian).

Appa Rao, G., and Raghu Prasad, B.K. (2004). "Size Effect in Structural High Strength Concrete." *Proc., 5th International Conference on Fracture Mechanics of Concrete and Concrete Structures (FraMCOS-5)*, Vail, Colorado, USA, April 12-16, 1083-1089.

Appa Rao, G., and Sundaresan, R. (2012). "Evaluation of size effect on shear strength of reinforced concrete deep beams using refined strut-and-tie model." *Proc., Sadhana (Indian Academy Proceedings in Engineering Science)*, 37(1), 89–105.

Badalamenti, V. (2010). "Analisi teorico-sperimentale del comportamento ciclico delle connessioni tra travi prefabbricate reticolari miste e pilastri in cemento armato. (Theoretical and experimental analysis of the cyclic behavior of hybrid steel trussed concrete beam-to-column connections)." Ph.D. thesis, Università degli Studi di Palermo-Dipartimento di Ingegneria Strutturale, Aerospaziale e Geotecnica.

Badalamenti, V., Colajanni, P., La Mendola, L., Pucinotti, R., and Scibilia, N. (2008a). "Prove di push-out su travi reticolari miste. (Push-out tests on Hybrid Steel Trussed Concrete Beams)." *Proc., 17th C.T.E. Congress*. Rome, November 6-8, 183-192 (in Italian).

Badalamenti, V., Colajanni, P., La Mendola, L., Pucinotti, R., and Scibilia, N. (2008b). "Indagine Sperimentale su Tralicci in Acciaio di Travi Reticolari Miste. (Experimental investigation on steel trusses of hybrid trussed beams)." *Proc., 17th C.T.E. Congress*. Rome, November 6-8, 193-202.

Badalamenti, V., La Mendola, L., and Colajanni, P. (2009). "Analisi teorico-sperimentale del comportamento ciclico di sezioni di estremità di travi prefabbricate reticolari miste. (Theoretical-experimental analysis of the ciclic behavior of end-sections of hybrid precast trussed beams)." *Proc., 13th ANIDIS congress "L'Ingegneria Sismica in Italia"*, 28th June - 2nd July, Bologna (Italy), 1-10 (in Italian).

Badalamenti, V., La Mendola, L., and Colajanni, P. (2010). "Seismic behavior of hybrid steel trussed concrete beams." *Proc., 14th European Conference Earthquake Engineering*, Ohrid, Macedonia, CD-ROM, paper ID 1527, 1-8.

Bangash, M. (2001). *Manuals of numerical methods in concrete - Modelling and applications validated by experimental and site-monitoring data*. Thomas Telford, ASCE Press, Reston.

Bažant, Z. (1979). "Instability, ductility and size effect in strain-softening concrete." *Journal of Engineering Mechanics Division*, 102(2), 331–344.

Bažant, Z. (1984). "Size Effect in Blunt Fracture: Concrete, Rock, Metal." *J. Eng. Mech.*, 110(4), 518–535.

Bažant, Z. (1997). "Fracturing Truss Model: Size Effect in Shear Failure of Reinforced Concrete." *J. Eng. Mech.*, 123(12), 1276–1288.

Bažant, Z. P. (2000). "Size effect." *International Journal of Solids and Structures*, 37, 69-80.

Bažant, Z. P. (2005). *Scaling of Structural Strength*, 2nd Edition, Hermes-Penton Science, London, ISBN-9780750668491.

Bažant, Z. P., and Kazemi, M. T. (1988). "Brittleness and size effect in concrete structures." *Proc., Engineering Foundation Conference on Advances in Cement Manufacture and Use*, Trout Lodge, Potosi, Missouri, August 1-5, Paper ID n. 5.

Bažant, Z., and Oh, B. (1983). "Crack band theory for fracture of concrete." *Materials and Structures*, 16(93), 155–177.

Bažant, Z.P., and Kim, J. K. (1984). "Size effect in shear failure of longitudinally reinforced beams." *ACI Struct. Journal*, 81(5), 456-468.

Bažant, Z.P., and Yu, Q. (2004). "Size effect in concrete specimens and structures: New problems and progress." *Proc., 5th International Conference on Fracture Mechanics of Concrete and Concrete Structures (FraMCOS-5)*, Vail, Colorado, USA, April 12-16,153-162.

Bentz, E.C., and Collins, M.P. (2006). "Simplified form of the modified compression field theory (MCFT) for the analysis of beams." *Proc., 2nd Int. Conf. Fib*, June 5-8, Naples (Italy), ID 3-56.

C.S.LL.PP. Italian standard commission for constructions (2011). "Linee guida per l'utilizzo di travi tralicciate in acciaio conglobate nel getto di calcestruzzo collaborante e procedure per il rilascio dell'autorizzazione

all'impiego. (Guide Lines for the utilize of steel trussed beams embedded in collaborating concrete and procedures for the release of the authorization to the usage)."
<http://www.cslp.it/cslp/index.php?option=com_content&task=view&id=101&Itemid=20>

Campione, G. (2013). "Flexural and shear resistance of steel fiber-reinforced lightweight concrete beams." *ASCE J. Struct. Eng.*, DOI: 10.1061/(ASCE)ST.1943-541X.0000887.

Campione, G., Cucchiara, C., and Monaco, A. (2013). "Flexural and shear resistance of High-strength concrete beams", *Journal of Civil Engineering and Science (JCES)*, in press.

Campione, G., Fossetti, M., Minafò, G., and Papia, M. (2012). "Influence of steel reinforcements on the behavior of compressed high strength R.C. circular columns." *Eng. Struct.*, 34, 371–82.

Campione, G., Monaco, A., and Minafò, G. (2013). "Shear strength of High-strength concrete beams: modeling and design recommendations", *Eng. Struct.*, in press.

Canadian Standards Association (2004). CAN CSA A23.3-04 Design of concrete structures. CSA, Rexdale, Ontario, 2004.

Carpinteri, A. (1994a). "Fractal nature of material microstructure and size effects on apparent mechanical properties." *Mechanics of Materials*, 18, 89-101.

Carpinteri, A. (1994b). "Scaling laws and renormalization groups for strength and toughness of disordered materials." *International Journal of Solids and Structures*, 31, 291-302.

Cedolin, L., and Cusatis, G. (2007). "Cohesive fracture and size effect in concrete." *Proc., 6th International Conference on Fracture Mechanics of Concrete and Concrete Structures (FraMCOS-6)*. Catania (Italy). June 18-21, 17-29, ISBN 978-0-415-44065-3.

Cedolin, L., and Cusatis, G. (2008). "Identification of concrete fracture parameters through size effect experiments." *Cement and Concrete Composites*, January 2008, DOI:10.1016/j.cemconcomp.2008.05.007.

Chen, W. (1982). *Plasticity in reinforced concrete*. McGraw-Hill Book Company Inc., New York.

Chen, W., and Han, D. (1995). *Plasticity for structural engineers*. Gau Lih Book Co., Ltd, Taiwan.

Colajanni, P., La Mendola, L., and Monaco, A. (2011). "Modelli per l'interpretazione dei risultati di prove di push-out su travi reticolari miste (Models for the interpretation of push-out tests results on hybrid trussed beams)." *Proc., 14th ANIDIS congress "L'Ingegneria Sismica in Italia"*, Bari (Italy), September 18-22, CD-ROM (in Italian).

Colajanni, P., La Mendola, L., and Monaco, A. (2012). "Analisi sperimentale del comportamento ciclico di nodi di travi SER e pilastri in c.a. (Experimental analysis of the cyclic behavior of SER beam-to-R.C. column joints)." *Proc., 19th C.T.E. congress*, Bologna (Italy), November 8-10, 171-180 (in Italian).

Colajanni, P., La Mendola, L., and Monaco, A. (2014). "Stress transfer mechanisms investigation in hybrid steel trussed-concrete beams by push-out tests." *J. Constr. Steel Res.*, 95, 56-70.

Colajanni, P., La Mendola, L., and Recupero, A. (2013a). "Experimental test results vs. analytical prediction of welded joint strength in Hybrid Steel Trussed Concrete Beams (HSTCBs)." *EJECE*, 17(8), 742–59.

Colajanni, P., La Mendola, L., Monaco, A., Latour, M., and Rizzano, G. (2013b). "Assessment of push-out test response of hybrid steel trussed-concrete beams by FE model". *Proc., 15th ANIDIS congress "L'Ingegneria Sismica in Italia"*, Padova (Italy), 30th June - 4th July 2013, CD-ROM.

Cornelissen, H., Hordijk, D., and Reinhardt, H. (1986). "Experimental determination of crack softening characteristics of normal weight and lightweight concrete." *Heron*, 31(2), Delft University of Technology, Delft.

D. M. LL. PP. (1996). Norme Tecniche per le Costruzioni (Construction Technical Codes). Gazzetta Ufficiale, 9th Jan 1996 (in Italian).

D. M. LL. PP. (2008). Norme Tecniche per le Costruzioni (Construction Technical Codes). Gazzetta Ufficiale, 14th Jan 2008 (in Italian).

De Borst, R. (2002). "Fracture in quasi-brittle materials: a review of continuum damage-based approaches." *Engineering Fracture Mechanics*, 69(2), 95–112.

Desiderio, G., Latour, M., and Rizzano, G. (2011) "Modellazione analitica e FEM del meccanismo di trasferimento degli sforzi tra fondello in acciaio e calcestruzzo nelle travi PREM (Analytical and FE modeling of the stress transfer mechanism between the steel plate and the concrete in the PREM beams)." *Proc., 14th ANIDIS congress "L'Ingegneria Sismica in Italia"*, Bari (Italy), September 18-22, CD-ROM (in Italian).

Elfgren, L. (1989). *Fracture mechanics of concrete structures - From theory to applications*, Report of the Technical Committe 90-FMA Fracture

Mechanics to Concrete - Applications, RILEM Edition. Chapman and Hall Ltd, London.

Eligehausen, R., Popov, E.P., and Bertero, V.V. (1983). "Local bond stress-slip relationships of deformed bars under generalized excitations." Report No. UCB/EERC 83-23, Univ. of California, Berkeley (Ca, USA).

Eurocode 2 (1992). Design of Concrete Structures – Part 1: General rules and rules for buildings. European Committee for Standardization (CEN).

Eurocode 2 (2005). Design of Concrete Structures – Part 1: General rules and rules for buildings. European Committee for Standardization (CEN).

Eurocode 3 (2005). Design of steel structures – Part 1-1: General rules and rules for buildings. European Committee for Standardization (CEN).

Eurocode 4 (2005). Design of composite steel and concrete structures - Part 1–1: general rules and rules for buildings. European Committee for Standardization (CEN).

Faella, C., Piluso, V., and Rizzano, G. (2000). "Structural steel semirigid connections." CRC Press, Boca Raton.

Gálvez, J., Cervenka, J., Cendón, D., and Saouma, V. (2002). "A discrete crack approach to normal/shear cracking of concrete." *Cement and Concrete Research*, 32(10), 1567–1585.

Gelfi, P., and Giuriani, E. (1987). "Modello teorico del legame costitutivo per le connessioni a piolo. (Theoretical model of the constitutive relationship for studded connections)." *Studi e ricerche per le costruzioni*, F.lli Pesenti, eds., Milan, 9, 323-341 (in Italian).

Grassl, P., and Rempling, R. (2007). "Influence of volumetric-deviatoric coupling on crack prediction in concrete fracture tests." *Engineering Fracture Mechanics*, 74(10), 1683–1693.

Harajli, M. (2004), "Comparison of Bond Strength of Steel Bars in Normal- and High-Strength Concrete." *J. Mater. Civ. Eng.*, 16(4), 365–374.

Harajli, M.H., Hout, M., and Jalkh, W. (1995). "Local Bond Stress-Slip Behavior of Reinforcing Bars Embedded in Plain and Fiber Concrete." *ACI Materials Journal*, 92(4), 343-354.

Hibbitt, H., Karlsson, B., Sorenson, E. (2011). *ABAQUS Analysis User's Manual (Version 6.11)*. Pawtucket, Rhode Island.

Hillerborg, A. (1985). "The theoretical basis of a method to determine the fracture energy G_f of concrete." *Materials and Structures*, 18(4), 291–296.

Hillerborg, A., Modéer, M., and Petersson, P. (1976). "Analysis of crack formation and growth in concrete by means of fracture mechanics and finite elements." *Cement and Concrete Research*, 6(6), 773–782.

Hsu, H.L., Hsieh, J.C., and Juang, J.L. (2004). "Seismic performance of steel-encased composite members with strengthening cross-inclined bars." *J. Constuct. Steel Research*, 60, 1663-79.

Izzo, L., Minelli, F., and Plizzari, G. (2006). "Le travi reticolari miste nel cammino verso la normativa. (The hybrid trussed beams on the path toward the code)." *Proc., 16th C.T.E. Congress*. Parma (Italy), November 9-11, CD-ROM (in Italian).

Jirásek, M., and Bažant, Z. (2002). *Inelastic analysis of structures*. John Wiley & Sons, New York.

Johnson, R.P. (1994). *Composite structures of steel and concrete. Beams, slabs, columns and frames for buildings*, Blackwell Scientific Publication, London.

Ju, J. (1989). "On energy-based coupled elastoplastic damage theories: constitutive modeling and computational aspects." *International journal of solids and structures,* 25(7), 803–833.

Ju, Y.K., Kim, J.Y., and Kim, S.D. (2007). "Experimental evaluation of new concrete encased steel composite beam to steel column joint." *ASCE J. Struct. Eng.*, 133(4), 519-29.

Kachanov, L. M. (1958). "Time of the rupture under creep conditions." *Izvestiya Akademii Nauk SSSR,* Otdelenie, Techn. Nauk., 8, 26-31.

Karihaloo, B. (2003). "Failure of concrete." *Comprehensive Structural Integrity*, 2(10), 475–546.

Korol, E., and Tejchman, J. (2012). "Numerical studies on size effects in concrete baems. Architecture." *Civil Engineering, Environment, ACeE*, 2, 67-78.

Korol, E., and Tejchman, J. (2013). "Experimental and numerical investigations of size effects in reinforced concrete beams with steel or basalt bars." *Proc., 8th International Conference on Fracture Mechanics of Concrete and Concrete Structures (FraMCOS-8,* University of Castilla La-Mancha, Toledo, Spain, March 10-14.

Kupfer, H., and Gerstle, K. (1969). "Behavior of concrete under biaxial stresses." *Journal of Engineering Mechanics Division*, 99(4), 853–866.

La Mendola, L., Scibilia, N., Colajanni, P., and Badalamenti, V. (2009). "Indagine sperimentale su nodi di tralicci in acciaio di travi reticolari miste. (Experimental investigation on joints of steel trusses of hybrid trussed beams)." *Meccanica dei Materiali e delle Strutture*, 1(1), 108-123 (in Italian).

Lee J., and Fenves G.L. (1998). "Plastic-damage model for cyclic loading of concrete structures." *Journal of Engineering Mechanics*, 124(8), 892–900.

Lepech, M., and Li, V. C. (2003). "Preliminary Findings on Size Effect in ECC Structural Members in Flexural." *Proc., 7th International Symposium on Brittle Matrix Composites*, Warsaw, Poland, October 13-15, 57-66.

Lepech, M., and Li, V. C. (2004). "Size Effect in ECC Structural Members in Flexure." *Proc., 5th International Conference on Fracture Mechanics of Concrete and Concrete Structures (FraMCOS-5)*, Vail, Colorado, USA, April 12-16,1059-1066

Lubliner, J., Oliver, J., Oller, S., and Onate, E. (1989). "A plastic-damage model for concrete." *International Journal of Solids and Structures*, 25(3), 299–326.

Malm, R. (2009). "Predicting shear type crack initiation and growth in concrete with non-linear finite element method." Ph.D. thesis, Royal Institute of Technology (KTH) - Department of Civil and Architectural Engineering - Division of Structural Design and Bridges, Stockholm, Sweden.

Mang, H., Lackner, R., Meschke, G., and Mosler, J. (2003). "Computional modelling of concrete structures." *Comprehensive Structural Integrity*, 3(10), 536–601.

Mele, M., and Sassone, M. (2002). "Sistemi strutturali composti ad armatura superficiale: indagine sperimentale sul comportamento di nodi travi - pilastro soggetti a carichi ciclici. (Composite structural systems with superficial reinforcement: experimental investigation on the behavior under cyclic loads of beam-to-column joints)." *Proc., 5th Italian Workshop on Composite Structures*, Fisciano (Italy), November 28-29, 2, 191-200 (in Italian).

Mele, M., Ciampoli, M., and Menegatti, E. (1993). "Nuovi sistemi strutturali composti di acciaio e calcestruzzo: prime analisi sperimentali del comportamento sotto azioni cicliche dei nodi travi - pilastro. (New structural steel-concrete composite systems: first experimental analyses of beam-to-column joints under cyclic actions)." *Proc., 1st Italian Workshop on Composite Structures*, Trento (Italy), June 17-18, 85-98 (in Italian).

Millard, S. G., and Johnson, R. P. (1984). "Shear transfer across cracks in reinforced concrete due to aggregate interlock and to dowel action." *Magazine of Concrete Research*, 36(126), March 1984.

Ožbolt., J., Eligehausen, R., and Petrangeli, M. (1994). *The size effect in concrete structures*. E&FN Spon., eds., 2-6 Boundary Row, London, ISBN: 0419190406.

Puhali, R., and Smotlack, I. (1980). "Relazione sulle prove di push-out atte a determinare le leggi di carico-scorrimento delle travi in sistema composto tipo REP. (Report on the push-out tests fit for the determination of load–slip laws of REP composite truss beams)." *Science of Constructions Institute Acts.* University of Trieste (in Italian).

Rabotnov Y.N. (1969). *Creep problems in structural members*, North-Holland, Amsterdam 1969.

RILEM 50-FMC (1985). "Determination of the fracture energy of mortar and concrete by means of three-point bend tests on notched beams." *Materials and Structures*, 18(4), 285–290.

Rots, J. (2002). "Comparative study of crack models." *Proc., DIANA Conference*, October 2002, ISBN NR: 90 5809 530 4.

Saenz, I.P. (1964). "Discussion of equation for the stress-strain curve for concrete.", *ACI J.*, 61, 1229–1235.

Sanpaolesi, L., Caramelli, S., and Croci, P. (1987). "Indagine sperimentale su nodi di elementi prefabbricati trave- pilastro sotto fatica in campo plastico. (Experimental investigation on beam-to-column precast joints under fatigue in the plastic field)." *Proc., AICAP*, Stresa (Italy), April 23-25, 543-557 (in Italian).

Sanpaolesi, L., Croci, P., and Viviani, M. (1988). "Influenza del confinamento del calcestruzzo sul comportamento a fatica oligociclica di nodi trave – pilastro prefabbricati: indagine sperimentale (Concrete confinement influence on the oligocyclic fatigue behavior of precast beam-to-column joints: experimental investigation)." *Proc., 7th C.T.E. Congress*, Venezia (Italy), November 4-6, 63-70 (in Italian).

Sassone, M., and Casalegno, C. (2011). "La viscosità delle Travi Prefabbricate Reticolari Miste. (Viscosity of Precast Composite Truss Beams)." *Guida Tecnico Operativa per il professionista. Progettare con le Travi Prefabbricate Reticolari Miste PREM*, ISBN 978-88-481-2636-6, Tecniche Nuove, eds., Milan, 219-235 (in Italian).

Sassone, M., and Chiorino, M.A. (2005). "Design Aids for the Evaluation of Creep Induced Structural Effects." *Shrinkage and Creep of Concrete*, Gardner & Weiss eds., SP-227, 239-259.

SIA 262 (2003). Concrete structures. Code, Swiss society of Engineers and Architects, Zurich.

Swamy, R.N., Jones, R., and Chiam, A.T.P. (1993). "Influence of steel fibers on the shear resistance of lightweight concrete I-beams." *ACI Structural Journal*, 90(1), 103-114.

Tesser, L., and Scotta, S. (2013). "Flexural and shear capacity of composite steel truss and concrete beams with inferior precast concrete base." *Eng. Struct.*, 49, 135–45.

Tullini, N., and Minghini, F. (2013). "Nonlinear analysis of composite beams with concrete-encased steel truss." *J. Constr. Steel Res.*, 91, 1–13.

Tullini, N., Reato, P., and Cappellozza, M. (2006). "Indagini sperimentali su travi miste acciaio-calcestruzzo con connessione a traliccio. (Experimental investigations on hybrid steel–concrete beams with truss connection)." *Proc., 16th C.T.E. Congress*. Parma (Italy), November 9-11, CD-ROM (in Italian).

Verderame, G.M., De Carlo, G., Ricci, P., and Fabbrocino, G. (2009). "Cyclic bond behavior of plain bars. Part II: Analytical investigation." *J. Construction and Building Materials*, 23(2099), 3512-3522.

Vincenzi, L., and Savoia, M. (2010). "Stabilità di tralicci PREM in prima fase (Stability of PREM-beams in the first phase)." *Proc., 18th C.T.E. Congress*, Brescia (Italy), November 11-13, 849 - 858 (in Italian).

Vintzēleou, E.N., and Tassios, T.P. (1990). "Eccentric Dowels Loaded against Core of Concrete Sections." *ASCE Journal of Structural Engineering*, 116(10), 2621-2633.

VV. AA. (1987 and 1990). "Prove a flessione ed a taglio effettuate nell'ambito del Consorzio Produttori Travi Rep nel laboratorio della RDB a Pontenure - 1987 e 1990. (Bending and shear tests executed by the Producers Consortium Rep-beams at the RDB Laboratory in Pontenure - 1987 and 1990)." Available at CSP-Prefabbricati Industry.

VV.AA. (2011). *Guida Tecnico Operativa per il professionista. Progettare con le Travi Prefabbricate Reticolari Miste PREM*, ISBN 978-88-481-2636-6, Tecniche Nuove, eds., Milan.

Weibull, W. (1939). *A statistical theory of the strength of materials*. Generalstabens Litografiska Anstalts Forlag, Stockholm.

Weihe, S., Kröplin, B., De Borst, R. (1998). "Classification of smeared crack models based on material and structural properties." *International Journal of Solids and Structures*, 35(12), 1289–1308.

Willam, K. J. and Warnke, E. P. (1975). "Constitutive models for the triaxial behavior of concrete." *Proc., International Assoc. for Bridge and Structural Engineering*, 19, 1- 30.

Yasir Alam, S., and Loukili, A. (2010). "Application of digital image correlation to size effect tests of concrete." *Proc., 7th International Conference on Fracture Mechanics of Concrete and Concrete Structures (FraMCoS-7)*. B. H. Oh et al., eds., Korea Concrete Institute, Seoul, ISBN 978-89-5708-180-8.

Zararis, P.D. (2003). "Shear strength and minimum shear reinforcement of reinforced concrete slender beams." *ACI Structural Journal*, 100(2), 203-214.